Experimental and Analytical Studies on Reinforced Concrete Buildings with Seismically Vulnerable Beam-Column Joints

Sangjoon Park
Khalid M. Mosalam
Department of Civil and Environmental Engineering
University of California, Berkeley

Experimental and Analytical Studies on Reinforced Concrete Buildings with Seismically Vulnerable Beam-Column Joints

Sangjoon Park

Khalid M. Mosalam

Department of Civil and Environmental Engineering
University of California, Berkeley

ABSTRACT

Existing reinforced concrete (RC) buildings designed prior to the 1970s are vulnerable to shear failure of beam-column joints under earthquake excitations because of insufficient transverse reinforcement in the joint region. The failure of such "unreinforced" joints, especially corner joints, has played a crucial role in building collapses in past earthquakes. The accurate prediction of shear strength and flexibility for these unreinforced beam-column joints is therefore essential to assess the seismic risk of older-type RC buildings characterized by having unreinforced beam-column joints. To predict shear strength, two shear-strength models were developed previously, as a part of this larger study. A practical shear-strength model combining the two previously developed models is presented in this report.

To validate the shear strength models and to develop a moment-rotation relationship (backbone relationship) of unreinforced corner beam-column joint, four full-scale unreinforced corner beam-column joint specimens with two orthogonal beams and floor slab were tested under quasi-static cyclic load reversals simulating earthquake loading. The test results show that the joint shear strengths decrease with increase of the joint aspect ratio, and for a certain joint aspect ratio, the joint shear strengths are proportional to the beam longitudinal reinforcement ratio within the range of variables investigated in the test matrix. The proposed three models accurately predicted the shear strengths of the tested specimens. Based on the measured joint responses and visual observations of the tested four corner joint specimens, a backbone relationship was developed for nonlinear joint macro-modeling. Furthermore, the proposed backbone relationship was modified to be applicable to interior and roof beam-column joints. The strength parameters in the backbone relationships were defined using the proposed joint shear strength models. These backbone relationships were validated by accurate reproduction of the force-drift responses of the tested four corner joint specimens in this study and eight other exterior and interior joint specimens taken from the literature. Using these backbone relationships, nonlinear dynamic simulations were performed on three hypothetical prototype RC building frames. These simulations indicate that consideration of the flexibilities for unreinforced joints is important for seismic assessment of older-type RC buildings characterized by having unreinforced joints.

ACKNOWLEDGMENTS

CONTENTS

LIST OF FIGURES

LIST OF TABLES

1 Introduction

1.1 MOTIVATION

Numerous reinforced concrete (RC) buildings designed prior to 1970s still exist in the western United States and in other seismically active regions worldwide. These older RC buildings were usually designed for gravity load only or with little consideration of seismic forces and detailing. Accordingly, insufficient shear reinforcement was provided in columns and beam-column joint regions. To assess the risk of such seismically vulnerable RC buildings, significant experimental and analytical research activities have been conducted to investigate the capacity of shear-critical columns and to predict their axial failure [Lynn 2001; Sezen 2002; Elwood and Moehle 2003; Ghannoum 2007; Shin 2007]. Meanwhile, most studies on beam-column joints (hereafter beam-column joints are referred to as joints) have been performed to improve requirements for new joint seismic designs so that they have adequate strength and ductility. Relatively fewer studies have focused on seismic performance of older-type joints without transverse reinforcement in the joint region (referred to hereafter as "unreinforced"), an exception being the studies conducted at Cornell University in the early 1990s [Pesski et al. 1990; El-Attar et al. 1991; Beres et al. 1992]. However, because the specimens tested at Cornell University included unreinforced joints as well as other beam and column non-seismic details typically found in the eastern United States, the results are limited.

Earthquake reconnaissance reports [Uang et al. 1999; Sezen et al. 2000; Li et al. 2008; Günay and Mosalam 2010] have shown that the older-type RC buildings are prone to collapse due to failure of unreinforced joints, especially corner joints, see Figure 1.1. Currently, ASCE/SEI 41-06 [2006], referred to hereafter as ASCE 41, provisions have been widely adopted to predict the shear strength and drift capacity of joints observed in existing RC buildings. To investigate the relevance of the strength recommendations in ASCE 41, Park and Mosalam [2009] collected unreinforced exterior or corner joint test data of 62 previously tested specimens from 22 published papers and reports. The selection criteria were as follows: (1) beam longitudinal reinforcement hook is bent into the joint region; (2) beam width is equal to or smaller than column width; and (3) column shear and lap splice failures do not govern the response.

An evaluation of the joint shear strength reported in the collected database reveals that ASCE 41 may underestimate the shear strength of unreinforced exterior joints. Therefore, Park and Mosalam [2009] performed a parametric study using the test data from collected database and proposed two shear-strength models. This parametric study revealed that the shear strength of unreinforced exterior joints is strongly affected by two parameters: (1) the joint aspect ratio, which is defined as the ratio of beam to column cross-sectional depth; and (2) joint shear demand

related to the amount and strength of beam longitudinal reinforcement and the specimen geometry.
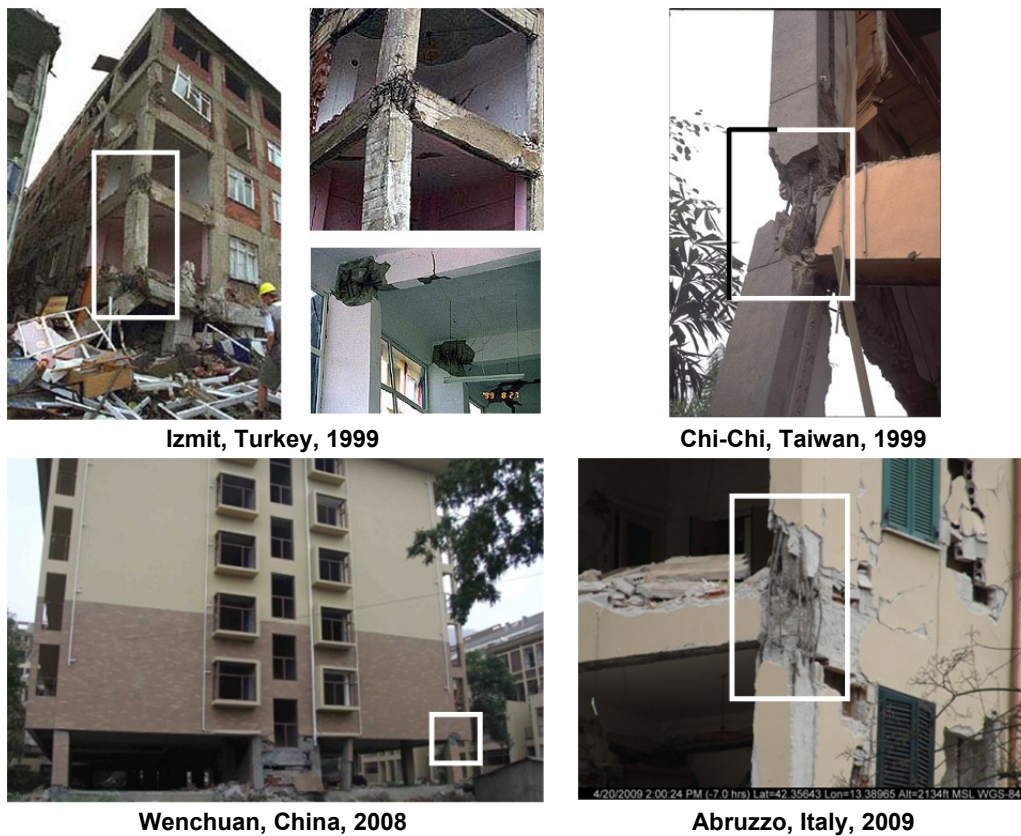
Figure 1.1   Failure of corner joints in past earthquakes.

However, the majority of tests in the database collected by Park and Mosalam [2009] were constructed without transverse beams and floor slabs and tested under constant column axial load for convenience, see Figure 1.2. Such planar exterior joints rarely occur in real buildings where transverse beams and floor slabs exist. Moreover, exterior and corner column axial loads do not remain constant under earthquake excitation due to the overturning moment of the building. In some tests, results obtained from small-scale specimens were questionable because of size effect, small size of aggregate, and use of uncommon reinforcing bar sizes. Given these limitations, full-scale tests on unreinforced joint specimens having transverse beams and floor slabs under variable column axial loads are necessary.

In simulation of RC buildings, beam-column joints are generally modeled as nodes where one-dimensional (1D) beam and column elements intersect each other, i.e., the orthogonality between beams and supporting columns is maintained during analysis. However, joint deformation may make a significant difference in the lateral response of RC buildings, particularly if the buildings contain unreinforced joints. To account for joint flexibility, several types of joint macro-models have been proposed by other researchers, such as separating joint shear deformation from slip rotation (referred to as explicit modeling) and combining the two types of deformations into a single variable (referred to as implicit modeling). Implicit modeling is a more practical option for simulating a building having a large number of degrees of freedom

in terms of numerical efficiency. For implicit modeling and for simulating old RC buildings accounting for joint flexibility, representative moment-rotation relationships for unreinforced joints are necessary.
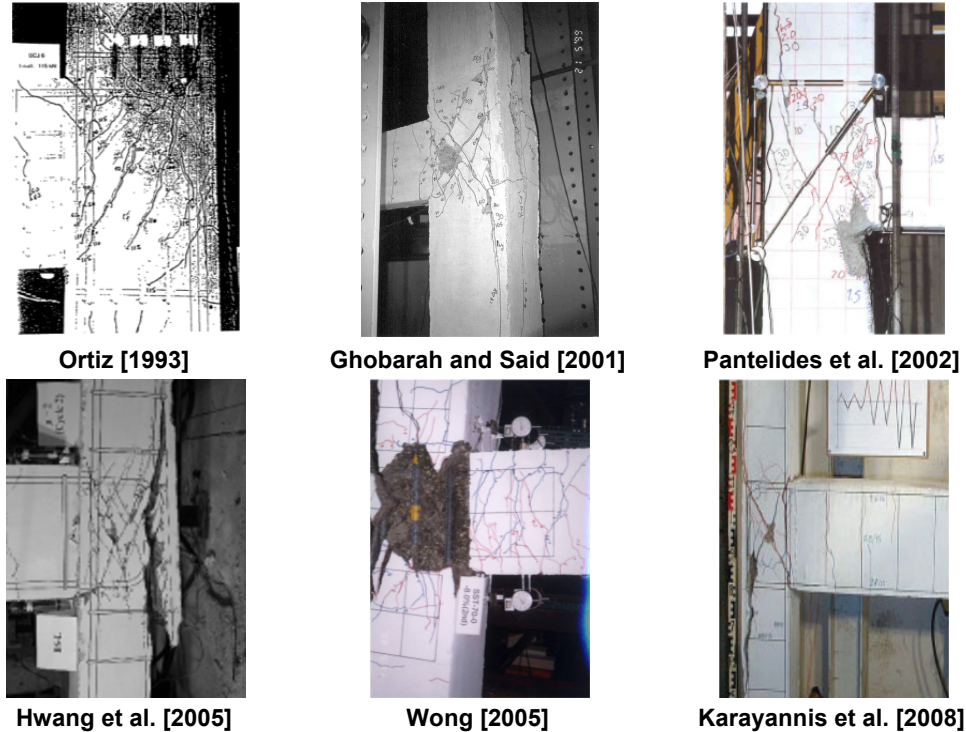
Figure 1.2   Tests on planar exterior joints in the literature.

1.2   RESEARCH OVERVIEW

This study was initiated as a key part of a collaborative project (NEES-Grand Challenge) aimed at assessing collapse risk and developing mitigation strategies for older-type RC buildings. The overview of the project is shown in Figure 1.3. Among several topics in the project, the behavior of unreinforced joints under earthquake loads is of interest in this study as indicated by the gray colored boxes in Figure 1.3. In this study, extensive analytical and experimental investigations were conducted to ultimately simulate the progressive collapse of older-type RC buildings and generate collapse fragility curves.

This study describes an experimental program that develops moment-rotation relationships (backbone relationships) of unreinforced joints to conduct simulations of beam-column subassemblies and hypothetical prototype building frames. For shear-strength prediction, two shear-strength models were developed by semi-empirical and analytical approaches [Park and Mosalam 2009], and a new practical model was developed. Testing of four full-scale unreinforced corner joint specimens was conducted to verify the proposed shear-strength models and to provide benchmark information for developing backbone relationships of unreinforced exterior joints. The developed backbone relationships were validated by accurate reproduction of the load-displacement responses of the tested four exterior joint specimens and four other planar exterior joint specimens taken from the literature. As a prelude of progressive collapse analysis

for older-type RC buildings, nonlinear dynamic simulations were performed on three hypothetical building frames using the developed backbone relationships.
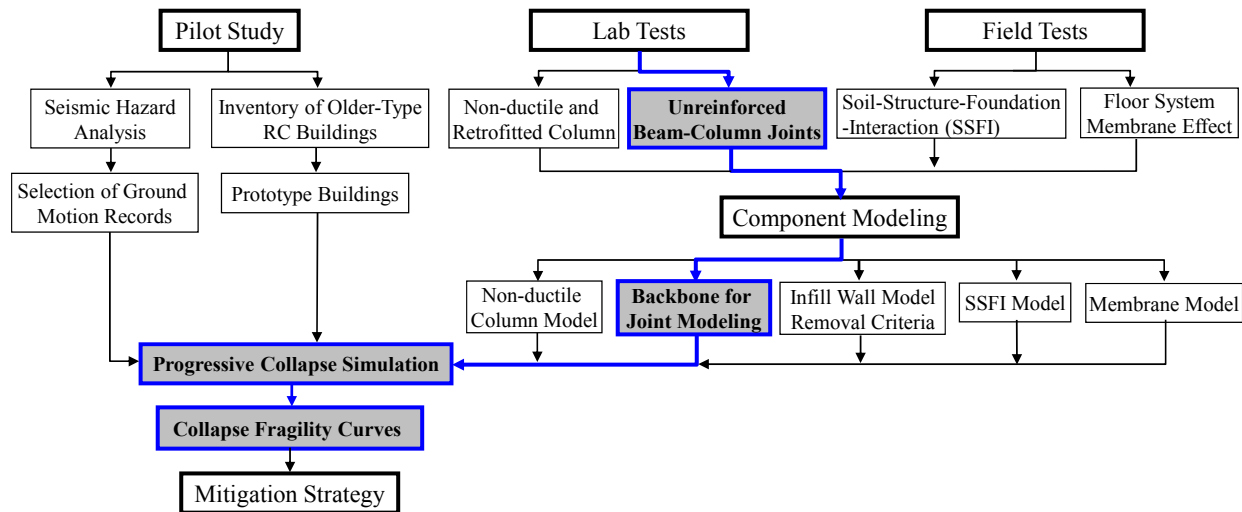
Figure 1.3   Overview of the research on older-type RC buildings (NEES-Grand Challenge).

1.3   SCOPE, OBJECTIVES, AND DEFINITIONS

This study investigated the behavior and modeling of unreinforced joints located in perimeter frames, see Figure 1.4. Joints included in interior frames were not considered in this study. Since the scope of this study was limited to the behavior of unreinforced joints without addressing failures of the column and beams adjacent to the joint, this study considered a strong column-weak beam configuration, and the anchorage details of the beam longitudinal top and bottom bars were those of bars bent into the joint region with 90° standard hooks.

As part of this experimental study, four full-scale unreinforced corner joint specimens were tested with the following objectives:

1. To investigate the effect of two key parameters on the shear strength of unreinforced exterior and corner joints: (1) joint aspect ratio; and (2) joint shear demand by control of beam longitudinal reinforcement ratio;

2. To verify the proposed shear strength models; and

3. To provide benchmark data for developing backbone relationship of unreinforced corner joints.

Simulations of RC building—including joint flexibility—were conducted with the following objectives:

1. To develop backbone relationships for unreinforced joints in the manner of an implicit joint macro-model;

2. To verify the developed backbone relationships and compare them with the ASCE 41 joint provisions; and

4

3. To investigate the importance of joint flexibility to the lateral responses of RC buildings by comparing the model with joint flexibility and the conventional model with rigid joints.

Terms consistently referred to throughout this report are as follows:

1. Beam-column joints are referred to as joints;

2. Unreinforced joints are defined as joints without transverse reinforcement in the joint region;

3. The longitudinal beam is the one that frames into the joint in the direction of loading for which the joint shear is being considered;

4. The transverse beam is the one that frames into the joint in a direction perpendicular to the longitudinal beam;

5. The corner and exterior joint is defined as a joint with columns above and below (only column below for the roof) and one longitudinal beam framing into the joint with one and no transverse beam, respectively, see Figure 1.4;

6. The interior joint is defined as a joint with columns above and below (only column below for the roof) and two longitudinal beams framing into the joint with one or no transverse beam, see Figure 1.4;

7. The joint aspect ratio is defined as the ratio of the total beam height, h_b, to column cross-sectional height, h_c, i.e., h_b/h_c;

8. The horizontal joint shear stress (v_{jh}) is referred to as joint shear stress;

9. The horizontal joint shear stress divided by the square root of the concrete standard compressive strength $\left(\sqrt{f'_c}\right)$ is referred to as normalized joint shear stress, i.e., $\gamma = v_{jh}\left/\sqrt{f'_c}\right.$;

10. Negative bending for a beam is defined as the flexural loading that causes tension in top reinforcement of the beam or tension in slab (in the case of the beam having a floor slab); and

11. Positive bending for a beam is defined as the flexural loading that causes tension in bottom reinforcement of the beam or compression in slab (in the case of the beam having a floor slab).
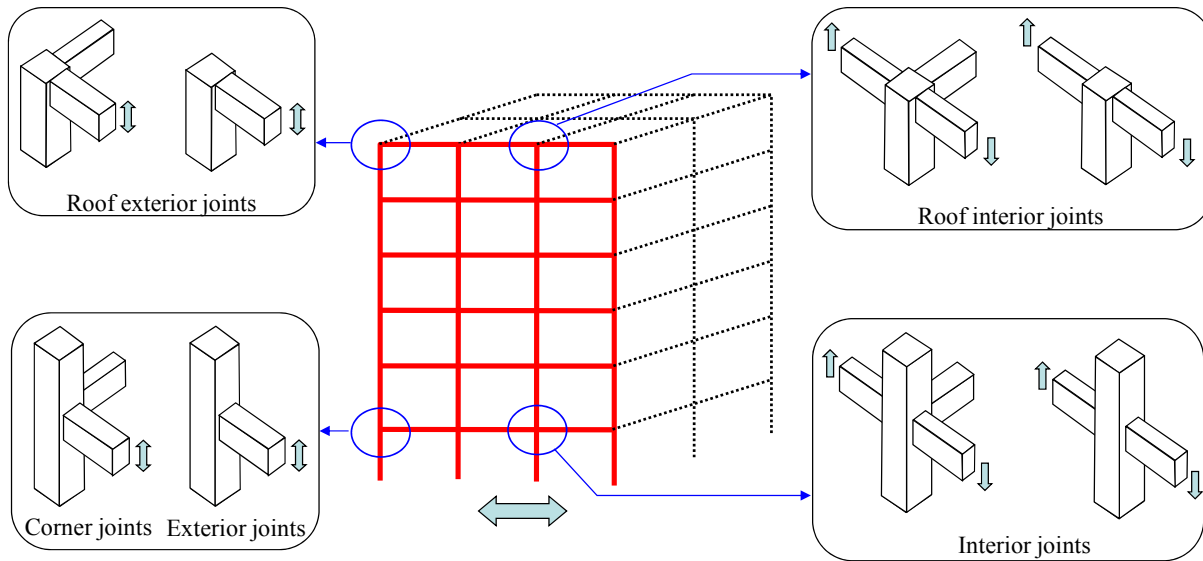
Figure 1.4   Considered beam-column joints and their definitions.

1.4   OUTLINE

This report consists of seven chapters and two appendices. Chapter 1 presents the motivation, overview, and contribution of this research to the collaborative NEES-Grand Challenge project, and the research objectives. The following main chapters are categorized into three parts as presented in Figure 1.5: (1) development of shear strength models for unreinforced exterior joints; (2) experimental tests on unreinforced corner joints; and (3) structural simulation using the developed shear strength models and backbone relationships.

In the previous report [Park and Mosalam 2009], a large experimental dataset of unreinforced exterior joints were collected from the published literature and parametric studies were performed using this database. Based on the parametric studies and overview of existing joint shear strength models, two shear strength models were developed using semi-empirical and analytical approaches. Chapter 2 presents summary of the derivations of the two shear strength models together with a third model that is more practical and combines these two models into a unified framework.

Chapter 3 describes the experimental program of four full-scale corner joint specimens including the details of specimen design and construction, material properties, loading protocol, test set up, and instrumentation plans. The evaluation of the test results and observations follow in Chapter 4, and the evaluated test results are discussed in Chapter 5.

The results of the structural simulations including joint flexibility are discussed in Chapter 6. Backbone relationships that represent the moment-rotation relationship of unreinforced joints were developed based on the measured joint responses and visual observations of joint damage propagation from the tests of the four specimens. For verification of the proposed backbone relationships, simulations were performed on the beam-column subassemblies of the specimens tested in the experimental part of this study and eight other specimens taken from the literature. Furthermore, nonlinear dynamic simulations were performed on three hypothetical building frames considered herein.

Chapter 7 presents a summary of the main findings and conclusions of this research. Several future research topics are listed to extend this research to progressive collapse analysis of older-type RC buildings.

Finally, this report includes two appendices. Appendix A presents the detailed design drawings of the four test specimens and test set up. Appendix B presents the concrete and reinforcing steel material properties obtained from sample tests.

Introduction	**Chapter 1: Introduction** 1. Motivations and Overview 2. Objectives, Scope, and Definitions
Joint Shear Strength Models	**Chapter 2: Development of Joint Strength Models** 1. Semi-Empirical Approach 2. Analytical Approach ⇒ Refer to *PEER Report 2009/106* (Park and Mosalam) 3. Practical Approach by unifying the two previously developed models
Experimental Tests and Discussion	**Chapter 3: Experimental Program** 1. Specimen Design 2. Loading Protocol 3. Instrumentation Plan **Chapter 4: Experimental Results** 1. Load-Drift Response 2. Visual Observations 3. Joint Shear Stress-Rotation Response **Chapter 5: Discussion of Experimental Results** 1. Comparison with Strength Predictions by Proposed Models 2. Effect of Joint Aspect Ratio 3. Effect of Beam Longitudinal Reinforcement Ratio 4. Effect of Column Axial Load, Slab, Loading Sequence, Column Intermediate Bars 5. Deformability of Unreinforced Corner Joints
Structural Simulation with Joint Flexibility	**Chapter 6: Simulation with Joint Flexibility** 1. Development of Backbone Relationships for Joint Modeling 2. Simulations of Beam-Column Subassemblies for Validation 3. Nonlinear Dynamic Simulations of Hypothetical Building Frames
Concluding Remarks	**Chapter 7: Summary, Conclusions and Future Extensions** 1. Summary and Conclusions of Performed Studies 2. Future Extensions for Progressive Collapse Analysis

Figure 1.5   Outline of the report.

7

2 Joint Shear Strength Models

This chapter presents ASCE 41 provisions and three shear-strength models to predict the response of unreinforced exterior joints to earthquake loading. The first two models were reported in Park and Mosalam [2009]. One mode—referred to as the empirical model--was developed based on mechanistic and empirical approaches, while the other model—referred to as the analytical model—is developed based on analytical approach utilizing available mechanistic concepts and formulae. A third model has been developed that integrates these two models into a unified framework with practical simplifications.

2.1 ASCE 41 PROVISIONS FOR JOINT STRENGTH

The ASCE 41 provisions are widely adopted to predict the shear strength of beam-column joints in existing RC buildings. According to ASCE 41, nominal joint shear strength is defined as

$$V_n = \gamma_n \sqrt{f_c'} b_j h_c \qquad (2.1)$$

where γ_n is the joint shear strength as a multiple of $\sqrt{f_c'}$, f_c' is the concrete compressive strength, h_c is the column cross-sectional height, and b_j is the effective joint width defined by either ACI 318-11 [2011] or ACI-ASCE 352-02 [2002]. The values of γ_n for joint shear strength calculation are presented in Table 2.1. Note that the joint shear strength of unreinforced exterior joints without transverse beams is $\gamma_n = 6$ psi$^{0.5}$ [0.5 MPa$^{0.5}$], which can be implicitly applicable to corner joints. If the joints are properly confined, the strength increases up to $\gamma_n = 12$ psi$^{0.5}$ [1.0 MPa$^{0.5}$], which is identical with the strength recommendation in ACI-ASCE 352-02 [2002].

Table 2.1   Values of γ_n for joint strength calculation in ASCE 41.

ρ''^{*}	γ_n [psi$^{0.5}$(MPa$^{0.5}$)]				
	Interior joint with transverse beams	Interior joint w/o transverse beams	Exterior joint with transverse beams	Exterior joint w/o transverse beams	Knee joint with or w/o transverse beams
< 0.003	12 (1.0)	10 (0.8)	8 (0.7)	6 (0.5)	4 (0.3)
≥ 0.003	20 (1.7)	15 (1.2)	15 (1.2)	12 (1.0)	8 (0.7)

[*] Volumetric ratio of the transverse reinforcement within the joint region.

2.2   SEMI-EMPIRICAL MODEL

Two key parameters, namely the joint aspect ratio and the beam longitudinal reinforcement ratio, were selected to derive the shear strength equation; the axial load ratio was not included due to its little and unclear influence on the joint shear strength. A parametric equation for each of these two parameters was derived based on mechanistic approaches, and some coefficients in the two equations were determined relying on a large number of laboratory test data collected from the literature. For consistency with current practice, the joint shear strength was assumed to be proportional to the square root of the concrete standard compressive strength [ACI 318-11 2011].

2.2.1 Joint Aspect Ratio Parameter

Assuming that a single diagonal strut carries all the horizontal shear force in the joint panel, as illustrated in Figure 2.1, the equilibrium equation is derived as follows,

$$V_n = c_0 \, D \cos\theta, \ \ \theta = \tan^{-1}\left(h_b / h_c\right), \text{ and } \ D = \sigma_d \, b_j h_s \tag{2.2}$$

where $c_0 \leq 1.0$ is a constant to be determined from the database, D is the compressive force in the diagonal strut, σ_d is concrete strength of the diagonal strut based on a softening concrete strength model, and h_s is the width of the diagonal strut at the C-C-T nodal zone, see Figure 2.1. To express the joint shear strength in terms of the square root of the concrete standard compressive strength $\left(\sqrt{f_c'}\right)$ and consider the simplicity of a linear reduction (in the denominator) of the compressive strength with the increase of the principal tensile strain, a softening concrete model suggested by Vollum [1998] is adopted to develop a relevant model for the concrete panel of unreinforced joints, i.e.,

$$\sigma_d = \frac{a_1 \sqrt{f_c'}}{0.8 + 170 \, \varepsilon_1} \tag{2.3}$$

where a_1 is a constant with value of 71.3 for psi units (5.9 for MPa units), and ε_1 is the principal tensile strain. As a validation of Vollum's model [1998], Table 2.2 shows that Equation (2.3) is almost identical— to within $0.003 \leq \varepsilon_1 \leq 0.004$ where the joint failure is generally expected— with another softened concrete strength model proposed by Zhang and Hsu [1998],

$$\sigma_d = \frac{\widetilde{a}_1 \sqrt{f_c'}}{\sqrt{1 + 250 \, \varepsilon_1}} \tag{2.4}$$

where $\widetilde{a}_1$ is a constant with value of 69.9 for psi units (5.8 for MPa units). Zhang and Hsu's model [1998] was developed using their test data and has been adopted by other researchers [Hwang and Lee 1999; Wong 2005].
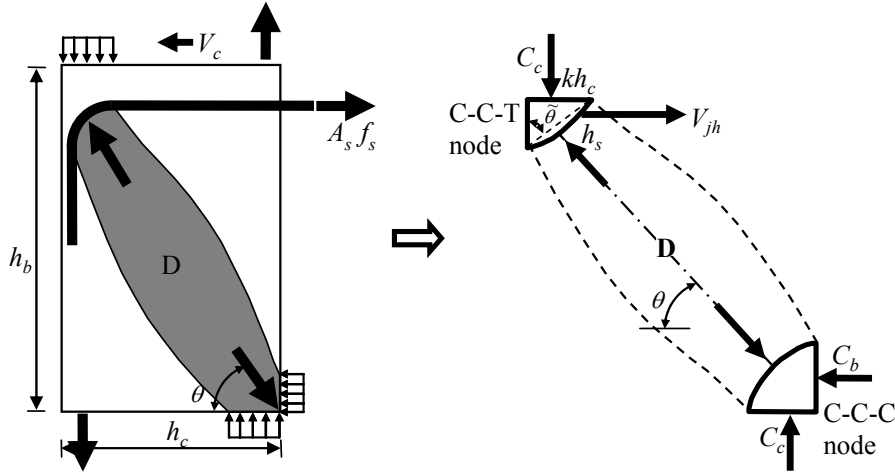
Figure 2.1   Single diagonal strut mechanism.

Table 2.2   Comparison of the softened concrete strength models.

f_c' **(psi)**	$\varepsilon_1 = 0.0030$		$\varepsilon_1 = 0.0035$		$\varepsilon_1 = 0.0040$	
	σ_{Vollum} [1]	σ_{Zhang} [2]	σ_{Vollum} [1]	σ_{Zhang} [2]	σ_{Vollum} [1]	σ_{Zhang} [2]
3000	2981	2894	2799	2796	2639	2707
4000	3442	3342	3233	3229	3047	3126
5000	3849	3736	3641	3610	3407	3495
6000	4216	4093	3959	3954	3732	3829
7000	4554	4421	4276	4271	4031	4135
8000	4868	4726	4572	4566	4309	4421
9000	5163	5013	4849	4843	4570	4689
10000	5443	5284	5111	5105	4818	4943
$\sigma_{\text{Vollum}} / \sigma_{\text{Zhang}}$	**1.03**		**1.00**		**0.97**	

[1] strain-softened concrete compressive strength using Vollum model [Equation (2.3)]
[2] strain-softened concrete compressive strength using Zhang and Hsu model [Equation (2.4)]

In existing analytical models [Hwang and Lee 1999; Wong 2005], average strain compatibility equations in the joint are adopted to determine ε_1, assuming that the principal tensile direction is simply orthogonal to the assumed diagonal strut. The average strain compatibility equations are generally valid for the membrane element having longitudinal and transverse reinforcement, but may not be applicable to unreinforced joints in the same way because there is no longitudinal and transverse reinforcement in the joint region. For example, Hwang and Lee [1999] used tensile yield strains of the beam and column longitudinal bars as the horizontal and vertical strains, respectively, of the joint to calculate the principal tensile strain. However, the yield strains of the beam and column bars do not represent the average horizontal and vertical strain of the joint, especially if the reinforcement does not yield.

Instead of using the average strain compatibility equation, this study approximated the principal tensile strain using the following two approaches. The first approach compared the

strength reduction calculated using the softening concrete strength model, i.e., Equation (2.3), with that of C-C-T node suggested by previous researchers and current codes. The selection of the C-C-T node was supported by the following published experimental results: (1) the joint shear failure was initiated adjacent to the top node when the beam top reinforcement was in tension [Vollum 1998]; and (2) the joint crack morphology implied that the crack opening was greatest at the C-C-T node, which led to the reduction of the strength of the diagonal strut. The second approach calculated the principal tensile strain using the joint shear strains measured from Clyde et al. [2000] and Pantelides et al. [2002].

From the results of these two approaches, the principal tensile strain at joint shear failure is approximated to be 0.0035 for joint aspect ratio of 1.0, which is close to the value of 0.003 proposed in Vollum [1998]. In addition, the principal tensile strain was assumed to be slightly greater for a higher joint aspect ratio based on the joint shear strains measured in tests from the subsequent experimental tests of this study. For simplicity, the principal tensile strain is proposed to be 0.0035 for $h_b/h_c = 1.0$ and 0.0040 for $h_b/h_c = 2.0$ as follows,

$$\varepsilon_1 \approx 0.003 + 0.0005\left(h_b/h_c\right) \tag{2.5}$$

The horizontal length of the C-C-T node, see Figure 2.1, is expressed using a constant s as follows,

$$h_s \sin\widetilde{\theta} = sh_c \tag{2.6}$$

where $\widetilde{\theta}$ is the angle of C-C-T node. Substituting Equations (2.3) and (2.6) into Equation (2.2), the horizontal equilibrium in the joint becomes

$$V_n = c_0 \left[\frac{a_1\sqrt{f_c'}\,b_j s h_c}{\left(0.8 + 170\varepsilon_1\right)\sin\widetilde{\theta}}\right]\cos\theta \tag{2.7}$$

Replacing ε_1 by Equation (2.5) and dividing both sides by $\sqrt{f_c'}b_j h_c$, Equation (2.7) becomes

$$\frac{V_n}{b_j h_c \sqrt{f_c'}} = a_2 \frac{\cos\theta}{1.31 + 0.085\left(h_b/h_c\right)} \tag{2.8}$$

where $a_2 = c_0 a_1 s/\sin\widetilde{\theta}$ is a constant determined in the following manner: for the upper bound of the shear strength of unreinforced joints, a_2 is selected as 23 for psi units (1.9 for MPa units) so as to be bounded by the shear strength of transversely reinforced joints as suggested by Moehle et al. [2006] for joint aspect ratio $h_b/h_c = 1.0$. This value was also obtained by selecting the coefficients as follows: (1) the maximum value of $c_0 = 1.0$; (2) original value of a_1, i.e., 71.3 for psi units (5.9 MPa units) according to Vollum [1998]; (3) $k = 0.325$ as the mean value of minimum, 0.25, and maximum, 0.4, values from Hwang and Lee [1999] and Vollum [1998], respectively; and (4) $\sin\widetilde{\theta} = 1$ as assumed by Hwang and Lee [1999]. For the lower bound of the shear strength of unreinforced joints, a_2 was selected as 10 for psi units (0.8 for MPa units)

based on the comparison with the experimental database as well as the recommendations by Hakuto et al. [2000] and Moehle et al. [2006]. Figure 2.2 shows that Equation (2.7) and the selected two values of a_2 represent the upper and lower bounds of the joint shear strength from the database for different values of the joint aspect ratio with reasonable accuracy.
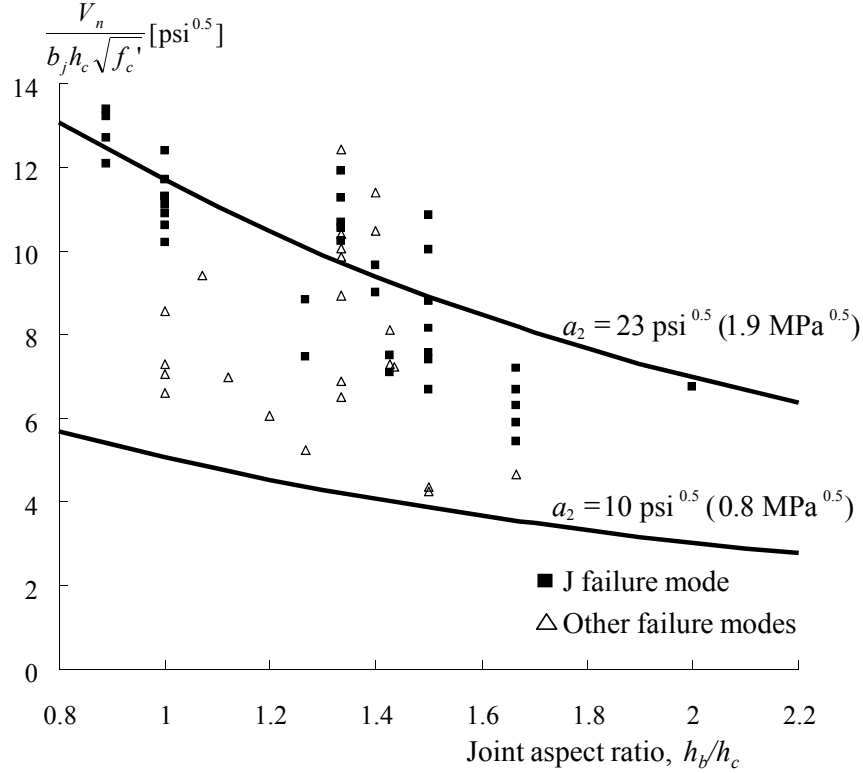
Figure 2.2   Comparison of the proposed joint aspect ratio equation with database.

2.2.2 Beam Longitudinal Reinforcement Ratio Parameter

The global equilibrium equation is derived from Figure 2.3 as follows,

$$M_b = V_b \times L = A_s f_s \times jd_b \tag{2.9a}$$

$$V_c = \frac{L + h_c/2}{H} V_b \tag{2.9b}$$

where V_b and V_c are the beam and column shear forces, respectively, L is the length from the beam inflection point to the column face, H is the height between upper and lower column inflection points, A_s and f_s are the area and stress of beam longitudinal reinforcement in tension, respectively, d_b is the effective depth of the beam, and jd_b indicates the internal moment arm of the beam cross-section at the column face. Accordingly, the horizontal shear force of the joint panel is calculated using Equations (2.9a) and (2.9b) as follows,

13

$$V_{jh} = A_s f_s - V_c = A_s f_s \left(1 - \frac{L + h_c/2}{H} \frac{jd_b}{L} \right)$$ (2.10)

It is assumed that the beam longitudinal reinforcement ratio affects only the case of joint shear failure with beam reinforcement yielding, referred to as "BJ-type" failure. This assumption is based on the observation from Figure 2.4 that for the case of joint shear failure prior to beam reinforcement yielding, referred to as "J-type" failure, the joint shear strength does not increase with joint shear demand beyond a certain limit. Assuming that the beam longitudinal reinforcement yields and dividing Equation (2.10) by $\sqrt{f_c'} b_j h_c$, the following equation is obtained,

$$\frac{V_{jh}}{b_j h_c \sqrt{f_c'}} = \left(\frac{A_s f_y}{b_j h_c \sqrt{f_c'}} \right) \left(1 - \frac{L + h_c/2}{H} \frac{jd_b}{L} \right)$$ (2.11)

In section analysis, an internal moment arm at yielding of beam longitudinal bars is generally close to 0.87 times the effective depth of beam cross section, i.e., $jd_b = 0.87 d_b$, based on $jd_b = d_b - \eta d_b/3$ where η is estimated as 0.4 [Hakuto et al. 1999]. Then, the effective depth is conservatively approximated as 0.9 times the total height of the beam cross section, i.e., $d_b = 0.9 h_b$, considering that cover depth is close to 10% of the total height in standard beam cross section. Therefore, the internal moment arm is estimated as 0.8 times the total height, i.e., $jd_b = 0.8 h_b$. Accordingly, the following approximation can be made as

$$jd_b = 0.8 h_b \Rightarrow \frac{L + h_c/2}{H} \frac{jd_b}{L} = \frac{L + h_c/2}{L} \frac{0.8 h_b}{H} \approx 0.85 \frac{h_b}{H}$$ (2.12)

Finally, Equation (2.11) can be simplified as follows,

$$\frac{V_{jh}}{b_j h_c \sqrt{f_c'}} \approx \left(\frac{A_s f_y}{b_j h_c \sqrt{f_c'}} \right) \left(1 - 0.85 \frac{h_b}{H} \right) = SI_j$$ (2.13)

where the non-dimensional parameter SI_j is previously referred to as the joint shear index and represents the joint shear demand at the onset of beam longitudinal reinforcement yielding. Note that the terminology "joint shear index" replaces the beam reinforcement index referred to in the previous report [Park and Mosalam 2009] to emphasize the physical meaning of joint shear demand.

$$V_{jh} = T - V_c = A_s f_s - V_c = \frac{M_b}{jd_b} - V_c = \frac{V_b L}{jd_b} - V_c$$
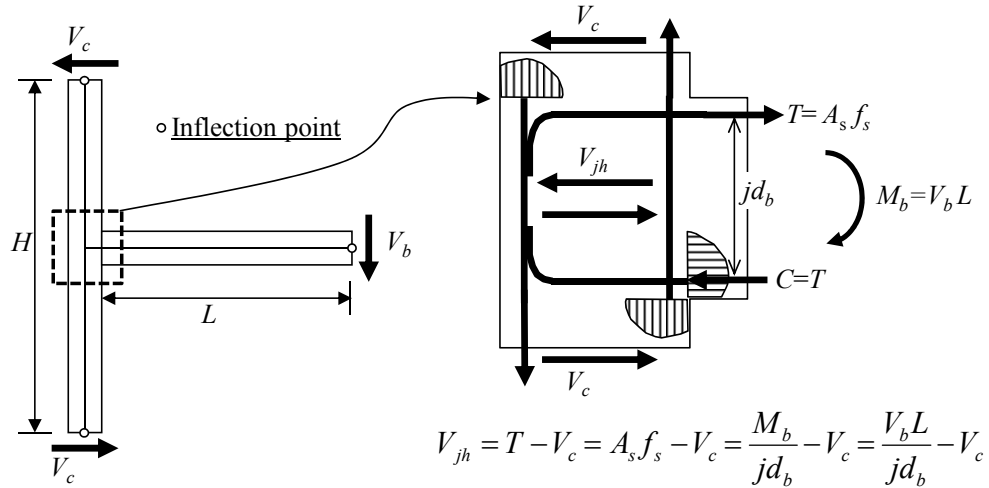
Figure 2.3   Global equilibrium of an exterior beam-column joint.

(a) low joint aspect ratio, $0.9 \leq h_b/h_c \leq 1.3$ (b) high joint aspect ratio, $1.4 \leq h_b/h_c \leq 2.0$
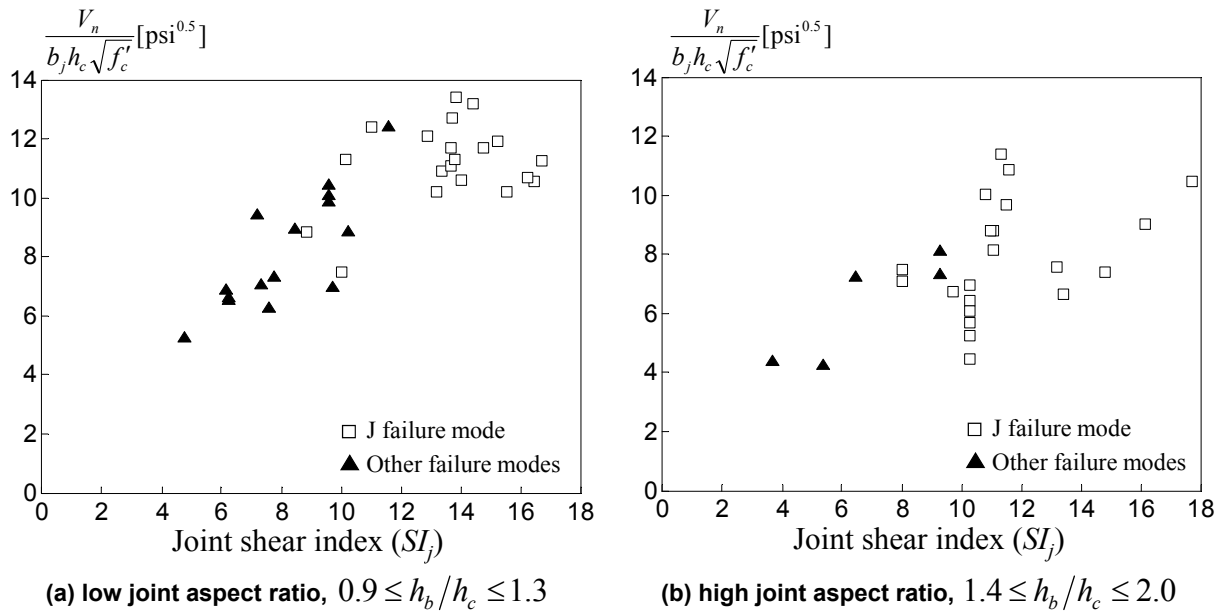
Figure 2.4   Plot of database with respect to the proposed joint shear index.

2.2.3 Development of Semi-Empirical Model

To develop a semi-empirical model, two basic assumptions were made: (1) maximum and minimum joint shear strengths are affected by the joint aspect ratio, i.e., they are independent of the joint shear index; and (2) joint shear strength is linearly proportional to joint shear index between the maximum and minimum joint shear strengths. The first assumption is supported by the plots of Equation (2.8) on Figure 2.2. The second assumption reflects the observation in Figure 2.4.

When the joint shear index is located between the maximum and minimum strengths determined by Equation (2.8), the joint shear strength is equal to the joint shear index multiplied

15

by an over-strength factor, $\Phi \geq 1.0$. This factor considers the increase of beam reinforcement tensile stress due to strain hardening after beam reinforcement yielding. The over-strength factor is larger for a smaller joint shear index because a larger plastic strain is expected. For simplicity, Φ is assumed to be 1.25, i.e., $f_s = 1.25 f_y$, at the minimum joint shear strength and decreases linearly to $\Phi = 1.0$, i.e., $f_s = f_y$ at the maximum joint shear strength, see Figure 2.5. Note that the over-strength factor 1.25 is commonly adopted to account for the effect of strain hardening for large curvature ductility [French and Moehle 1991]. Finally, the shear strength equation is proposed as follows:

$$\gamma_n = \frac{V_n}{b_j h_c \sqrt{f_c'}} = \Phi\left[\left(\frac{A_s f_y}{b_j h_c \sqrt{f_c'}}\right)\left(1 - 0.85\frac{h_b}{H}\right)\right] \tag{2.14a}$$

$$a_{\min} \frac{\cos\theta}{1.31 + 0.085\left(h_b/h_c\right)} \leq \frac{V_n}{b_j h_c \sqrt{f_c'}} \leq a_{\max} \frac{\cos\theta}{1.31 + 0.085\left(h_b/h_c\right)} \tag{2.14b}$$

where $a_{\min}$ is 10 for psi units (0.8 for MPa units) and $a_{\max}$ is defined as 23 for psi units (1.9 for MPa units). The semi-empirical model predicts joint shear strength by the following procedures:

1. Input the joint geometry, concrete strength, and joint aspect ratio;

2. Determine X_1 at the lower bound, $Y_{\min}$, and X_2 at the upper bound, $Y_{\max}$, as shown in Figure 2.5;

3. Calculate the joint shear index (SI_j) by Equation (2.13);

4. If $X_1 \leq SI_j \leq X_2$, calculated the over-strength factor, Φ, by interpolation as shown in Figure 2.5; and

5. Calculate the joint shear strength by Equation (2.14).
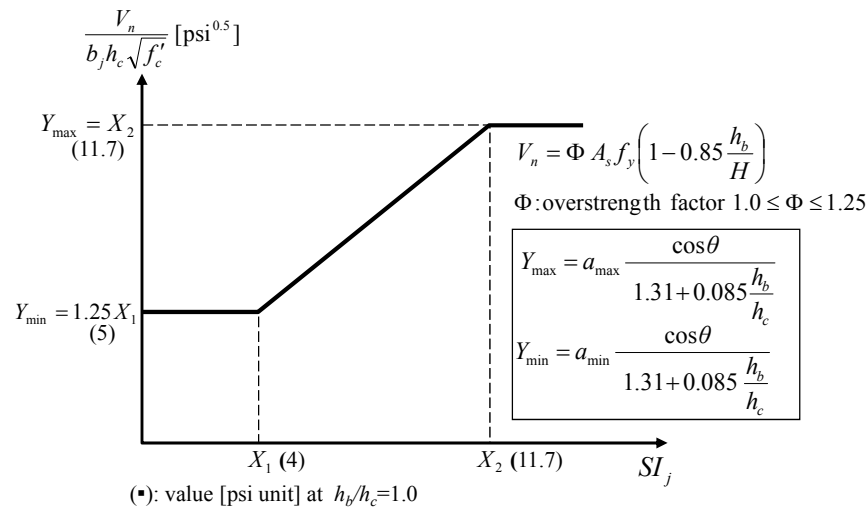
Figure 2.5   Illustration of the proposed semi-empirical model.

16

2.3   ANALYTICAL MODEL

Many analytical studies have assessed the shear strength of unreinforced joints. As a result, several analytical models have been adopted for predicting shear strength of unreinforced joints based on the average principal tensile stress limit or the strut-and-tie (SAT) approach using the average strain compatibility. However, existing models have a conceptual limitation: the average principal stress and strain compatibility equation does not adequately represent the behavior of unreinforced exterior joints where the joint shear failure is localized. In addition, the SAT approach is primarily concerned with estimating the diagonal strut area because the joint shear strength is sensitive to this estimated area [Hwang and Lee 2002].

Depending on the joint shear demand, two types of joint failure—J-type failure (joint shear failure prior to beam reinforcement yielding) and BJ-type failure (joint shear failure with beam reinforcement yielding) —have been commonly recognized by other researchers. The joint shear strength of the BJ-type failure is less than that of the J-type failure due to relatively lower beam longitudinal reinforcement ratio. To predict the reduced shear strength for the BJ failure type, ductility factors are utilized in the existing models. However, ductility can be defined in different ways to include the deformation of other members in addition to the joint distortion.

The proposed analytical model has been developed to fulfill the following objectives:

1. The new approach uses a consistent procedure to predict two different types of joint shear failure, i.e., without beam reinforcement yielding (denoted as J type) or with beam reinforcement yielding (denoted as BJ type), without the need for including ductility factors.;

2. The solution algorithm is suitable for practical applications;

3. The new approach does not require the estimation of the diagonal strut area, A_{str}.

2.3.1 Assumption

The proposed model first assumes that two inclined struts resist the horizontal joint shear (Figure 2.6) in parallel, where the horizontal joint shear force is carried by the sum of the two horizontal components of the two struts, but the shear distortion is uniformly distributed over the two struts. The strut named as "ST1" is developed by the 90° hook of the beam reinforcement, while the other inclined strut (ST2) is developed by the bond resistance of the concrete surrounding the beam reinforcement. In this analytical model, the only anchorage detail of beam longitudinal bars considered is the 90° hook on top and bottom bars bent into the joint region. Presumably, the fraction of each strut in this detail can be determined by the level of beam reinforcement tensile stress, which is related to the bond resistance as discussed later in this section.

The second assumption is that the joint shear failure is initiated adjacent to the top node of ST1 under the loading condition of top beam longitudinal reinforcement in tension, as mentioned in the semi-empirical model.

The third assumption is that the proposed model uses the softening concrete model suggested by Vollum [1998]—Equation (2.3) —and the principal tensile strain equation proposed in the semi-empirical model—Equation (2.5) —for developing this analytical model

2.3.2 Equilibrium

The joint shear force is estimated from the global equilibrium of a joint panel as derived in Equation (2.10). By approximation, the equation is simplified as follows,

$$V_{jh} = A_s f_s - V_c \approx A_s f_s \left(1 - 0.85 \frac{h_b}{H}\right) \tag{2.15}$$

Total horizontal joint shear force is assumed to be the sum of shear resistances by the two struts ST1 and ST2 shown in Figure 2.6. The equilibrium of each strut in horizontal direction is derived using the bond stress between the beam longitudinal reinforcement and the surrounding concrete in the joint region.

$$V_{jh} = V_{jh,ST1} + V_{jh,ST2} \tag{2.16a}$$

$$V_{jh,ST1} = A_s f_s - n \pi \phi_b \int_0^{l_h} \mu(f_s) dx \tag{2.16b}$$

$$V_{jh,ST2} = n \pi \phi_b \int_0^{l_h} \mu(f_s) dx - V_c \tag{2.16c}$$

where n is the number of beam longitudinal bars in tension with diameter ϕ_b, and V_c is the shear force in the column. Note that $\mu(f_s)$ is the bond stress distribution along the beam longitudinal bar (Figure 2.6) as a function of the tensile stress of the bar, f_s, which varies with the distance x, i.e., $f_s = f_s(x)$. The x-axis and l_h are depicted in Figure 2.6. In this model, the horizontal projection l_h is recommended to be $0.65 h_c$.

The column shear force is excluded in the equilibrium of the diagonal strut ST1, Equation (2.16b), and included in the equilibrium of the inclined strut ST2, Equation (2.16c), because most of the column shear force is resisted by the middle portion of the column cross section due to flexural cracks forming at both sides of the rectangular column cross-section under reversed cyclic loading. In addition, the vertical component of ST2 is equilibrated by an inclined strut in the column, as shown in Figure 2.6, where the horizontal components of ST2 and this inclined strut in the column are represented by $V_{jh,ST2}$ in Equation (2.16c).

18
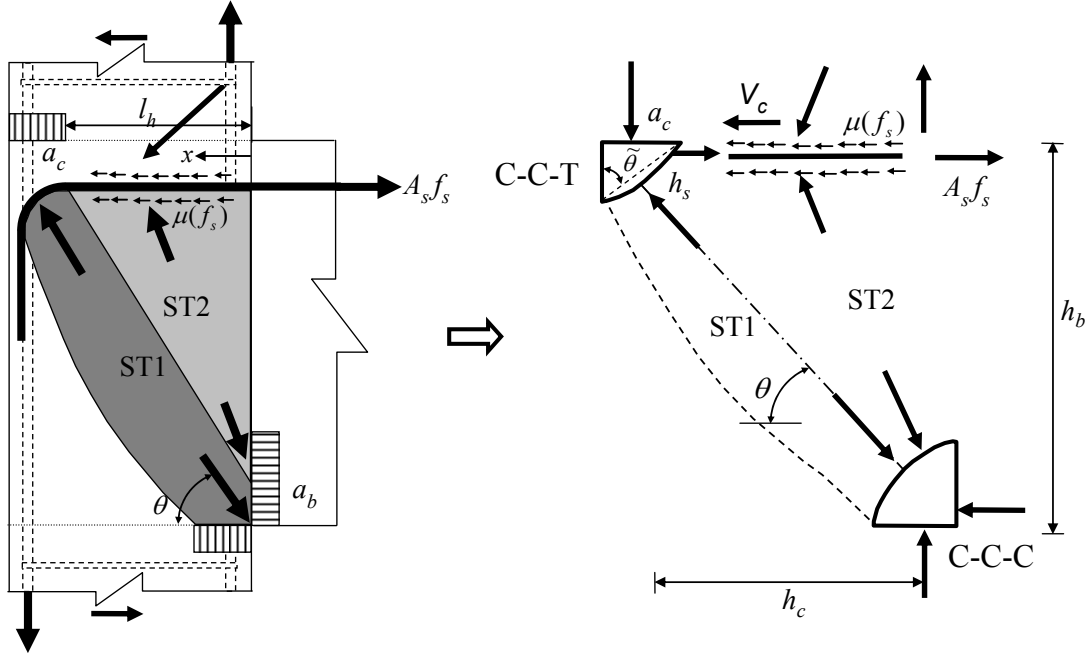
Figure 2.6   Two inclined struts in unreinforced exterior joints.

2.3.3 Fraction Factor

The contribution of struts ST1 and ST2 shown in Figure 2.6 to the total horizontal joint shear force can be expressed using a fraction factor α as follows,

$$V_{jh,ST1} = \alpha V_{jh} \tag{2.17a}$$

$$V_{jh,ST2} = (1-\alpha)V_{jh} \tag{2.17b}$$

This fraction factor is expressed as a function of the tensile stress of the beam reinforcement because it is related to the bond deterioration of this reinforcement. Obviously, the fraction factor increases as the bond strength deteriorates because ST1 strut contribution dominates after bond failure occurs [Booth 1994]. In this model, the bi-uniform bond strength model proposed by Lehman and Moehle [2000] is extended to be tri-uniform and adopted to represent the tri-linear behavior of the reinforcing steel. The bond strength in elastic beam tensile reinforcement, μ_E, is $12\sqrt{f_c'}\ \text{psi}^{0.5}$ ($1.0\sqrt{f_c'}\ \text{MPa}^{0.5}$) and that in inelastic beam tensile reinforcement, μ_Y, is $0.5\mu_E$. The residual bond strength, μ_R, is selected from the CEB-FIP [1993] as $0.15\mu_E$. The considered bond strength model is illustrated in Figure 2.7 with reference to the CEB-FIP model [1993].
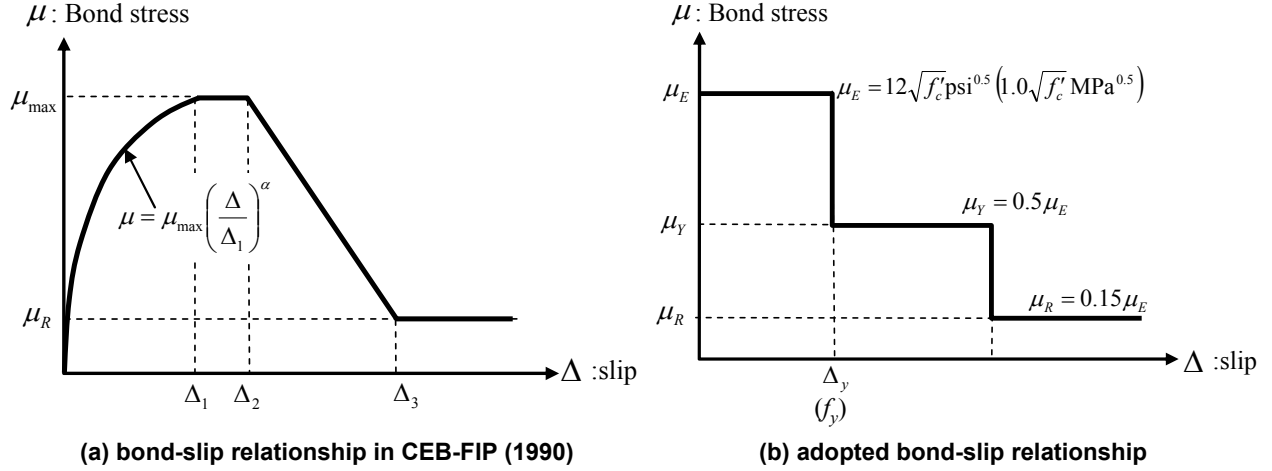
Figure 2.7   Adopted bond strength model.

Using Equations (2.14) through (2.16) and the above bond strength, the fraction factor α is derived as follows:

$$A_s f_s - n\pi\varphi_b \int_0^{l_h} \mu(f_s)\,dx = \alpha\, A_s f_s \left(1 - 0.85\frac{h_b}{H}\right) \Rightarrow \alpha$$

$$= \frac{H}{H - 0.85 h_b}\left(1 - \frac{4}{\varphi_b}\frac{\int_0^{l_h}\mu(f_s)\,dx}{f_s}\right) \qquad (2.18)$$

where in Equation (2.18), $A_s = n\pi\phi_b^2/4$ is used. It is assumed that all beam longitudinal bars are detailed using standard development length and hook, and the bar stress and strain are extended to the tail of the hook considering cylindrical bearing stress along the hook. As shown in Figure 2.8, the assumed breaking points of beam longitudinal bar stress (f_o, f_p, and f_r) and intermediate values of the fraction factor (α_1 and α_2) are derived below.

DERIVATION OF f_o

The contribution of ST1 is negligible as long as the bond strength of ST2 is able to resist all of the horizontal shear force. The tensile stress of beam reinforcement at this point, f_o in Figure 2.8, is given by

$$f_o = \frac{4}{\phi_b}\mu_E l_h \qquad (2.19)$$

DERIVATION OF α_1

The fraction factor α_1 corresponds to the onset of yielding of beam reinforcement at the column face. Therefore,

$$\alpha_1 = \frac{H}{H - 0.85h_b}\left(1 - \frac{4}{\phi_b}\frac{\mu_E}{f_y}l_h\right)$$

(2.20)

where f_y is the yield strength of the beam longitudinal reinforcement.

DERIVATION OF f_p AND f_r

The tensile stress f_p is defined when the beam reinforcement yielding propagates over the width of ST2. Therefore, the bond strength of concrete surrounding the beam reinforcement is equal to μ_Y over the entire length l_h. Accordingly (see Figure 2.8), one obtains the following,

$$f_p = f_y + \frac{4}{\phi_b}\mu_Y l_h$$

(2.21)

Using Equation (2.18), the tensile stress f_r corresponding to $\alpha = 1.0$ is expressed implicitly since the bond distribution cannot be explicitly defined at $\alpha = 1.0$. Note that the tensile stress f_p can be equated to f_r if α_2 corresponding to f_p is equal to 1.0, see Figure 2.8. Therefore, the tensile stress value of the beam reinforcement f_r corresponding to $\alpha = 1.0$ is expressed as follows,

$$f_r = \frac{4}{\phi_b}\frac{H}{0.85h_b}\int_0^{l_h}\mu(f_r)dx \geq f_p$$

(2.22)

DERIVATION OF α_2

The fraction factor α_2 is defined when the tensile stress of the beam longitudinal reinforcement at the column face reaches f_p. Therefore,

$$\alpha_2 = \frac{H}{H - 0.85h_b}\left(1 - \frac{4}{\phi_b}\frac{\mu_Y}{f_y + \frac{4}{\phi_b}\mu_Y l_h}l_h\right) \leq 1.0$$

(2.23)
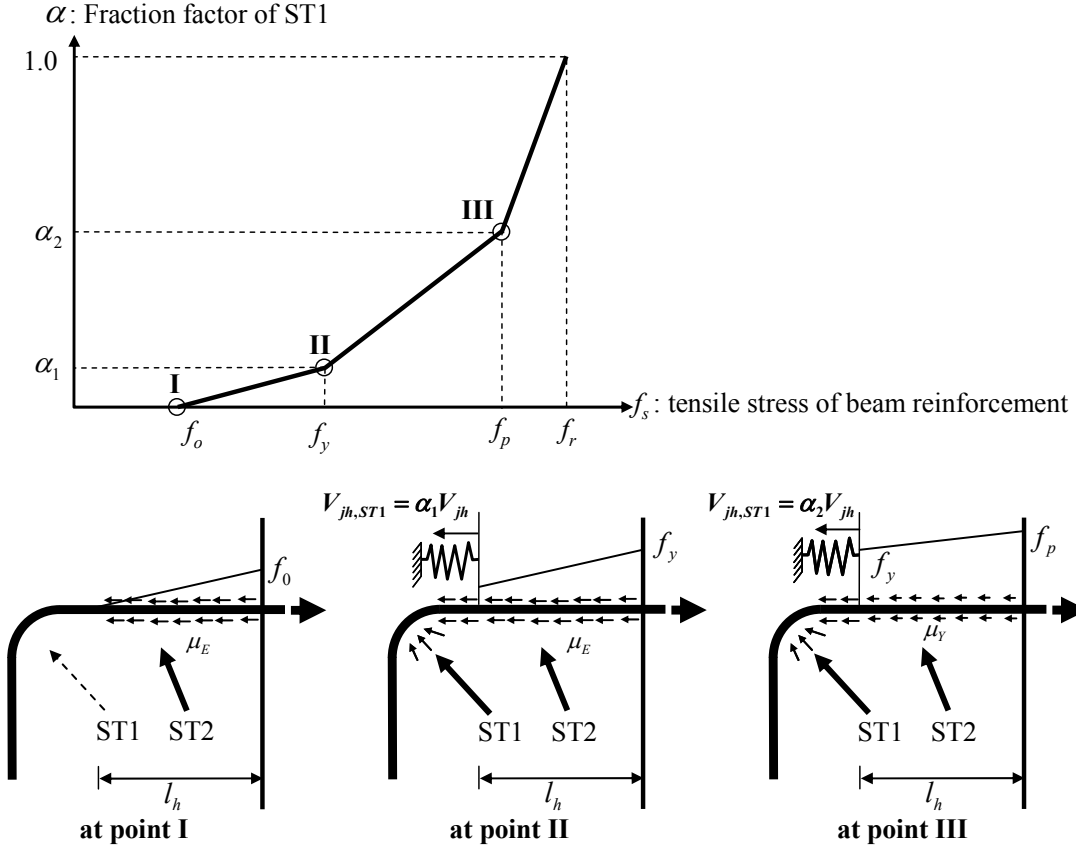
Figure 2.8   Tri-linear curve of fraction factor.

2.3.4 Definition of Joint Failure

The joint shear strength is defined as the horizontal joint shear force when the horizontal shear force carried by ST1 ($V_{jh,ST1}$) reaches its capacity ($V_{jh,ST1,max}$). The capacity of ST1 can be estimated as the minimum joint shear strength at which ST1 takes all horizontal joint shear force, i.e., the fraction factor can be set to 1.0. Using the parametric equation of joint aspect ratio, Equation (2.8), the horizontal shear capacity of ST1 is obtained as

$$V_{jh,ST1,max} = c \frac{b_j\, h_c\, \sqrt{f_c'}\, \cos\theta}{1.31 + 0.085\left(\dfrac{h_b}{h_c}\right)}, \quad \theta = \tan^{-1}\left(\frac{h_b}{h_c}\right) \tag{2.24}$$

where c is a constant to be determined by test data taken from the literature. The expression in Equation (2.24) makes use of the findings from the effect of joint aspect ratio in the semi-empirical model. To predict the joint shear strength, the constant c is obtained for the case of the minimum joint shear strength at which the fraction factor can be set to 1.0. From Hakuto et al. [2000], the normalized horizontal joint shear stress $\gamma = 4$ psi$^{0.5}$ (0.33 MPa$^{0.5}$) is taken as the minimum joint shear strength to trigger the joint shear failure for a joint aspect ratio, $h_b / h_c = 500/460 \approx 1.1$, i.e., $\theta = 0.83$ rad. Applying this suggestion to define the constant c, one obtains

$$c\frac{\cos(0.83)}{1.31+0.085\times1.1}=\gamma \Rightarrow c=2.07\gamma \tag{2.25}$$

Following the fraction factor function in Figure 2.8 and the determined value of c from Equation (2.24), the joint shear strength is calculated by an iterative procedure using the algorithm illustrated in Figure 2.9.

Input: $f_c', f_y, b_b, h_b, b_c,$ h_c, H, ϕ_b, A_s, l_h

Calculate: f_o (Eq. 2.19), f_p (Eq. 2.21), f_r (Eq. 2.22), α_1 (Eq. 2.20), α_2 (Eq. 2.23), $V_{jh,ST1,max}$ (Eq. 2.24)

Assume: $f_{s,i}$

Determine: α_i (Fig. 2.8)

Define: $V_{jh,i}=A_s f_o(1-0.85h_b/H)$

Calculate: $V_{jh,i}$ (Eq. 2.15), $V_{jh,ST1,i}$ (Eq. 2.17a)

Yes

Check: $f_{s,i}<f_o$ Yes   Check: $V_{jh,ST1,i}\geq V_{jh,ST1,max}$ No

No

Define: $V_{jh}=V_{jh,i}$

End
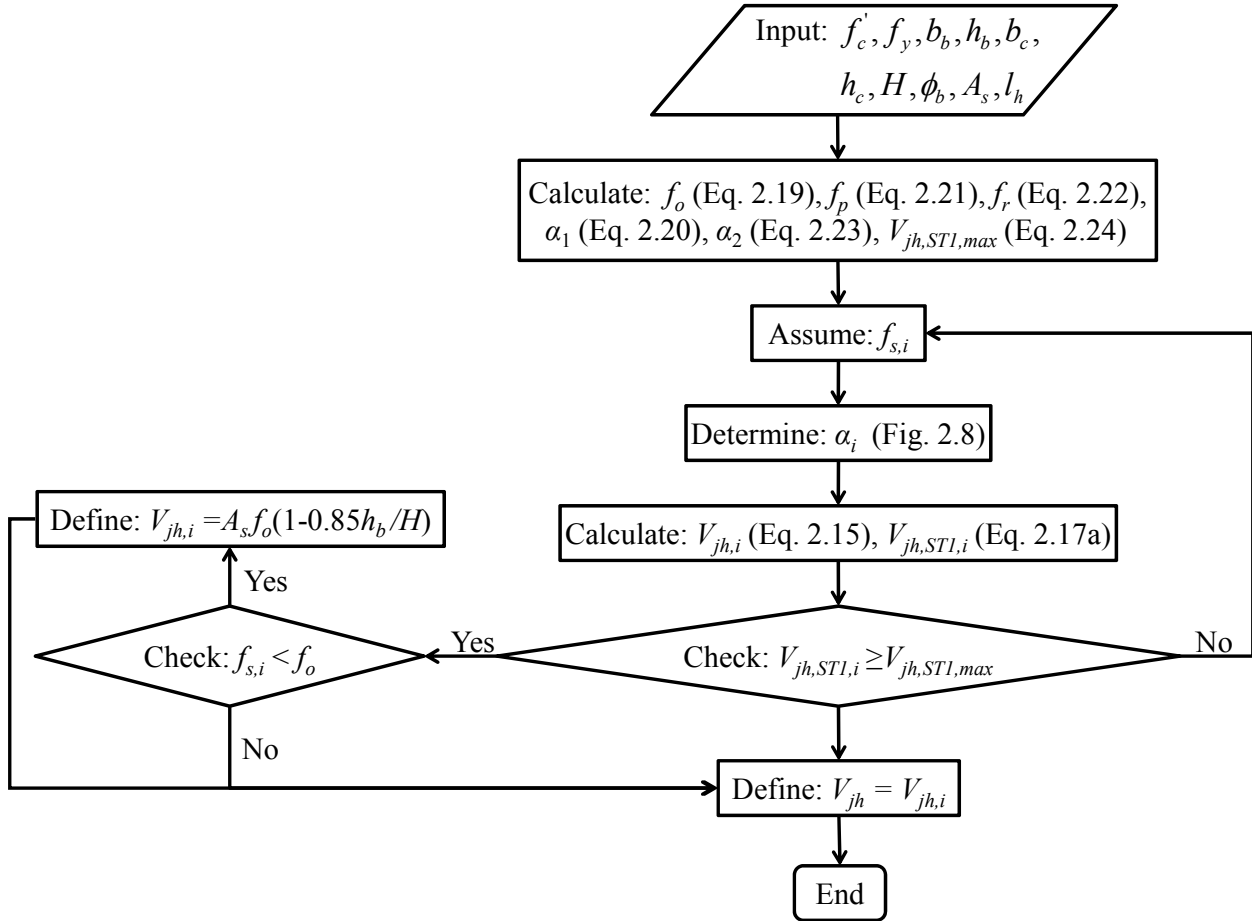
Figure 2.9   Solution algorithm of proposed analytical joint shear strength model.

2.3.5 Principle of Analytical Model

The basic approach of the proposed model is to model a joint region with two inclined struts; the contribution of each strut to the total joint shear is formulated using the bond resistance of the concrete surrounding the beam longitudinal bars in tension. The failure of joint is controlled by the diagonal strut STI whose shear capacity is, for example, $4.2b_j h_c \sqrt{f_c'}$ for the joint aspect ratio of $h_b/h_c =1.0$. For a certain joint aspect ratio, the minimum joint shear strength is equal to the capacity of the diagonal strut ST1 because the joint horizontal shear force is carried by ST1 only, i.e., the fraction factor $\alpha =1.0$. If joint failure occurs before completely losing the bond strength, the strut ST2 has a contribution to joint horizontal shear resistance, i.e., the fraction factor becomes less than 1.0 in the analytical model. The contribution of ST2 increases, i.e., the

23

fraction factor decreases, if joint failure occurs under better bond conditions such as a J-type failure. Consequently, the reduction of the fraction factor increases the joint shear strength because the multiplication of the joint shear strength and the fraction factor, i.e., the capacity of the diagonal strut ST1, is fixed for a given joint aspect ratio. From the evaluation of the literature dataset, the contribution of ST1 is bounded between approximately 0.31 and 0.77 for J-type mode failure and BJ-type mode failure, respectively. Selecting 0.35 and 0.80 as the minimum and maximum fraction factors, respectively, for a joint aspect ratio of $h_b/h_c =1.0$, the upper and lower limits of the joint shear strength become $\gamma = 4.2/0.35 = 12.0$ and $\gamma = 4.2/0.80 = 5.4 \, [\text{psi}^{0.5}]$, respectively, which show good agreement with experimental results taken from the literature, see Figure 2.2. Note that $4.2 b_j h_c \sqrt{f_c'}$ corresponds to the capacity of ST1 (i.e., $\alpha = 1$) at $h_b/h_c = 1.0$. The following equations help to understand the above,

$$V_{jh,ST1,\max} = 4.2 b_j \, h_c \, \sqrt{f_c'} \, \frac{\cos\theta}{\cos(\pi/4)} = 5.9 b_j \, h_c \, \sqrt{f_c'} \cos\theta \tag{2.26a}$$

$$V_{jh} = \frac{1}{\alpha} V_{jh,ST1,\max} = \frac{1}{\alpha} 5.9 b_j h_c \sqrt{f_c'} \cos\theta, \; 0.35 \le \alpha \le 0.8 \tag{2.26b}$$

Coincidentally, the equation of joint shear strength—if vertical stress is included—is similar to the equation of column shear capacity proposed by Sezen and Moehle [2004],

$$V_c = \beta \left(\frac{6\sqrt{f_c'}}{a/d} \sqrt{1 + \frac{P}{6\sqrt{f_c'}A_g}} \right) A_g \tag{2.27}$$

where β is a modifier to account for strength degradation and a/d is shear span to depth ratio of the column that is related to the cosine term in Equation (2.26). From this finding, the analytical model is simplified in the subsequent section.

2.4   SIMPLIFIED MODEL

The evaluation of the literature test dataset found that the fraction factor is bounded between 0.35 and 0.8. These values are related to the upper and lower limit of joint shear strength, respectively, as shown in Figure 2.2. In other words, the minimum fraction factor is obtained in the case of joint shear failure before or at the onset of beam reinforcement yielding, i.e., J-type failure mode, in which joint shear strength corresponds to the upper limit. The correlation between maximum fraction factor and lower limit of joint shear strength can be understood in the same manner but for the BJ-type failure.

In this practical model, joint shear failure is defined as when the principal tensile stress reaches a certain coefficient (κ) times the square root of the standard concrete compressive strength, see Figure 2.10. At shear failure, shear stress (v_{jh}) is determined by

$$v_{jh} = \kappa\sqrt{f_c'}\sqrt{1 + \frac{\sigma_y}{\kappa\sqrt{f_c'}}} \qquad (2.28)$$
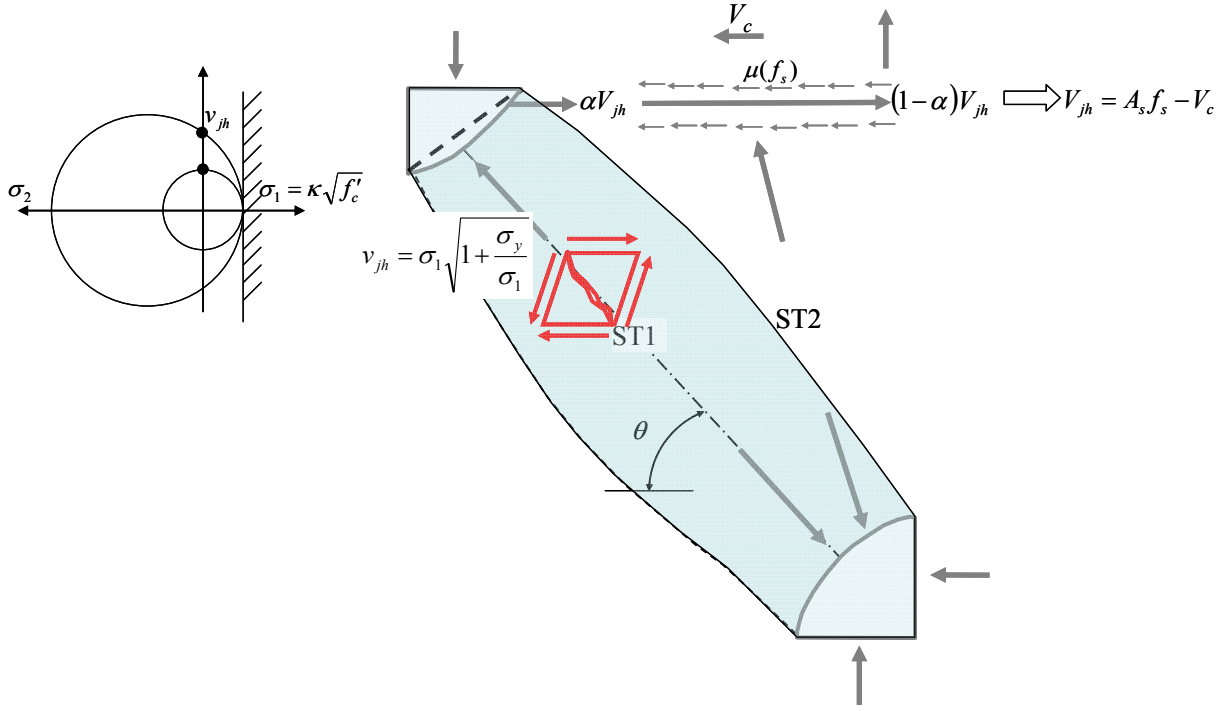
Figure 2.10   Joint shear failure mechanism based on principle tensile strength of ST1.

where σ_y is the axial compressive (positive) stress in the column, and the axial stress in the beam is assumed to be negligible.

Equation (2.28) shows that joint shear stress increases as higher compressive axial load is applied to the column, because maximum principal tensile stress limit is adopted as a failure criterion, as shown in Figure 2.10. However, it has not been proven that the compressive column axial load improves the joint shear strength [Park and Mosalam 2009]. It is also possible that the maximum principal tensile stress limit may not exactly represent the shear failure of concrete. Hence, the term including the column axial stress (σ_y) in Equation (2.28) is ignored and joint shear stress is expressed as $\kappa\sqrt{f_c'}$.

The effect of joint aspect ratio is formulated in Equation (2.8) based on local equilibrium in the joint panel and geometry of the nodal zone. A simple statically determinant truss structure is used to illustrate the effect of the joint aspect ratio in Figure 2.11. The inclined strut ST2 is not included in the truss structure for simplicity, assuming that bond deterioration is significant and thus does not contribute to the joint shear resistance. Clearly, joint shear strength decreases for cases with high joint aspect ratios. Assuming that the axial capacity of the diagonal strut ST1 (D_{ST1}) is constant, the ratio of joint shear strength between low and high joint aspect ratio is close to the ratio of the cosine values for the two inclination angles of ST1 from the horizontal.

25

Selecting the maximum principal tensile stress as $4\sqrt{f'_c}$ for joint aspect ratio, $h_b/h_c = 1.0$, one obtains the following,

$$V_{jh,ST1} = 4\sqrt{f'_c}\, b_j h_c \qquad\qquad \text{for } \theta = \pi/4 \qquad\qquad\qquad (2.29a)$$

$$V_{jh,ST1} = 4\sqrt{f'_c}\, b_j h_c \frac{\cos\theta}{\cos(\pi/4)} \quad \text{for any } \theta \qquad\qquad\qquad (2.29b)$$

By the definition of joint shear failure in the analytical model, joint shear strength is obtained from Equation (2.29b) as,

$$V_n = \frac{1}{\alpha} V_{jh,ST1} = \frac{1}{\alpha} 4\sqrt{f'_c}\, b_j h_c \frac{\cos\theta}{\cos(\pi/4)} \qquad\qquad\qquad (2.30)$$

Using Equation (2.30), the upper and lower limits of the joint shear strength are plotted in Figure 2.12 for the fraction factors, $\alpha_1 = 0.33$ and $\alpha_2 = 0.80$, respectively, which are close to the minimum and maximum fraction factors (i.e., 0.31 and 0.77, respectively) observed in the evaluation of the database using the analytical model. Note that the upper and lower limits shown in Figure 2.12 are almost identical to those in Figure 2.2. Accordingly, it can be concluded that the analytical model provides similar range of joint shear strength for a certain joint aspect ratio depending on the joint shear index as that provided by the simplified Equation (2.30).

(a) low joint aspect ratio   (b) high joint aspect ratio
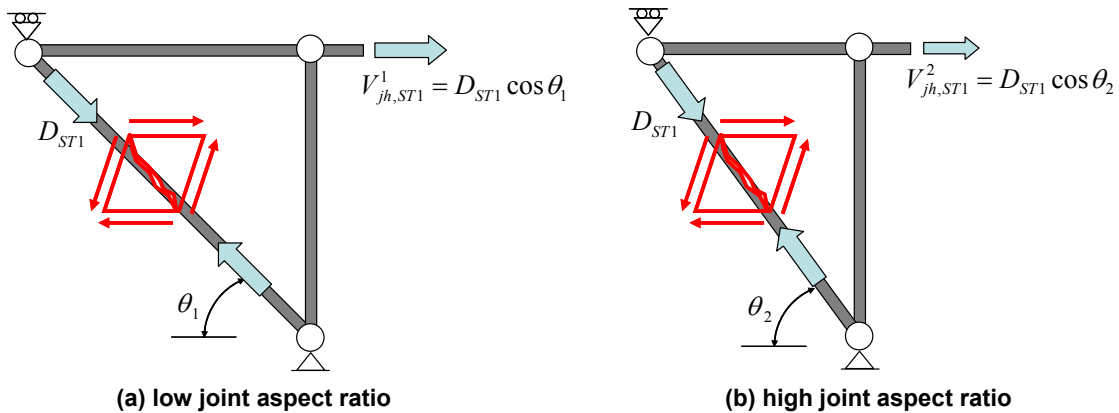
Figure 2.11   Illustration of joint aspect ratio effect using truss analogy.
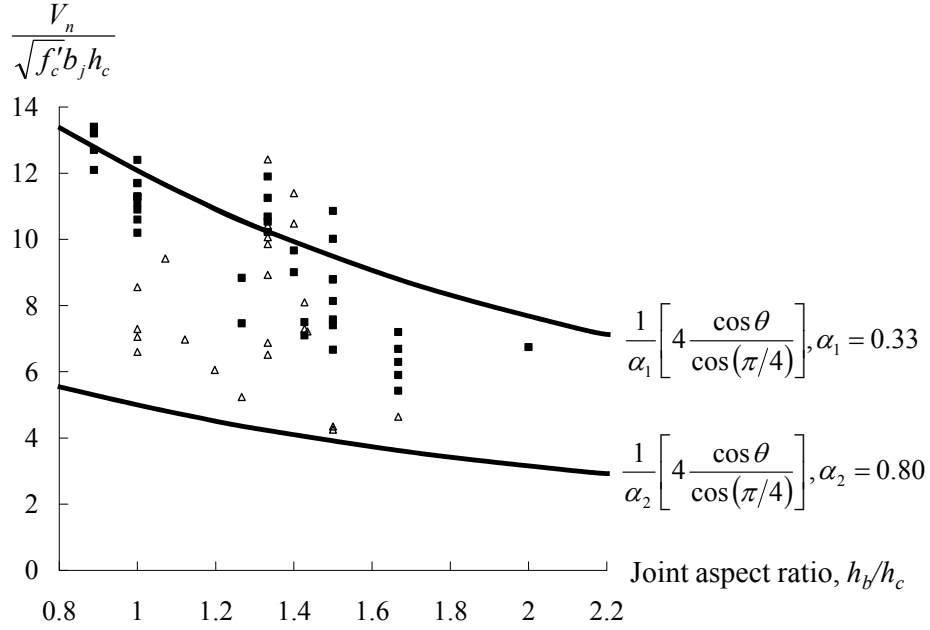
Figure 2.12   Upper and lower limit of joint shear strength using the proposed equation.

Using the minimum of the fraction factor, i.e., the upper limit of joint shear strength, a strength factor, k, is newly introduced from the fraction factor as follows,

$$k = \frac{1}{\alpha} \frac{4}{\gamma_{ext}}$$

(2.31)

where γ_{ext} is equal to 12.0 psi$^{0.5}$ (1.0 MPa$^{0.5}$), corresponding to the upper limit of joint shear strength for joint aspect ratio, $h_b/h_c = 1.0$, in Figure 2.12. For reference, the shear strength for Type 2 exterior joints is also equal to $\gamma = 12.0$ 12.0 psi$^{0.5}$ (1.0 MPa$^{0.5}$) in ACI 352-02. Subsequently, the vertical axis of the simplified fraction factor relationship is replaced by the strength factor, k, as shown in Figure 2.13.

In Figure 2.13(b), the tensile stress of beam longitudinal bars on the horizontal axis cannot be used to predict the corresponding strength factor without an iterative procedure. Therefore, a new parameter is needed. In general, a ductility factor is been adopted to reduce the joint shear strength with increase of strain hardening of the beam longitudinal bars by other researchers (Park 1997 [Figure 2.14(a)]; Hakuto et al. 2000). However, the ductility factor can be defined in different ways such as curvature ductility and displacement ductility, and it includes the deformation of other members in addition to the joint distortion. Because it is necessary to monitor the ductility factor during the analysis of the frame, this means that it is impossible to predict the joint shear strength before analyzing the whole frame. Moreover, Figure 2.14(b) shows an unclear correlation between the joint shear strength and the displacement ductility factor [Hassan et al. 2010].

Instead, the joint shear index is used to replace the tensile stress of the beam reinforcement in Figure 2.13(b). The joint shear index represents the joint shear demand at the onset of beam longitudinal bar yielding. In other words, joint shear failure occurs at a lower

27

tensile stress of beam longitudinal bars if the joint shear index is larger. Accordingly, the joint shear index is inversely proportional to the tensile stress of beam longitudinal bars at the onset of joint shear failure. Furthermore, the joint shear index values corresponding to the elastic limit (f_y) and the fully inelastic (f_p) stage are defined as upper limit of the joint shear strength and the shear capacity of ST1, respectively, as shown in Figure 2.15. Note that the adopted joint shear index values are the same as those used in the semi-empirical model.

$$\frac{V_n}{\sqrt{f_c'}\,b_j h_c} = \frac{1}{\alpha}\left[4\,\frac{\cos\theta}{\cos(\pi/4)}\right]$$

$$\frac{V_n}{\gamma_{ext}\sqrt{f_c'}\,b_j h_c} = k\left[\frac{\cos\theta}{\cos(\pi/4)}\right],\ \gamma_{ext}=12$$

$$\boxed{\alpha : \text{Fraction factor of ST1}} \Longleftrightarrow \frac{1}{\alpha}\frac{4}{\gamma_{ext}} = k \Longrightarrow \boxed{k}$$

$\alpha_2 = 0.80$

$\alpha_1 = 0.33$

f_y f_p

f_s : tensile stress of beam reinforcement

(a) simplified fraction factor relationship with upper and lower limits

$=1.0$

≈ 0.4

f_y f_p

f_s : tensile stress of beam reinforcement
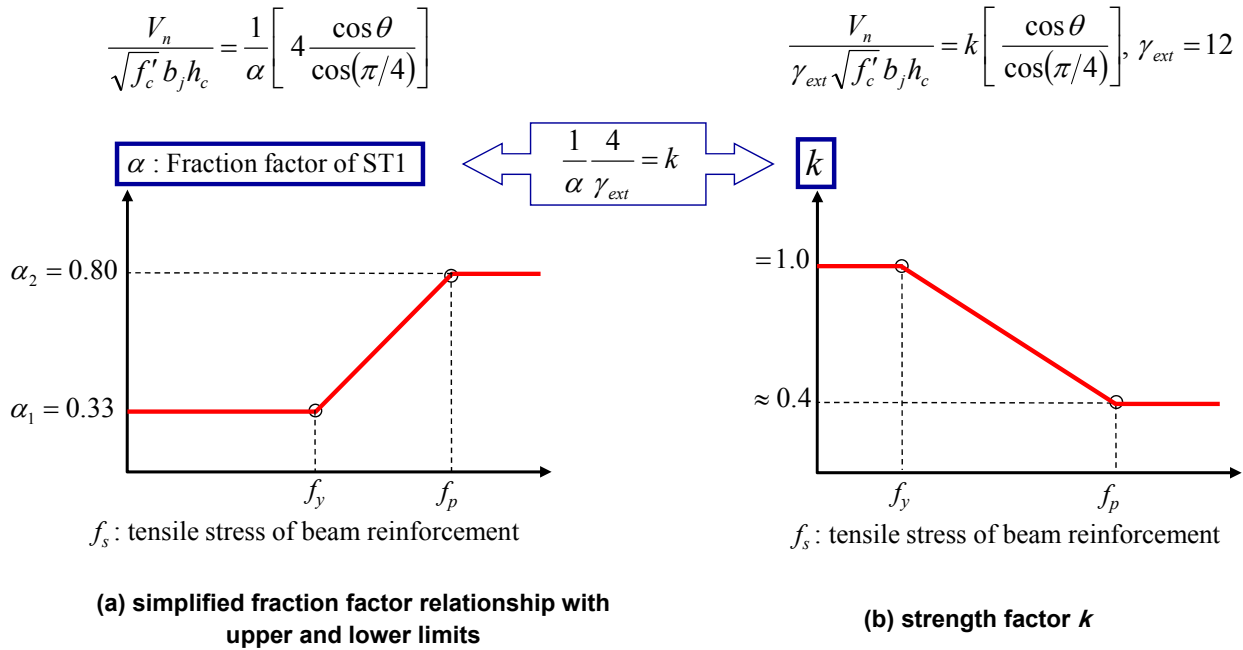
(b) strength factor k

Figure 2.13   Derivation of strength factor, k.

k

1.0

0.3

Available joint horizontal shear stress

$v_{jh} = k\sqrt{f_c'}$ MPa
$(12k\sqrt{f_c'}$ psi$)$

2   9

Imposed Curvature Ductility Factor, ϕ_u/ϕ_y

(a) joint shear strength degradation by curvature ductility factor [Park 1997]

γ_{test}

V_n, ASCE 41

μ_D Displacement Ductility Factor

(b) joint shear strength versus displacement ductility factor [Hassan et al. 2010]
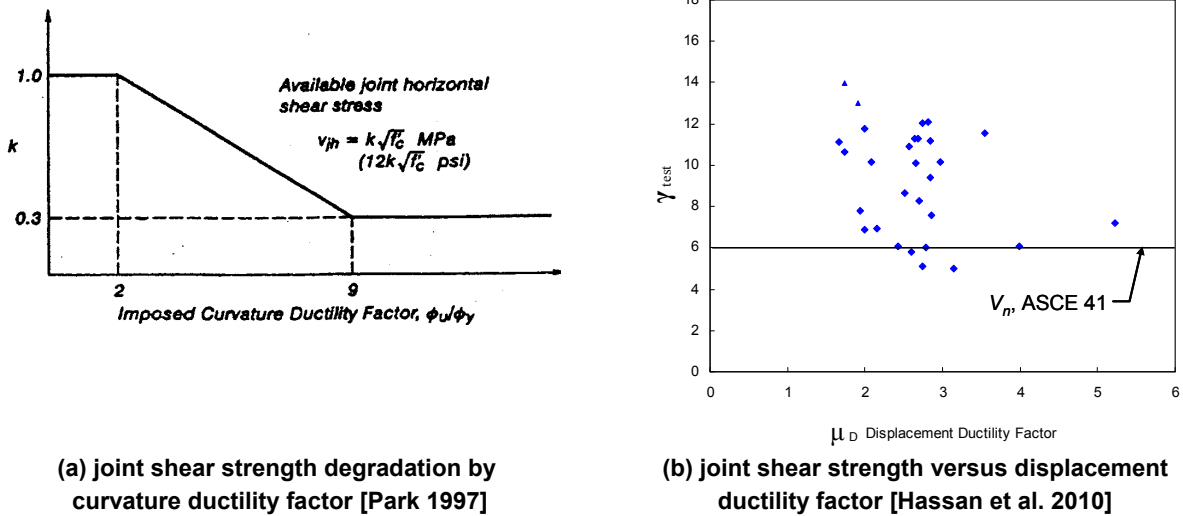
Figure 2.14   Relationship between joint shear strength and ductility factor.

28
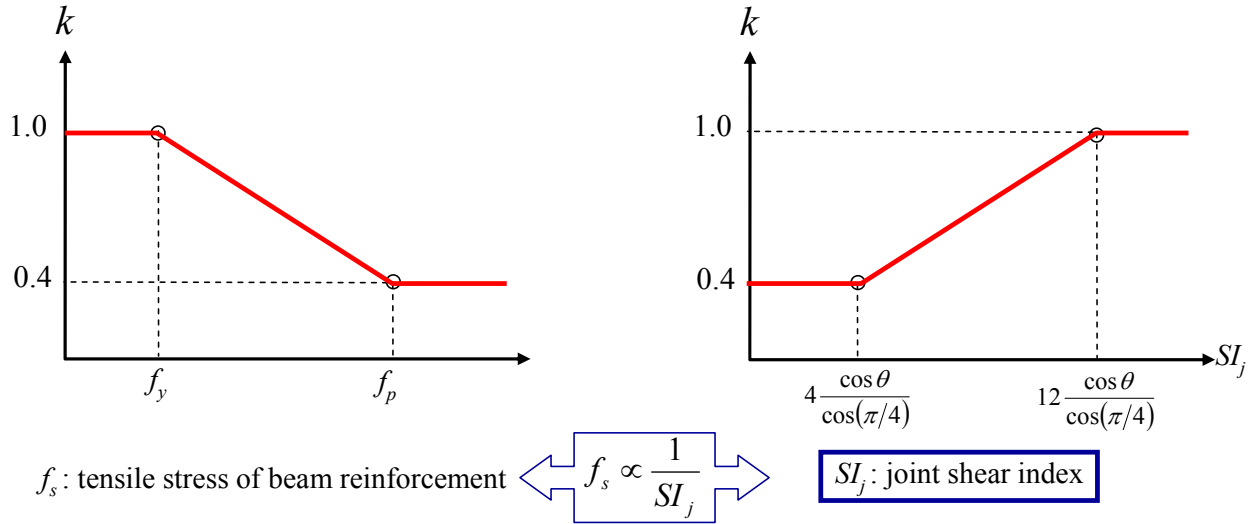
Figure 2.15   Strength factor relationship.

Benefitting from and combining the two models discussed previously, the practical joint shear strength model is proposed in a unified framework as follows:

$$V_n = k\left[\gamma_{ext}\sqrt{f_c'}\,b_j h_c \frac{\cos\theta}{\cos(\pi/4)}\right] \tag{2.32a}$$

$$k = 0.4 + 0.6\left[\frac{SI_j - X_1}{X_2 - X_1}\right],\ X_1 = 4\frac{\cos\theta}{\cos(\pi/4)}\ \text{and}\ X_2 = 12\frac{\cos\theta}{\cos(\pi/4)} \tag{2.32b}$$

For joint aspect ratio, $h_b/h_c = 1.0$, this practical model predicts the lower limit of joint shear strength, $\gamma = 4.8$, for the joint shear index, $SI_j = 4.0$, and predicts the upper limit of joint shear strength, $\gamma = 12.0$, for the joint shear index, $SI_j = 12.0$. These predictions are identical to those used in the semi-empirical model if the maximum over-strength factor is assumed to be 1.2, i.e., $4.8/4$, instead of 1.25, i.e., $5/4$, see Figure 2.5. Consequently, this practical model is derived from the analytical model and almost identical to the semi-empirical model.

The proposed practical model predicts the joint shear strengths of the database with a mean value of 0.97 for the ratio between the test results and model predictions and the corresponding coefficient of variation (COV) of 0.13 as shown in Figure 2.16. This comparison demonstrates the good accuracy of this practical version of the shear strength model for unreinforced exterior beam-column joints.
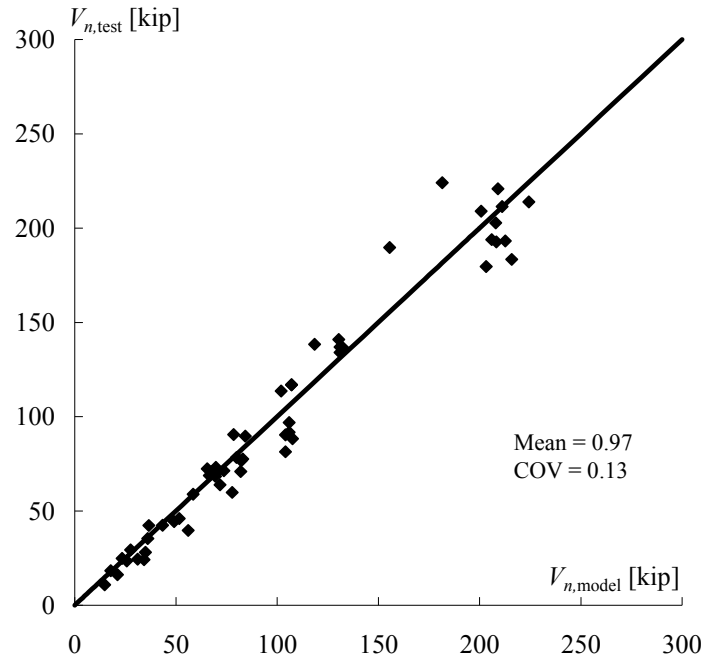
Figure 2.16   Validation of the practical joint shear strength model.

3　Experimental Program

This chapter describes the details of the experimental program on unreinforced exterior joint tests including: (1) specimen design, (2) construction, (3) material properties, (4) loading protocol, (5) test set up and (6) instrumentation. The experimental program was performed in the *nees@berkeley* laboratory located at Richmond Field Station, University of California, Berkeley.

3.1　SPECIMEN DESIGN AND DETAILS

Four full-scale unreinforced corner joint specimens were built to investigate their behavior under cyclic loading simulating earthquake loads. Based on the previous parametric study, the specimens were designed considering two parameters: (1) joint aspect ratio and (2) beam longitudinal reinforcement ratio. For different joint aspect ratios, the beams were designed with two different cross-section heights, but the column cross-section height was identical for the four specimens so as to produce low and high joint aspect ratios of 1.0 and 1.7, respectively, as shown in Figure 3.1. Two types of beam longitudinal bars were adopted: 4-#6 at the top and bottom as low beam longitudinal reinforcement ratio, and 4-#8 at the top and 4-#7 at the bottom as high beam longitudinal reinforcement ratio, as shown in Figure 3.1. Note that the selection of the beam longitudinal reinforcement was intended to achieve two different types of joint failure for each joint aspect ratio, i.e., a BJ-type failure for SP1 and SP3 fail and a J-type failure for SP2 and SP4.

Specimen SP1 had a low joint aspect ratio and low beam reinforcement ratio, specimen SP2 had a low joint aspect ratio and high beam reinforcement ratio, specimen SP3 had a high joint aspect ratio and low beam reinforcement ratio, and specimen SP4 had a high joint aspect ratio and high beam reinforcement ratio. The joint aspect ratio and joint shear index (SI_j) of the four specimens are presented in Table 3.1. Note that the joint shear index was calculated separately for negative and positive bending, and the slab reinforcement within the effective slab width according to ASCE 41 is included in the calculation of the joint shear index for negative bending, i.e., slab in tension.

Since the experimental program focused on the seismic performance of unreinforced corner joints without addressing failures of the column and beams adjacent to the joint, the beams and columns were designed as strong column/weak beam with proper details. Accordingly, the whole spectrum of poor seismic details found in older RC buildings such as widely spaced column hoops and lap splice was not considered. As a result, the column-to-beam flexural strength ratios of the specimens were greater than 1.4 as specified in Table 3.1, where

M_R is defined as the sum of the flexural capacities of the columns above and below the joint divided by that of the beam.

According to the survey of 15 RC buildings located in California and Washington [Mosier 2000], the column-to-beam flexural strength ratios of those buildings ranged broadly and the average value was 2.0. However, for a conservative estimation of M_R, the beam flexural strengths were calculated including the slab reinforcement within the effective slab width according to ASCE 41, while the increase of column flexural strength due to the compressive axial load (which was smaller than the balanced load) was ignored. Eight column longitudinal bars were uniformly distributed on the sides of the column cross-section, i.e., three bars per side, considering the possible role of the column intermediate bars as ties in the joint region [Hwang et al. 2005] and avoiding excessive confinement of the joint region by the column longitudinal bars.

Table 3.1   Values of design parameters of test specimens.

Specimen	h_b/h_c	SI_j, psi$^{0.5}$ (MPa$^{0.5}$)		$M_R^* = \dfrac{\sum M_{col}}{M_{beam}}$
SP1	1.0	Neg.	8.3 (0.69)	2.8
		Pos.	6.8 (0.56)	
SP2	1.0	Neg.	12.8 (1.06)	1.9
		Pos.	8.7 (0.72)	
SP3	1.7	Neg.	7.7 (0.64)	2.0
		Pos.	6.2 (0.52)	
SP4	1.7	Neg.	11.1 (0.93)	1.4
		Pos.	7.5 (0.63)	

Note: *beam strengths are calculated for negative bending, i.e., slab in tension.

All four specimens had the same slab section and reinforcement: 6 in. (152.4 mm) thickness and #3@12 in. (304.8 mm) in both directions for the top and bottom layers. Slab top reinforcement extended to the back of the orthogonal beam with 90° hooks, while the slab bottom reinforcement stopped at 6 in. (152.4 mm) from the beam-slab interface without 90° hooks. The configuration of the specimens and their design details are summarized in Figure 3.1, and complete drawings are presented in Appendix A.

Figure 3.1   Specimen details and test matrix.
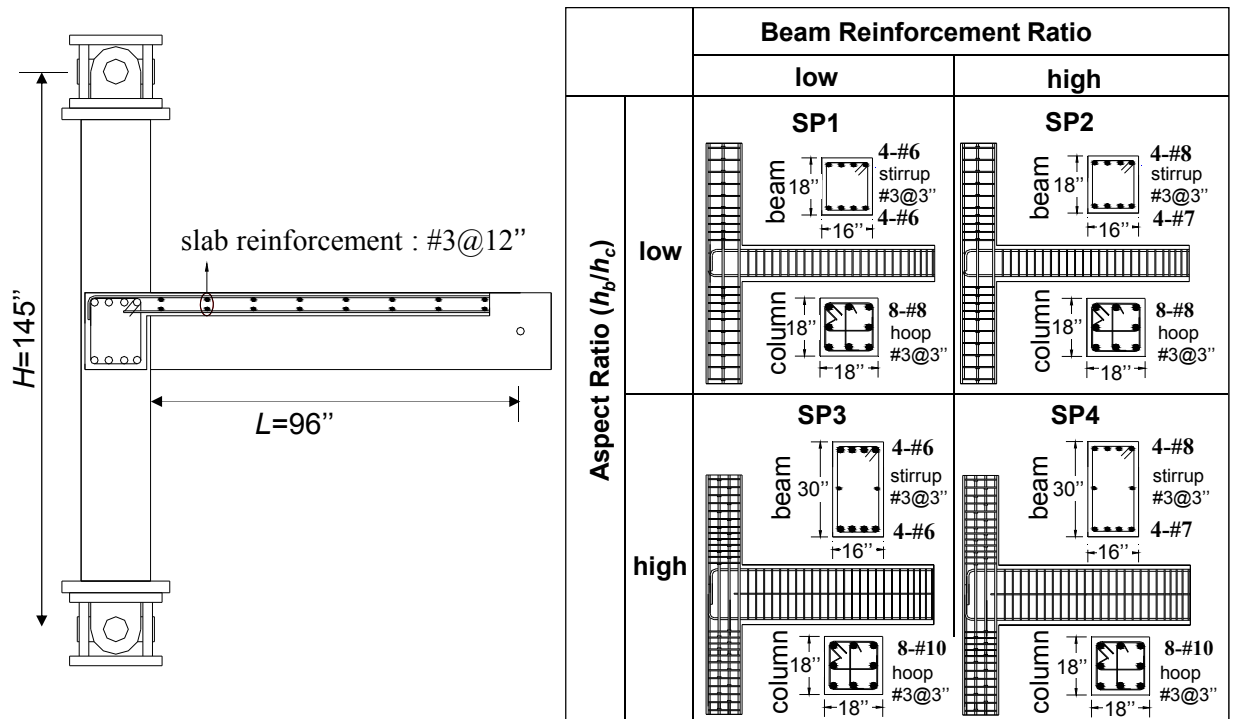
Notes: 1. SIj is joint shear index calculated using Equation (2.13)
2. 1" = 25.4 mm

3.2   SPECIMEN CONSTRUCTION

The four specimens were constructed outside the *nees@berkeley* laboratory. The specimen construction sequence is illustrated in Figure 3.2. A local contractor constructed the specimens in two phases: the first phase included SP1 and SP2 (low joint aspect ratio specimens) and the second phase included SP3 and SP4 (high joint aspect ratio specimens). In each phase of construction, different concrete mixes were used. The ratio of water to cement (W/C) was 0.75 in the first phase and 0.62 in the second phase. The details of the two concrete mix designs are presented in Appendix B.

The design details of the beams and the column longitudinal reinforcement introduced a design conflict of placing the beam and column of exterior (Ext.) and interior (Int.) bars in the joint region. To resolve this conflict, the beams exterior and interior bars were placed inside the column exterior and interior bars as shown in Figure 3.3(a). Another design dilemma was that the longitudinal bars of the two orthogonal beams were crossing each other in the joint region. Thus, the top and bottom reinforcing bars of the east-west (EW) beam were placed under those of the north-south (NS) beam, see Figure 3.3(b). Due to these reinforcement details, the two orthogonal beams, assumed to be nominally identical, had different cover concrete thickness in the beams' cross section. The cover concrete thickness of the beam cross sections were measured after testing; their values are listed in Table 3.2.

Couplers, embedded screw-type headed bars were in the column as shown Figure 3.4, were utilized to install the bi-directional swivels on top and bottom of the column. Concrete was placed and vibrated in the vertical position from the pre-mix truck. Concrete casting was

33

performed in two stages: (1) the lower column, beam, and slab; and (2) the upper column. Specimens SP1 and SP2 were cured for 60 days prior to stripping their forms, while specimens SP3 and SP4 were cured for 20 days before stripping their forms Prior to testing of each of the four specimens, a forklift was used to transport the specimens from outside the laboratory to the test rig inside the laboratory. Figure 3.5 shows two photographs of SP1 during and after transporting it to the test rig.

(a) formwork	(b) installation of reinforcing bars
(c) concrete casting	(d) stripped specimen

Figure 3.2   Specimen SP1 construction sequence.
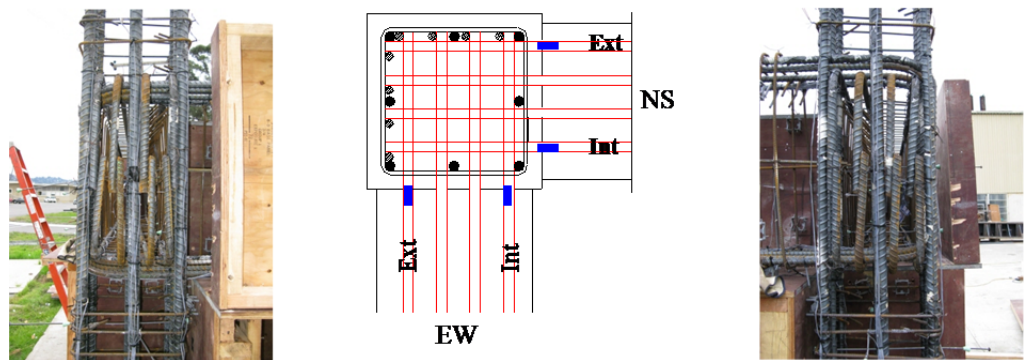
(a) conflict of the beams and column longitudinal bars

EW direction

NS direction

(b) conflict of EW and NS beams longitudinal bars

Figure 3.3   Placement of beam and column reinforcement at corner of the joint.

Table **3.2**   **Measured cover concrete thickness of beam cross sections.**

Specimen	Cover concrete thickness [in. (mm)]			
	EW		NS	
	Top	Bottom	Top	Bottom
SP1	3.00 (76.2)	1.50 (38.1)	2.50 (63.5)	2.00 (50.8)
SP2	2.50 (63.5)	1.50 (38.1)	1.50 (38.1)	2.00 (50.8)
SP3	3.00 (76.2)	1.50 (38.1)	2.50 (63.5)	2.00 (50.8)
SP4	3.00 (76.2)	1.25 (31.8)	2.00 (50.8)	2.25 (57.2)

(a) couplers at the bottom of column   (b) couplers at the top of column

Figure 3.4   Couplers and headed bars at top and bottom of column.

(a) curing transporting SP1   (b) placing SP1 on the test rig

Figure 3.5   Transportation of specimen SP1.

3.3   MATERIAL PROPERTIES

A design concrete compressive strength for the tested full-scale specimens was selected based on the values take from the literature and joint specimens and substructuring of old existing RC buildings. The mean concrete compressive strength in a database of 56 non-ductile column specimens was 3.7 ksi (25.5 MPa) in Ghannoum [2007] and the design concrete strength of unreinforced joint specimens tested in Cornell University was 3.5 ksi (24.1 MPa) in Beres et al. [1992]. Based the above values, concrete strength of all specimens targeted a 28 day compressive strength of 3.5 ksi (24.1 MPa). Maximum aggregate size was 1 in. (25.4 mm) to be relevant for the full-scale specimen. Two mix designs were used because the first mix showed less strength than specified after 28 days. The concrete properties of the four specimens are summarized in Table 3.3. More information including mix design and strength gain with time are provided in Appendix B.

Grade 60 A706 deformed reinforcing steel bars were used for all the specimens. Used bar sizes in metric units were 10 mm (D10), 19 mm (D19), 22 mm (D22), 25mm (D25), and 32mm (D32) compatible with #3, #6, #7, #8, and #10 in US standard bars, respectively. The summary of reinforcing steel bar properties is given in Table 3.4. More information of properties of reinforcing steel bars from coupon tests is presented in Appendix B.

Table 3.3   Concrete material properties.

Property	SP1	SP2	SP3	SP4
Compressive strength f_c' [ksi (MPa)]	3.58 (24.7)	3.53 (24.3)	3.60 (24.8)	3.96 (27.3)
Strain at peak stress ε_o	0.0019	0.0019	0.0024	0.0024
Initial tangent modulus E_c [ksi (GPa)]	3570 (24.6)	3850 (26.5)	3130 (21.5)	3300 (22.7)
Splitting tensile strength f_{ct} [ksi (MPa)]	0.34 (2.34)	0.34 (2.34)	0.32 (2.21)	0.44 (3.03)
Age of testing [days]	295	358	378	421

Table 3.4   Reinforcing steel material properties.

Property	#3 (D10)	#6 (D19)	#7 (D22)	#8 (D25)	#10 (D32)
Yield stress f_y [ksi (MPa)]	73.5[*] (507)	78.6 (542)	73.3 (505)	72.2 (498)	68.3 (471)
Ultimate stress f_u [ksi (MPa)]	115.0 (794)	104.5 (721)	103.1 (711)	102.6 (708)	100.5 (693)
Yield strain ε_y	0.0035[*]	0.0028	0.0027	0.0025	0.0023
Ultimate strain ε_u	0.105	0.120	0.120	0.120	0.120
Elastic Modulus E_s [ksi (GPa)]	28200 (195)	27900 (193)	26700 (184)	28900 (213)	29600 (204)

[*]yield stress and strain are estimated using 0.1% offset method

3.4   LOADING PROTOCOLS

This section discusses the beams lateral and column axial loading protocols. The lateral loads were specified at the tested beam ends using displacement controls, while the column axial load was specified using force control.

3.4.1 Beam Lateral Loading

Cyclic lateral loading was quasi-statically [0.02 in./sec (0.51 mm/sec)] applied to the end of each beam, which was assumed to be inflection point of the beams in a building frame according to the displacement-controlled pattern shown in Figure 3.6. The applied displacement alternated between the two beams, i.e., one beam was remained at a stationary point during the loading of the other orthogonal beam. The applied displacement history was defined in terms of yield displacement (δ_y) so that each specimen was subjected to similar number cyclic loading until the beams yielded and thereafter. Using OpenSees [2010], the yield displacements were estimated to be 1.24 in. (31.5 mm) for SP1 and SP2, and 0.92 in. (23.4 mm) for SP3 and SP4. Note that the *nonlinearBeamColumn* element in OpenSees was used to model the beams and columns, and the confined concrete and reinforcement of their cross sections were modeled using *Concrete04* and *ReinforcingSteel* materials, respectively. The corresponding drift was about 1.2% and 0.9%, respectively.

Both beams were pulled down to one-quarter of the estimated yield displacement (δ_y), which was defined as a stationary point, $\delta_0 = -\delta_y/4$. This initial pull-down loading was intended to simulate gravity loads prior to lateral loading and to make the beam yield first in response to downward loading so that the contribution of slab reinforcement could be estimated. To avoid unnecessary low-cycle fatigue on the join, three loading groups were applied incrementally up to the yield displacement. In inelastic loading groups, the peak displacement of the current loading group was defined as 1.5 times that of the previous loading group. In each group of loading, two reversed cycles were applied to each direction of the beam. After each group of cycles in the inelastic loading groups, a single low-level cycle one-third the previous displacement level was applied to quantify the stiffness degradation. The sequence and protocol of the displacement-controlled loading are depicted in Figure 3.6, and the applied beam displacement history is presented in Table 3.5.

(a) loading sequence

(b) applied beam displacement history
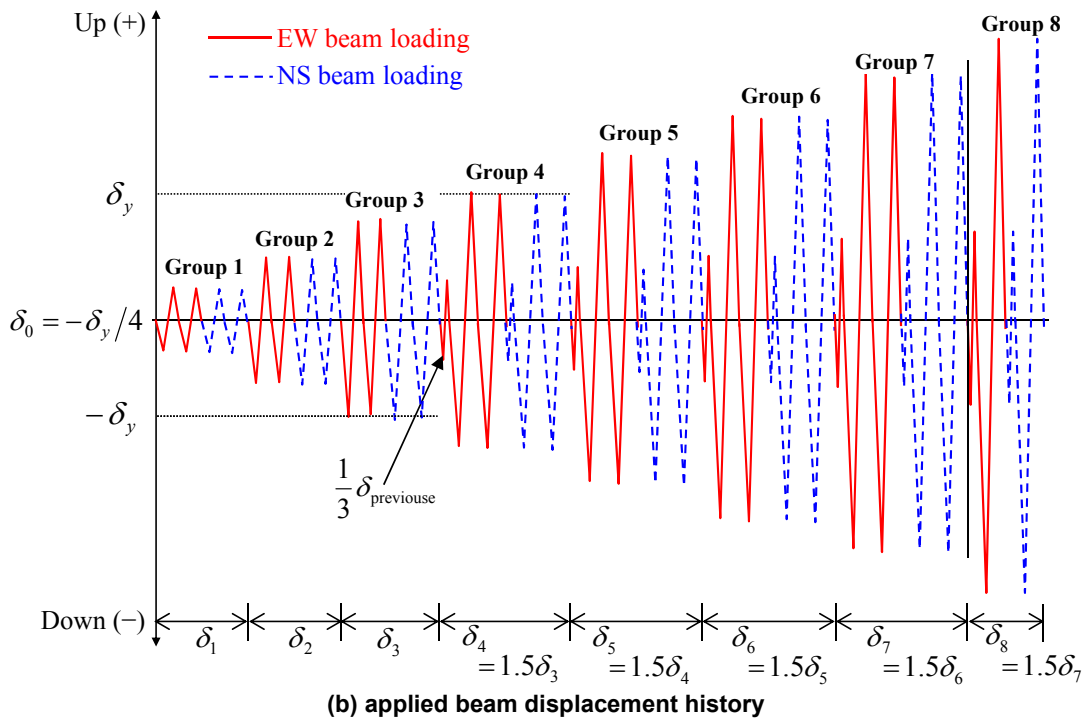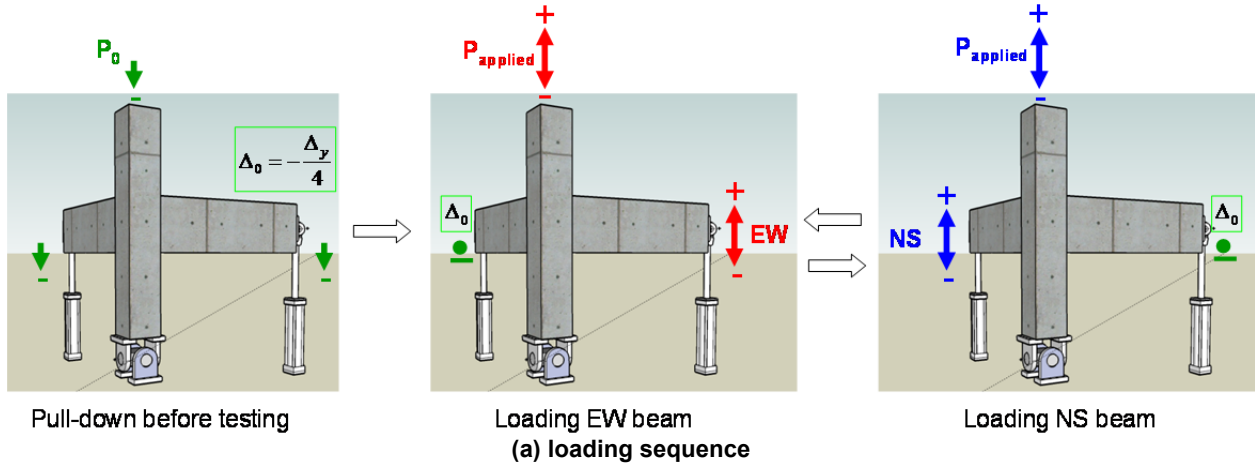
Figure 3.6   Loading sequence and applied beam displacement history.

Table 3.5   Applied beam displacement values for loading groups.

	Pull-down	Group 1	Group 2	Group 3	Group 4	Group 5	Group 6	Group 7
Up	$-0.25\Delta_y$	0	$0.25\Delta_y$	$0.50\Delta_y$	$1.00\Delta_y$	$1.75\Delta_y$	$2.88\Delta_y$	$4.56\Delta_y$
Down		$-0.50\Delta_y$	$-0.75\Delta_y$	$-1.00\Delta_y$	$-1.50\Delta_y$	$-2.25\Delta_y$	$-3.38\Delta_y$	$-5.06\Delta_y$

Note: Δ_y = 1.24 in. (31.5 mm) for SP1 and SP2; Δ_y = 0.92 in. (23.4 mm) for SP3 and SP4

39

3.4.2 Column Axial Loading

Column axial load varied during earthquake shaking due to the overturning moment effect on columns, especially corner columns. To simulate this variation of column axial load, a relationship between the axial load of corner column and the beam shear force was derived from pushover analysis of a non-ductile RC prototype building, the 7-story Van Nuys Holiday Inn located in the San Fernando Valley of Los Angeles, California. Damaged during 1994 Northridge earthquake, the structural details of this building can be found in Krawinkler [2005]. Note that this building was used for structural simulations in Chapter 6 where the details of beams and columns are presented.

3.4.2.1 Estimate of Column Axial Load

The transverse (NS direction) perimeter frame of the prototype building was selected, and its beams and columns were modified to have similar dimensions of the test specimens as follows:

1. Column layout was changed from rectangular to square plan with three bays in each direction corresponding to the transverse perimeter frame of the prototype building, as shown in Figure 3.7;

2. Column cross-section ($b_c \times h_c$) was changed from 14×20 in. (356×508 mm) to 18×18 in. (457×457 mm) considering the change of column layout;

3. Beam width was increased from 14 in. (356 mm) to 16 in. (406 mm) considering the increase of column width;

4. Gravity load on the first story corner column was adjusted to be $0.15 f_c' A_g$ identical to the original prototype building; and

5. Slab contribution to beam flexural strength was not considered.
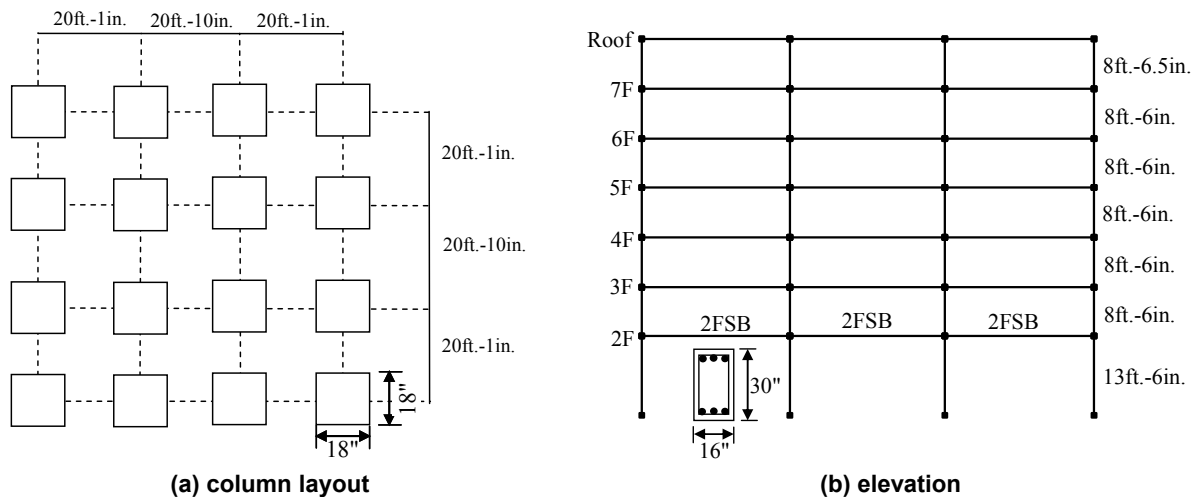
Figure 3.7   Modified prototype building.

Using OpenSees [2010] to estimate the range of axial load variation in corner columns, a nonlinear static (pushover) analysis was performed for the above modified prototype building

frame. In order to check the accuracy of this analysis, analytical materials and element models in OpenSees [2010] were selected to be similar to those adopted by Paspuleti [2002].

1. Concrete material: *Concrete01* for all beam and column cross-section;

2. Reinforcing bars: *Steel02* with hardening ratio of 2%;

3. Beam and column elements: *beamWithHinges* with plastic hinge length being equal to beam depth; and

4. Effective moment of inertia (I_g) for elastic region: $0.5I_g$ for the beams and columns.

The pushover analysis was stopped when the second-floor exterior beam reached the negative ultimate moment capacity calculated from section analysis. From the pushover analysis results, additional compressive axial load on the first story corner column due to overturning moment was approximately 60% of the gravity load ($0.15f_c'A_g$) for each direction in the 7-story building.

Total axial load on the first story corner column was estimated for uni-directional and simultaneous bi-directional loading as follows:

For uni-directional loading

$$0.15f_c'A_g\left(1-0.6\right)=0.06f_c'A_g \le P \le 0.15f_c'A_g\left(1+0.6\right)=0.24f_c'A_g \tag{3.1a}$$

For simultaneous bi-directional loading

$$0.15f_c'A_g\left(1-0.6\times2\right)=-0.003f_c'A_g \le P \le 0.15f_c'A_g\left(1+0.6\times2\right)=0.33f_c'A_g \tag{3.1b}$$

Note that column axial load P is positive for compression. As shown in Figure 3.8, the range of column axial load is plotted on the P-M interaction diagram of the first story corner column of the prototype building. Based on Equations (3.1a) and (3.1b), the axial load on the first-story corner column ranged within compression (positive) from $0.06f_c'A_g$ to $0.24f_c'A_g$ for uni-directional loading (under which most unreinforced joint tests from literature were conducted), and for simultaneous bi-directional loading, it varied from small tension (negative) to $0.33f_c'A_g$.
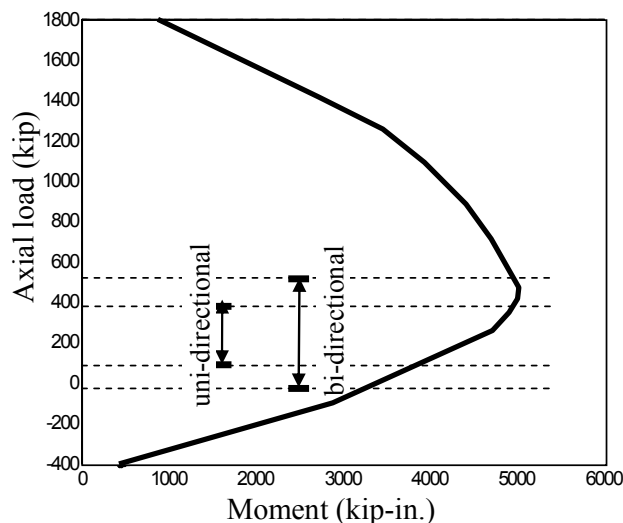
Figure 3.8   Range of column axial load variation in the P-M interaction diagram.

41

3.4.2.2 Column Axial Loading Equation

The relation between the beam shear and column axial load was obtained from the pushover analysis. The beam shear was calculated by dividing the beam-end moment by the distance from the beam inflection point to column face which was assumed to be 8 ft. (2.44 m) considering the specimen dimension. Due to the assumed square plan, the beam shears were assumed to be identical for the two orthogonal directions. The derived equation was applicable to specimens SP3 and SP4 that have the same dimensions of the first story beams and columns: beam and column dimensions were 16×30 in. (406×762 mm) and 18×18 in. $(457 \times 457 \, \text{mm})$, respectively, as shown in Figure 3.7. The coefficient was adjusted for SP1 and SP2 such that similar column axial loads were applied at the onset of beam yielding for each pair of specimens, i.e., SP1 and SP3, and SP2 and SP4. The beam shear forces for the EW and NS directions, $V_{b,\text{EW}}$ and $V_{b,\text{NS}}$, respectively, at each step were recorded in real time and these forces directly determined the applied column axial load using the following linear equations:

$$P_{\text{applied}} = 95 - 4V_{b,\text{EW}} - 4V_{b,\text{NS}} \quad \text{for specimens SP1 and SP2} \qquad (3.2a)$$

$$P_{\text{applied}} = 95 - 2V_{b,\text{EW}} - 2V_{b,\text{NS}} \quad \text{for specimens SP3 and SP4} \qquad (3.2b)$$

As noted in Figure 3.9, the applied column axial load, P_{applied}, was positive for compression, and the beam shear forces, $V_{b,\text{EW}}$ and $V_{b,\text{NS}}$, were positive for the upward loading, i.e., additional compressive loads were applied during the downward loading of the beams. The determined column axial load was applied by two hydraulic actuators located on each side of column, and these two actuators were constrained to move equally in the vertical direction.
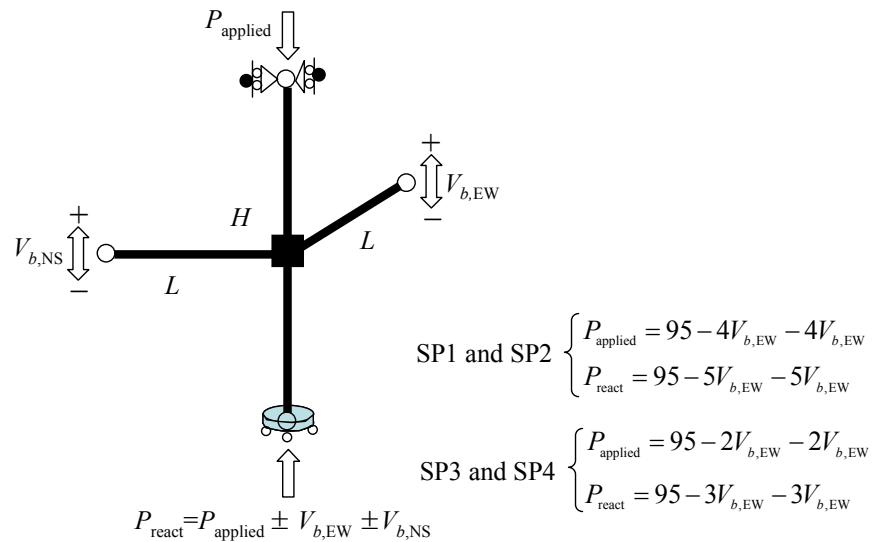
Figure 3.9 Applied column axial load for the four specimens.

3.5 TEST SET UP

As shown in Figure 3.10, a special test set up and devices were designed to achieve hinge boundary condition at top and bottom of the column in order to apply variable column axial load

with restraining lateral movement of the specimen. For the hinge boundary conditions, two bi-directional swivels were designed to carry 500 kips of compression and 200 kips of tension. These swivels were connected to the column using embedded couplers and to the vertical loading test frame by bolt connections.

Two W $16 \times 1/2 \times 36$ steel beams and built-up boxes were used to apply column axial load using two hydraulic actuators (360 kip capacity for retraction). The two hydraulic actuators for column loading were supported on the top flange of the bottom W $16 \times 1/2 \times 36$ beam and connected to the top W $16 \times 1/2 \times 36$ beam using the built-up boxes.

The lateral restraining frame was designed to allow vertical movement of the two column actuators without lateral movement of the specimen at the top end of the column. Two HSS $12 \times 12 \times 1/2$ members were bolted to the reaction wall at one end and were connected each other by welding tubes of the same size between them. Additional fabrication was performed to provide a space for the built-up box to slide vertically between the two tube members. Another HSS $8 \times 8 \times 1/2$ diagonal member was used to provide lateral restraint of the frame. As a result, no P-Δ effects were taken into account in this test set up.

In total, four hydraulic actuators were used: two 360-kip-capacity actuators for column loading and two 120-kip-capacity actuators for beam loading. All actuators were connected to adaptor plates. The top and bottom ends of the column were artificially confined by filling hydro-stone between the column and surrounding cylindrical steel ring to prevent local failure during testing, see Figure 3.11. The sequence of test set up assemblage is presented in Figure 3.12. Drawings of the complete test set up are presented in Appendix A.

(a) vertical frame and bidirectional swivels   (b) lateral restraining frame
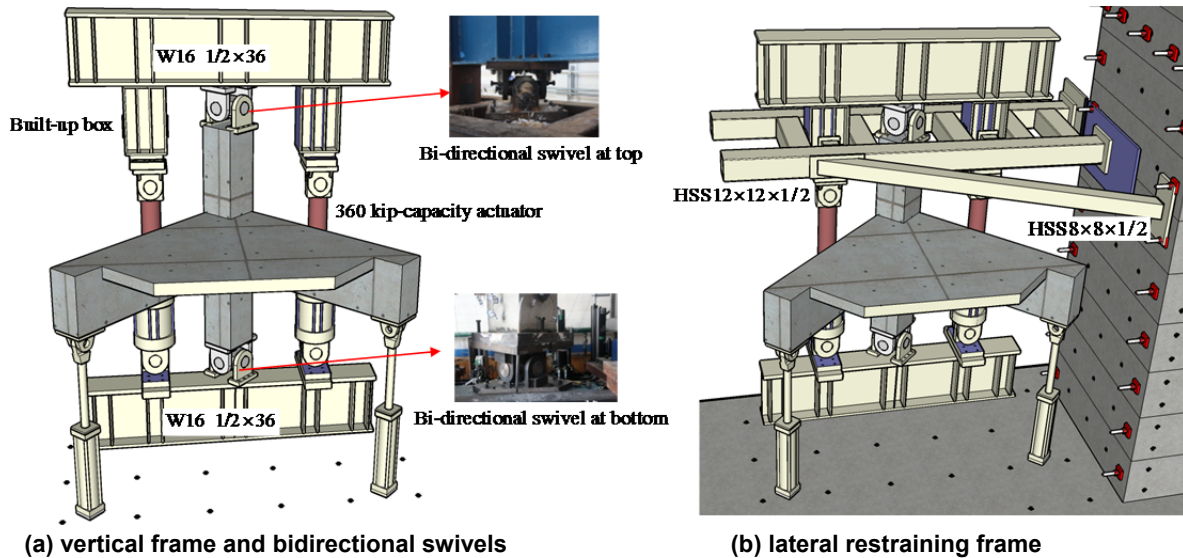
Figure 3.10   Design of test frame.
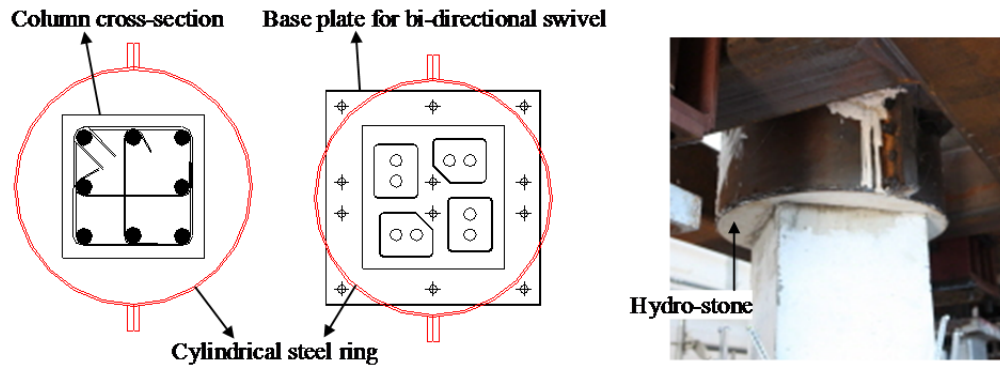
Figure 3.11   Confinement of the column at the boundary.

| bottom support beam | vertical actuators | specimen in place |
| specimen ready for testing | top loading beam | lateral restraining frame |
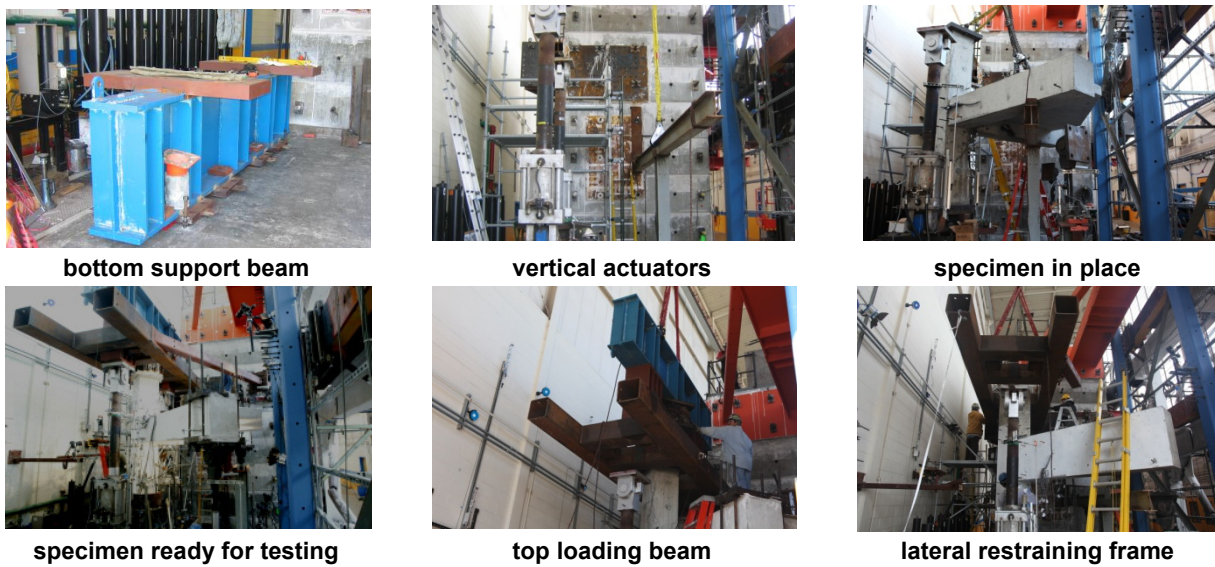
Figure 3.12   Assembling test set up.

3.6   INSTRUMENTATION

During the tests, external and internal instrumentations monitored the following: (1) beam shear and column axial forces; (2) beams and column deformations; (3) joint shear strains; (4) strain of reinforcing bars; and (5) global translations. Four load cells measured forces in actuators, and seventy eight displacement transducers and seventy seven strain gages were used.

3.6.1 Beam Shear and Column Axial Forces

The two 360-kip-capacity and two 120-kip-capacity hydraulic actuators were used to apply column axial load and beam shear forces, respectively. As described in Section 3.4, two beam actuators were operated under displacement control, and two column actuators were driven by force control to apply the total forces calculated from beams shear forces. Applied forces were monitored by built-in load cells in the actuators. The load cells were calibrated before testing, as shown in Figure 3.13. On each actuator, a displacement transducer was installed for beam actuators to apply beam shear by displacement control and for column actuators to have equal vertical displacement during loading of both actuators.

Figure 3.13   Calibration of load cell of the column axial loading actuator.

3.6.2 Beam Shear and Column Deformations

Forty six of displacement transducers were installed on the column and beam to measure flexural curvature of the beams and column, column axial deformation, relative deformation at beam-joint interface, and twisting of the beams. Threaded rods, 7/16 in. (11.1 mm) in diameter, were placed on pre-defined locations. Most of the length of each rod except the middle 3 in. (76.2 mm) were wrapped by Teflon tubes in advance to avoid bond between the rod and surrounding concrete, as shown in Figure 3.14.
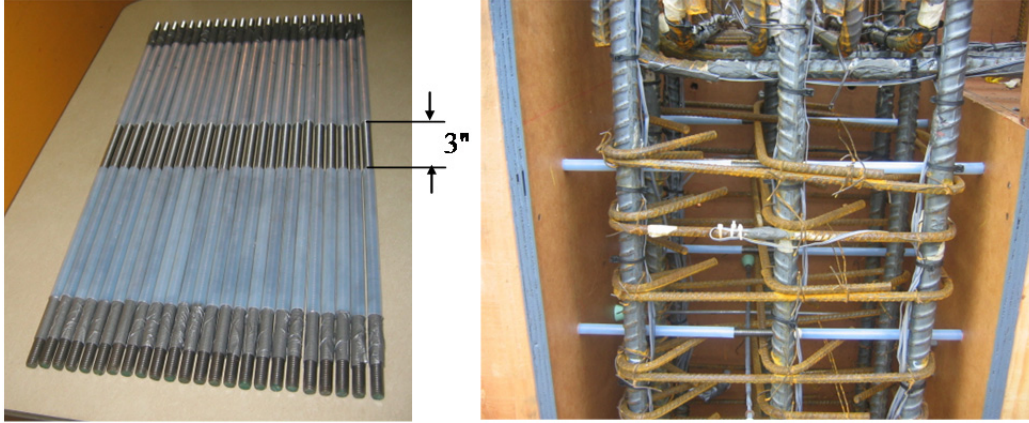
Figure 3.14 Threaded rods for instrumentation.

As shown in Figure 3.15, the beam and column were divided into several segments to evaluate the variation of curvature. The average curvature of each segment in the column and beams was calculated by the relative deformations between tension and compression zones. For example, the curvature of the beam i^{th} segment, $\phi_{B,i}$, was obtained from

$$\phi_{B,i} = \frac{\Delta_{B,b,i} - \Delta_{B,t,i}}{b_{b,i} h_{b,i}} \tag{3.3}$$

where $\Delta_{B,b,i}$ and $\Delta_{B,t,i}$ were deformation of bottom and top displacement measuring gages in the beam i^{th} segment, respectively, and $b_{b,i}$ and $h_{b,i}$ were gage length and vertical distance between gages of the beam i^{th} segment, respectively. The column curvature was calculated by a similar equation below with averaging relative deformations in each two opposite two sides, see Figure 3.15.

$$\phi_{C,i} = \frac{\overline{\Delta}_{C,l,i} - \overline{\Delta}_{C,r,i}}{b_{c,i} h_{c,i}} \tag{3.4}$$

where $\overline{\Delta}_{C,l,i}$ and $\overline{\Delta}_{C,r,i}$ are respectively average deformation of left and right displacement measuring gages of the column i^{th} segment, respectively, in one direction of bending, and $b_{c,i}$ and $h_{c,i}$ are gage length and horizontal distance between gages of the column i^{th} segment, respectively, as shown in Figure 3.15.
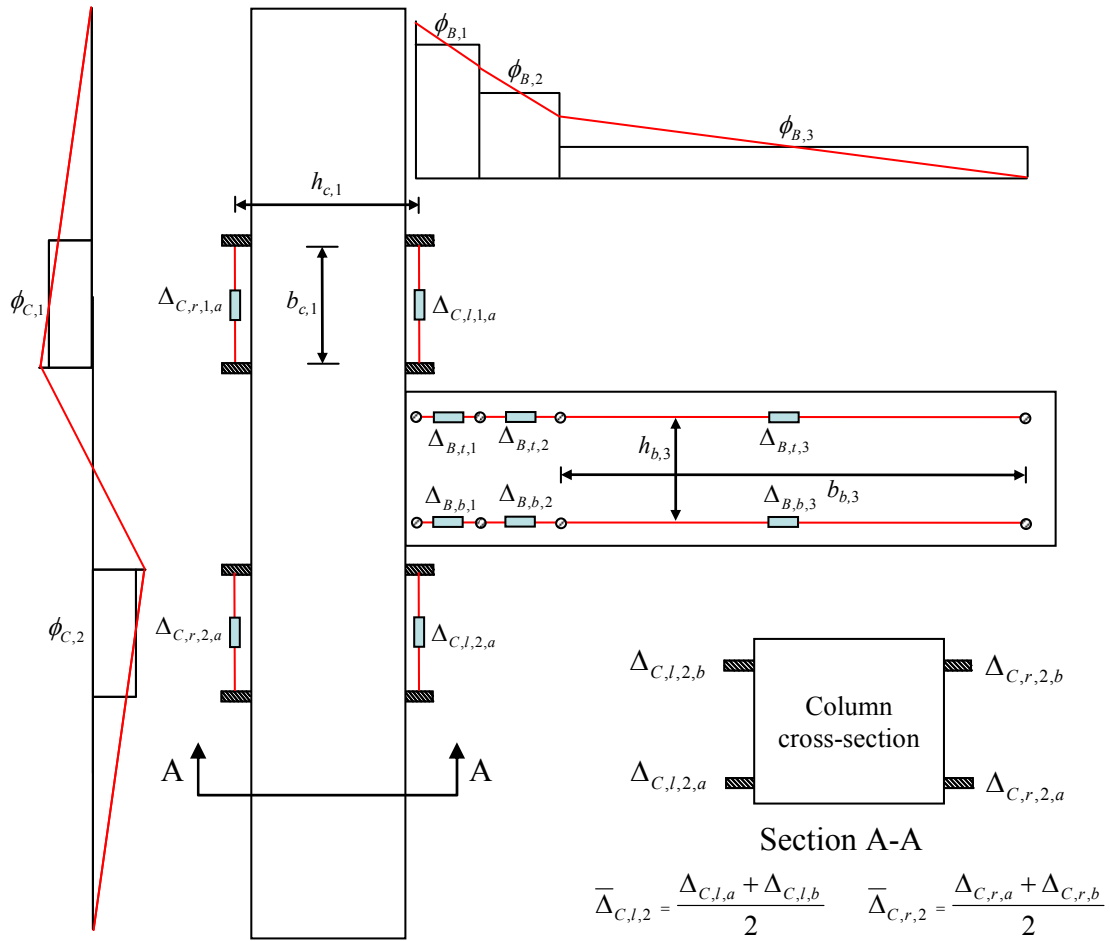
Figure 3.15   Instrumentation for beam and column flexural deformations.
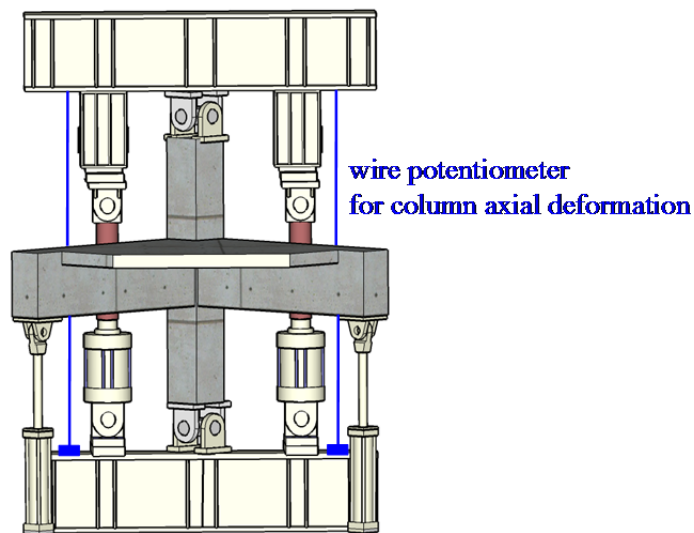
Figure 3.16   Instrumentation for column axial deformation.
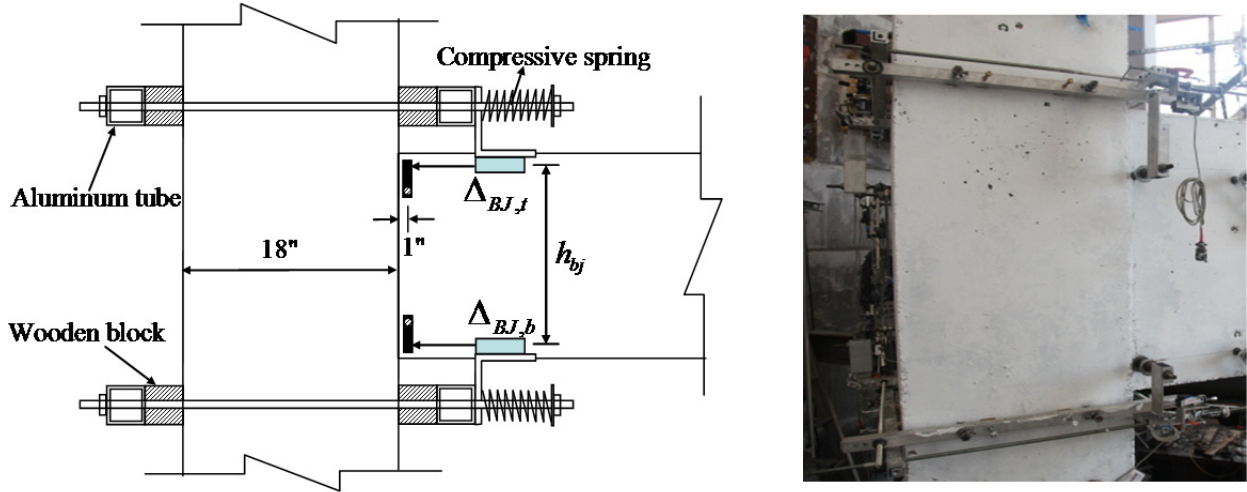
Figure 3.17   Instrumentation for rotation at the beam-joint interface.

During testing, the column axial deformation was measured by two wire potentiometers installed between the top and bottom W $16 \times 1/2 \times 36$ steel beams on both sides of the column, see Figure 3.16. The column axial deformation was determined as the average of these two measurements.

The relative deformation at the beam-joint interfaces was measured and transformed into the rotation. Two displacement transducers were mounted on angles attached to aluminum tubes, which were rigidly attached to the column face by the spring tension. Frictionless plates were firmly bolted to threaded rods embedded in the beam 1 in. (25.4 mm) from the beam-joint interface, as shown in Figure 3.17. The relative deformations, $\Delta_{BJ,b}$ (bottom) and $\Delta_{BJ,t}$ (top), were assumed to be the relative translation between displacement transducer and frictionless plate. Dividing the relative deformations by the distance between top and bottom transducer, h_{bj}, the rotation at the beam-joint interface, θ_s, is obtained:

$$\theta_s = \frac{\Delta_{BJ,b} - \Delta_{BJ,t}}{h_{bj}} \tag{3.5}$$

Due to the presence of the RC slab, a beam in the longitudinal direction is subjected to torsion during transverse beam loading. Twisting of the longitudinal beam was measured at three locations along its span, as shown in Figure 3.18. The twisting angle at the ith location, $\theta_{T,i}$, is calculated by

$$\theta_{T,i} = \frac{\Delta_{L,i} - \Delta_{R,i}}{b_t} \tag{3.6}$$

where $\Delta_{L,i}$ and $\Delta_{R,i}$ are the vertical displacement of left and right side at i^{th} location, respectively, and b_t is the distance between the left and right transducers.
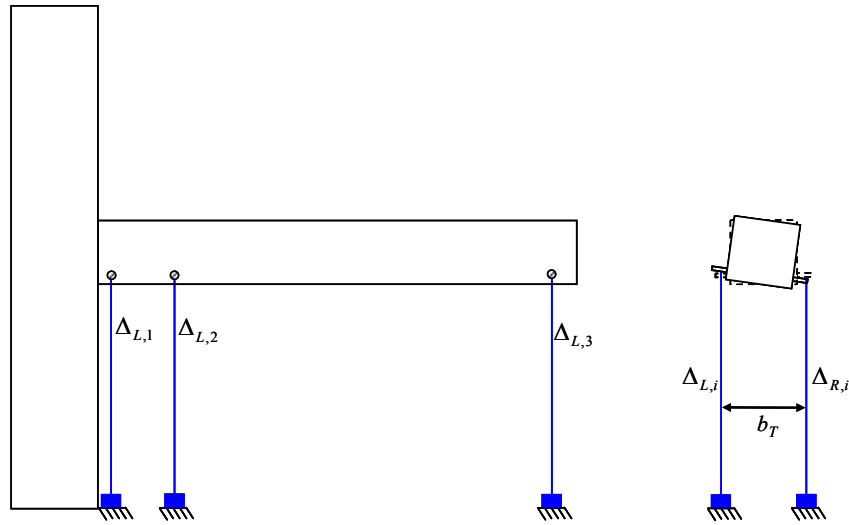
Figure 3.18   Instrumentation for beam twisting.

3.6.3 Joint Shear Strains

Based on the literature review of tests measuring joint shear strain as depicted in Figure 3.19. the instrumentation of four sides and two diagonals was adopted. Fixtures were installed in the outside of joint panel to allow expansion due to crack opening and sliding as shown in Figure 3.20. The rational for placement of the joint shear strain instrumentation was as follows: (1) test data from the literature show that joint shear cracks propagated to the column above and below the joint, requiring that instrumentation fixtures be installed outside the joint panel; and (2) shear strain measurements within the joint panel was highly affected by the crack location, particularly in the case of unreinforced joints. In this case, the concrete split into several pieces and moved freely due to absence of transverse reinforcement, which also required measurements outside the joint panel to avoid constraining or missing recording of such movement.
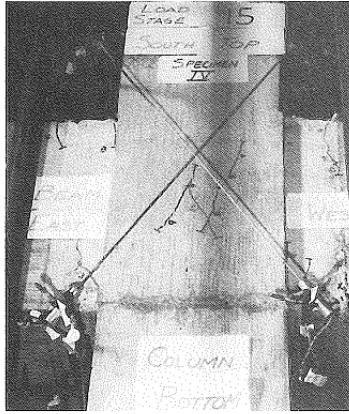
(a) two diagonals measurement [Meinheit and Jirsa 1977]

(b) two relationship beam-column deformations [Pampanin et al. 2003]
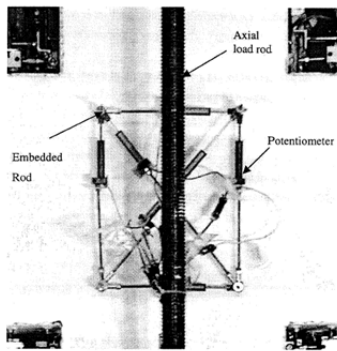
(c) six measurements using rods within the joint region [Walker 2001]
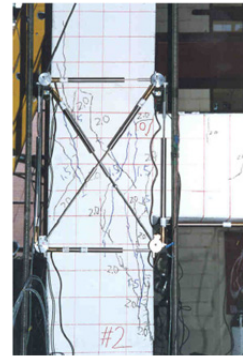
(d) six measurements using rods outside the joint [Pantelides et al. 2002]

Figure 3.19   Joint shear strain instrumentations in literature.
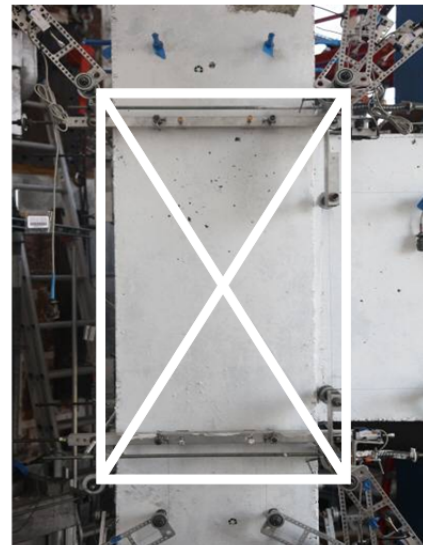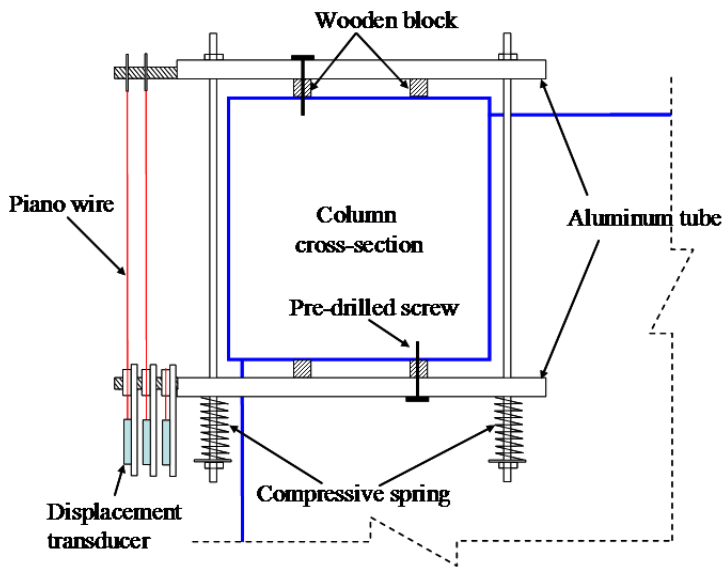
Figure 3.20   Instrumentation for joint shear strain in this study.

From this instrumentation, joint shear strain, γ_{xy}, can be calculated using trigonometric law as

$$\gamma_{xy} = \frac{1}{4}\left\{\sum_{i=1,2,5,6}\left(\omega_i' - \omega_i^0\right) - \sum_{j=3,4,7,8}\left(\omega_j' - \omega_j^0\right)\right\} \tag{3.7}$$

where ω_i^o and ω_i' are the initial angle and deformed angle of the ith corner in the joint panel, respectively. These angles in undeformed and deformed shapes are illustrated in Figure 3.21.

(a) original joint geometry   (b) deformed joint geometry
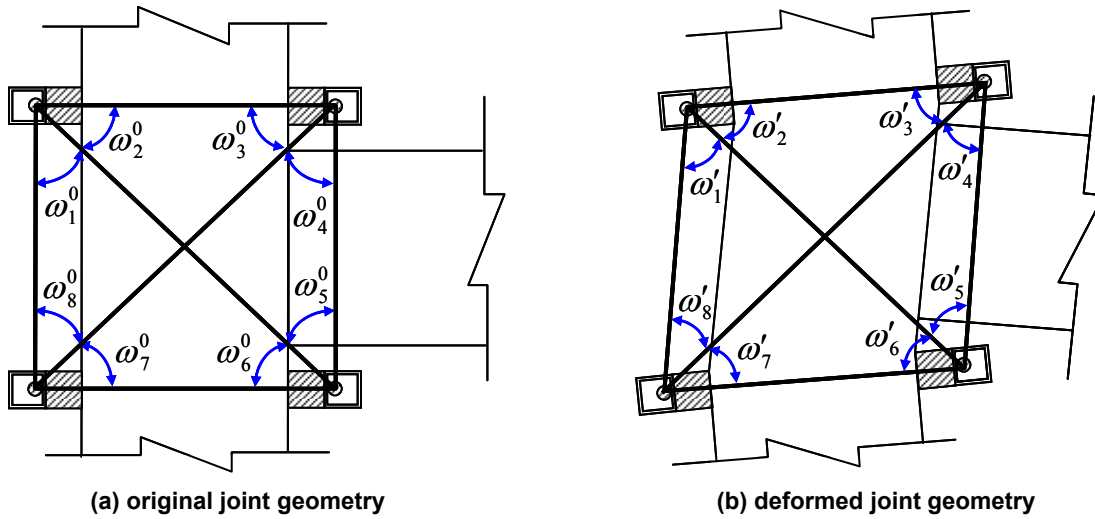
Figure 3.21   Joint shear strain calculation.

3.6.4 Strain Gages

A total of seventy five strain gages were installed on the longitudinal and transverse beam reinforcement, column reinforcement, and slab reinforcement. The used strain gages had a post-yield deformation capacity of 10–15% strain with gage size of 0.20 in.×0.08 in. (5 mm×2 mm). Each strain gage glued to the surface of a reinforcing bar was coated by wax, butyl rubber, and epoxy.

Among the beam reinforcements, four beam longitudinal bars located on interior and exterior bars at top and bottom were selected for measuring strains. Each bar had 5 strain gages located here: (1) on the hook tail; (2) at the hook bending point; (3) at the middle of joint; (4) on the beam-column interface; and (5) $d_b/2$ from the interface, where d_b was the effective beam depth. Figure 3.22 shows the layout of strain gages on beam reinforcement. The instrumentation of beam reinforcement strains was intended to determine the onset and propagation of the beam longitudinal bars yielding, to evaluate the bond deterioration within the joint region, and to calculate the joint shear stresses. Because shear failure was not expected in any of the beams, only one stirrup was instrumented with one strain gage, see Figure 3.22.

In the column, strain gages were mounted on four longitudinal bars at each corner and two intermediate bars only on the open sides where the beams were not framed in. The layout of strain gages on column reinforcement is shown in Figure 3.23. Strain gage data at corners were

used to confirm that the column longitudinal bars were elastic during testing, and strain gages of the intermediate bars were used to investigate whether these bars acted as tension ties as postulated in Hwang et al. [2005]. Because shear failure was not expected in any of the columns, only two transverse ties were instrumented with two strain gages each, as shown in Figure 3.23.

In the slab, four top and two bottom reinforcing bars were gaged with strain gages in each direction. Figure 3.24 shows the layout of strain gages on the slab reinforcement. The slab reinforcement strain data were used to estimate the effective slab width and to observe the behavior of possible insufficient anchorage detail of the bottom bars.
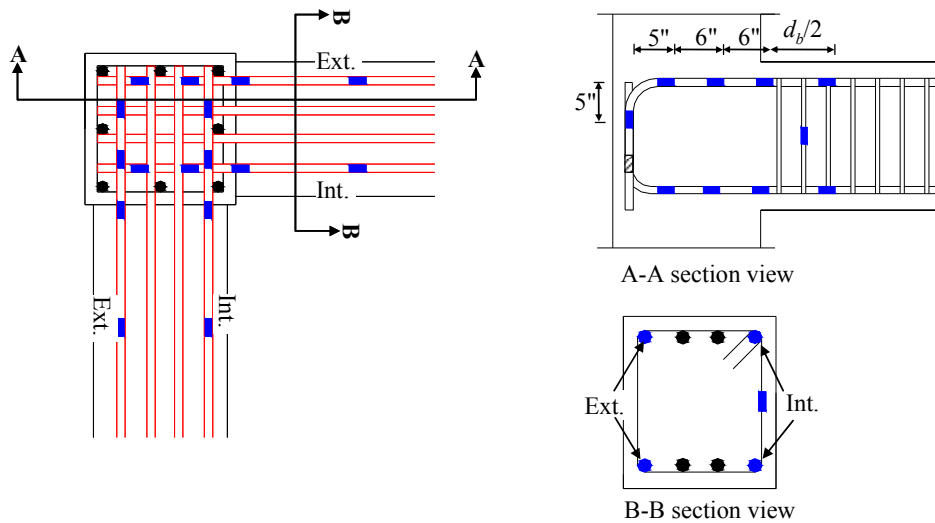
Figure 3.22   Strain gages on beam reinforcement.
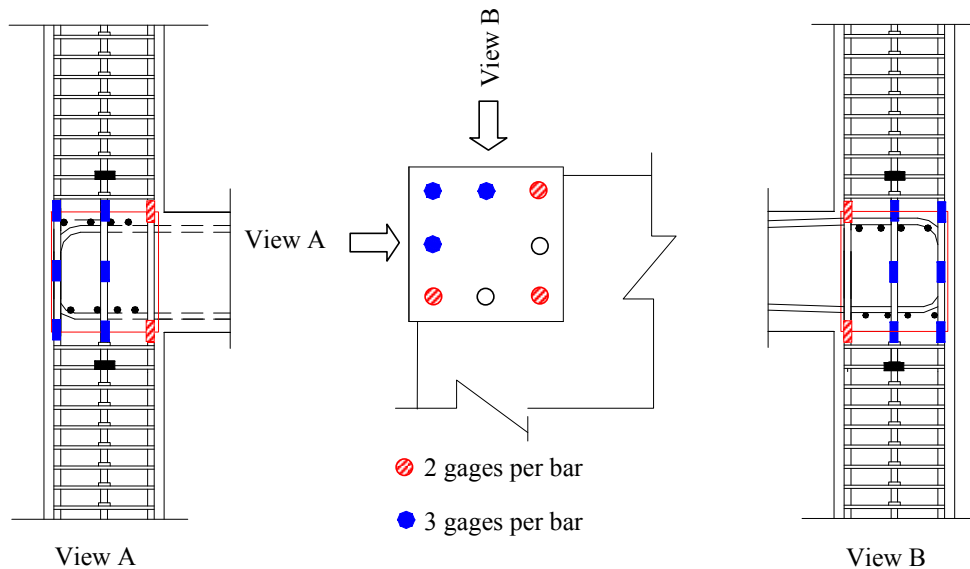
Figure 3.23   Strain gages on column reinforcement.

52
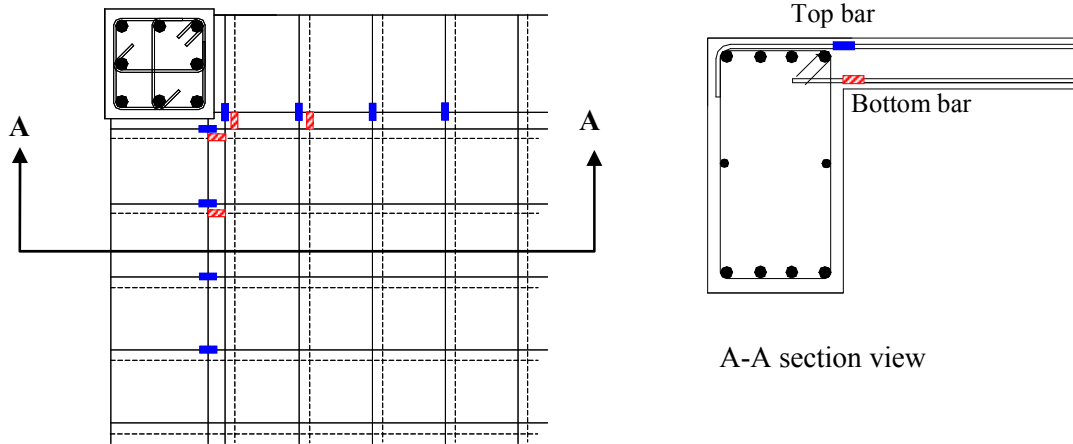
Figure 3.24   Strain gages on slab reinforcement.

3.6.5 Global Translations

The global translations of the test frame and the specimen were measured by displacement transducers and strain gages, as shown in Figure 3.25. Translations of top beam of the vertical test frame and the column were monitored to check if the lateral restraining frame functioned as expected. At bottom of column, rotation of the bi-directional swivel was measured to determine if the bi-directional swivel functioned as a true hinge. In addition, relative translations between the top and the bottom of the joint panel were measured during longitudinal beam loading. Two strain gages were installed on the diagonal tube bracing member to monitor the stability of the lateral restraining frame.

Monitoring relative translation of joint panel region

Monitoring relative translation of base plate

(a) global translations of specimen

Top of beam

Top of column

Lateral restraining frame

Top of beam

Top of column

Strain gages

(b) global translations of test frame (top view)
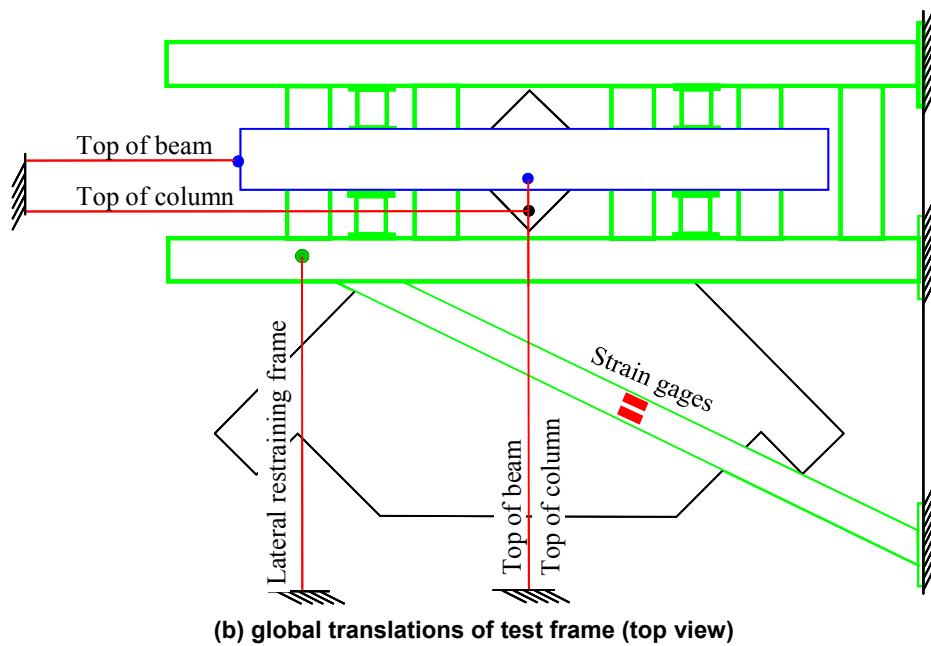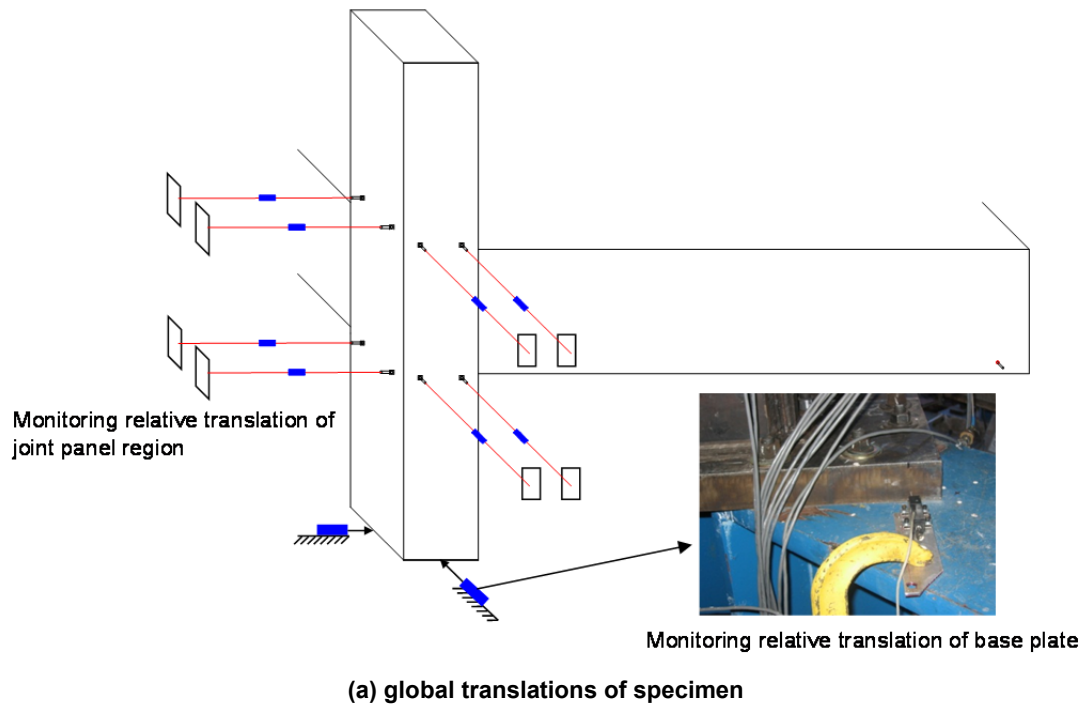
Figure 3.25   Instrumentation for global translation.

4   Experimental Results and Observations

Test results including the measured data and observed damage progression of each specimen are presented next. First, the hysteretic load-drift responses are presented based on the data measured at the tip of the beams. The applied load was recorded by the load cell embedded in the beams actuators. The drift (Δ) is defined as the beam tip displacement (δ) divided by the length of $L+0.5h_c$, where L=8 ft. (2.44 m) is the tested beam length from the column face to the beam loading point, and h_c=18 in. (457 mm) is the column cross-sectional depth, as illustrated in Figure 3.1. The beam tip displacement was determined by averaging two displacements measured at both sides of the loading point. In addition, the variation of the axial load and vertical displacement of the column is presented.

Second, the observed damage in each specimen is described in terms of the formation and propagation of cracks and failure of the joint region, beams, and slab, aided by high-resolution photographs. For clarifying the damage progression, the description of EW direction is followed by NS direction in the sequence of important events, such as first cracking, yielding, and peak loading. The damage description is split into two parts: (1) joint region, and (2) beam and slab in each direction. Subsequently, the common observations of the joint region, beams, and slab in both directions are summarized.

Third, the joint shear stress-rotation responses are presented. Joint shear stresses (v_{jh}) are evaluated using a constant moment arm between the tension and compression resultants in the beam L-shaped cross section, including the effective slab width estimated by ASCE 41. The constant moment arm is defined as a fraction of the effective depth (d_b) of the beam cross section. This fraction is selected as $0.875d_b$ until beam reinforcement yields based on $jd_b = d_b - \beta d_b/3$; βd_b is the neutral axis depth in compression, and β is estimated as 0.4 [Hakuto et al. 1999]. After yielding, the internal moment arm is assumed to be $0.9d_b$ as commonly adopted in estimating the horizontal joint shear forces [Wong 2005]. For comparison with the joint shear strength of ASCE 41, joint shear stresses were normalized by the square root of the concrete compressive strength, $\sqrt{f'_c}$, i.e., $\gamma = v_{jh}/\sqrt{f'_c}$. For joint rotation responses, joint shear strain γ_{xy} and rotation at beam-joint interface θ_s due to slip or crack opening were measured separately. To aid in developing an implicit joint macro-model in this study, the total joint rotation, θ_j, is defined as the sum of joint shear strain and rotation at the beam-joint interface. The joint rotations were directly evaluated from the recorded data. Detailed information about instrumentation and data reduction are provided in Chapter 3.

Lastly, the strains on beam, slab, and column longitudinal reinforcement are presented. The locations corresponding to the strain gage data are specified in Figures 3.22 and 3.23. Some of the strain gages were damaged during specimen construction or during testing. The unrecorded data of these damaged strain gages are presented as blank bars marked as not applicable (N/A) in the different plots.

4.1   SPECIMEN SP1

4.1.1   Load versus Drift Response

Hysteresis curves of the lateral load versus drift are shown in Figure 4.1, and the values at the first peak of each cyclic loading group are given in Table 4.1. Theoretical beam shear force V_y corresponding to the beam yield strength (ignoring the slab contribution) is shown as horizontal dashed lines in Figure 4.1. Note that the negative (−) and positive (+) signs correspond to beam downward loading and upward loading, respectively.

The first yielding of top reinforcement in both the EW and NS beams was captured from strain gage data between the third loading group ($\Delta = -1.16\%$, the average of EW directional displacement(Δ_{EW}) and NS directional displacement(Δ_{NS})) and fourth loading group ($\Delta = -1.72\%$ on average) for the downward loading. Meanwhile, the bottom reinforcement yielding in the EW and NS beams was observed during the fifth loading group ($\Delta = 2.07\%$ on average). Note that the drift at beam yielding was analytically estimated to be 1.18% which corresponded to the drift at the third group for the downward loading and the fourth group for the upward loading, see Table 3.5. The discrepancy between the measured and analytical yield displacement could be attributed to the joint rotations because the analytical yield displacement was estimated without consideration of joint rotation, as mentioned in Chapter 3.

The peak loads of EW beam were reached at the sixth loading group where the respective drift and applied load were -3.86% and -24.1 kips (-107.2 kN) for the downward loading, and 3.21% and 26.4 kips (117.5kN) for the upward loading. The NS beam reached its peak load at the fifth loading group, which is one group prior to the EW beam peak loading. Because the joint was already damaged during the previous EW beam loading, the NS beam loading could not increase after the peak of the EW beam. Note that the peak loads are greater than the value calculated from beam flexural strength without considering slab contribution, implying that slab reinforcing bars contributed to resisting the applied lateral load. After reaching the peak load, the applied beam load sharply reduced. This reduction was more severe for the downward loading, i.e., slab in tension, than for the upward loading, i.e., slab in compression. The hysteretic curves in Figure 4.1 clearly show pinching behavior that was induced by the slip of the beam longitudinal bars, especially the bottom ones, through the joint core due to bond deterioration.

The column axial load was controlled to follow the pre-defined axial loading equation in terms of applied beam shear forces, as presented in Equation (3.2a). The column axial load started incorrectly from 83 kips (369 kN) in compression, which was less than the intended value of 144 kips (641 kN) as shown in Figure 4.2(a). Note that column axial load in the vertical axis of Figure 4.2(a) is positive for compression, therefore, the true equation of column axial loading used for SP1 is as follows,

$$P_{\text{applied}} = 34 - 4V_{b,\text{EW}} - 4V_{b,\text{NS}} \quad \text{true column axial loading for specimen SP1} \quad (4.1)$$

During the test, the peak column axial load in compression was equal to 123 kips (547 kN), corresponding to $0.11 f'_c A_g$; the peak tensile column axial load was equal to 77 kips (343 kN), corresponding to $0.07 f'_c A_g$, as shown in Figure 4.2(a). Assuming that the column axial load started correctly, the column axial load might be in the range from $0.16 f'_c A_g$ in compression to $0.01 f'_c A_g$ in tension. Note that $A_g = h_c \times b_c$. Accordingly, the column was subjected to less compression and greater tension than the force originally planned for SP1. However, this change of column axial loads applied was expected to have little effect on the joint shear strengths for the following reasons: (1) joint shear strengths were not affected by column axial load ratio within the range of less than $0.25 f'_c A_g$ [Park and Mosalam 2009]; and (2) the subsequently evaluated joint shear strengths were shown to be similar for both the column in compression and in tension.

The vertical displacements were recorded by position transducers installed on both sides of the column between the top and bottom of the test frame. The peak vertical average displacements from the measurements were 0.147 in. (3.73 mm) in elongation and 0.043 in. (1.09 mm) in contraction, see Figure 4.2(b). Note that vertical displacement in the vertical axis of Figure 4.2(b) is positive for contraction.

Table 4.1   Load versus drift response of SP1.

Group No.	SP1							
	EW direction				NS direction			
	Downward (−)		Upward (+)		Downward (−)		Upward (+)	
	Δ(%)	V_b (kip)	Δ (%)	V_b (kip)	Δ (%)	V_b (kip)	Δ (%)	V_b (kip)
1	-0.57	-12.4	-0.02	7.1	-0.56	-12.0	-0.01	7.6
2	-0.87	-15.8	0.27	10.3	-0.85	-17.3	0.28	9.9
3	-1.17	-18.5[*1]	0.55	14.2	-1.14	-19.2	0.61	13.8
4	-1.77	-22.4	1.15	20.6	-1.67	-22.7[*1]	1.25	20.6
5	-2.66	-24.0	2.03	25.4[*1]	-2.57	-22.9[*2]	2.11	24.2[*1*2]
6	-3.86	-24.1[*2]	3.21	26.4[#2]	-3.77	-21.1	3.29	23.8
7	-5.36	-19.0	4.99	24.0	-5.31	-12.6	5.05	18.6
8	-7.71	-9.3	7.27	17.4	-	-	-	-

[*1] first yielding of beam reinforcement
[*2] peak loading
Note: 1 kip = 4.45 kN

(a) EW direction
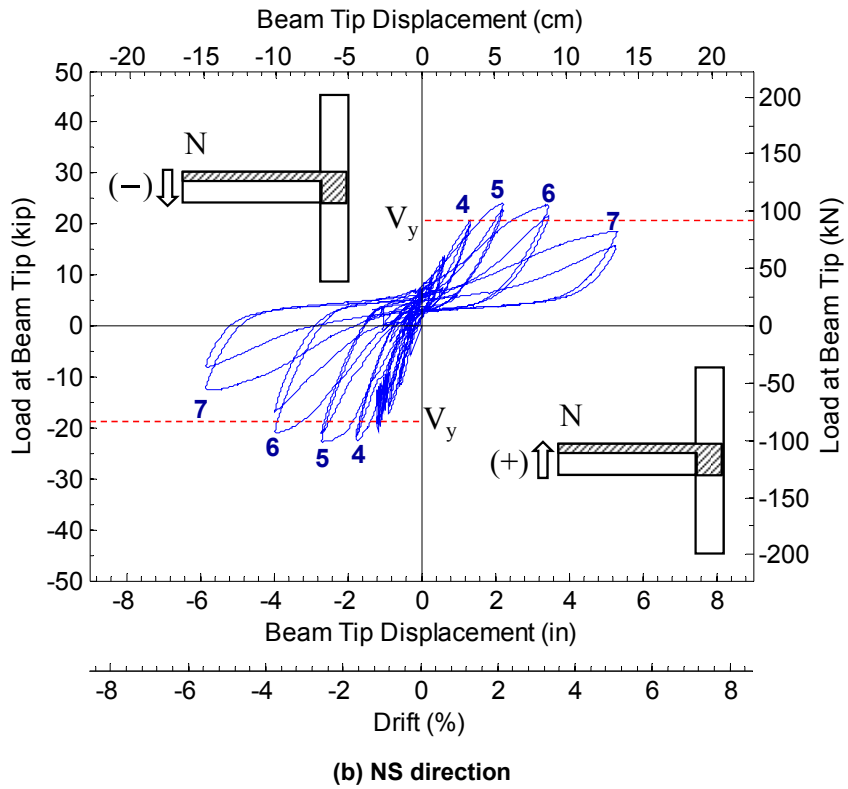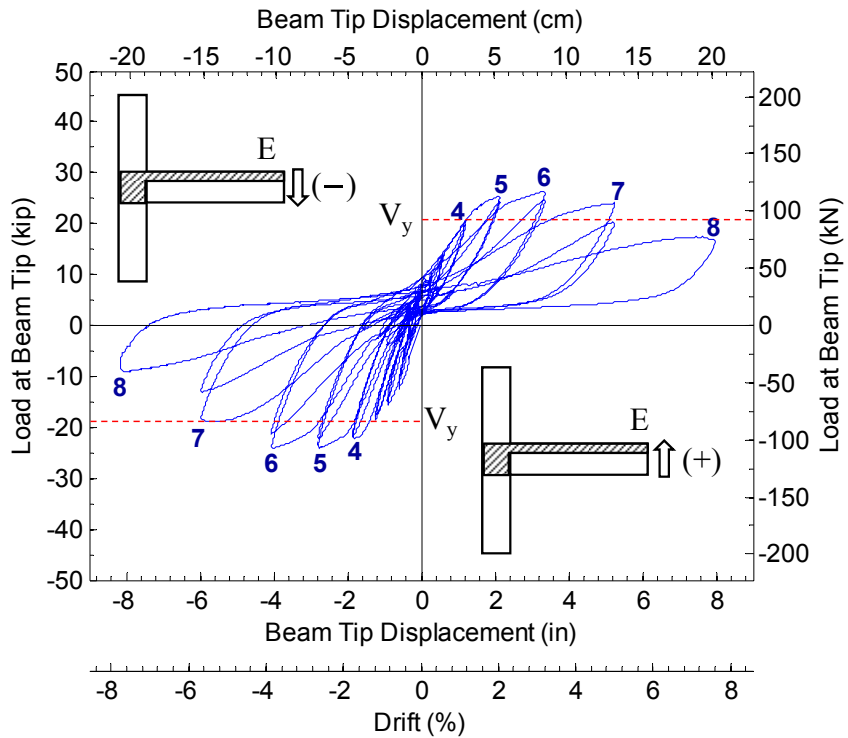
(b) NS direction

Figure 4.1   Load versus drift response of SP1.

58
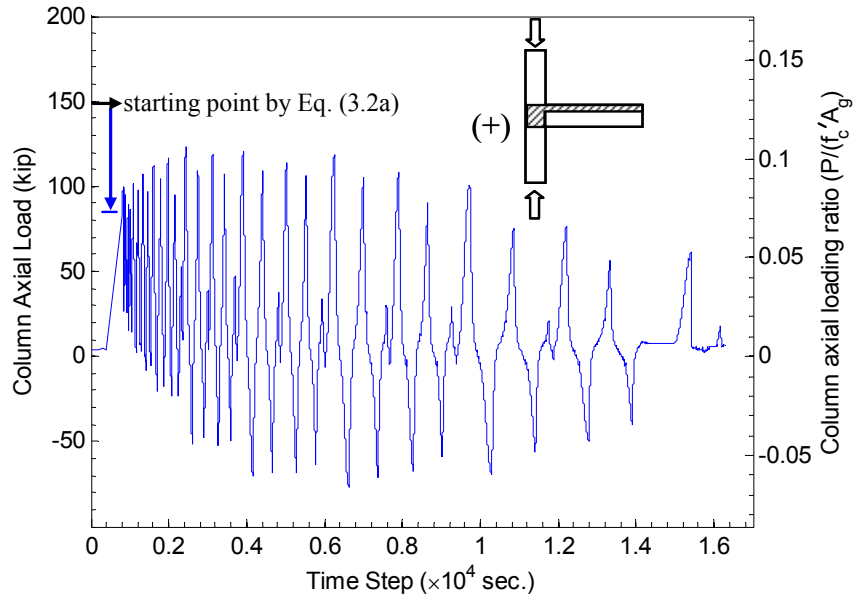
(a) column axial load
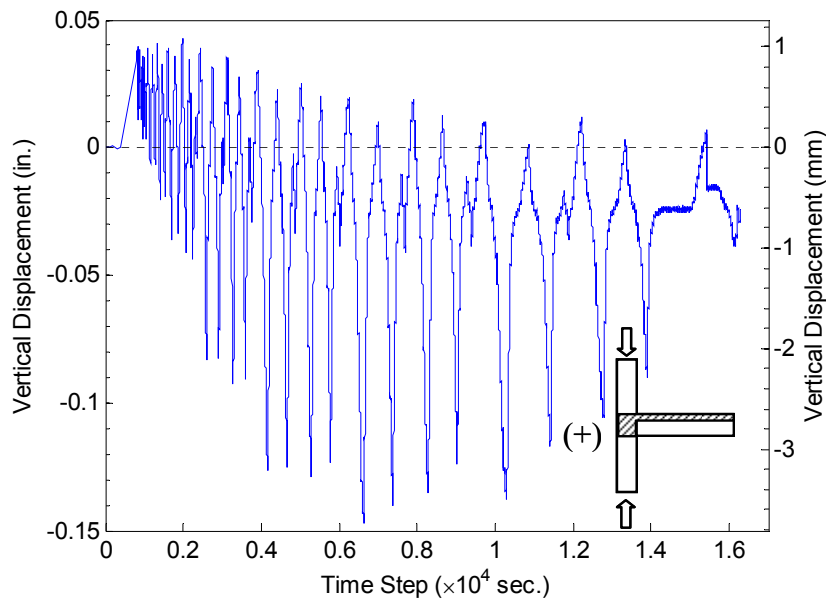
(b) vertical displacement

Figure 4.2   Column response of SP1.

4.1.2 Observed Damage Progression

The damage progression of the joint in both directions is qualitatively summarized in Table 4.2. For the purpose of presentation, nearly invisible hairline cracks have been enhanced by added lines to the photographs. Residual cracks in the beams and slab were marked when the specimen was removed from test frame.

4.1.2.1 EW Direction

JOINT REGION

The joint showed a typical "X" shape diagonal crack pattern during the EW beam cyclic loading, i.e., longitudinal beam loading. A first hairline diagonal crack (↘) caused by the downward loading, which is referred to as downward diagonal crack hereafter, occurred at the second group $\left(\Delta_{EW} = -0.87\%\right)$, while another diagonal crack (↗) caused by the upward loading, which is referred to as upward diagonal crack hereafter, appeared at the fourth group of loading $\left(\Delta_{EW} = 1.15\%\right)$, see Figure 4.3(a). For the fifth group, the first downward diagonal crack propagated without new cracks initiating, while a new upward diagonal crack initiated at the location of the 90° hook of the beam reinforcement, as shown in Figure 4.3(b). At the sixth group when the peak load was achieved, two major diagonal cracks significantly propagated and extended from the joint region to the column, as shown in Figure 4.3(c). From the seventh group of loading, the concrete of the joint panel began bulging and dilating away from the column, particularly at the top edge of the joint on the side where there was no beam. At the end of the test, the joint cover concrete was completely detached, and joint core concrete was split into several parts bounded by the diagonal cracks, as shown in Figure 4.3(d).

During the upward loading of NS beam, a horizontal crack was observed at the top of the EW joint panel, but no cracks appeared during the downward loading. At the third group of the NS beam upward loading, a hairline horizontal crack initiated from the top of the interface between the column and the EW beam, propagating across the whole width of the joint panel at the subsequent groups of upward loading, as shown in Figure 4.4(a); the location of this horizontal crack was close to the top reinforcement in the EW beam.

BEAM AND SLAB

A first flexural hairline crack at the top of the EW beam appeared during pull-down loading prior to testing. At the first group of EW beam downward loading, a splitting crack developed at the top of the beam-joint interface. Simultaneously, splitting cracks developed along the line of beam-slab interface in the L-shape beam cross section. Up to the peak load, the splitting crack at the beam-joint interface opened wider, and the number and width of flexural cracks in the beam and slab increased. In particular, the splitting crack at the NS beam-slab interface significantly opened after the EW beam yielding. Cracks on the slab originated from beam flexural cracks; thus they were connected to each other. Joint cracks continued to significantly widen until the end of testing. Flexural cracks did not propagate any further, and their width actually decreased after peak loading because joint deformation prevailed in the global behavior of the specimen; therefore, plastic hinge mechanism did not form in the beam. The existing cracks in the EW beam and slab after testing are shown in Figure 4.5.

During the NS beam loading, inclined cracks occurred at the top of the EW beam due to torsion, and these cracks crossed over the whole depth of the EW beam as testing continued. Moreover, the existing splitting cracks at the beam-joint interface widened by the induced torsion during the NS beam loading.

Table 4.2   Qualitative damage description of SP1.

Drift (%)	EW direction	NS direction
$\Delta_0 = 0.3$	- First flexural crack from top of beam	-
$\Delta_{up} = -0.02$ $\Delta_{down} = -0.57$	- Additional flexural cracks in beam and slab	- First flexural crack at top of beam
$\Delta_{up} = 0.28$ $\Delta_{down} = -0.86$	- First downward diagonal crack in joint - Splitting crack at beam-joint interface	- Additional flexural cracks in beam and slab
$\Delta_{up} = 0.58$ $\Delta_{down} = -1.16$	- First yielding of one of beam top bars	-
$\Delta_{up} = 1.20$ $\Delta_{down} = -1.72$	- First upward diagonal crack in joint	- First downward diagonal crack in joint - First upward diagonal crack in joint - Yielding of beam top bars
$\Delta_{up} = 2.07$ $\Delta_{down} = -2.62$	- Second upward diagonal crack in joint - Propagation of splitting crack at beam-joint interface - First yielding of beam bottom bars	- Additional upward diagonal cracks in joint - First yielding of beam bottom bars
$\Delta_{up} = 3.25$ $\Delta_{down} = -3.72$	- Large opening of joint diagonal cracks - Large opening of splitting crack at beam-joint interface	- Large opening of joint diagonal cracks
$\Delta_{up} = 5.02$ $\Delta_{down} = -5.34$	- Bulging of joint cover concrete - Separation of concrete wedge from corner of joint on the free side where there is no beam - Reduction of width of beam flexural cracks	- Spalling of joint cover concrete - Separation of concrete wedge from corner of joint on the free side where there is no beam - Reduction of width of beam flexural cracks
$\Delta_{up} = 7.27$ $\Delta_{down} = -7.71$	- Spalling of joint cover concrete - Crushing of joint core concrete	-

4.1.2.2 NS Direction

JOINT REGION

The diagonal joint cracking in the NS joint panel showed a different pattern compared with the EW joint crack pattern. The first downward diagonal crack (↙) occurred at the fourth loading group, $\Delta_{NS} = -1.67\%$. During the upward loading at the same loading group, a short hairline diagonal crack (↖) and short hairline horizontal cracks developed appeared in the joint panel.

For the subsequent NS beam downward loading, the existing downward diagonal crack was growing longer and wider without formation of new diagonal cracks, while multiple upward diagonal cracks newly developed under the upward loading. A significant increase of crack width was observed at the sixth group of NS beam loading, which was subsequent to the peak of the EW beam loading. The NS joint concrete split into several pieces and bulged out at the

seventh group, which was similar to the observation made in the EW joint panel. The NS joint damage progression is shown in Figure 4.6.

Two horizontal cracks were observed at the top of the NS joint panel during the EW beam upward loading in the fourth group of loading. Between these two horizontal cracks, the upper crack closed but the lower crack widened went subjected to the fifth group of loading, as shown in Figure 4.4(b). Unlike the EW joint panel, a horizontal crack also formed at the bottom of the NS joint panel during the EW beam downward loading in the fifth group of loading, but its width was much smaller than the top horizontal crack width. The upper horizontal crack was on the line of the slab top surface, and the lower horizontal crack at the top of joint and another horizontal crack at the bottom of the joint were close to the top and bottom reinforcement of the NS beam, respectively.

BEAM AND SLAB

Multiple flexural cracks, which propagated slowly, took place in the beam and slab. A splitting crack developed along the EW beam-slab interface line during the NS beam loading, as was observed in the NS beam-slab interface for the EW beam loading. In general, the crack pattern of the beam and slab appeared similar for the EW and NS loadings, but crack propagation was more severe in the EW side. The splitting crack propagation at the beam-joint interface was observed during the sixth group of loading, as indicated by the arrow in Figure 4.6(c). During the EW beam loading, torsionally inclined cracks also occurred in the NS beam. The existing cracks in the NS beam and slab after testing are shown in Figure 4.5.

4.1.2.3 Summary

During the longitudinal beam loading, flexural cracks initiated in the beam and slab at the early stage of loading, followed by diagonal cracks in the joint region and splitting crack at the beam-joint interface. With an increase of loading, existing diagonal cracks in the joint region as well as flexural cracks in the beam and slab propagated and widened. In particular, slab cracks formed a grid pattern on the top of the slab in both directions of loading [Figure 4.5(c)]. Finally, joint cracks dominated the failure of the specimen at the peak loading.

Joint diagonal cracks occurred between the drift levels of 1.20% and 1.72%, except for first downward joint crack in the EW direction, which appeared at the loading to 0.87% drift. The early occurrence of joint crack for the EW beam downward loading is attributed to the larger cover concrete thickness of the EW beam cross section. Significant propagation of joint diagonal cracks was observed from the fifth group of loading to the subsequent peak loading ($\Delta_{down} = -3.72\%$ and $\Delta_{up} = 3.25\%$). Thereafter, the cover concrete of the joint panel began to bulge and finally spalled off. The joint core concrete was also crushed based on observation of joint damage after removing the loose cover concrete.

Splitting cracks at beam-joint interface and beam-slab interface also showed significant propagation, but flexural cracks were not severe. No plastic hinge mechanisms formed in any of the beams. Figure 4.7 confirms that most damage of the specimen was concentrated on the joint region.

Two different types of cracks were observed in the transverse direction. Inclined cracks took place on the side of the transverse beam when the longitudinal beam was loaded downward, while horizontal cracks developed at the top of the joint panel in the transverse direction during

the longitudinal beam upward loading. These two types of cracks remained minor and, in fact, closed when the beam loading was switched to the orthogonal beam. For example, the horizontal and inclined cracks formed in the joint and beam in the EW direction during the NS beam loading, but these cracks closed during the subsequent EW beam loading. Therefore, it was expected that the joint responses in the longitudinal direction were not significantly affected by these cracks, which occurred during previous loading of the orthogonal beam.

(a) first joint crack
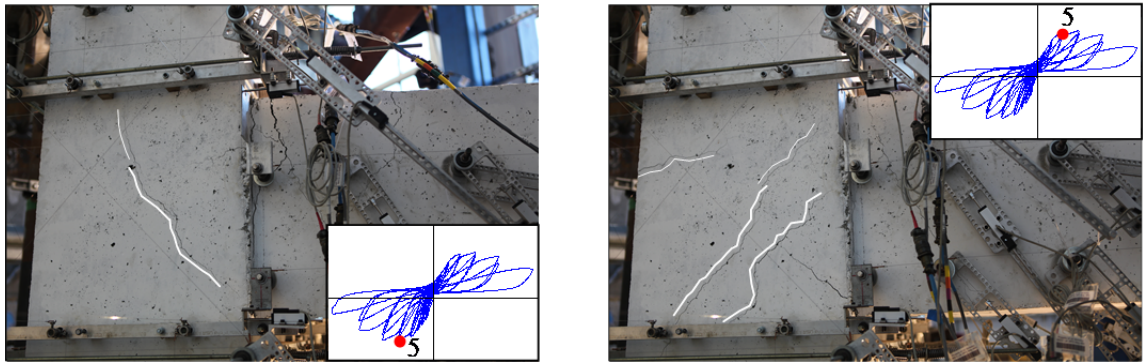
(b) propagation of joint cracking
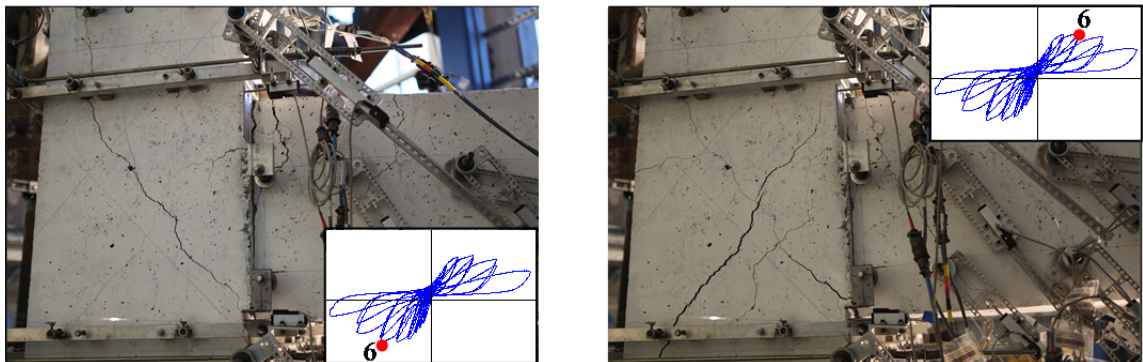
(c) joint cracking before joint failure
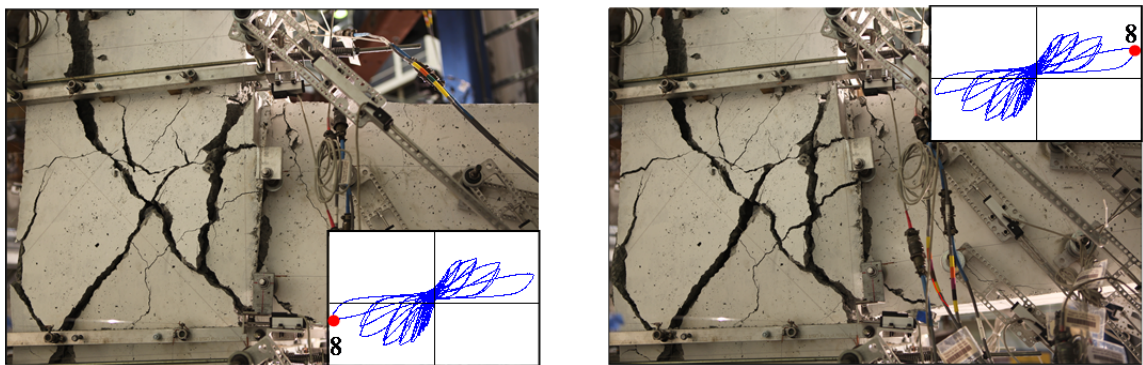
(d) joint damage at end of test

Figure 4.3   Damage progression of joint in EW direction, SP1.

$\Delta_{NS} = 0.61\%$ $\Delta_{NS} = 2.11\%$

(a) horizontal crack in EW joint by NS beam loading

$\Delta_{EW} = 1.15\%$ $\Delta_{EW} = 2.03\%$

(b) horizontal cracks in NS joint by EW beam loading
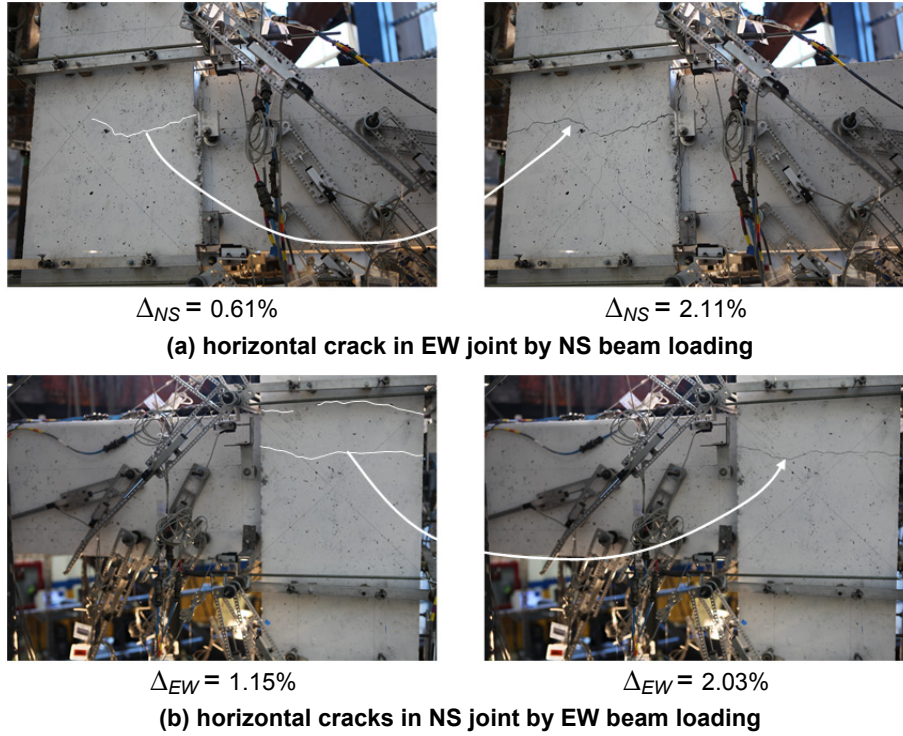
Figure 4.4   Propagation of horizontal crack in joint panel, SP1.

(a) cracks in EW beam

(b) cracks in NS beam

(c) cracks on slab
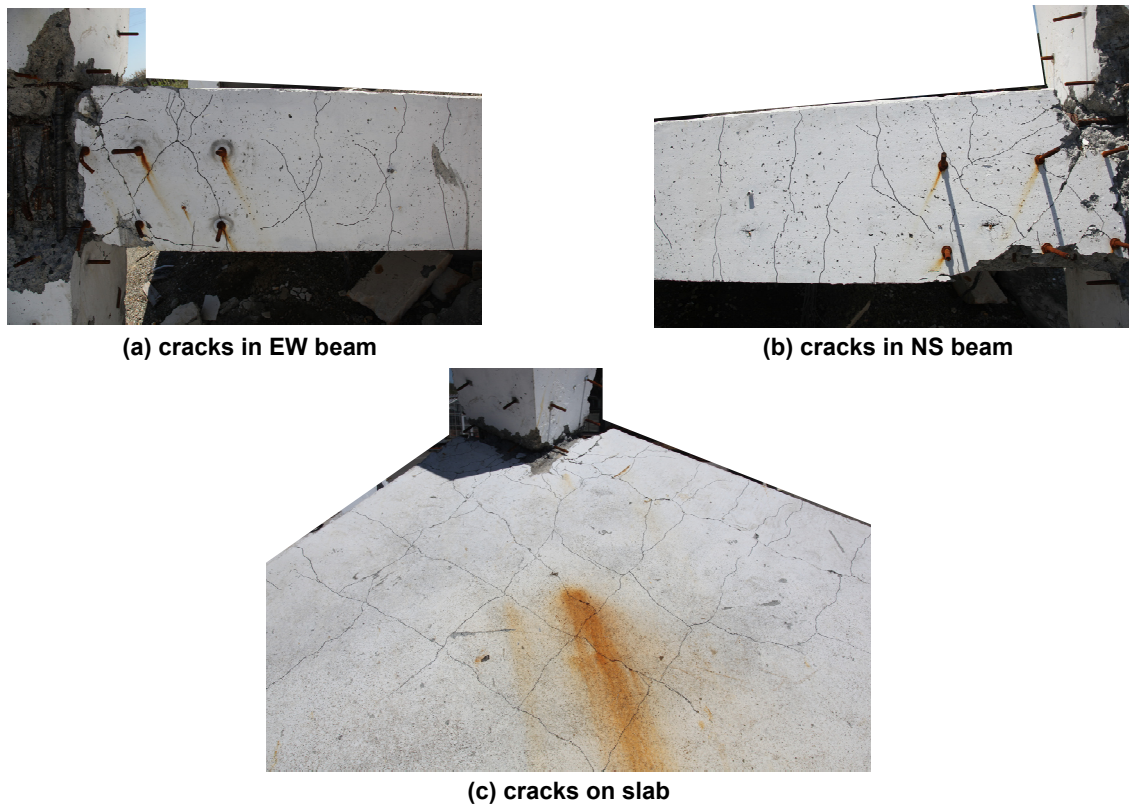
Figure 4.5   Existing cracks after testing, SP1.
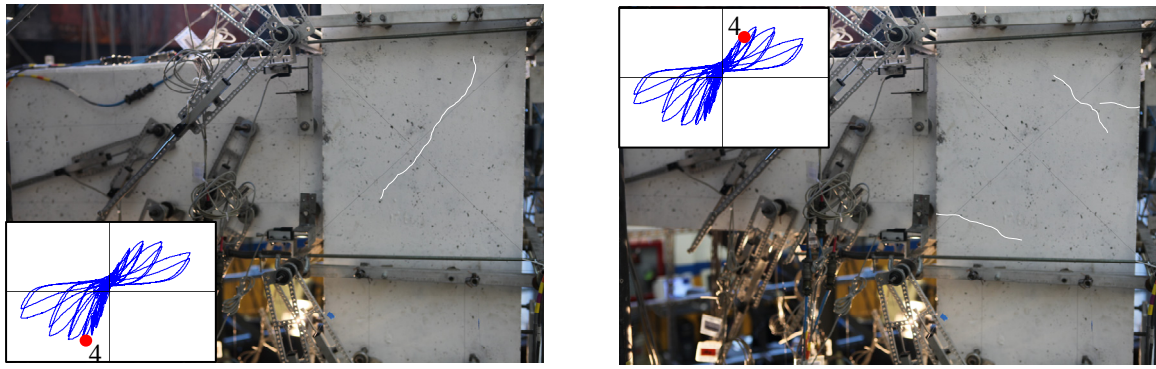
(a) first joint crack
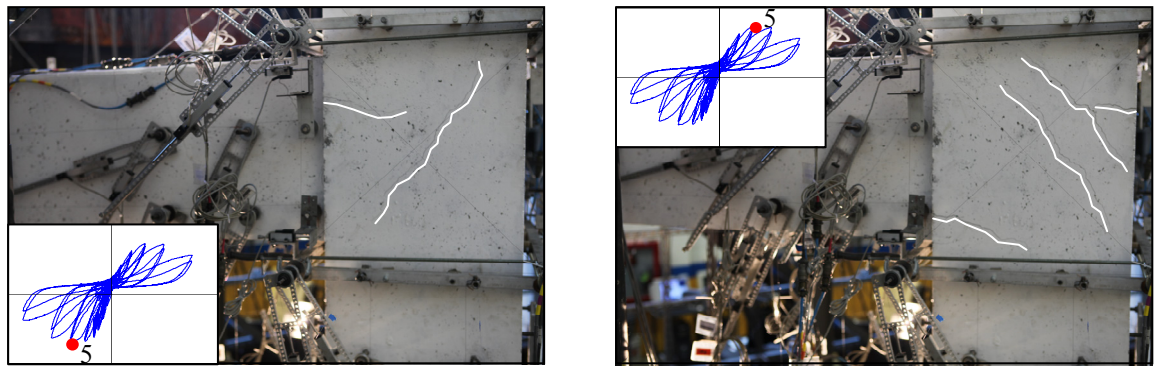
(b) propagation of joint cracking
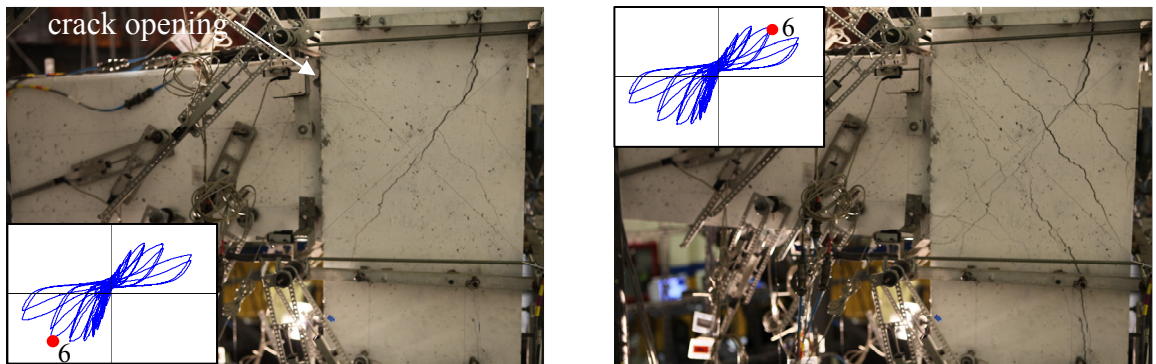
(c) joint cracking before joint failure
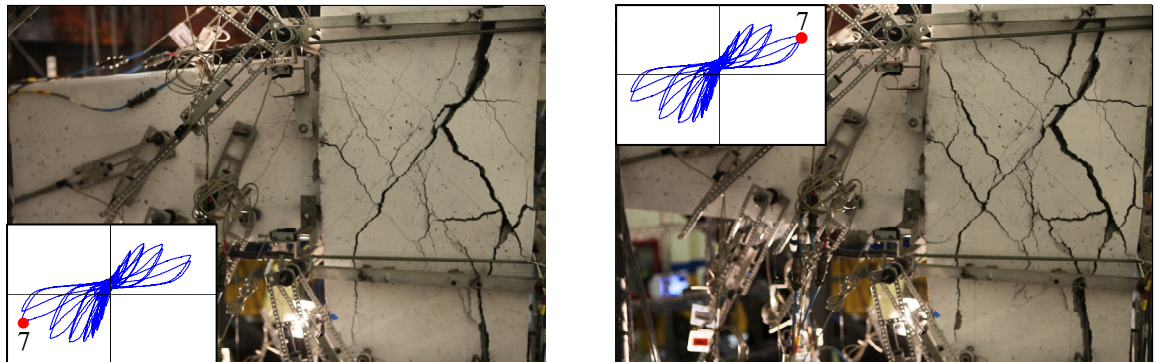
(d) joint damage at end of test

Figure 4.6   Damage progression of joint in NS direction, SP1.

(a) global view of specimen

(b) inside corner joint

(c) NS beam

(d) EW beam
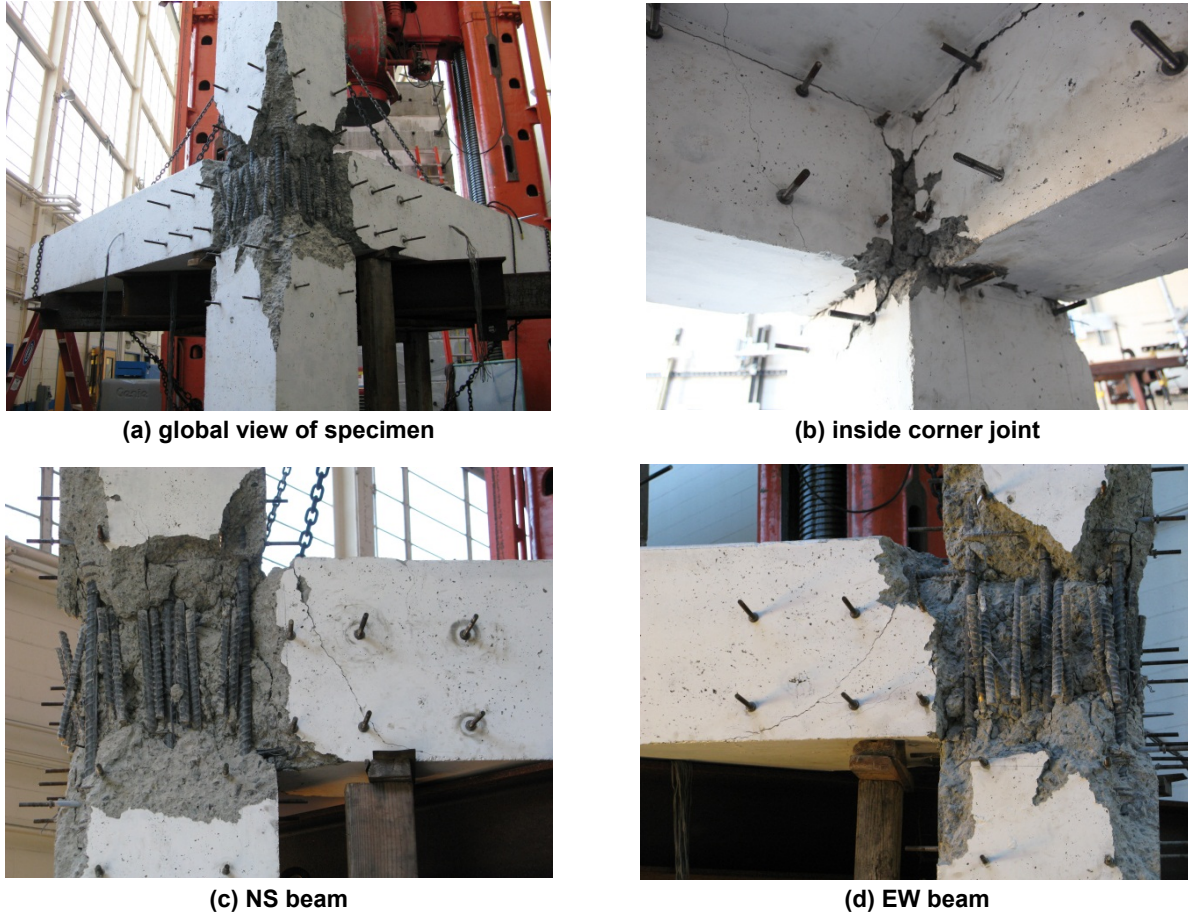
Figure 4.7   Failure of SP1 after removing concrete fragments.

4.1.3 Joint Shear Stress versus Rotation Response

The hysteretic responses of joint shear stress versus strain are presented in Table 4.3 and Figure 4.8. The joint shear stress was estimated using a constant moment arm that was assumed to be 0.9 times the effective beam depth because beam longitudinal reinforcement yielded before joint shear failure. According to the effective slab width in ASCE 41, slab top four reinforcing bars were considered in estimating the effective beam depth for negative bending, i.e., beam downward loading. The calculated joint shear stresses in the EW direction at the peak load were 509 psi (3.51 MPa) for the downward loading and 508 psi (3.51 MPa) for the upward loading; the corresponding values of $\gamma = v_{jh}/\sqrt{f_c'}$ were 8.5 psi$^{0.5}$ (0.71 MPa$^{0.5}$) for both downward and upward loading. The peak joint shear stresses in the NS direction were 474 psi (3.27 MPa) for the downward loading and 482 psi (3.33 MPa) for the upward loading; the corresponding values of $\gamma = v_{jh}/\sqrt{f_c'}$ were 7.9 psi$^{0.5}$ (0.66 MPa$^{0.5}$) and 8.1 psi$^{0.5}$ (0.67 MPa$^{0.5}$), respectively. Note that the peak loads in both directions were greater for the upward loading, but the joint shear stresses were calculated to be similar for the downward loading than that for the upward loading. This is because the effective beam depth was smaller for the downward than that for the upward loading. In other words, contribution of the slab reinforcement and larger cover concrete thickness reduced the effective beam depth for negative bending. Note that the joint shear strengths, which were defined as the maximum normalized joint shear stress, were greater than the shear strength

suggested by the ASCE41, i.e., $\gamma = 6.0$ psi$^{0.5}$ (0.50 MPa$^{0.5}$), as indicated by the dashed lines in Figure 4.8.

The joint shear strains measured in the EW and NS joint panels at the peak load were 0.0024 rads and 0.0002 rads, respectively, for the downward loading, and 0.0079 rads and 0.0042 rads, respectively, for the upward loading, see Figure 4.8. The smaller joint shear strains were generally measured during the downward loading than during the upward loading. Conversely, the rotations at the beam-joint interface measured were greater for the downward loading, see Figure 4.9. Consequently, the total joint rotation, which was defined in this study as the sum of joint shear strain and the rotation at the beam-joint interface, was almost symmetric for both downward and upward loadings, as shown in Figure 4.10. For instance, the total rotations at the peak load were 0.017 rads for the downward loading and 0.019 rads for the upward loading in the EW direction; 0.014 rads for the downward loading and 0.012 rads for the upward loading in the NS direction. In general, the total rotation in the NS joint panel was greater than that in the EW joint panel at the same drift level, resulting from the sequence of beam loading that the EW beam loading preceded the NS beam loading.

Table 4.3 shows that the contribution of joint rotation to total drift started to increase after beam reinforcement yielding. Subsequently, total drift after the peak loading was mostly due to this joint rotation.

Table **4.3**   **Joint response of SP1.**

Dir.	EW											
	Downward						Upward					
Group No.	v_{jh} (psi)	γ (psi$^{0.5}$)	Δ (rad)	γ_{xy} (rad)	θ_j (rad)	θ_j/Δ	v_{jh} (psi)	γ (psi$^{0.5}$)	Δ (rad)	γ_{xy} (rad)	θ_j (rad)	θ_j/Δ
1	262	4.4	0.0057	-	-	-	137	2.3	0.00	-	-	-
2	334	5.6	0.0087	0.0003	0.0029	0.33	198	3.3	0.0027	0.00	0.0001	0.04
3	391[*1]	6.5	0.0117	0.0006	0.0026	0.22	274	4.6	0.0055	0.0004	0.0023	0.42
4	473	7.9	0.0177	0.0007	0.0039	0.22	397	6.6	0.0115	0.0017	0.0054	0.47
5	507	8.5	0.0266	0.0009	0.0066	0.25	489[*1]	8.2	0.0203	0.0048	0.012	0.59
6	509[*2]	8.5	0.0386	0.0024	0.017	0.44	508[*2]	8.5	0.0321	0.0088	0.019	0.59
7	401	6.7	0.0536	0.014	0.037	0.69	462	7.7	0.0499	0.013	0.028	0.56
8	197	3.3	0.0771	-	-	-	335	5.6	0.0727	-	-	-

Dir.	NS											
	Downward						Upward					
Group No.	v_{jh} (psi)	γ (psi$^{0.5}$)	Δ (rad)	γ_{xy} (rad)	θ_j (rad)	θ_j/Δ	v_{jh} (psi)	γ (psi$^{0.5}$)	Δ (rad)	γ_{xy} (rad)	θ_j (rad)	θ_j/Δ
1	248	4.2	0.0056	-	-	-	151	2.5	0.00	-	-	-
2	358	6.0	0.0085	0.00	0.0029	0.34	197	3.3	0.0028	0.00	0.0004	0.14
3	397	6.6	0.0114	0.00	0.0031	0.27	275	4.6	0.0061	0.0004	0.0013	0.21
4	469[*1]	7.8	0.0167	0.00	0.0063	0.38	410	6.9	0.0125	0.0017	0.0046	0.37
5	474[*2]	7.9	0.0257	0.0002	0.014	0.54	482[*1*2]	8.1	0.0211	0.0047	0.012	0.57
6	436	7.3	0.0377	0.0036	0.024	0.64	474	7.9	0.0329	0.012	0.022	0.67
7	261	4.4	0.0531	0.0091	0.037	0.70	371	6.2	0.0505	0.027	0.046	0.91
8	-	-	-	-	-	-	-	-	-	-	-	-

*1 first yielding of beam reinforcement
*2 peak loading

Note: 1 psi = 0.0069 MPa; $1.0\sqrt{f_c'}$ psi$^{0.5}$ $= 0.083\sqrt{f_c'}$ MPa$^{0.5}$
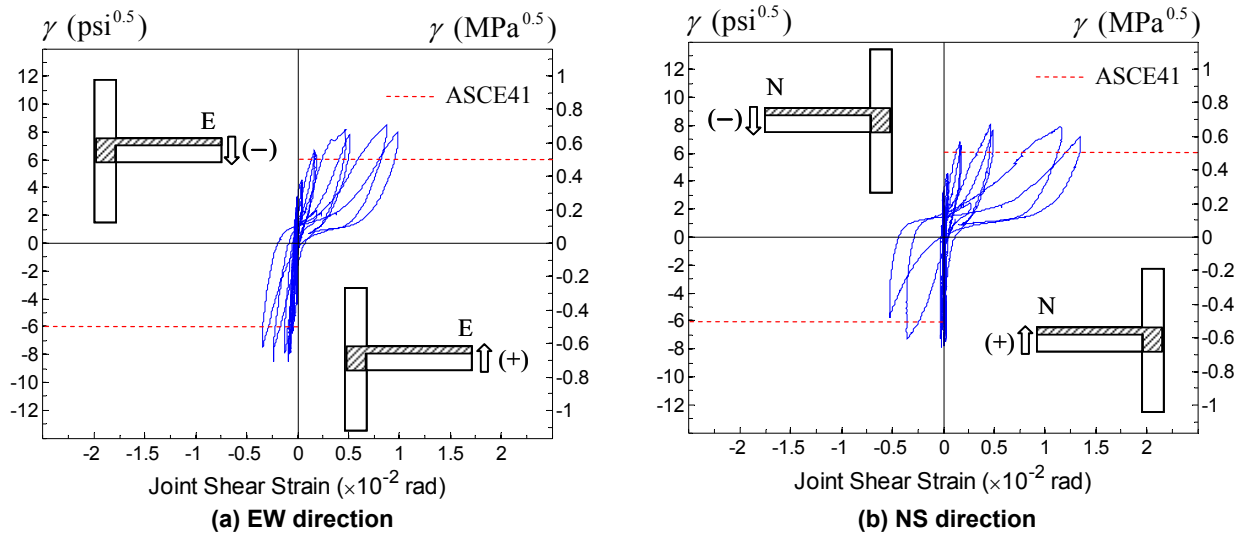
Figure 4.8   Joint shear stress versus strain response of SP1.
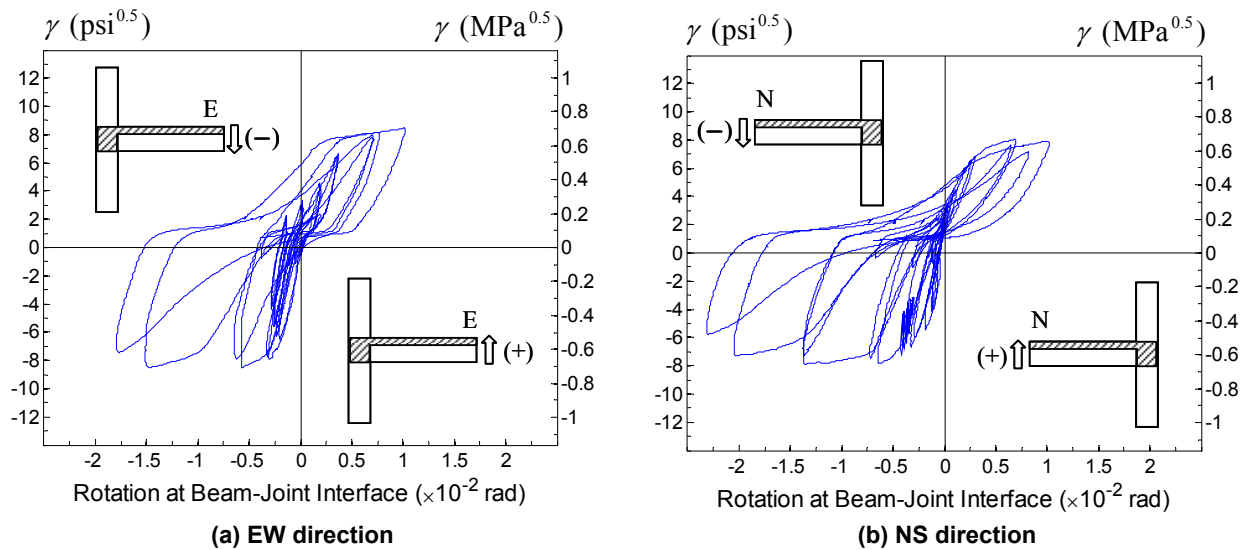
Figure 4.9   Joint shear stress versus rotation at beam-joint interface of SP1.

70
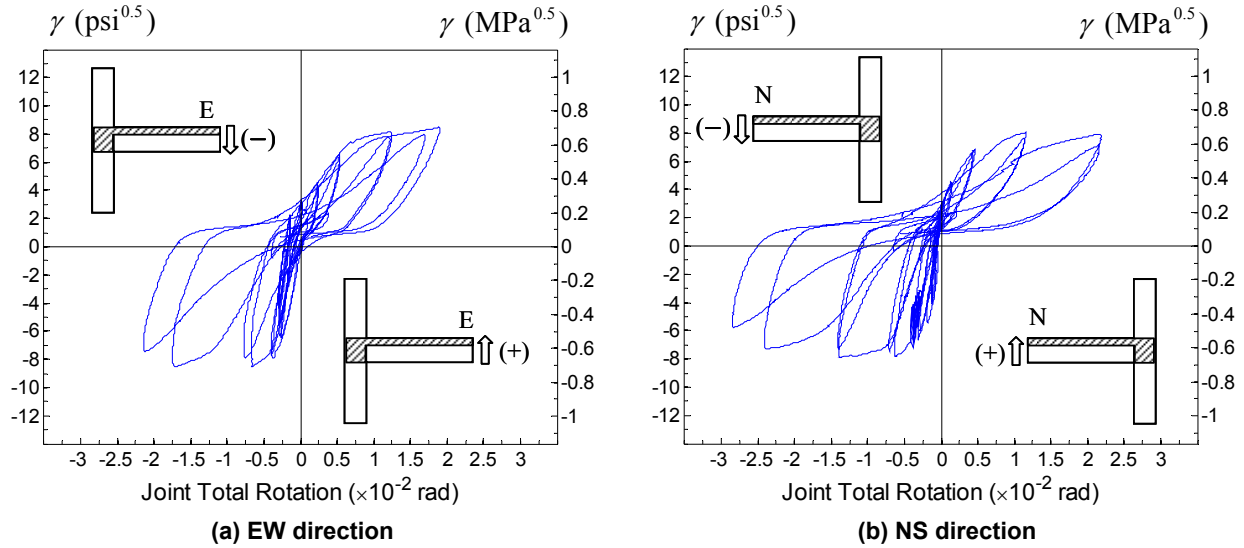
Figure 4.10   Joint shear stress versus rotation of SP1.

4.1.4 Strain Measurement

4.1.4.1 Beam Reinforcement

The strains (vertical axis) of the beam longitudinal bars in the EW and NS directions are plotted against the location of the strain gages (horizontal axis) with increasing drift levels in Figures 4.11 and 4.12. The labeled drift levels correspond to the loading from the third loading group through the sixth loading group. The strain values in the vertical axis are normalized by the yield strain (ε_y) measured from the coupon tests of reinforcing bars. The notation and numbering of strain gages are illustrated at the top of Figures 4.11 and 4.12.

Based on the measured strain data, the first yielding of the beam top longitudinal bars in both directions occurred at the beam-joint interface between the drift level of $\Delta = -1.16\%$ and $\Delta = -1.72\%$, i.e., the third and fourth loading group. The bottom longitudinal bars yielded between the drift level of $\Delta = 1.20\%$ and $\Delta = 2.07\%$, i.e., the fourth and fifth loading group. With the increase of drift level after the first yielding, the strains at all gages increased and particularly the strains at the middle of the joint (gage number 2) showed a big jump at the sixth loading group as symbolized by open circles with solid line in Figures 4.11 and 4.12. This implies that the beam reinforcement yielding propagated into the joint as the applied drift levels increased. The strains of the EW beam reinforcing bars were generally observed to be greater than those of the NS beam reinforcing bars due to the previously mentioned loading sequence.

4.1.4.2 Slab Reinforcement

The strains of the slab reinforcing bars were measured at the beam-slab interfaces in the EW and NS directions, as shown in Figure 4.13. Note that the EW and NS slab reinforcing bars were placed in parallel to the EW and NS beams, respectively. For example, the EW slab reinforcing bars crossed the NS beam-slab interfaces and vice versa. The strain values of the EW slab reinforcing bars were greater than those of the NS slab reinforcing bars, confirming the observation that the splitting crack at the NS beam-slab interface was wider than the EW beam-

slab interface crack. Therefore, different amounts of slab reinforcing bars were taken into account for estimating the effective beam depth in each direction.

The first yielding of slab top reinforcing bar located next to the beam internal side occurred during the loading when the beam top internal bar yielded first, between the drift level of $\Delta = -1.16\%$ and $\Delta = -1.72\%$. At the peak loading, all measured top four reinforcing bars yielded in the EW slab, while the top two reinforcing bars yielded in the NS slab. On the other hand, the first bottom reinforcing bar yielded in the EW direction at the fifth group of loading, but this bar slipped from the beam side in the subsequent loading, as shown in Figure 4.13. The insufficient anchorage of the bottom reinforcement induced relatively low strain and slippage from the beam section in both directions. Moreover, considering the distance between slab bottom reinforcement and the neutral axis in the L-shape cross section, the slab bottom bars were ignored for calculation of joint shear stress and effective beam depth. As indicated in Section 4.1.3, calculating the effective beam depth included four top reinforcing bars for the EW direction and two top reinforcing bars for the NS direction.

4.1.4.3 Column Reinforcement

The strain gage measurements of column longitudinal bars within the joint region are presented in Figures 4.14 and 4.15. The measured strain data were assorted according to each of the EW and NS beam loading. The strains of all the column longitudinal bars were less than the yield strain (0.0025) until the peak loading, except for the top gage of the bar number 3 in the EW direction (which yielded when the column was in tension). The strain gage measurements show that the column longitudinal bars elongated due to the tension in the column during the EW and NS beams upward loadings. However, the tension in the column and consequent yielding of the one column bar did not significantly affect the joint shear strengths because the maximum joint shear strengths for the beams upward loading (column in tension) were close to those measured for the beams downward loading (column in compression).

To investigate the role of the column intermediate reinforcement, the strains were recorded over the height of the joint during the longitudinal loading in each direction. The tensile strain of the column intermediate bar at the joint mid-height was not greater than the strains measured at both top and bottom of the joint, which is discussed in Section 5.7.

Note: 1" = 25.4 mm

(a) EW-Top-Ext.

(b) EW-Top-Int.

(c) EW-Bottom-Ext.

(d) EW-Bottom-Int.
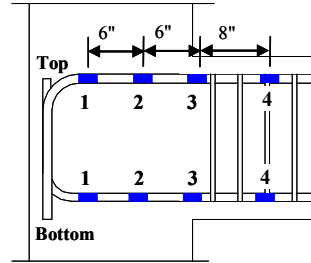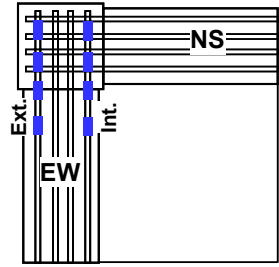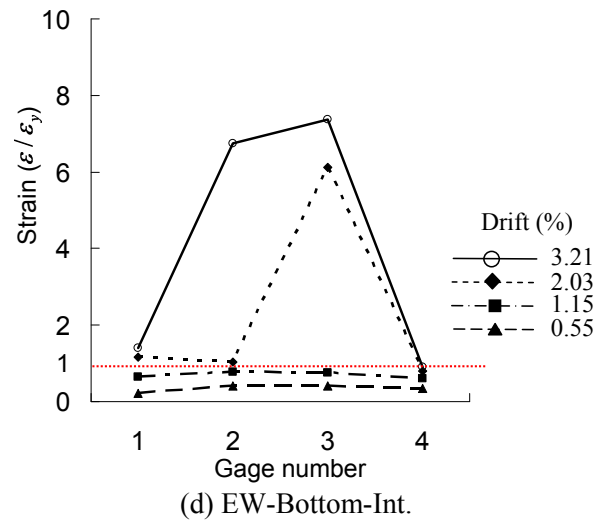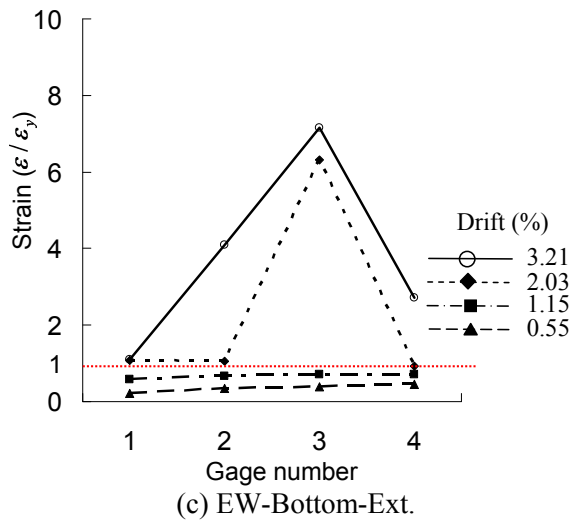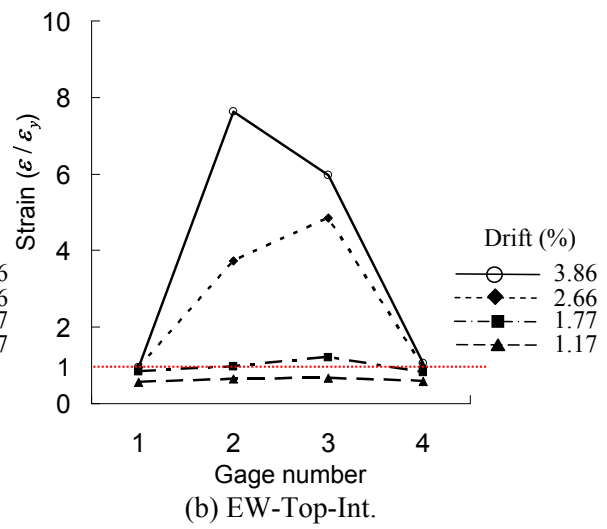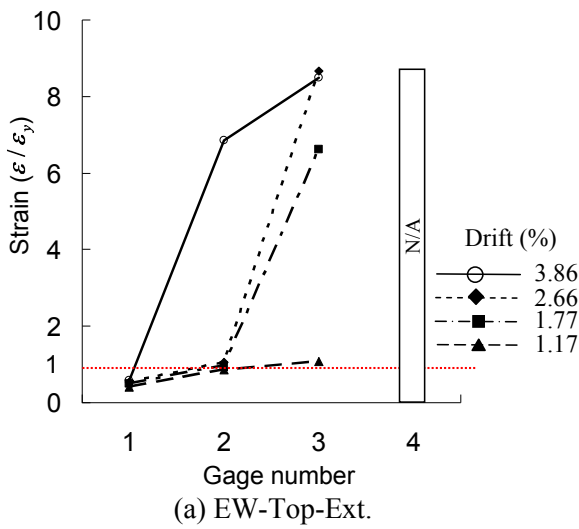
Figure 4.11   Strains of the EW beam longitudinal bars of SP1.

(a) NS-Top-Ext.

(b) NS-Top-Int.

(c) NS-Bottom-Ext.

(d) NS-Bottom-Int.
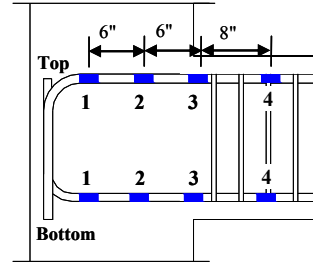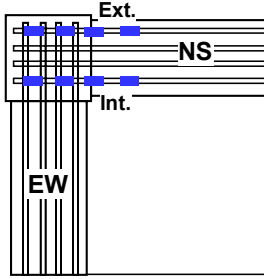
Note: 1" = 25.4 mm
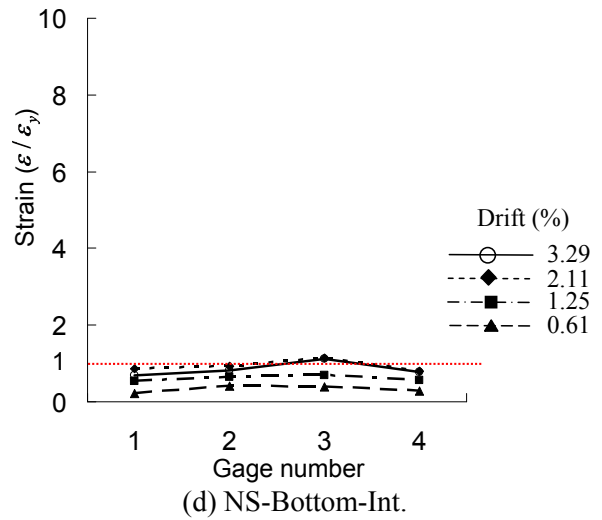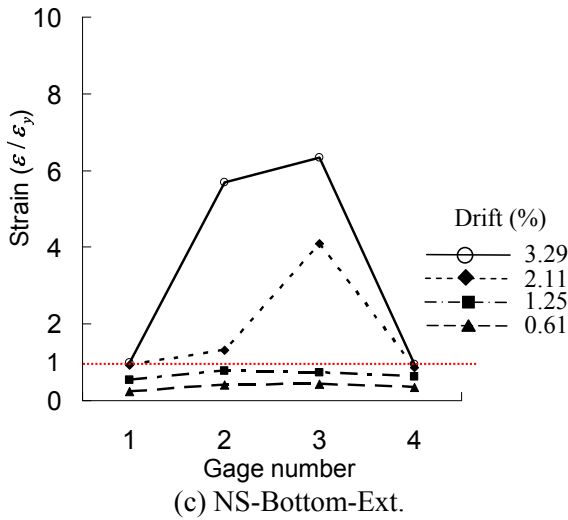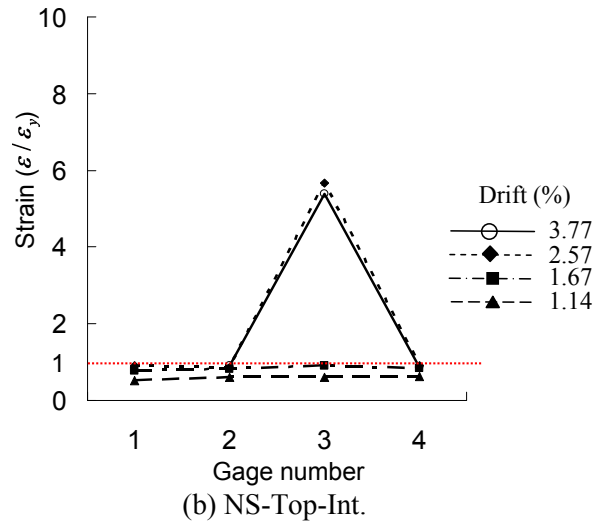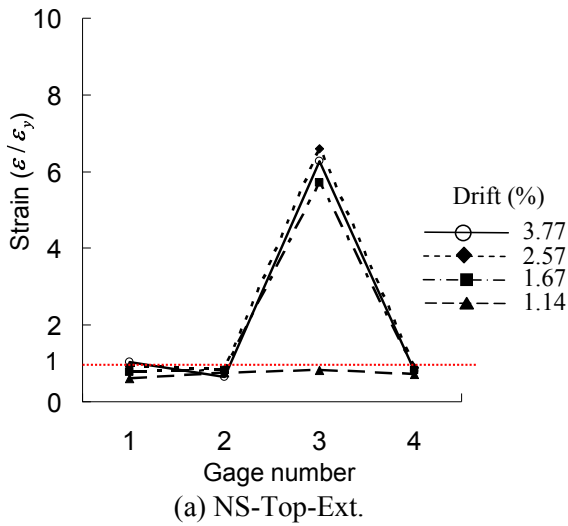
Figure 4.12   Strains of the NS beam longitudinal bars of SP1.

74
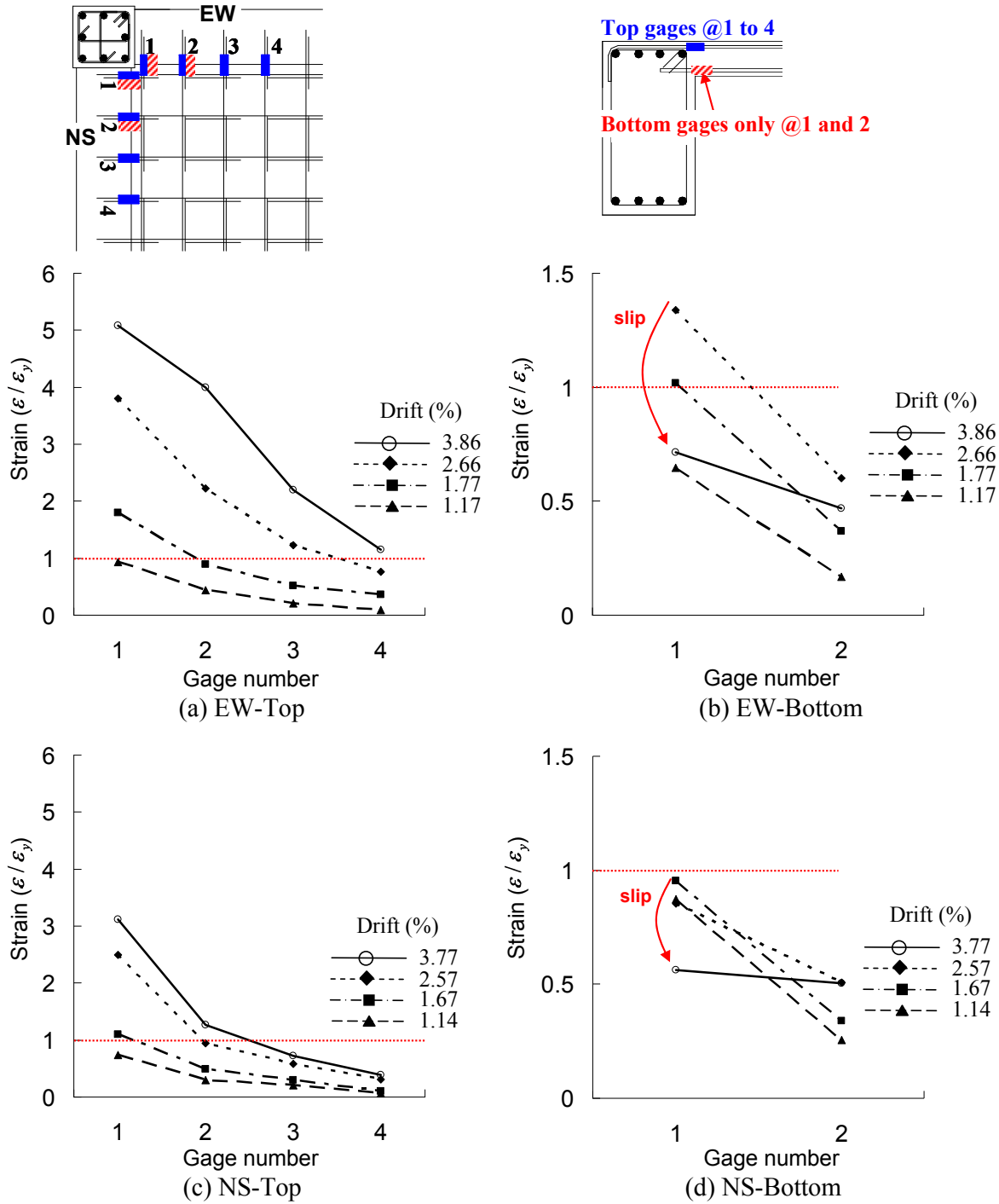
Figure 4.13   Strains of the slab reinforcing bars of SP1.
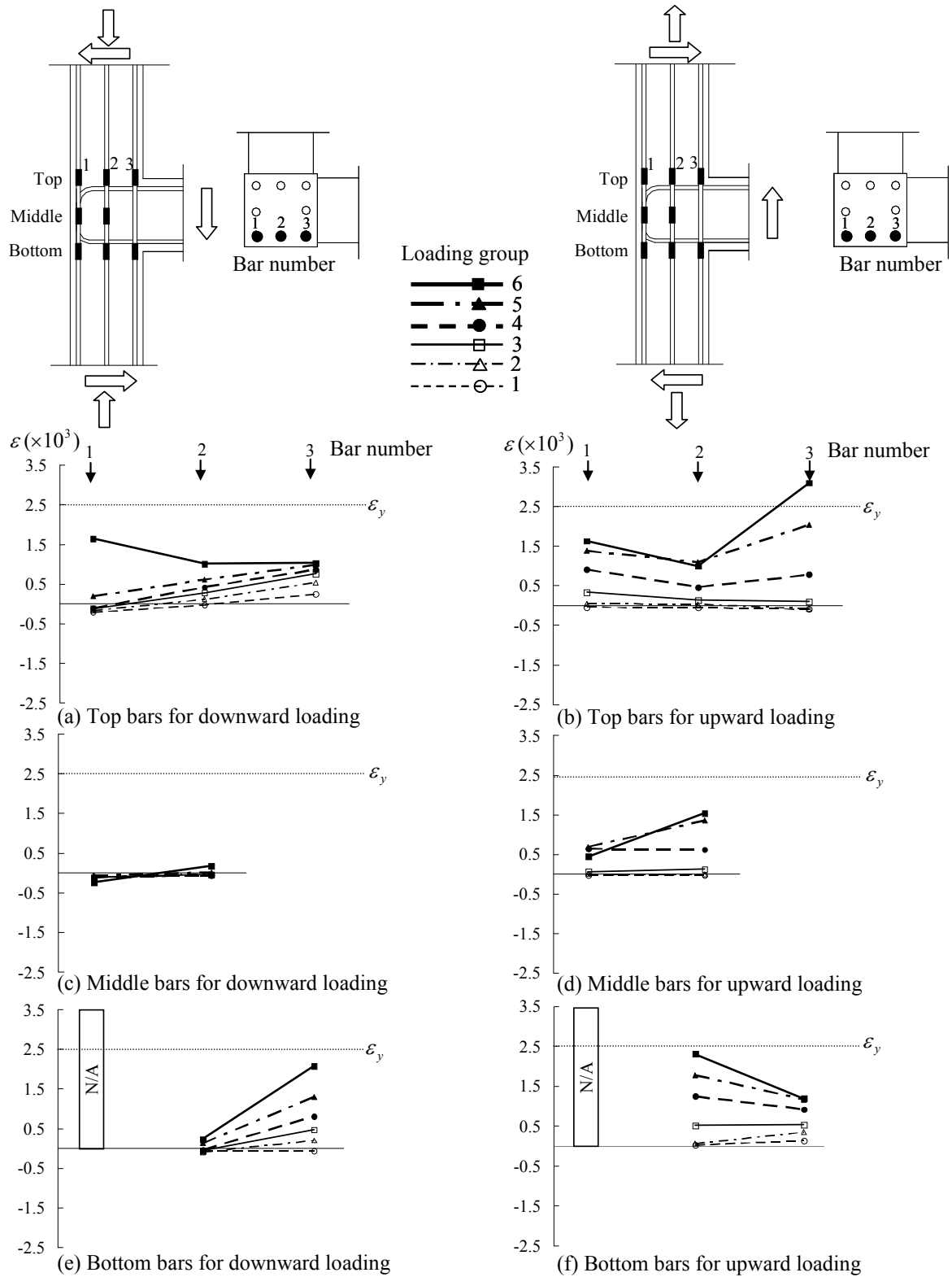
Figure 4.14   Strains of the column longitudinal bars for the EW beam loading, SP1.
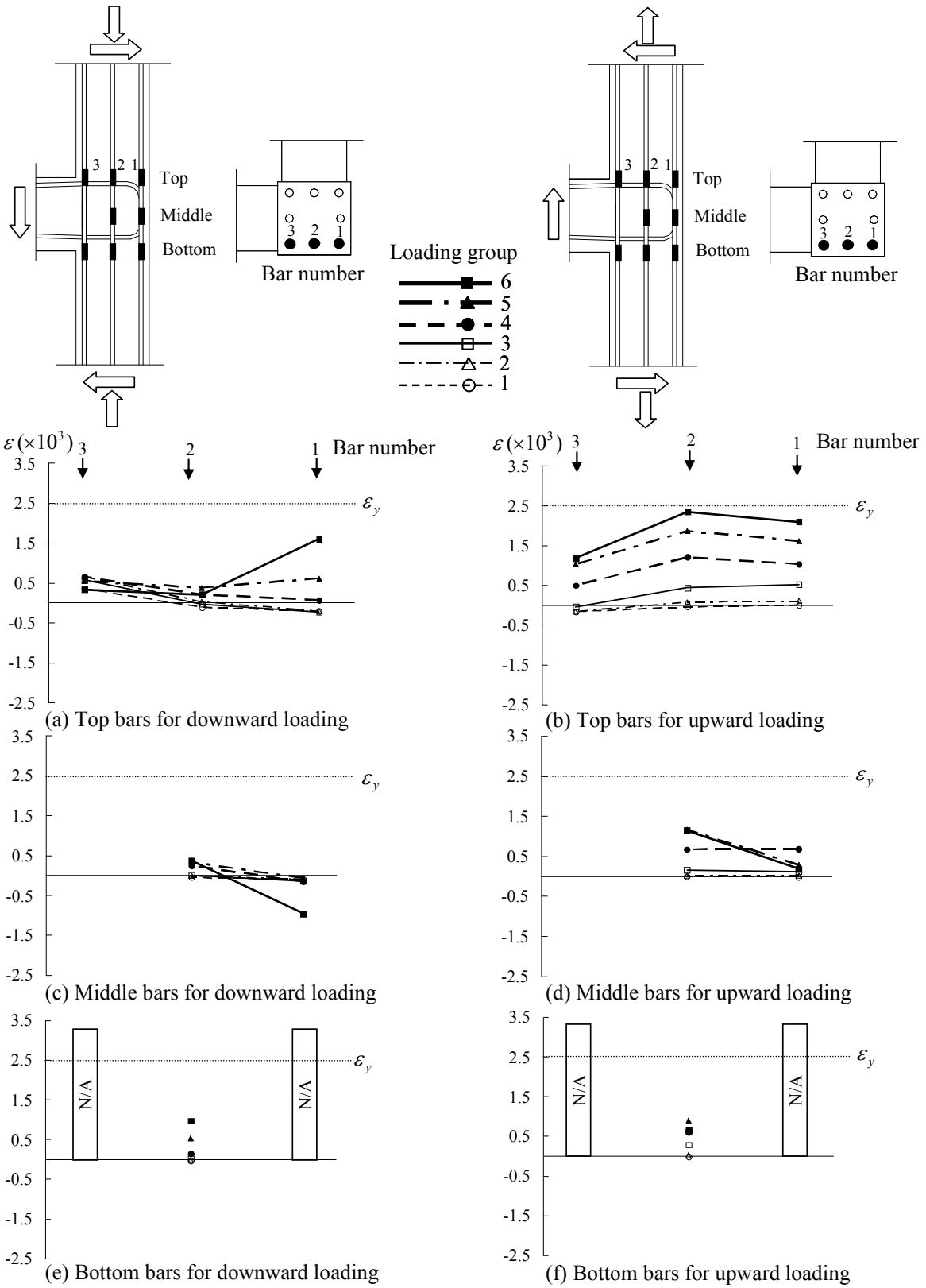
Figure 4.15   Strains of the column longitudinal bars for the NS beam loading, SP1.

4.2   SPECIMEN SP2

4.2.1   Load versus Drift Response

The hysteretic applied load versus drift responses of SP2 in the EW and NS directions are shown in Figure 4.16 and their values at the peak of each cyclic loading group are given in Table 4.4. Theoretical beam shear force V_y corresponding to the beam yield strength (ignoring the slab contribution) is shown as horizontal dashed lines in Figure 4.16. The first yielding of top reinforcement in both the EW and NS beam occurred during the fourth group of loading $(\Delta_{EW} = -1.75\%; \quad \Delta_{NS} = -1.76\%)$; when the applied loads were -36.0 kips (-160.1 kN) and -38.3 kips (-170.4 kN), respectively. The bottom reinforcement in both the EW and NS beams yielded during the fifth loading group ($\Delta_{EW} = 2.04\%$; $\Delta_{NS} = 2.06\%$) when the applied loads were 29.6 kips (131.7 kN) and 29.0 kips (129.0 kN), respectively. Note that the top and bottom reinforcement in the beam yielded before reaching the peak of fourth and fifth loading group based on the strain measurement of these bars. A comparison with the drift when the beam reinforcement yielded in SP1 found that the beam reinforcement yielding took place at a similar drift level, i.e., 1.7%. This coincidence can be explained by the fact that the yield curvature is minimally dependent on the flexural strength if the same dimensions of the cross-section and properties of materials are provided.

The EW beam load reached its peak at the fifth loading group, which was right after the loading group when the beam reinforcement yielded. The EW beam downward loading reached its peak at the fifth loading group ($\Delta_{EW} = -2.66\%$), while the peak load for the EW beam upward loading was achieved at the sixth loading group ($\Delta_{EW} = 3.22\%$). The peak loads of EW beam were -36.8 kips (-163.7 kN) for the downward loading and 31.0 kips (137.9 kN) for the upward loading. The peak loading in the NS beam was followed by the EW beam peak loading, which was the same pattern as observed in SP1 due to the loading sequence as mentioned in Section 4.1.1. After the peak loading in both the EW and NS beams, the applied beam loads slightly reduced during the subsequent group of loading, e.g., from -36.8 to -36.6 for the EW downward loading, and thereafter the applied loads sharply reduced. The strength degradation after peak loading was more severe for the downward loading–the slab in tension–than for the upward loading–the slab in compression. Pinching behavior caused by the slip of the beam longitudinal bars was observed after the sixth group of loading, refer to Figure 4.16. Based on the load-drift responses, the important events in both SP1 and SP2 were observed at similar drift levels although the applied loads of SP2 at the same drift levels were greater than that of SP1 due to the higher beam longitudinal reinforcement ratio in SP2.

The column response of SP2 is shown in Figure 4.17. During testing, the column axial loads determined from Equation (3.2a) were applied. In SP2, the column axial load varied from 22 kips (98 kN) in tension to 260 kips (1157 kN) in compression. The column axial load ratio, $P/(f_c' A_g)$, ranged from 2.0% (tension) to 22.7% (compression). The peak vertical displacements were 0.118 in. (3.00 mm) in elongation and 0.107 in. (2.72 mm) in contraction.

Table 4.4   Load versus drift response of SP2.

Group No.	EW direction				NS direction			
	Downward (-)		Upward (+)		Downward (-)		Upward (+)	
	Δ(%)	V_b (kip)	Δ (%)	V_b (kip)	Δ (%)	V_b (kip)	Δ (%)	V_b (kip)
1	-0.57	-16.5	-0.02	4.2	-0.57	-17.2	-0.01	6.5
2	-0.87	-22.9	0.27	12.4	-0.88	-24.1	0.28	13.9
3	-1.17	-28.4	0.56	15.4	-1.16	-31.0	0.57	17.9
4	-1.75	-36.0[*1]	1.15	24.3	-1.76	-38.3[*1*2]	1.18	23.1
5	-2.66	-36.8[*2]	2.04	29.6[*1]	-2.66	-38.1	2.06	29.0[*1*2]
6	-3.86	-36.6	3.22	31.0[#2]	-3.88	-33.8	3.24	28.4
7	-5.68	-29.1	4.99	28.5	-5.70	-23.6	5.01	22.9
8	-8.06	-19.5	7.30	24.0	-8.05	-17.3	7.31	18.8

[*1] first yielding of beam reinforcement
[*2] peak loading
Note: 1 kip = 4.45 kN
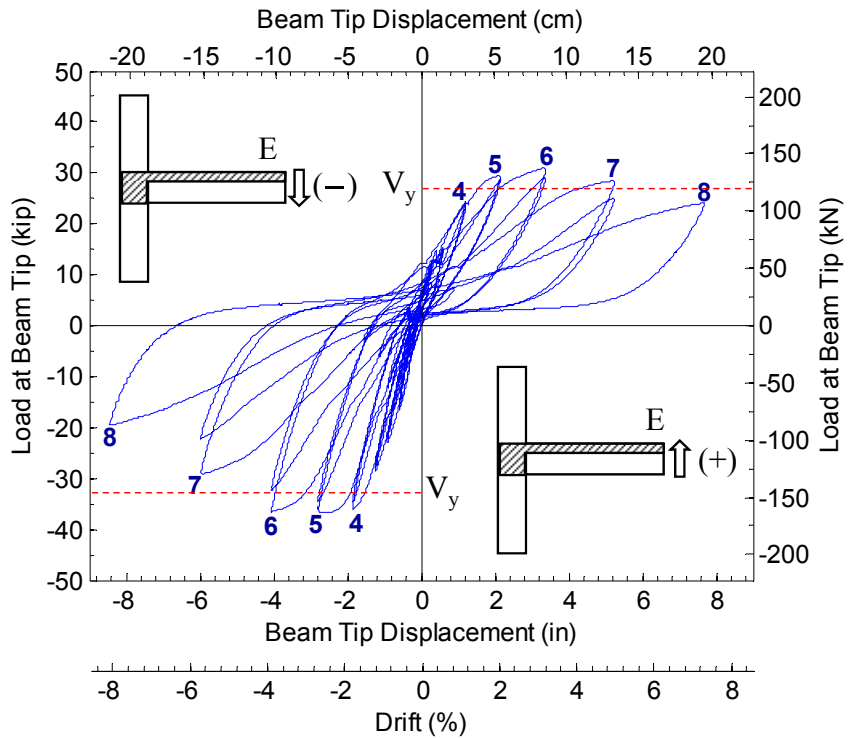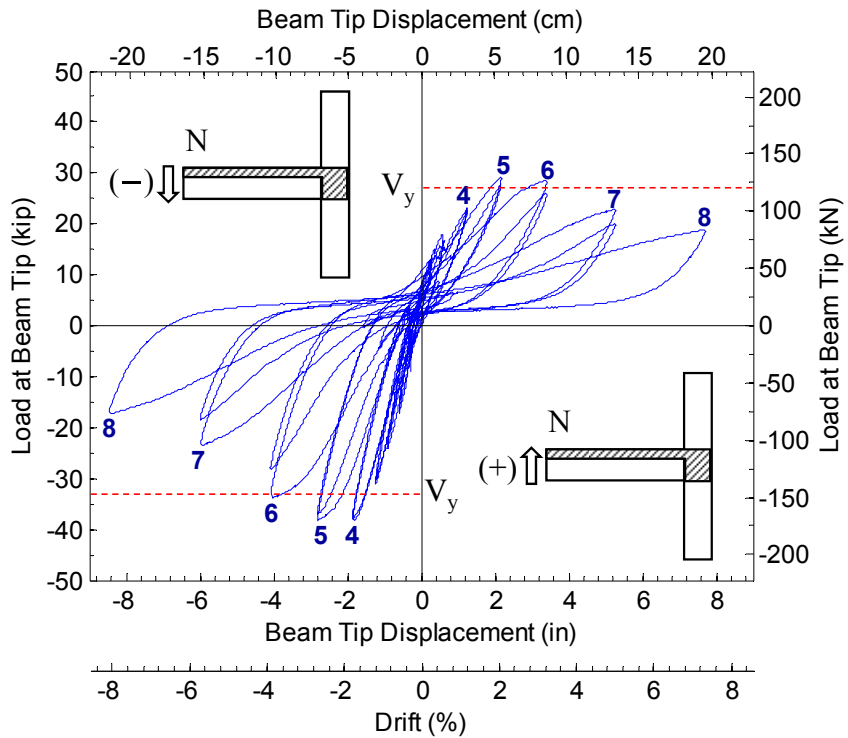
(a) EW direction

(b) NS direction

Figure 4.16   Load versus drift response of SP2.
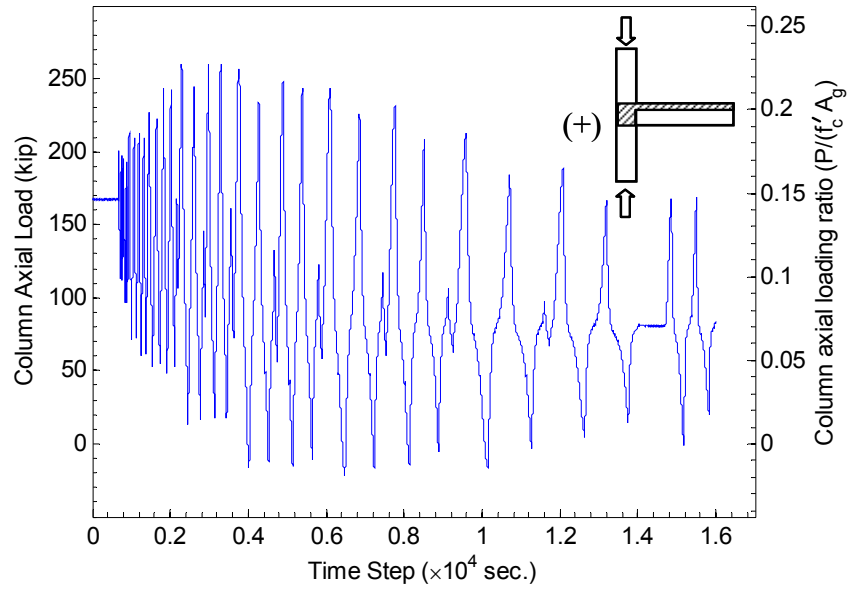
(a) column axial load
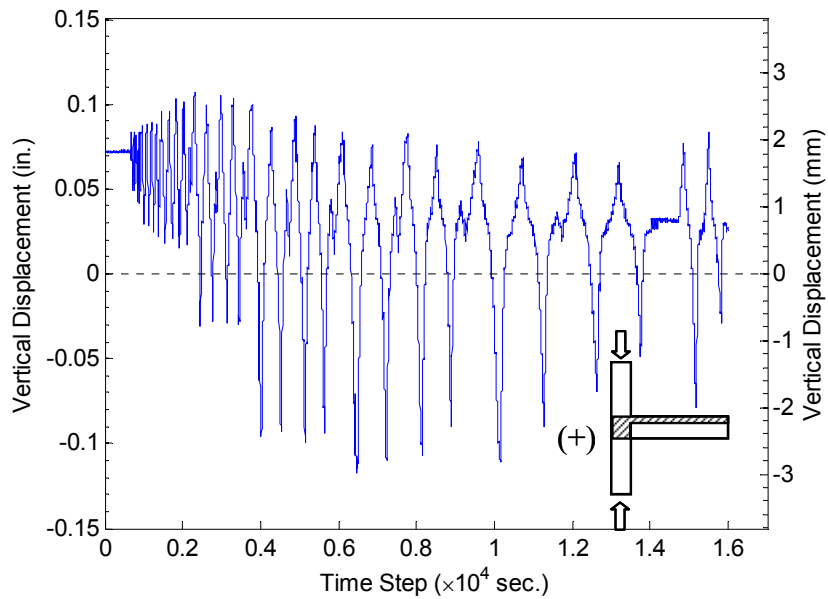
(b) vertical displacement

Figure 4.17   Column response of SP2.

4.2.2 Observed Damage Progression

The qualitative description of damage progression of SP2 is summarized in Table 4.5. The photographs of the specimen taken during testing and at the end of the test are presented in Figure 4.18 through 4.22.

81

4.2.2.1 East-West Direction

JOINT REGION

Diagonal cracks formed in the joint panel during testing, but their pattern was slightly different from that observed in SP1. Multiple cracks formed in the joint panel and "X" shape diagonal cracks became dominant with an increase of the applied beam loads. A first downward diagonal crack (↘) occurred at the second loading group ($\Delta_{EW} = -0.87\%$), while a first upward diagonal crack (↗) appeared at the fourth loading group ($\Delta_{EW} = 1.15\%$), see Figure 4.18(a). For the EW beam downward loading, additional diagonal cracks appeared at the fourth group $\left(\Delta_{EW} = -1.75\%\right)$ when the EW beam top reinforcement yielded, and the two diagonal cracks in the joint panel exclusively widened at the sixth loading group. For the EW beam upward loading, the first upward diagonal crack in the joint panel significantly widened accompanied by additional small cracks, as shown in Figure 4.18(b) and (c). Comparing this response to the crack propagation with SP1 at the same drift level, more cracks were observed in SP2 but they showed similar propagation and crack width. After the peak load, the cover concrete in the joint panel began to bulge and finally spalled off. The beam and column reinforcing bars were exposed at the seventh group of loading. At the last loading group, the core concrete in the joint region was crushed, but the exposed column reinforcing bars did not buckle, see Figure 4.18(d).

Two horizontal cracks were observed at the top of the EW joint panel during the NS beam upward loading, while no horizontal cracks formed during the downward loading. At the third group of the NS beam upward loading, the first horizontal crack developed from the top corner of the joint on the side without a beam, and the second horizontal crack appeared above the existing horizontal crack at the second cycle in the same loading group. In the subsequent fourth group of the NS beam upward loading, the upper horizontal crack widened, but the lower horizontal crack closed [Figure 4.19(a)]. Note that the location of the upper horizontal crack was close to slab top surface and the lower horizontal crack was close to the top reinforcement in the EW beam.

BEAM AND SLAB

During the first group of the EW beam downward loading ($\Delta_{EW} = -0.57\%$), two flexural cracks were observed at the top of the EW beam. These flexural cracks extended to the slab parallel to the NS beam. During the same group of downward loading, a splitting crack developed at the top of the beam-joint interface. Flexural cracks also developed at the bottom of the EW beam during the upward loading, but the width of these cracks was relatively small. With increasing the applied drift level, the splitting crack at the NS beam-slab interface extended towards the end of the NS beam, and the existing flexural cracks and splitting crack at the beam-joint interface widened until the peak loading. Thereafter, the width of flexural cracks reduced because the damage was localized in the joint region. Consequently, the plastic hinge mechanisms did not form in the beams similar to the observation of SP1.

During the NS beam loading, especially downward loading, inclined cracks occurred in the EW beam due to torsion. These inclined cracks remained minor until the peak loading and moreover these cracks generally closed during the EW beam loading. The residual cracks in the EW beam and slab after testing are illustrated in Figure 4.20.

4.2.2.2 North-South Direction

JOINT REGION

A first downward diagonal crack (↙) occurred at the third loading group ($\Delta_{NS} = -1.16\%$), while a first upward diagonal crack (↖) shortly developed during the fourth loading group $(\Delta_{NS} = 1.18\%)$ at the top corner of the joint panel on the side without a beam, see Figure 4.21(a). On the continued NS beam loading, multiple inclined cracks newly formed in the joint panel and the existing cracks further propagated, refer to Figure 4.21(b). A significant propagation of two existing diagonal cracks in the joint panel was observed at the sixth group of the NS beam loading, which was the subsequent loading to the peak of the EW beam, see Figure 4.21(c). At the last loading group, cover concrete in the joint panel spalled off and joint core concrete was crushed, refer to Figure 4.21(d).

As observed in the EW joint panel, a horizontal crack appeared in the top of the NS joint panel during the fourth group of the EW beam upward loading, as shown in Figure 4.19(b); the cover concrete in the joint panel spalled along this horizontal crack after peak loading. This horizontal crack was located at the same level as the top reinforcement of the NS beam.

BEAM AND SLAB

Several hairline flexural cracks and splitting crack at the beam-joint interface developed at the top of the NS beam for the second group of the NS beam loading. Simultaneously, a splitting crack along the EW beam-slab interface began to propagate. Generally, the propagation of flexural cracks was not easily observable, but the width of these cracks was expected to reduce after peak loading. Plastic hinge mechanisms did not form in the NS beam. The marked residual cracks in the beam and slab are shown in Figure 4.20(b). During the EW beam loading, inclined cracks occurred in the NS beam. In particular, the inclined crack at the bottom of the beam widened and the cover concrete in this beam detached, as indicated by the arrow in Figure 4.21(d).

4.2.2.3 Summary

In regards to joint cracking, a first joint crack appeared around the drift level of 1.2%, except for the downward diagonal crack in the EW joint where the first crack took place at the loading to 0.87% drift. As the applied drift increased up to the fifth loading group, multiple inclined cracks newly appeared, and finally the existing diagonal cracks propagated further. At the sixth group of loading ($\Delta_{down} = -3.87\%$; $\Delta_{down} = 3.23\%$), one or two of the existing diagonal cracks propagated exclusively. Beyond the sixth group of loading, the joint region was severely damaged showing the spalling of cover concrete and crushing of core concrete in the joint region.

For damage of the beam and slab, first flexural and splitting cracks developed during the first and second groups of loading, and these cracks widened up to the sixth group of loading. The propagation of these cracks in the beams and slab was not significant compared with the cracks in the joint panel. After peak loading, the width of flexural cracks in the beams and slab decreased, but splitting cracks at the beam-joint and beam-slab interfaces continuously widened. In SP2, no plastic hinge mechanism formed in both beams.

Horizontal cracks appeared at the top of joint panel in the NS direction for the EW beam upward loading, while inclined cracks developed in the beam in the NS direction for the EW

beam downward loading. The same crack pattern was observed in the EW side of joint panel and beam during the NS beam loading. During the subsequent same directional beam loading, these cracks were not observed, thus the joint responses were not influenced by the previous orthogonal beam loading. In other words, the EW joint responses were little affected by the horizontal and inclined cracks developed during the previous NS beam loading. Figure 4.22 illustrates that the failure of the specimen was attributed to the severe damage in the joint region.

Table 4.5   Qualitative damage description of SP2.

Drift (%)	EW direction	NS direction
$\Delta_0 = -0.3$	-	-
$\Delta_{up} = -0.02$ $\Delta_{down} = -0.57$	- Multiple flexural cracks in beam and slab - Splitting crack at beam-joint interface	- First flexural crack in beam
$\Delta_{up} = 0.28$ $\Delta_{down} = -0.88$	- First downward diagonal crack in joint	- Additional flexural cracks
$\Delta_{up} = 0.57$ $\Delta_{down} = -1.17$	-	- First downward diagonal crack in joint
$\Delta_{up} = 1.17$ $\Delta_{down} = -1.76$	- Second downward diagonal crack in joint - First upward diagonal crack in joint - First yielding of beam top bars	- First upward diagonal cracks in joint - First yielding of beam top bars
$\Delta_{up} = 2.05$ $\Delta_{down} = -2.66$	- Second upward diagonal crack in joint - Widening of existing joint cracks - First yielding of beam bottom bars	- Additional downward and upward diagonal cracks in joint - First yielding of beam bottom bars
$\Delta_{up} = 3.23$ $\Delta_{down} = -3.87$	- Large opening of joint diagonal cracks - Propagation of flexural and splitting crack at beam-joint interface	- Large opening of joint diagonal cracks
$\Delta_{up} = 5.00$ $\Delta_{down} = -5.69$	- Spalling of joint cover concrete - Reduction of width of beam flexural cracks	- Spalling of joint cover concrete - Reduction of width of beam flexural cracks
$\Delta_{up} = 7.31$ $\Delta_{down} = -8.0$	- Crushing of joint core concrete	- Crushing of joint core concrete
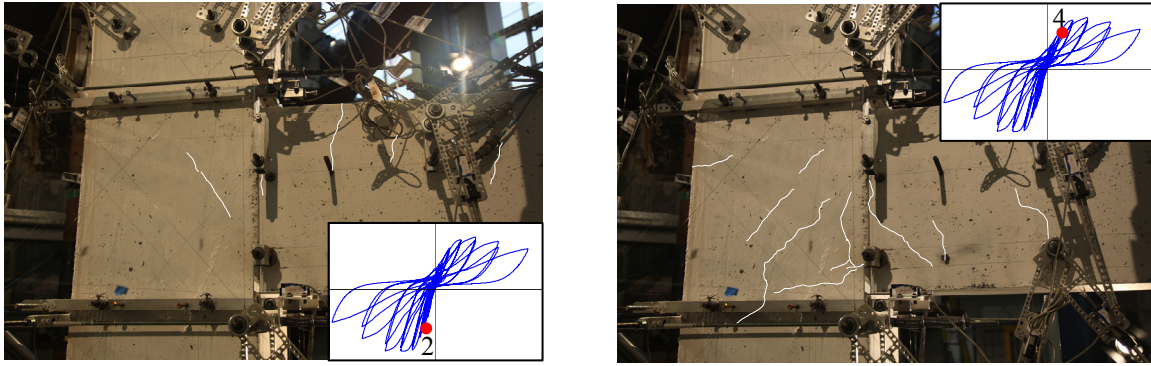
(a) first joint crack
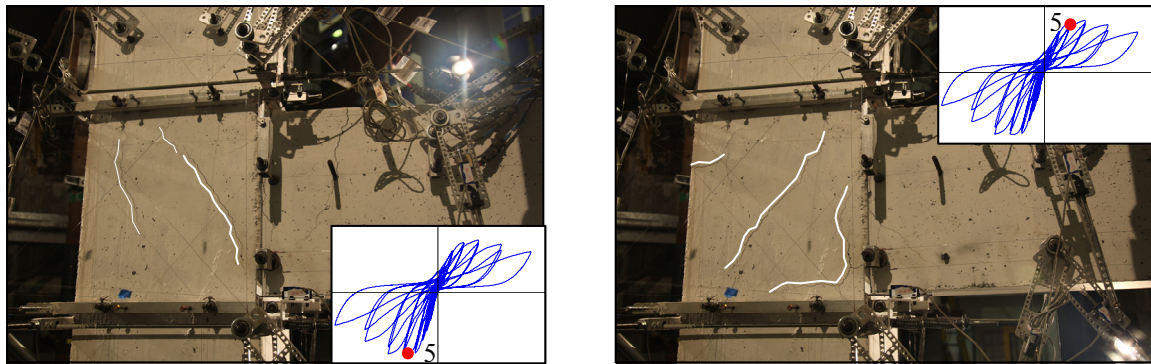
(b) propagation of joint cracking
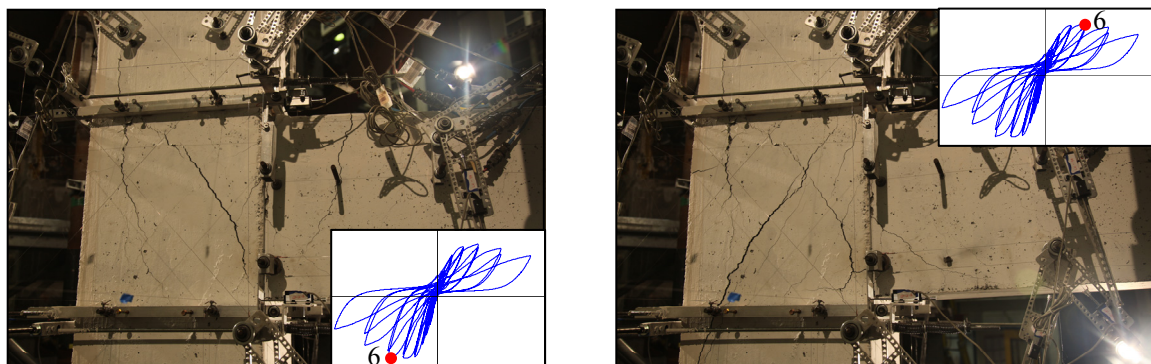
(c) joint cracking before joint failure
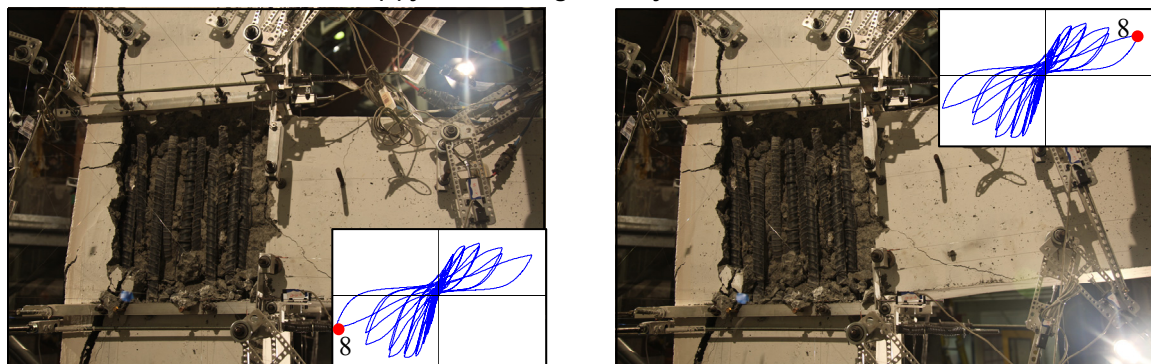
(d) joint damage at end of test

Figure 4.18   Damage progression of joint in EW direction, SP2.

85
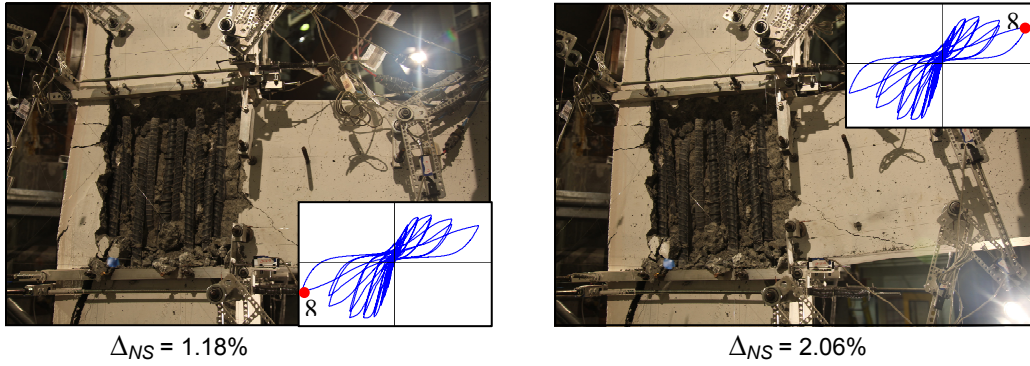
$\Delta_{NS} = 1.18\%$ $\Delta_{NS} = 2.06\%$

(a) horizontal crack in EW joint by NS beam loading
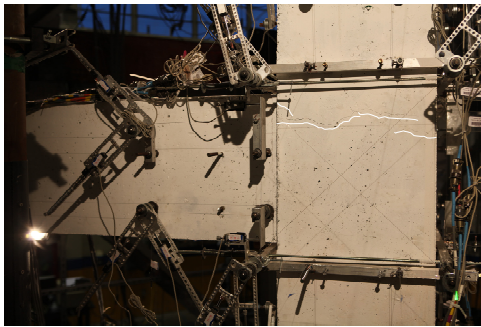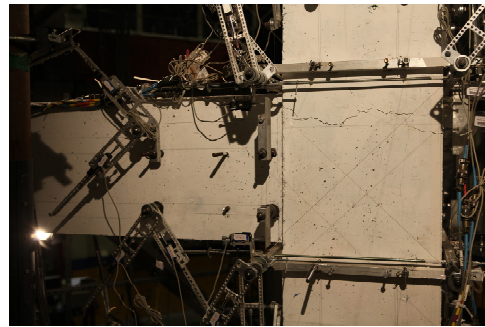
$\Delta_{EW} = 1.15\%$ $\Delta_{EW} = 2.04\%$

(b) horizontal cracks in NS joint by EW beam loading

Figure 4.19   Propagation of horizontal crack in joint panel, SP2.

(a) cracks in EW beam   **(b) cracks in NS beam**
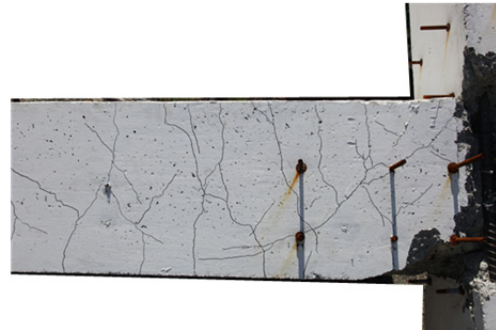
(c) cracks on slab

Figure 4.20   Existing cracks after testing, SP2.
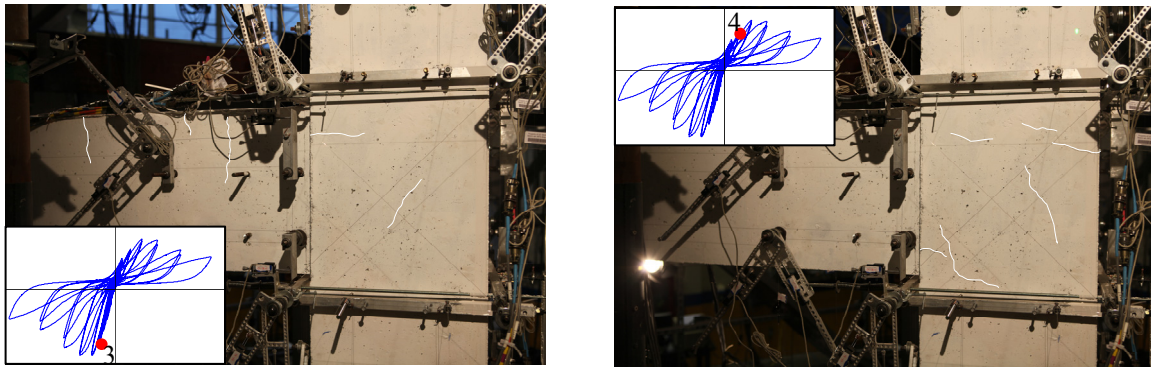
(a) first joint crack
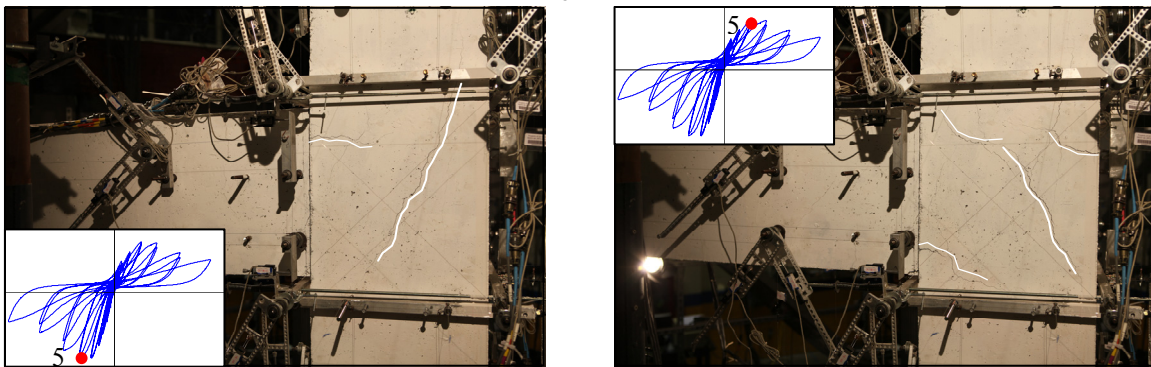
(b) propagation of joint cracking
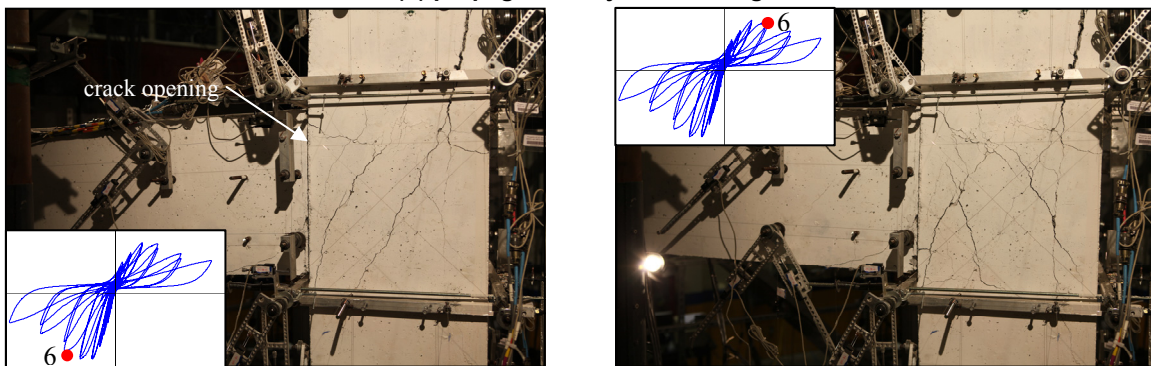
(c) joint cracking before joint failure
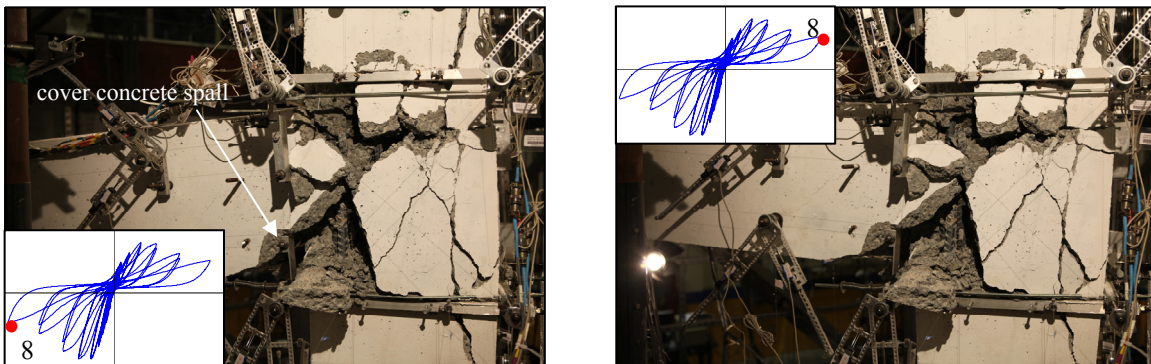
(d) joint damage at end of test

Figure 4.21   Damage progression of joint in NS direction, SP2.

(a) global view of specimen

(b) inside corner joint

(c) NS beam

(d) EW beam
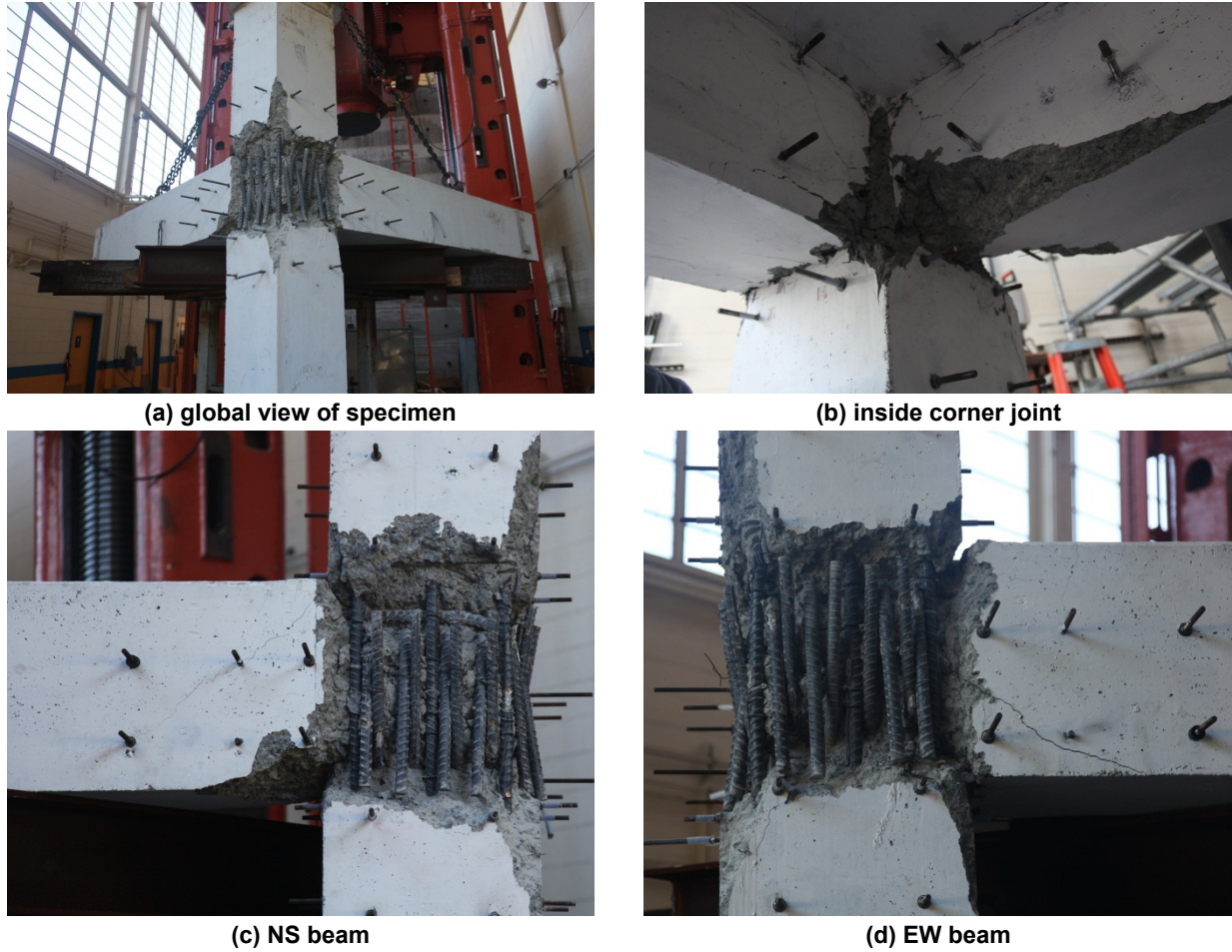
Figure 4.22   Failure of SP2 after removing concrete fragments.

4.2.3 Joint Shear Stress versus Rotation Response

The hysteretic responses of joint shear stress versus strain are presented in Table 4.6 and Figure 4.23. The assumed constant moment arm was taken to be 0.9 times the beam effective depths because beam reinforcing bars yielded, as shown in the subsequent section. Based on the subsequent discussion of slab reinforcement in Section 5.5, slab top four reinforcing bars were considered for estimating the effective depth in both EW and NS beams for negative bending. The maximum joint shear stresses in the EW direction were 747 psi (5.15 MPa) for the downward loading and 597 psi (4.12 MPa) for the upward loading; the corresponding values of $\gamma = v_{jh} / \sqrt{f_c'}$ were 12.6 $\text{psi}^{0.5}$ (1.05 $\text{MPa}^{0.5}$) and 10.0 $\text{psi}^{0.5}$ (0.83 $\text{MPa}^{0.5}$), respectively. In the NS direction, the maximum joint shear stresses were 735 psi (5.07 MPa) for the downward loading and 578 psi (3.99 MPa) for the upward loading; the corresponding values of $\gamma = v_{jh} / \sqrt{f_c'}$ were 12.4 $\text{psi}^{0.5}$ (1.03 $\text{MPa}^{0.5}$) and 9.7 $\text{psi}^{0.5}$ (0.81 $\text{MPa}^{0.5}$), respectively. Note that the NS beam peak loads were greater than those in the EW beam. The joint shear stresses were, however, similar for both directions because of the aforementioned different cover concrete thicknesses in the EW and NS beam cross sections. The test results showed that the maximum joint shear stresses were greater than the shear strength by the ASCE 41 in both directions, as shown in Figure 4.23, and also these values were greater than the maximum joint shear stresses of SP1.

Joint shear strains at the first cycle of peak loading were 0.0027 rads for the downward loading and 0.0117 rads for the upward loading in the EW direction. In the NS direction, the measured joint shear strains were 0.0012 rad. for the downward loading and 0.0059 rad. for the upward loading, as shown in Figure 4.23. The joint shear strains were similar for both SP1 and SP2 at the peak loads, but when compared at the same drift levels, the joint shear strains were larger in SP2 than those of SP1. Figure 4.24 presents the hysteretic response of the rotation at the beam-joint interface. The rotations measured in the EW and NS directions were very close each other at the same loading groups, i.e., the similar drift levels. The results of total joint rotations are presented in Figure 4.25. Total joint rotations at the peak load were 0.013 rads for the downward loading and 0.021 rads for the upward loading in the EW direction; 0.008 rads for the downward loading and 0.011 rads for the upward loading in the NS direction. Compared with the joint deformation response in SP1 at the same loading groups, SP2 showed larger joint shear strains but smaller rotations at the beam-joint interface; consequently, total rotations became similar for both specimens SP1 and SP2.

According to Table 4.6, the contribution of joint rotation to total drift was about 40% near the first yielding of beam reinforcement. Subsequently, this contribution increased to about 70%, which confirmed that the failure of specimen SP2 was caused by the joint shear failure.

Table 4.6   Joint response of SP2.

Dir.	EW											
Group No.	Downward						Upward					
	v_{jh} (psi)	γ (psi$^{0.5}$)	Δ (rad)	γ_{xy} (rad)	θ_j (rad)	θ_j/Δ	v_{jh} (psi)	γ (psi$^{0.5}$)	Δ (rad)	γ_{xy} (rad)	θ_j (rad)	θ_j/Δ
1	335	5.6	0.0057	-	-	-	80	1.3	0.00	-	-	-
2	465	7.8	0.0087	0.0005	0.0027	0.31	239	4.0	0.0027	0.00	0.0004	0.15
3	577	9.7	0.0117	0.0008	0.0038	0.32	296	5.0	0.0056	0.00	0.0009	0.16
4	731[*1]	12.3	0.0175	0.0015	0.0074	0.42	468	7.9	0.0115	0.0015	0.0032	0.28
5	747[*2]	12.6	0.0266	0.0027	0.013	0.49	570[*1]	9.6	0.0204	0.0047	0.0089	0.44
6	743	12.5	0.0386	0.0073	0.022	0.57	597[*2]	10.0	0.0322	0.012	0.021	0.65
7	591	9.9	0.0568	0.033	0.049	0.86	549	9.2	0.0499	0.019	0.036	0.72
8	396	6.7	0.0806	-	-	-	462	7.8	0.0730	-	-	-
Dir.	NS											
Group No.	Downward						Upward					
	v_{jh} (psi)	γ (psi$^{0.5}$)	Δ (rad)	γ_{xy} (rad)	θ_j (rad)	θ_j/Δ	v_{jh} (psi)	γ (psi$^{0.5}$)	Δ (rad)	γ_{xy} (rad)	θ_j (rad)	θ_j/Δ
1	330	5.6	0.0057	-	-	-	130	2.2	0.00	-	-	-
2	462	7.8	0.0088	0.0001	0.0020	0.23	277	4.7	0.0028	0.0001	0.0012	0.43
3	595	10.0	0.0116	0.0006	0.0031	0.27	360	6.0	0.0057	0.0004	0.0022	0.39
4	735[*1*2]	12.4	0.0176	0.0012	0.0076	0.43	461	7.8	0.0118	0.0019	0.0048	0.41
5	731	12.3	0.0266	0.0033	0.013	0.49	578[*1*2]	9.7	0.0206	0.0059	0.011	0.53
6	648	10.9	0.0388	0.016	0.030	0.77	566	9.5	0.0324	0.012	0.021	0.65
7	453	7.6	0.0570	-	-	-	457	7.7	0.0501	0.028	0.035	0.70
8	332	5.6	0.0805	-	-	-	375	6.3	0.0731	-	-	-

[*1] first yielding of beam reinforcement
[*2] peak loading

Note: 1 psi = 0.0069 MPa; $1.0\sqrt{f_c'}$ psi$^{0.5} = 0.083\sqrt{f_c'}$ MPa$^{0.5}$
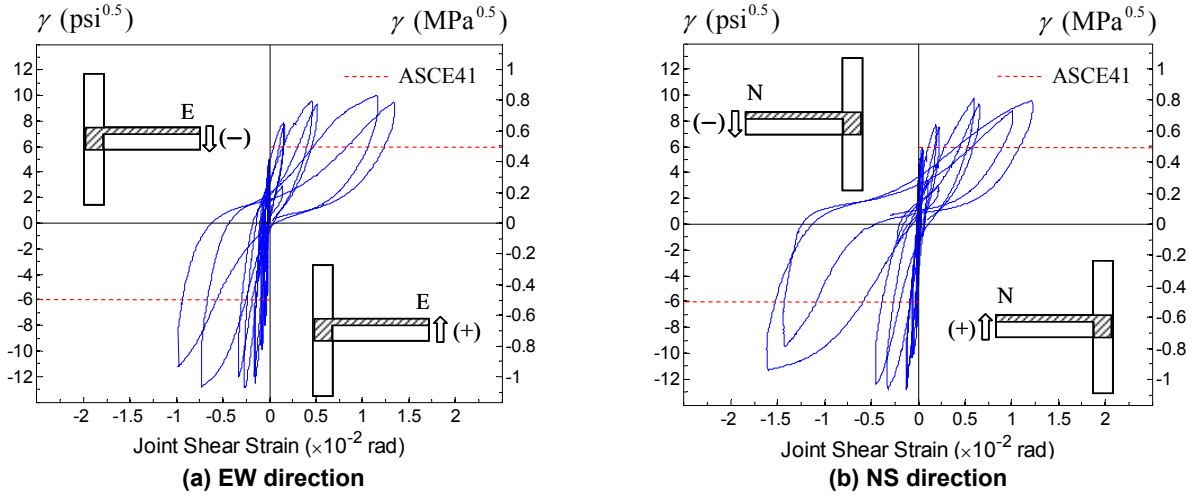
Figure 4.2   **Joint shear stress versus strain response of SP2.**
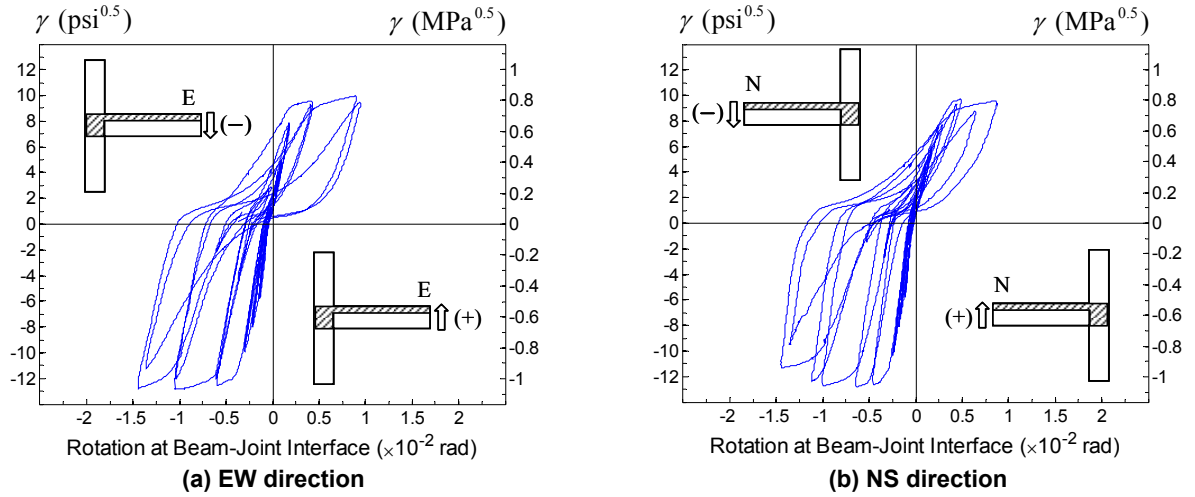
Figure 4.24   **Joint shear stress versus rotation at beam-joint interface of SP2.**
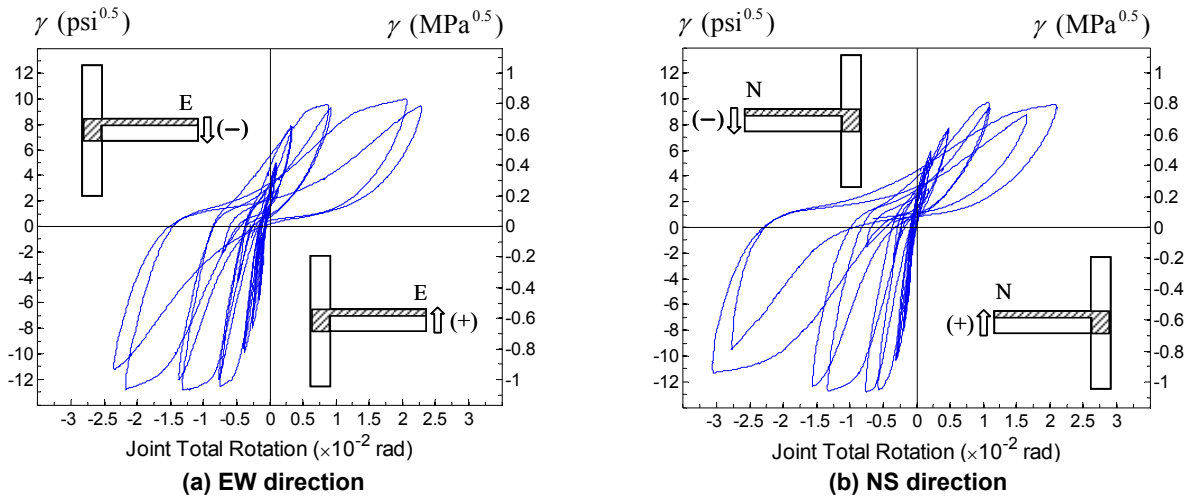
Figure 4.25   **Joint shear stress versus total rotation of SP2.**

91

4.2.4 Strain Measurement

4.2.4.1 Beam Reinforcement

The strain measurements of the EW and NS beam longitudinal bars are shown in Figures 4.26 and 4.27. The labeled drift levels correspond to the loading from the third group through the sixth group. Note that the data of the damaged strain gages are presented as blank bars marked as not applicable (N/A) in the plots. For better understanding of the strain distribution, a straight line passing the damaged gage was drawn between the values for the functioning gages. For example, a straight line connected gage numbers 1 and 3 passing through the damaged gage number 2 in Figure 4.26(b).

The first yielding of the beam top longitudinal bars occurred at the beam-joint interface between the drift level of $\Delta = -1.17\%$ and $\Delta = -1.76\%$, i.e., the third and fourth loading group, and the bottom longitudinal bars yielded between the drift level of $\Delta = 1.17\%$ and $\Delta = 2.05\%$, i.e., the fourth and fifth loading group. Note that the first yielding of SP1 beam top bars occurred at the same drift levels as the SP2 beam bars yielded. The strains of all the gages increased as the applied drift level increased. Based on the strain variation at the gage number 2, which was placed on the mid-width of the joint, the yielding of beam reinforcing bars propagated toward the inside of the joint (Figure 4.26), as observed in SP1. The yield propagation of the SP2 beam longitudinal bars, however, was not as severe as observed in SP1 because the flexural strengths of SP2 beams were greater than those of SP1 beams.

4.2.4.2 Slab Reinforcement

The strain gage measurements of the EW and NS slab reinforcing bars are presented in Figure 4.28. The slab bar strains were measured at the beam-slab interface. The first yielding of the EW and NS slab top reinforcement occurred at the same loading group when the beam top reinforcement yielded, between the drift level of $\Delta = -1.17\%$ and $\Delta = -1.76\%$. At the peak loading, top two reinforcing bars yielded in the EW and NS slab. Additional top slab bar of gage number 3 in the EW slab yielded during the sixth loading group ($\Delta_{EW} = -3.86\%$), while the top bars of gage number 3 and 4 in the NS slab remained elastic during the loading after the peak. In contrast, the first slab bottom reinforcing bar yielded in the EW direction only; the slippage of this bar was observed as shown in Figure 4.28. This was a consistent observation for both SP1 and SP2 because slab bottom bars were placed relatively close to the neutral axis of the L-shape section with insufficient anchorage.

4.2.4.3 Column Reinforcement

The strain gage measurements of the column longitudinal bars are presented in Figures 4.29 and 4.30. The strains of all the column longitudinal bars were less than the yield strain (0.0025) until peak loading, except for the top gage of the bar number 3 in the EW direction (which yielded at the sixth group of loading when the column was in tension). Because the column was subjected to small tension, the column longitudinal bars began to elongate from the fourth group of the EW and NS beams upward loading, as shown in Figures 4.29 and 4.30,.

The strain distribution of the column intermediate reinforcing bars was measured over the height in the joint region. The tensile strain in these bars at the joint mid-height was less than those at either or both top and bottom of the joint, which led to the conclusion that the column intermediate reinforcing bars did not act as a tension tie in the joint panel.

Note: 1" = 25.4 mm

(a) EW-Top-Ext.

(b) EW-Top-Int.
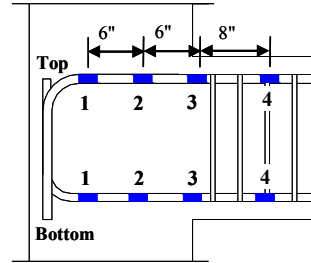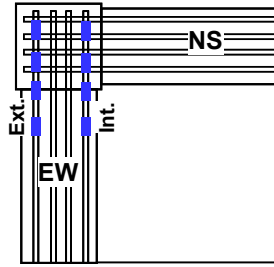
(c) EW-Bottom-Ext.
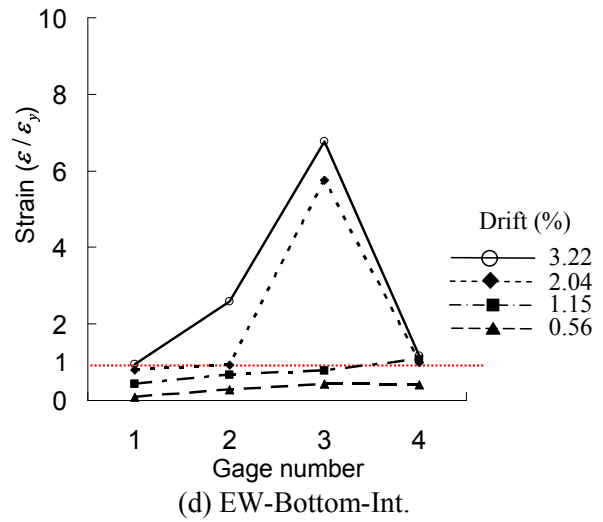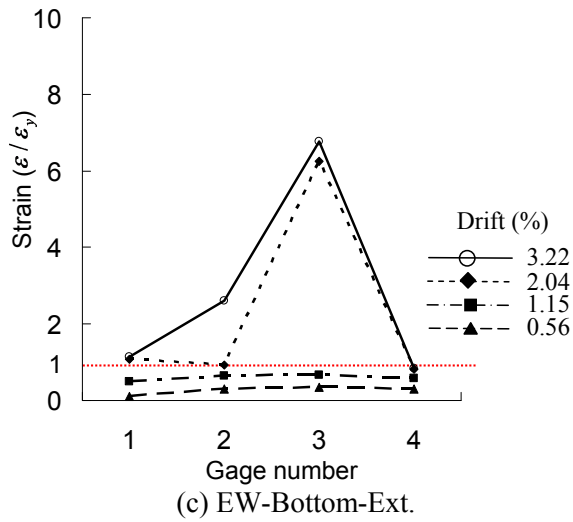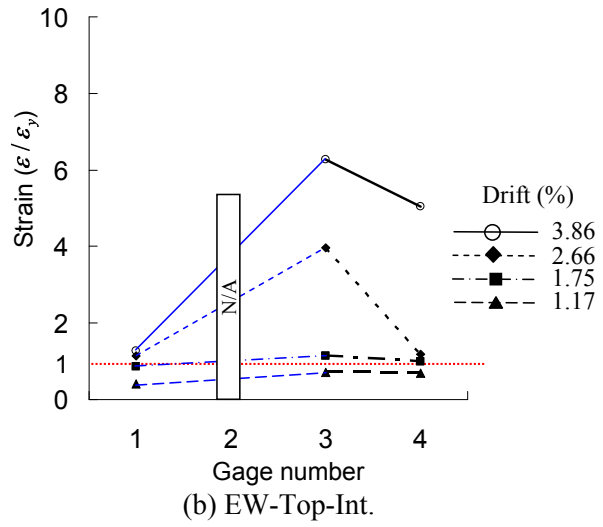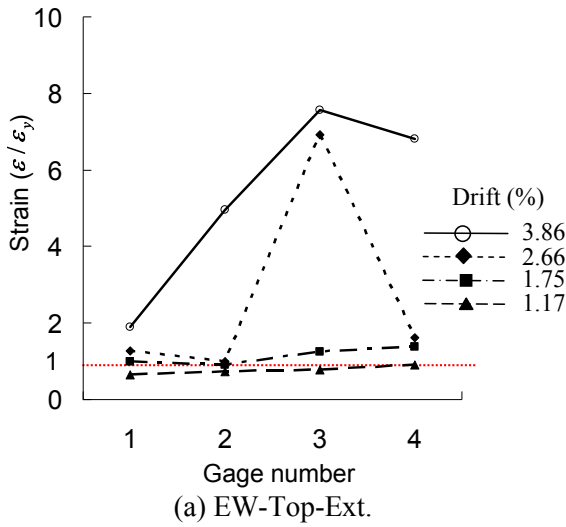
(d) EW-Bottom-Int.

Figure 4.26   Strains of the EW beam reinforcing bars of SP2.
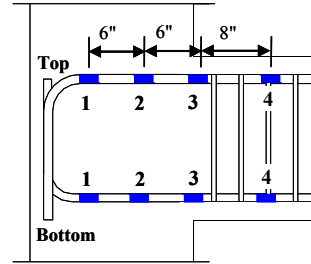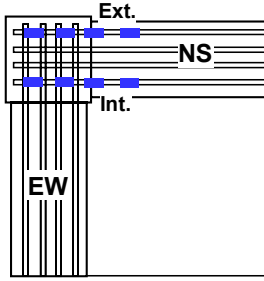
Note: 1" = 25.4 mm
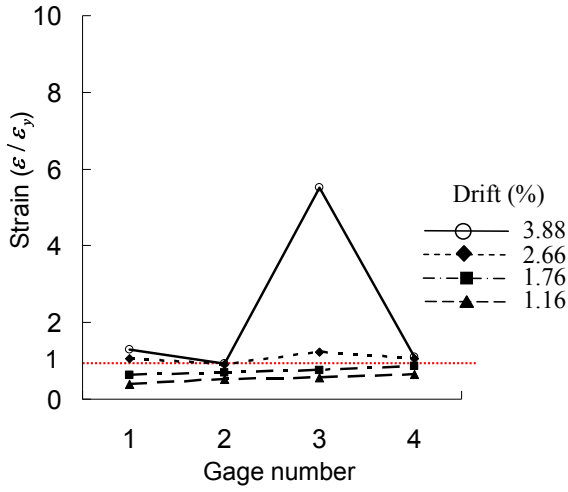
(a) NS-Top-Ext.
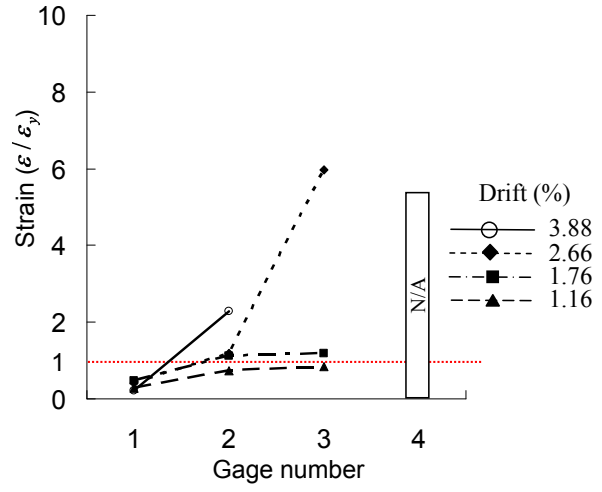
(b) NS-Top-Int.
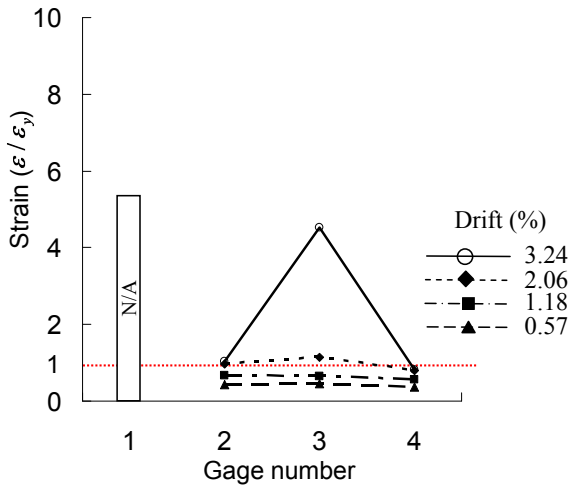
(c) NS-Bottom-Ext.
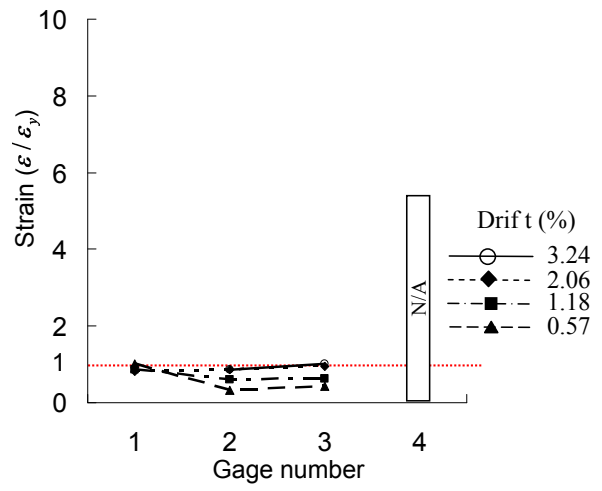
(d) NS-Bottom-Int.

Figure 4.27   Strains of the NS beam reinforcing bars of SP2.
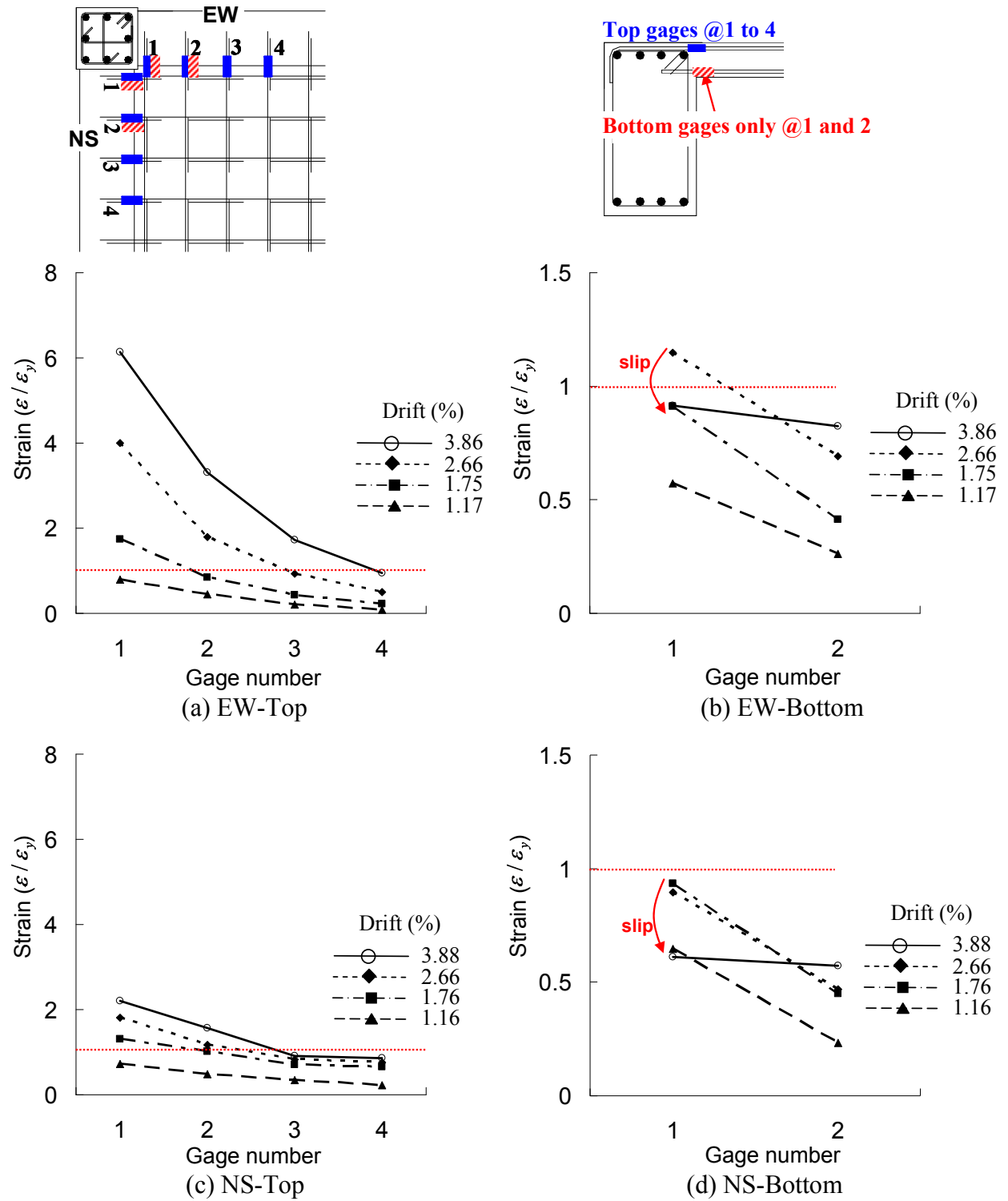
Figure 4.28   Strains of the slab reinforcing bars of SP2.
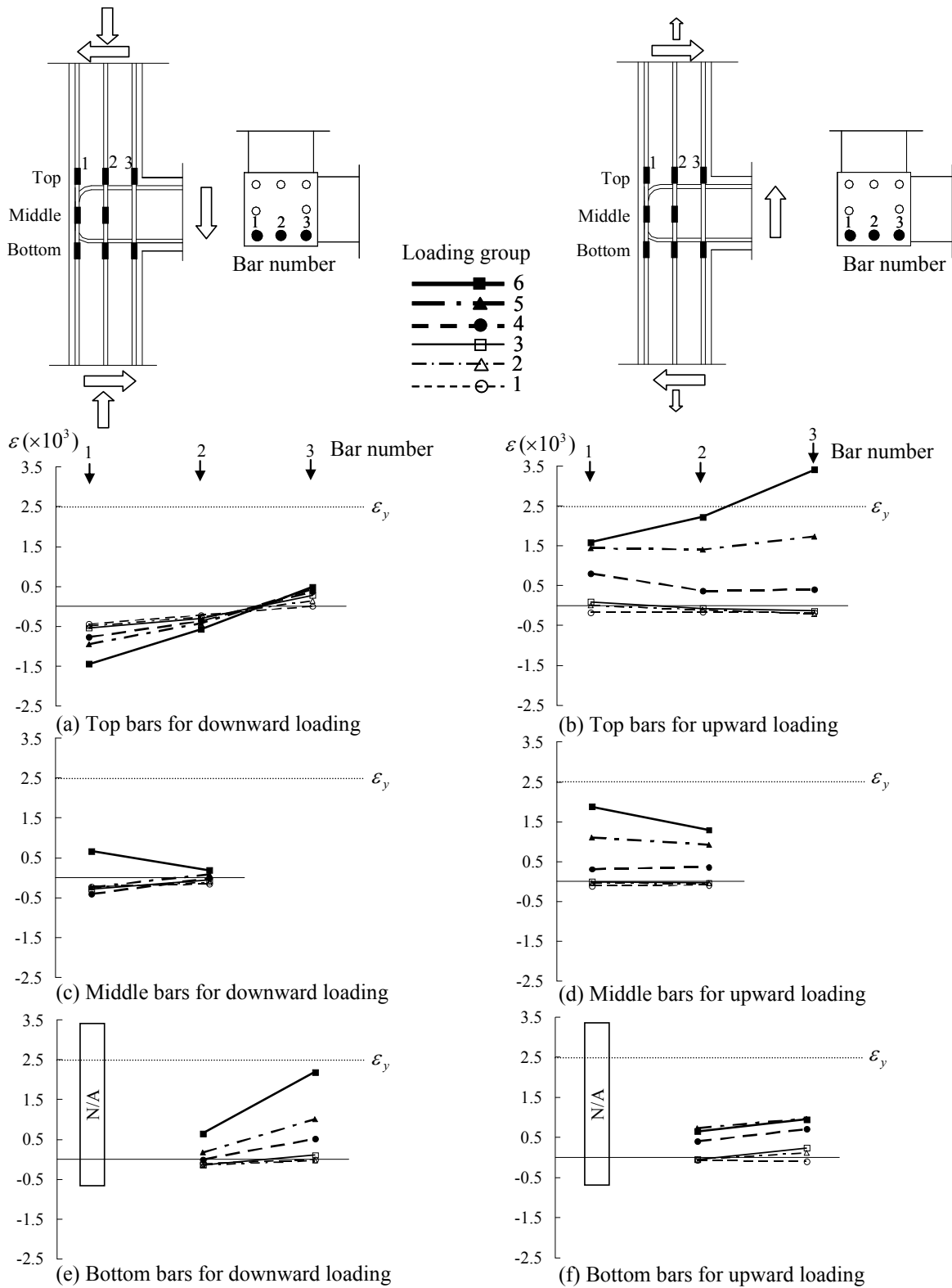
Figure 4.29   Strains of the column reinforcing bars for the EW beam loading, SP2.
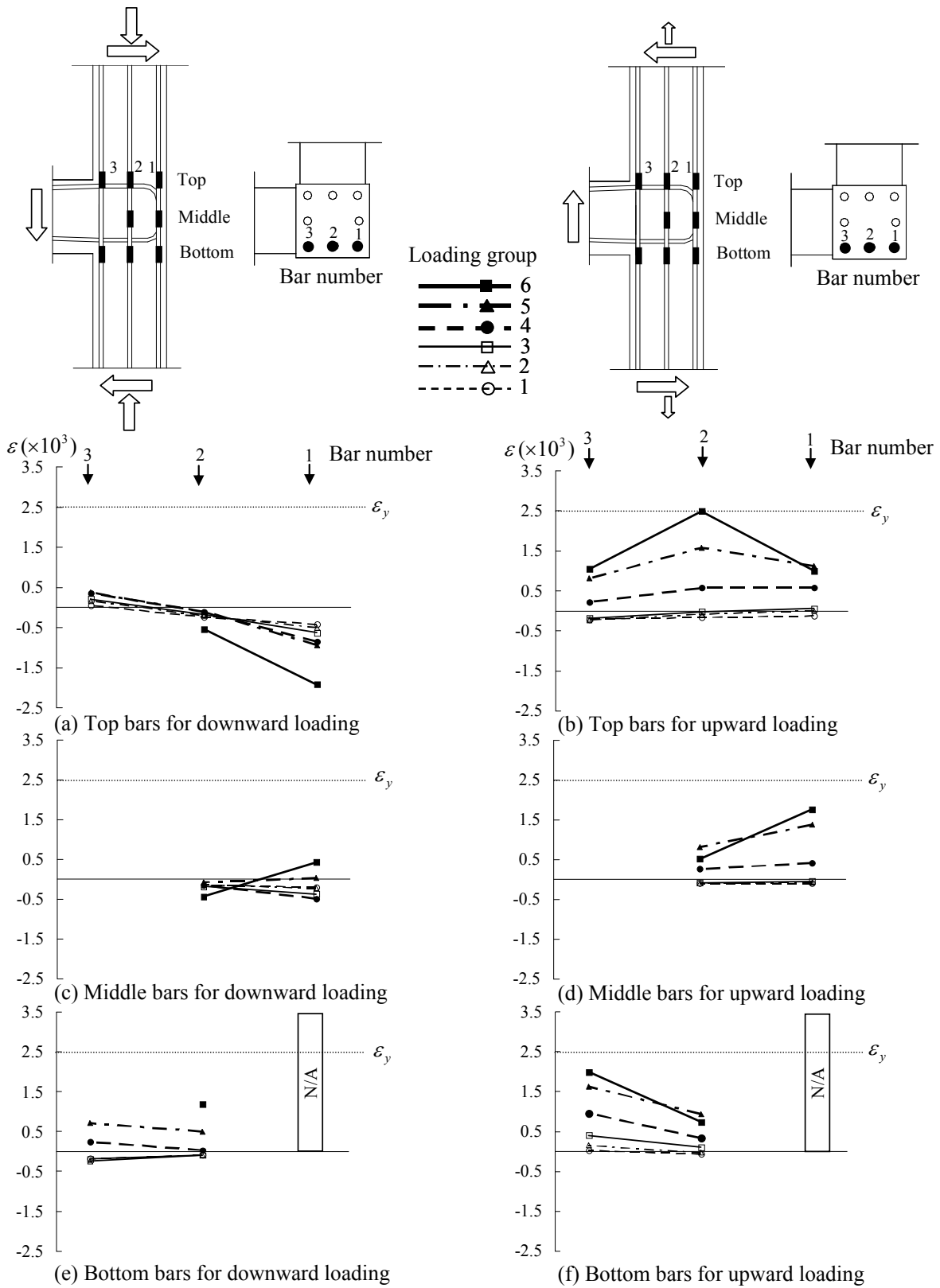
Figure 4.30   Strains of the column reinforcing bars for the NS beam loading, SP2.

4.3   SPECIMEN SP3

4.3.1   Load versus Drift Response

The hysteretic applied load versus drift responses of SP3 in the EW and NS directions are shown in Figure 4.31, and their values at the peak of each cyclic loading group are given in Table 4.7. Theoretical beam shear force V_y corresponding to the beam yield strength (ignoring the slab contribution) is shown as horizontal dashed lines in Figure 4.31. For the downward loading of the EW beam, the first yielding of the top reinforcement occurred during the fourth group of loading ($\Delta_{EW} = -1.23\%$). In the subsequent fifth group of loading ($\Delta_{EW} = -1.89\%$), the peak load was achieved to be -40.4 kips (-179.7 kN). For the upward loading, the bottom reinforcement in the EW beam yielded at the fifth group of loading ($\Delta_{EW} = 1.49\%$);, at this loading group, the peak load was achieved to be 37.8 kips (168.1 kN).

In the NS beam, the top and bottom reinforcement yielded during the fifth group of loading for both downward and upward loading ($\Delta_{NS} = -1.94\%$; $\Delta_{NS} = 1.43\%$). At the same loading group, the peak loads of the NS beam were -35.8 kips (-159.3 kN) for the downward loading and 33.1 kips (147.2 kN) for the upward loading. Table 4.7 shows that the applied loads in the NS beam were similar to those in the EW beam up to the third group of loading; thereafter, less loads were applied to the NS beam for the same drift levels compared with the forces applied to the EW beam. This reduction of applied loads in the NS beam resulted from the damage of the joint panel during the EW beam loading.

The top and bottom reinforcement in the EW and NS beams yielded at the average drift level of 1.5%. Note that the estimated yield drift was 0.88% which corresponded to the drift at the third group of loading. The estimated yield drift was determined by a conventional analysis for the beam-column subassemblies of the specimens using OpenSees [2010] without consideration of joint flexibility. This simplification in the computational model explains the difference between the measured and estimated yield drift levels. In addition, the relatively earlier yielding of top reinforcement in the EW beam was caused by a larger cover concrete thickness at the top of beam cross section, leading to the reduction of the effective beam depth.

Based on the hysteretic load-drift responses plotted in Figure 4.31, the applied loads increased up to the peak and thereafter reduced sharply without showing plateau, which was distinct from the previous two specimens, SP1 and SP2. The reduction of the applied beam loads after the peak was more significant than that observed in SP1 and SP2. Another remarkable observation was that the pinching behavior was not observed up to the peak; thereafter, this behavior appeared due to the propagation of existing cracks in the joint panel instead of splitting cracks at the beam-joint interface, see Figure 4.31. Finally, the applied beam loads reached their peak at the fifth group of loading in both directions when the beam reinforcement barely yielded.

The column response of SP3 is shown in Figure 4.32. During testing, the column axial loads determined from Equation (3.2b) were applied. In SP3, the column compressive axial load varied from 5 kips (22 kN) to 161 kips (716 kN). The peak compressive column axial load corresponded to $0.14 f'_c A_g$. Note that the column axial load equations, i.e., Equations (3.2a) and (3.2b), intended that similar column axial loads were applied for SP1 and SP3 to investigate the effect of joint aspect ratio only. In practice, the peak compressive column axial load ratio in SP3

was greater than that in SP1, i.e., $0.14 f'_c A_g$ for SP3 and $0.11 f'_c A_g$ for SP1. This difference of column axial load between SP1 and SP3 was expected to be negligible in comparison of the results between them because the peak compressive column axial load ratios of both SP1 and SP3 ranged within $0.2 f'_c A_g$. Note that joint shear strengths were not affected by column axial load ratio within the range of less than $0.2 f'_c A_g$ [Park and Mosalam 2009]. Finally, the peak vertical displacements were 0.073 in. (3.00 mm) in elongation and 0.102 in. (2.72 mm) in contraction, Figure 4.32(b).

Table 4.7   Load versus drift response of SP3.

Group No.	SP3							
	EW direction				NS direction			
	Downward (-)		Upward (+)		Downward (-)		Upward (+)	
	Δ (%)	V_b (kip)	Δ (%)	V_b (kip)	Δ (%)	V_b (kip)	Δ (%)	V_b (kip)
1	-0.40	-18.4	-0.02	6.8	-0.40	-17.5	-0.02	7.8
2	-0.58	-24.7	0.19	14.8	-0.62	-24.4	0.20	15.5
3	-0.82	-29.8	0.41	20.4	-0.84	-29.2	0.41	20.6
4	-1.23	-38.2[*1]	0.85	30.1	-1.27	-34.6	0.85	29.1
5	-1.89	-40.4[*2]	1.49	37.8[*1*2]	-1.94	-35.8[*1*2]	1.43	33.1[*1*2]
6	-2.82	-36.1	2.45	36.5	-2.91	-27.4	2.44	31.4
7	-4.39	-25.7	3.90	31.7	-4.44	-18.0	3.90	24.5
8	-6.58	-15.1	6.08	18.2	-6.59	-9.5	6.06	14.7

[*1]first yielding of beam reinforcement
[*2]peak loading
Note: 1 kip = 4.45 kN
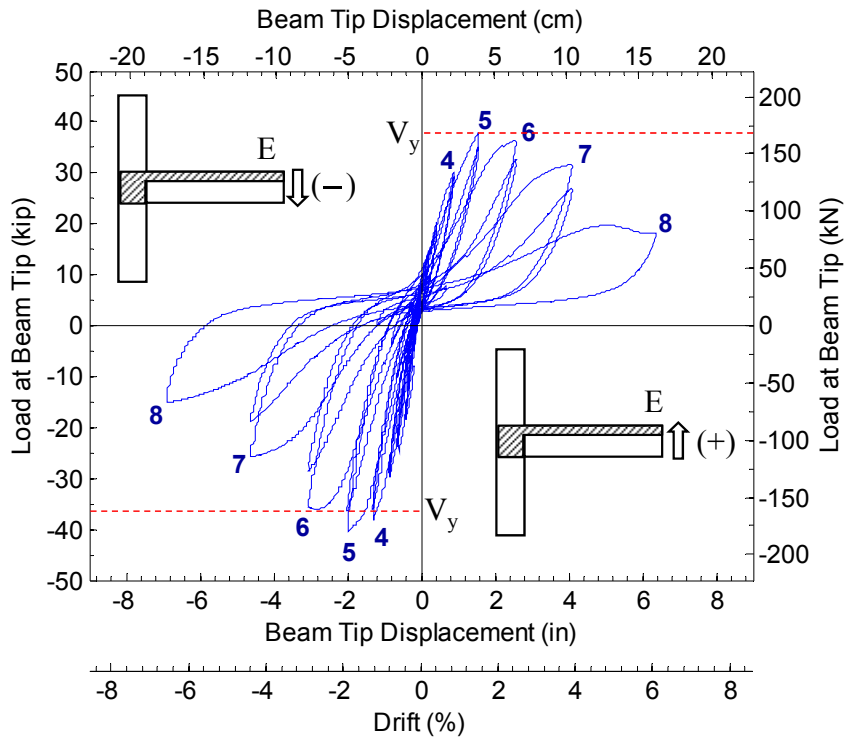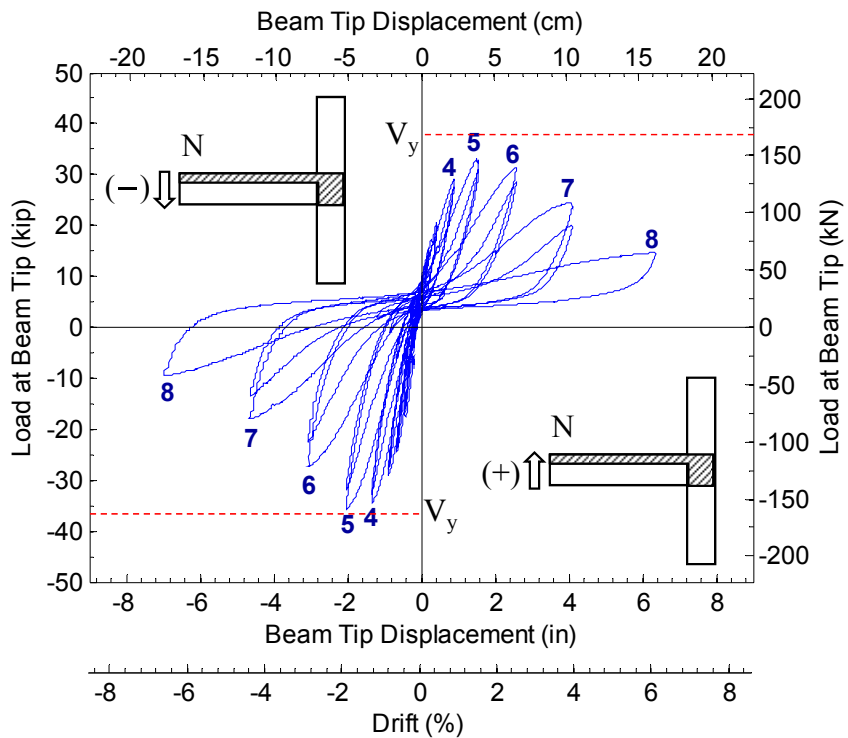
(a) EW direction

(b) NS direction

Figure 4.31   Load versus drift response of SP3.

100
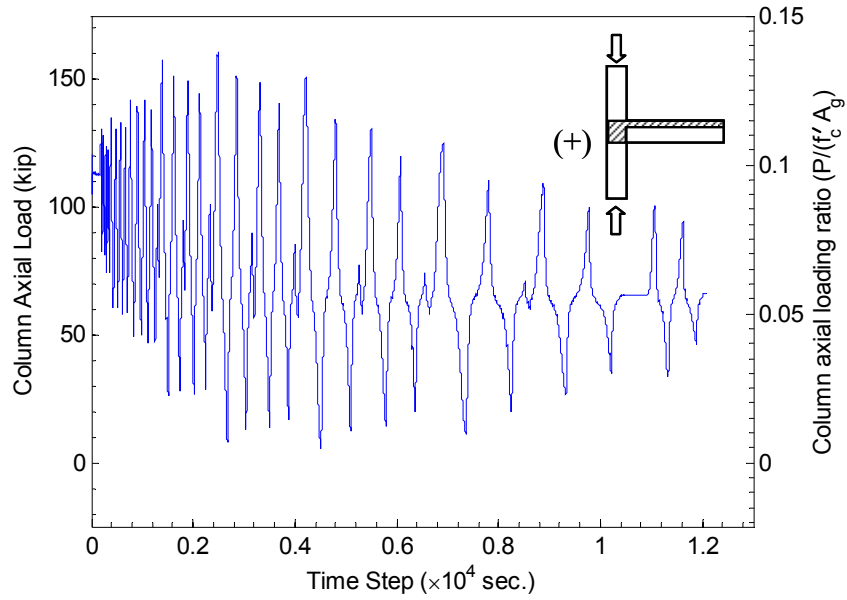
(a) column axial load
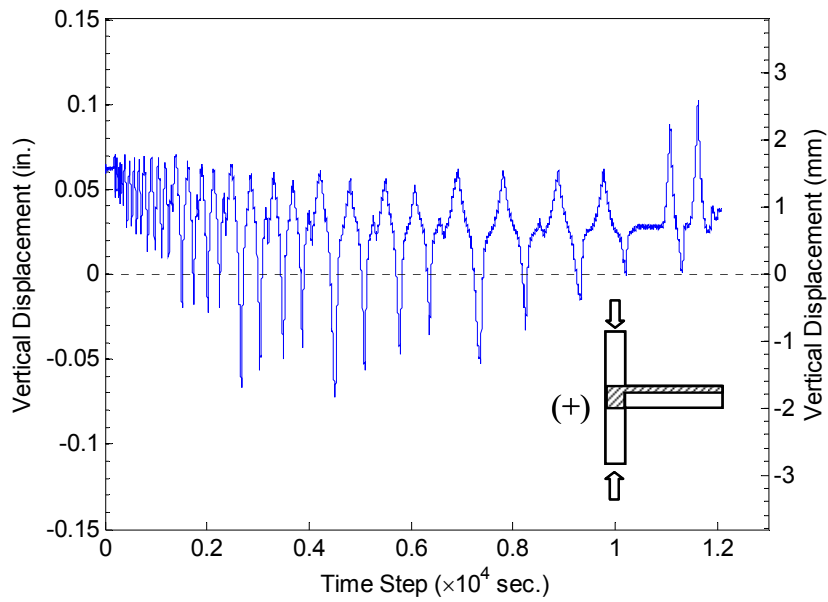
(b) vertical displacement

Figure 4.32   Column response of SP3.

4.3.2 Observed Damage Progression

The qualitative damage progression of SP3 is summarized in Table 4.8, and the photographs of the specimen taken during testing and at the end of the test are presented in Figures 4.33 through 4.35.

101

4.3.2.1 East-West Direction

JOINT REGION

Multiple diagonal joint cracks with steep angle were observed during the test. Due to inappropriate camera installation, the onset of the first joint crack in the EW direction was not captured. The first photographs of EW joint were taken at the fourth group of loading $\left(\Delta_{EW} = -1.23\%; \quad \Delta_{EW} = 0.85\%\right)$, showing two downward (↘) diagonal cracks and an upward (↗) diagonal crack in the joint, see Figure 4.33(a). Based on the extent of the downward diagonal cracks propagation, it is obvious that the first downward diagonal crack developed prior to the fourth group. The opening of existing diagonal cracks was significant at the peak loading, $\Delta_{EW} = -1.89\%$ and $\Delta_{EW} = 1.49\%$, see Figure 4.33(b). Beyond the peak loading, joint cover concrete spalled and reinforcing bars of beam and column were exposed. Crushing of joint core concrete was observed through the exposed reinforcing bars at the end of test [Figure 4.33(c)].

As observed in the EW joint panel, a horizontal crack appeared in the top of the NS joint panel during the fourth group of the EW beam upward loading, see Figure 4.19(b), and cover concrete in the joint panel spalled along this horizontal crack after the peak load. This horizontal crack was located at the same level as the top reinforcement of the NS beam.

During the NS beam upward loading, a horizontal crack was observed at the top of the EW joint panel as observed in specimens SP1 and SP2. In addition, a horizontal crack took place at the bottom of the joint panel during the NS beam downward loading. The location of the horizontal cracks at the top and bottom of the joint panel was close to the layer of beam top and bottom reinforcement, respectively. These horizontal cracks stopped at the middle of joint panel unlike those observed in SP1 and SP2. The crack pattern is shown in Figure 4.34(a).

BEAM AND SLAB

The first flexural crack initiated in the beam and slab during the first group of the EW beam loading down to $\Delta_{EW} = -0.40\%$. In the subsequent loading, additional flexural cracks developed in the beam and slab, accompanied by splitting cracks at the beam-joint and beam-slab interfaces. When the EW beam loading continued up to the fourth group, the existing cracks gradually grew wider. At the fifth group of loading, which was the peak of EW beam loading, the propagation of the splitting cracks at both beam-joint top interface and NS beam-slab interface was comparatively significant. The opening of the splitting cracks was confirmed by the instruments for rotation at the beam-joint interface. Beyond the peak load, flexural cracks retracted, while beam-joint interface was severely damaged by the splitting cracks. No plastic hinge occurred in the beam.

For the NS beam loading, multiple inclined cracks and splitting cracks occurred in the EW beam and beam-joint interface due to torsion [Figure 4.34(a)]. These cracks remained minor compared with those observed in SP1 and SP2, and they began to propagate after the peak of the NS beam loading. Figure 4.35 shows the existing cracks in the beam and slab after test.

4.3.2.2 North-South Direction

JOINT REGION

The observed crack pattern in the NS joint was similar to that shown in the EW joint. A first downward (↙) joint crack was observed during the second group of downward loading $(\Delta_{NS} = -0.62\%)$, while a first upward inclined crack (↖) appeared during the third group of upward loading ($\Delta_{NS} = 0.41\%$). Additional downward inclined cracks formed at the fourth group of loading. At the peak of NS beam loading, i.e., the fifth group of loading $(\Delta_{NS} = -1.94\% \quad \Delta_{NS} = 1.43\%)$, there was a big opening of two downward diagonal cracks. In the subsequent upward loading, however, the opening of the existing upward diagonal crack was noticeable although additional minor upward inclined cracks newly formed in the joint. After the peak load, joint cover concrete spalled and a wedge of corner concrete in the joint separated from the joint. Beam and column bars were exposed and crushing of the joint core concrete was observed. Figure 4.36 shows the progression of joint damages.

Under the EW beam loading, horizontal cracks developed at the top and bottom of the NS joint panel. The top horizontal crack continuously extended, while the bottom horizontal crack remained minor without further propagation. The top horizontal crack was close to the top reinforcement of the NS beam, Figure 4.34(b).

BEAM AND SLAB

A splitting crack was observed at the beam-joint interface during the pre-loading. Flexural cracks appeared in the beam and slab from the first loading group ($\Delta_{NS} = 0.40\%$), and more flexural cracks took place in the subsequent loading group. At the third group of downward loading $(\Delta_{NS} = -0.84\%)$, a splitting crack at the beam-slab interface developed. Flexural cracks and splitting cracks in the beam and slab slowly widened up to the peak load; thereafter, their propagation was not observed because total drift was mostly attributed to the joint damage. By the EW beam downward loading, inclined cracks were induced in the NS beam. These cracks remained minor and began to propagate after peak loading. Figure 4.35 shows the cracks that developed in the beam and slab during testing.

4.3.2.3 Summary

Based on the observation of NS joint only, the first joint cracks occurred at an average drift level of 0.5%. Until the fourth group of loading, the first developed diagonal crack for both downward and upward loadings propagated significantly. At the peak loading, i.e., the fifth group of loading ($\Delta = -1.92\%$; $\Delta = 1.46\%$), the second downward diagonal crack that developed propagated so that it had a similar width to the first diagonal crack, while the first upward diagonal crack propagated dominantly. Beyond the peak loading, the joint cover concrete spalled and core concrete crushed.

The damage of the beam and slab can be described as follows: the first flexural and splitting cracks developed during the first group of loading. Up to the fifth group of loading, additional flexural cracks occurred in the beam and slab and existing splitting cracks grew wider. Compared to SP1 and SP2, the flexural and splitting cracks of SP3 showed minor propagation up to peak loading since the peak loads were achieved right after beam reinforcement yielding.

After the peak loading, the flexural cracks retracted, while splitting cracks widened slightly further.

During the longitudinal beam loading, horizontal cracks and inclined cracks were observed in the transverse joint panel and beam, respectively. These two types of cracks remained minor until the EW and NS beam reached their peak loads. Therefore, the damage of the joint and beams induced by the orthogonal beam loading was not critical to be considered in the longitudinal responses. Figure 4.37 shows that the specimen was subjected to the severe damage in the joint region.

Table 4.8   Qualitative damage description of SP3.

Drift (%)	EW direction	NS direction
Δ_0 = -0.2	-	- Splitting crack at beam-joint interface
Δ_{up} = -0.02 Δ_{down} = -0.40	- First flexural crack in beam and slab	- First flexural crack in beam and slab
Δ_{up} = 0.20 Δ_{down} = -0.60	- Additional flexural cracks in beam and slab - Splitting crack at beam-slab interface	- First downward diagonal crack in joint - Additional flexural cracks in beam and slab
Δ_{up} = 0.41 Δ_{down} = -0.83	-	- First upward diagonal crack in joint - Splitting crack at beam-slab interface
Δ_{up} = 0.85 Δ_{down} = -1.25	- Two downward diagonal cracks in joint - Upward inclined crack in joint - Splitting crack at beam-joint interface - First yielding of beam top bars	- Additional downward diagonal cracks in joint - First upward diagonal cracks in joint
Δ_{up} = 1.46 Δ_{down} = -1.92	- Large opening of downward and upward diagonal cracks - First yielding of beam bottom bars	- Additional upward inclined cracks in joint - Large opening of an upward diagonal crack - First yielding of beam top bars - First yielding of beam bottom bars
Δ_{up} = 2.45 Δ_{down} = -2.87	- Spalling of joint cover concrete	- Spalling of joint cover concrete
Δ_{up} = 3.90 Δ_{down} = -4.42	- Crushing of joint core concrete - Reduction of beam flexural cracks width	- Crushing of joint core concrete - Reduction of beam flexural cracks width
Δ_{up} = 6.07 Δ_{down} = -6.59	- Straightening of beam bars anchorage tail	-
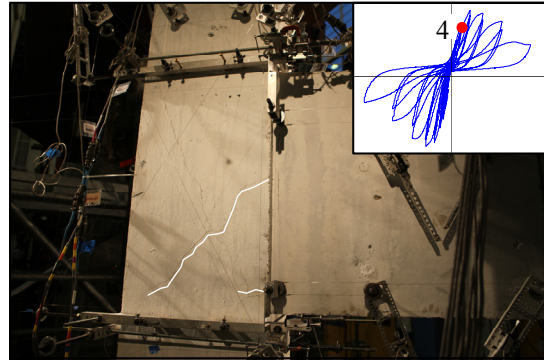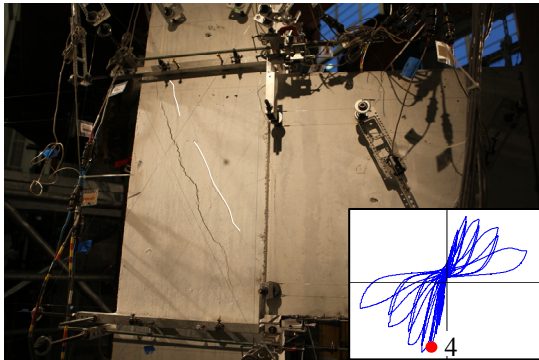
(a) propagation of joint cracking
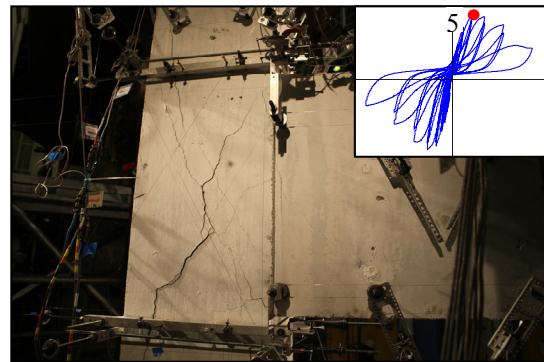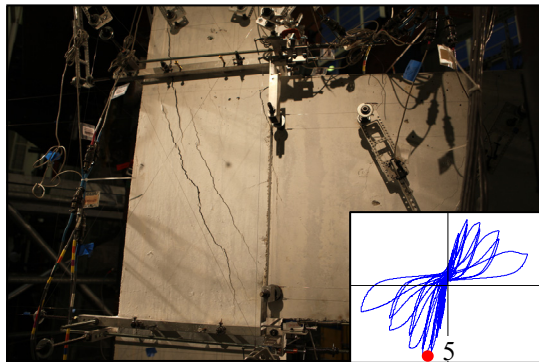
(b) joint cracking before joint failure
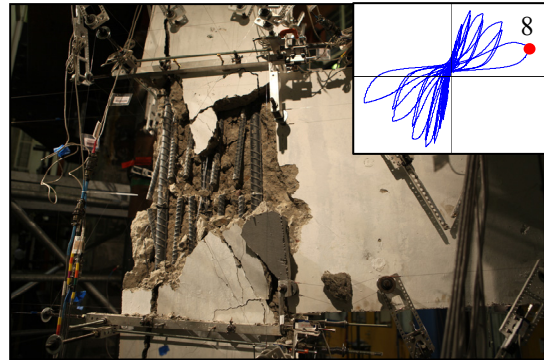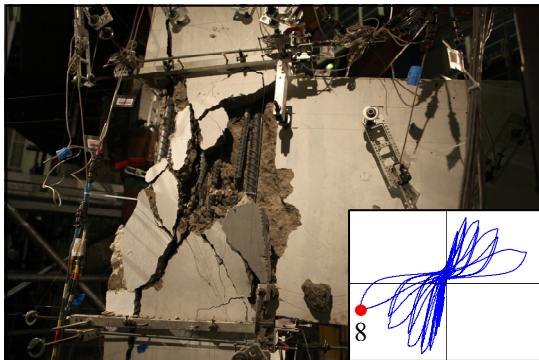
(c) joint damage at end of test

Figure 4.33   Damage progression of joint in EW direction, SP3.
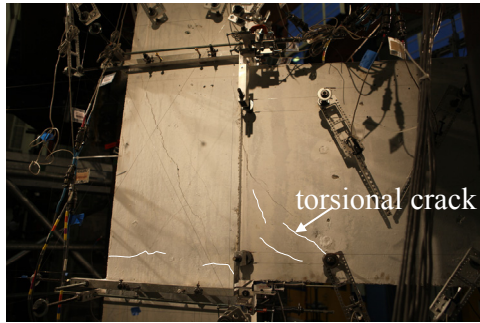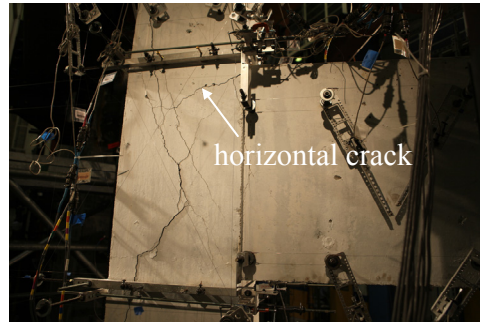
Δ_{NS} = -1.27% Δ_{NS} = 1.43%

(a) crack pattern in EW joint and beam by NS beam loading
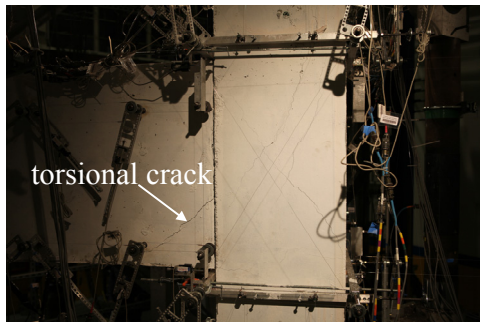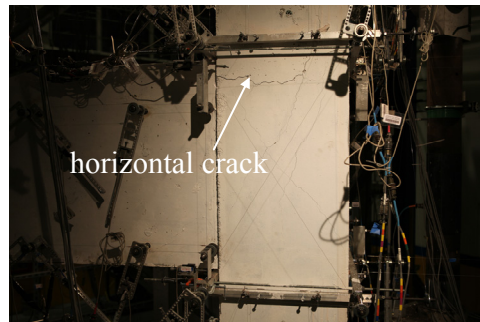
Δ_{EW} = -1.89% Δ_{EW} = 1.49%

(b) horizontal cracks in NS joint and beam by EW beam loading

Figure 4.34   Crack pattern for the orthogonal beam loading, SP3.

(a) cracks in EW beam   **(b) cracks in NS beam**

(c) cracks on slab

Figure 4.35   Existing cracks after testing, SP3.
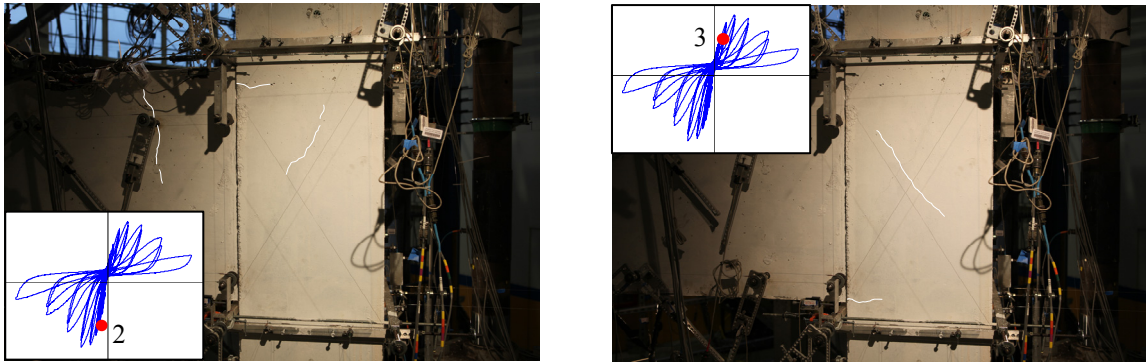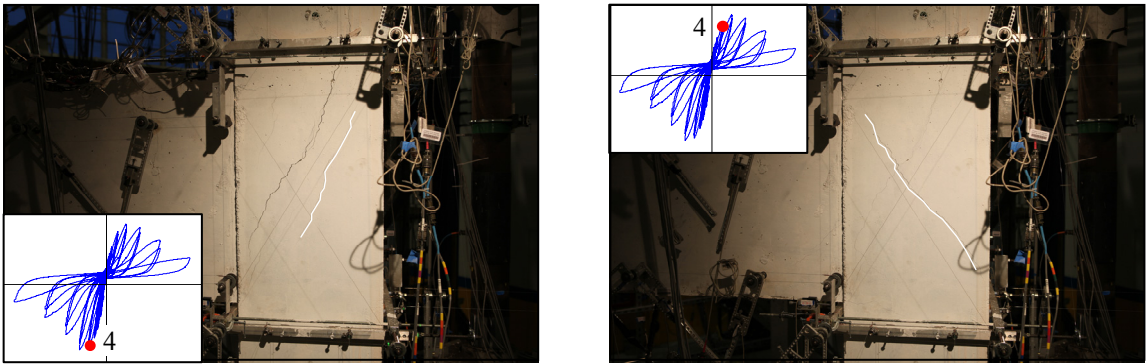
106

(a) first joint crack

(b) propagation of joint cracking
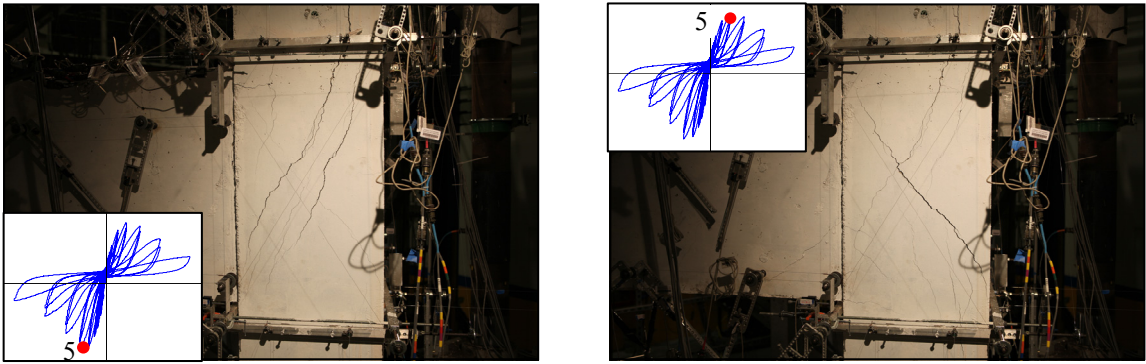
(c) joint cracking before joint failure
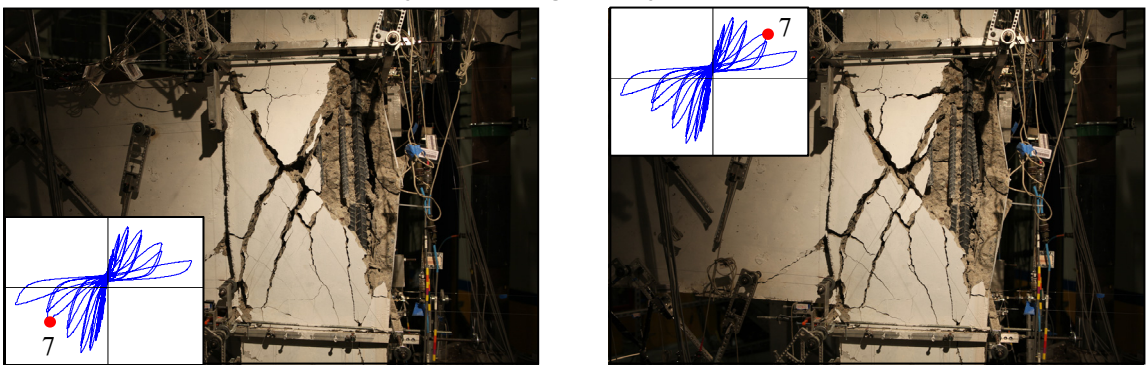
(d) joint damage at end of test

Figure 4.36   Damage progression of joint in NS direction, SP3.

(a) global view of specimen

(b) inside corner joint

(c) NS beam

(d) EW beam
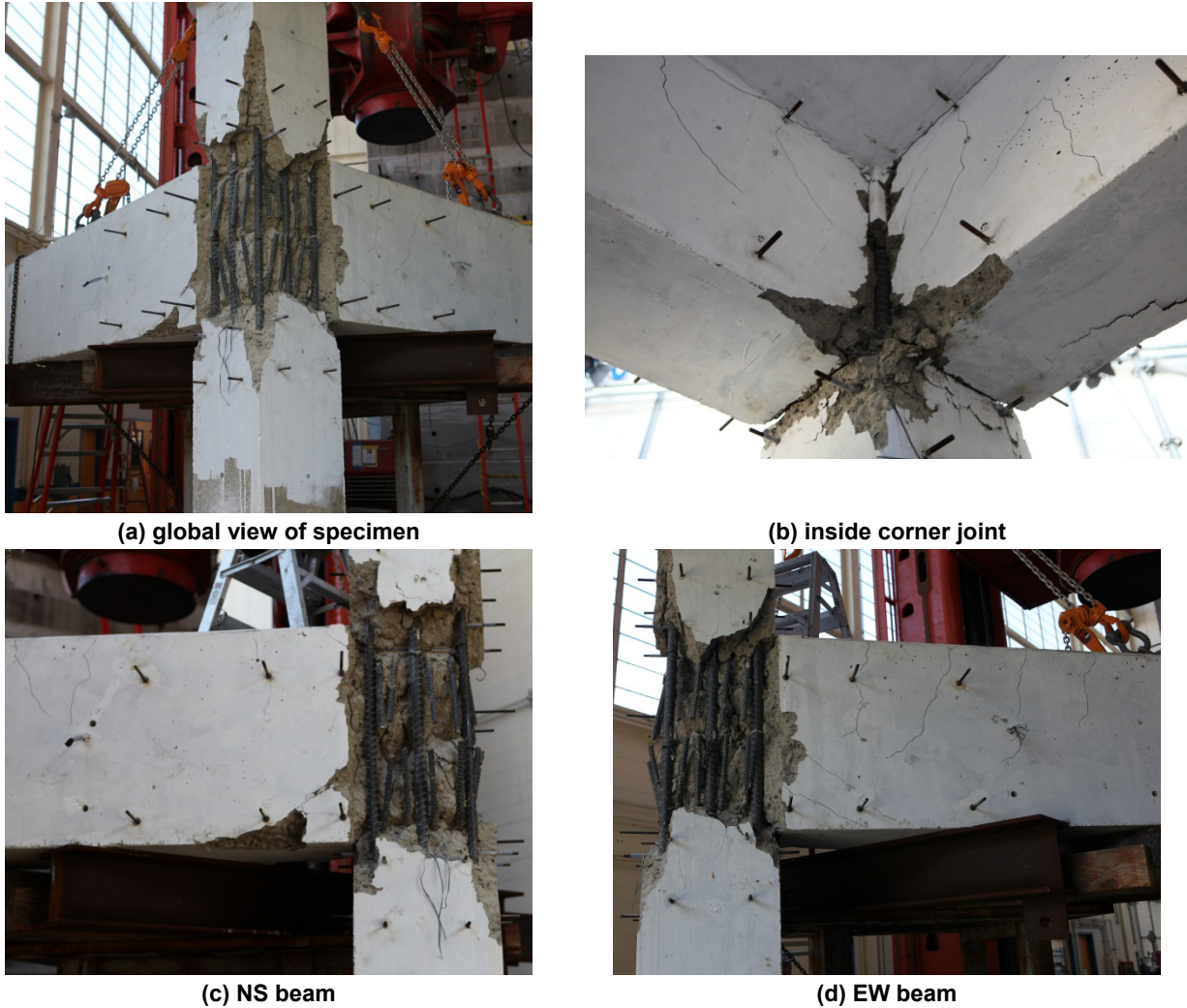
Figure 4.37   Failure of SP3 after removing concrete fragments.

4.3.3 Joint Shear Stress versus Rotation Response

The hysteretic responses of joint shear stress versus strain up to the sixth group of loading are presented in Table 4.9 and Figure 4.38. For the calculation of joint shear stress, 0.9 times the beam effective depths were assumed as constant moment arms. To estimate the effective depth for the downward loading, slab top four reinforcing bars were considered. The maximum joint shear stresses in the EW direction were 429 psi (2.96 MPa) for the downward loading and 379 psi (2.62 MPa) for the upward loading; the corresponding values of $\gamma = v_{jh} \big/ \sqrt{f_c'}$ were 7.2 psi$^{0.5}$ (0.60 MPa$^{0.5}$) and 6.3 psi$^{0.5}$ (0.52 MPa$^{0.5}$), respectively. In the NS direction, the maximum joint shear stresses were 375 psi (2.59 MPa) for the downward loading and 351 psi (2.42 MPa) for the upward loading; the corresponding values of $\gamma = v_{jh} \big/ \sqrt{f_c'}$ were 6.3 psi$^{0.5}$ (0.52 MPa$^{0.5}$) and 5.9 psi$^{0.5}$ (0.49 MPa$^{0.5}$), respectively. In SP3, the average value of the maximum joint shear stresses was close to the shear strength by the ASCE 41 as indicated by dashed lines in Figure 4.38. Note that the maximum joint shear stresses of SP3 were less than those of SP1. Recalling that both SP1 and SP3 had the same longitudinal reinforcement at the top and bottom of the beams, the strength reduction in SP3 can be explained by the effect of joint aspect ratio.

108

The joint shear strains at the peak load were 0.0060 rad. for the downward loading and 0.0073 rads for the upward loading in the EW beam. In the NS direction, they were 0.0091 rads for the downward and 0.0087 rads for the upward loading. The joint shear strain responses were more symmetric in both directions compared with the responses of SP1 and SP2. Joint shear strains gradually increased up to the peak and rapidly increased after the peak loading because joint cracks were widely opening. The rotations at the beam-joint interface are plotted in Figure 4.39. The rotations at the beam-joint interface in SP3 were less than those measured in SP1 and SP2. Combining the joint shear strain and rotation at the beam-joint interface, total joint rotations at the peak loading were 0.011 rad. for both downward and upward loadings in the EW direction; 0.013 rad. for the downward loading and 0.012 rad. for the upward loading in the NS direction, refer to Figure 4.40.

According to Table 4.9, the contribution of joint rotation to total drift was between 60% and 75% at the peak loading. Note that the joint rotation had more contribution to the total drift in SP3 compared with SP1 and SP2 results, because beam flexural deformation had smaller contribution in SP3.

Table 4.9   Joint response of SP3.

Dir.	EW											
Group No.	**Downward**						**Upward**					
	v_{jh} (psi)	γ (psi$^{0.5}$)	Δ (rad)	γ_{xy} (rad)	θ_j (rad)	θ_j/Δ	v_{jh} (psi)	γ (psi$^{0.5}$)	Δ (rad)	γ_{xy} (rad)	θ_j (rad)	θ_j/Δ
1	195	3.2	0.0040	-	-	-	68	1.1	0.00	-	-	-
2	262	4.4	0.0058	0.0011	0.0024	0.41	148	2.5	0.0019	0.00	0.0010	0.53
3	317	5.3	0.0082	0.0018	0.0035	0.43	205	3.4	0.0041	0.0004	0.0020	0.49
4	406[*1]	6.8	0.0123	0.0035	0.0061	0.50	302	5.0	0.0085	0.0023	0.0052	0.61
5	429[*2]	7.2	0.0189	0.0060	0.011	0.58	379[*1*2]	6.3	0.0149	0.0073	0.011	0.74
6	383	6.4	0.0282	0.010	0.016	0.57	366	6.1	0.0245	0.021	0.027	>1.0
7	273	4.5	0.0439	0.029	0.039	0.89	318	5.3	0.0390	0.032	0.042	>1.0
8	160	2.7	0.0658	-	-	-	183	3.0	0.0608	-	-	-

Dir.	NS											
Group No.	**Downward**						**Upward**					
	v_{jh} (psi)	γ (psi$^{0.5}$)	Δ (rad)	γ_{xy} (rad)	θ_j (rad)	θ_j/Δ	v_{jh} (psi)	γ (psi$^{0.5}$)	Δ (rad)	γ_{xy} (rad)	θ_j (rad)	θ_j/Δ
1	183	3.1	0.0040	-	-	-	83	1.4	0.00	-	-	-
2	256	4.3	0.0062	0.0005	0.0019	0.31	164	2.7	0.0020	0.0002	0.0005	0.25
3	306	5.1	0.0084	0.0014	0.0031	0.37	219	3.6	0.0041	0.0008	0.0015	0.37
4	363	6.0	0.0127	0.0038	0.0064	0.50	309	5.1	0.0085	0.0032	0.0047	0.55
5	375[*1*2]	6.3	0.0194	0.0090	0.013	0.67	351[*1*2]	5.9	0.0143	0.0091	0.012	0.84
6	287	4.8	0.0291	0.019	0.025	0.86	333	5.6	0.0244	0.022	0.024	0.98
7	189	3.1	0.0444	0.025	0.036	0.81	260	4.3	0.0390	0.045	0.046	>1.0
8	99	1.7	0.0659	-	-	-	156	2.6	0.0606	-	-	-

[*1]first yielding of beam reinforcement
[*2]peak loading

Note: 1 psi = 0.0069 MPa; $1.0\sqrt{f_c'}$ psi$^{0.5}$ = $0.083\sqrt{f_c'}$ MPa$^{0.5}$
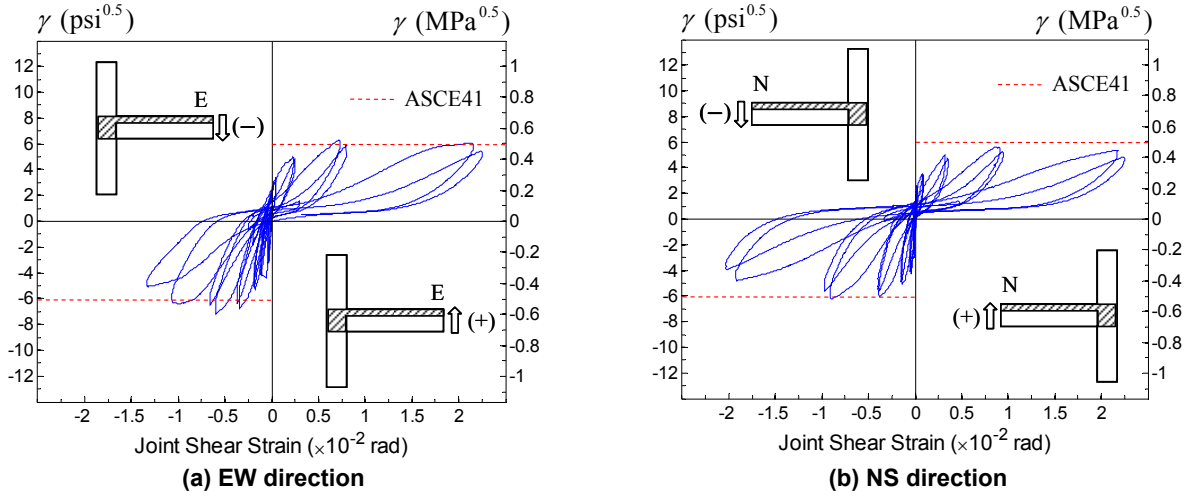
Figure 4.38   Joint shear stress versus strain response of SP3.
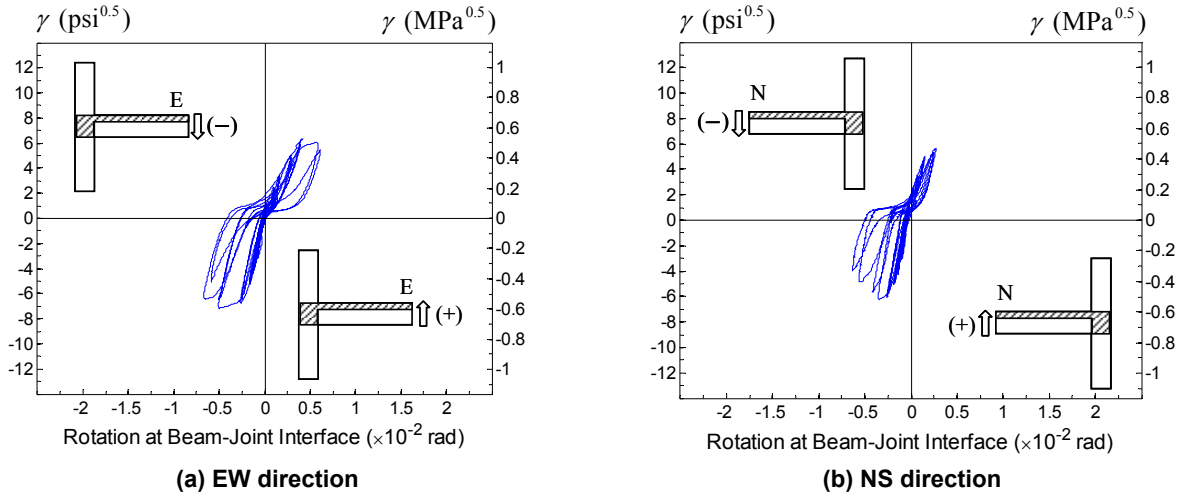
Figure 4.39   Joint shear stress versus rotation at beam-joint interface of SP3.
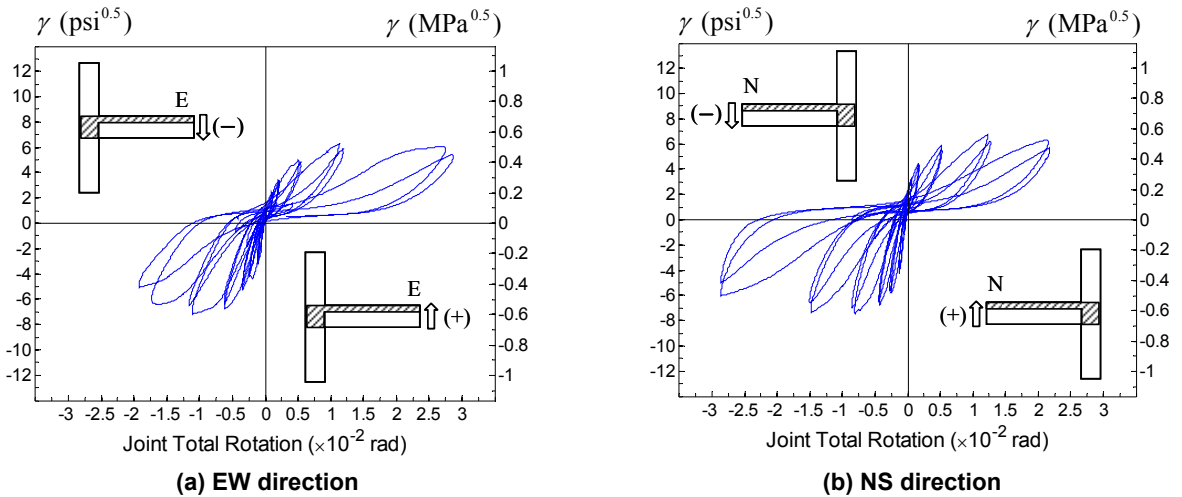
Figure 4.40   Joint shear stress versus total rotation of SP3.

4.3.4 Strain Measurement

4.3.4.1 Beam Reinforcement

The strain gage measurements of the EW and NS beam longitudinal bars are shown in Figures 4.41 and 4.42. The labeled drift levels correspond to the loading from the third group through the sixth group. It is noted that the drift levels applied in SP3 were different from those applied in SP1 and SP2. For example, the drift at the third loading group in SP3 was close to 0.88% but it was close to 1.18% in SP1 and SP2.

The first yielding of the EW beam top longitudinal bars was observed between the drift level of $\Delta = -0.82\%$ and $\Delta = -1.23\%$, i.e., the third and fourth loading group, and the EW beam bottom longitudinal bars yielded between the drift level of $\Delta = 0.85\%$ and $\Delta = 1.49\%$, i.e., the fourth and fifth loading group. The strains of the EW beam longitudinal bars increased even after the peak loads, possibly a result of the change of neutral axis in the beam cross section.

The NS beam top internal bar only yielded between the drift level of $\Delta = -1.27\%$ and $\Delta = -1.94\%$, and the NS beam bottom bars yielded between the drift level of $\Delta = 0.85\%$ and $\Delta = 1.43\%$, i.e., the fourth and fifth loading group. The strains of the NS beam longitudinal bars did not increase after yielding because it occurred at the peak of both downward and upward loading.

4.3.4.2 Slab Reinforcement

The strain gage measurements of the slab reinforcing bars in the EW and NS directions are presented in Figure 4.43, showing that the strain values measured in SP3 are less than those measured in specimens SP1 and SP2. The first yielding of slab top reinforcement in both directions occurred when the beam top longitudinal bars yielded, i.e., between the drift level of $\Delta = -0.82\%$ and $\Delta = -1.23\%$ in the EW direction and between the drift level of $\Delta = -1.27\%$ and $\Delta = -1.94\%$ in the NS direction, see Figure 4.43. Top two and one bottom reinforcing bars in the EW slab yielded at the peak load which corresponded to drift 1.89%, while only one top reinforcing bar yielded in the NS slab at the peak load, corresponding to drift 1.94%.

4.3.4.3 Column Reinforcement

The strain gage measurements of the column longitudinal bars are presented in Figures 4.44 and 4.45. For SP3 and SP4, column longitudinal reinforcement was designed with bar size of #10 (D32) to maintain the strong column/weak beam approach. The measured strains of all the column reinforcing bars were below the yield strain, i.e., 0.0023, up to the end of test, even though some damage was observed in the column. The strain distribution of the column intermediate reinforcing bars was measured over the height of the joint region. The tensile strains at the mid-height were less than the strains at either top or bottom in the EW joint, although greater than the strains at both of top and bottom in the NS joint. These results are insufficient to support the idea that the column intermediate reinforcing bar acted as a tension tie in the joint panel.

Note: 1" = 25.4 mm

(a) EW-Top-Ext.

(b) EW-Top-Int.

(c) EW-Bottom-Ext.

(d) EW-Bottom-Int.
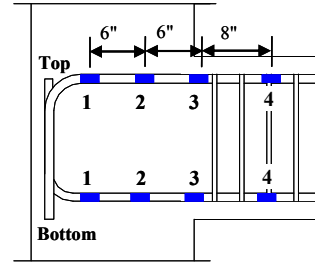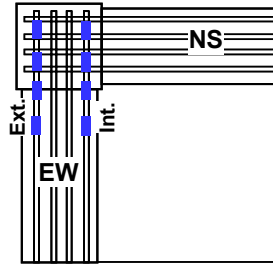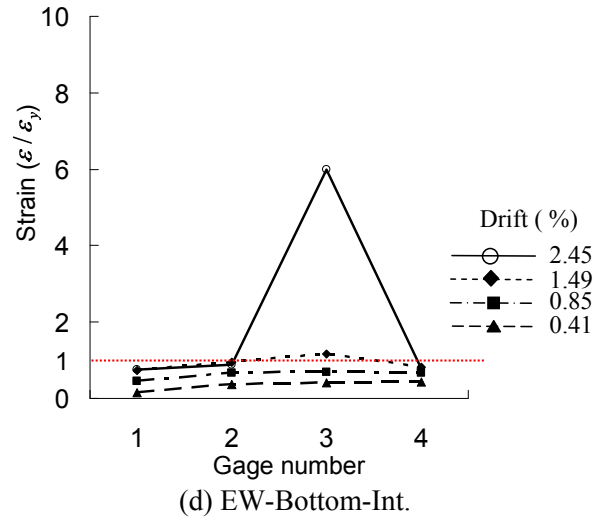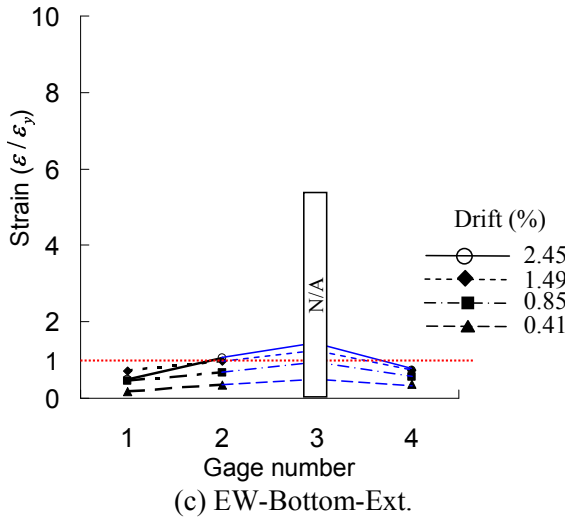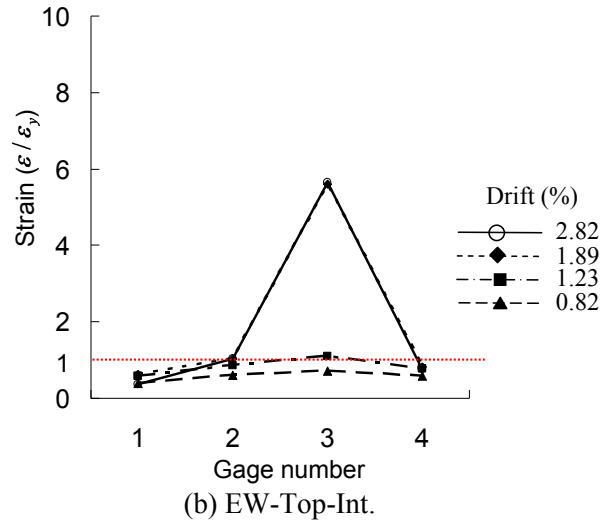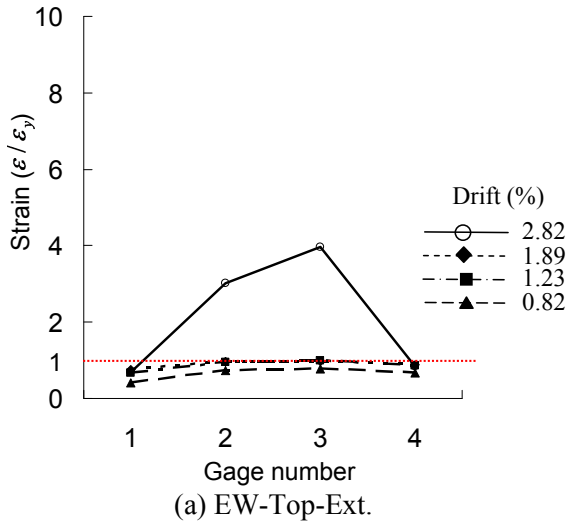
Figure 4.41   Strains of the EW beam reinforcing bars of SP3.

Note: 1" = 25.4 mm

(a) NS-Top-Ext.

(b) NS-Top-Int.

(c) NS-Bottom-Ext.

(d) NS-Bottom-Int.
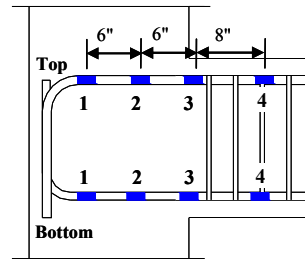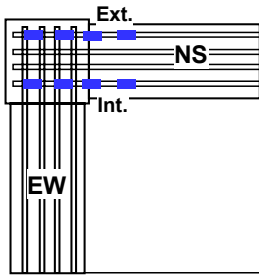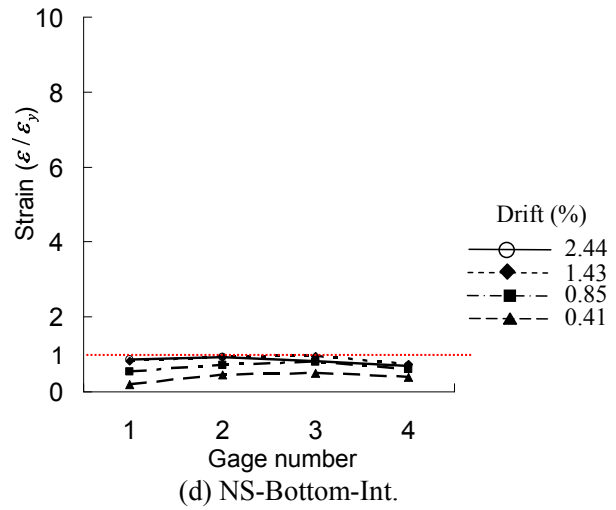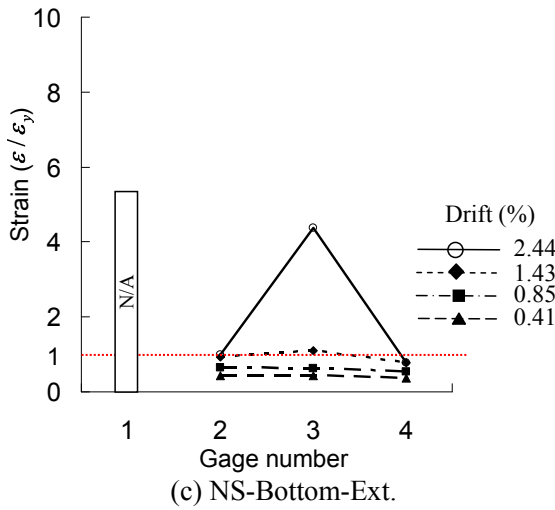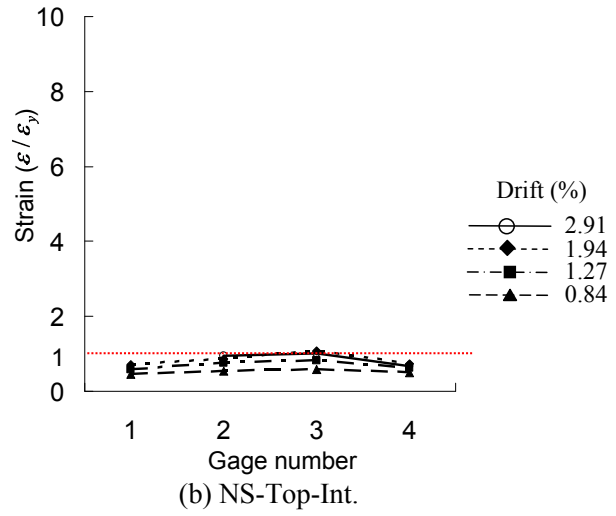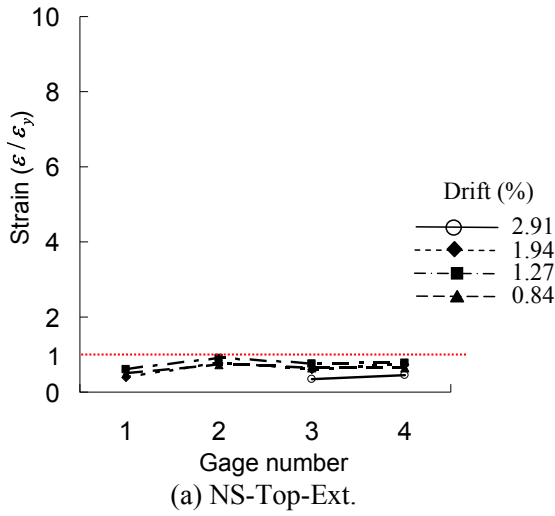
Figure 4.42   Strains of the NS beam reinforcing bars of SP3.
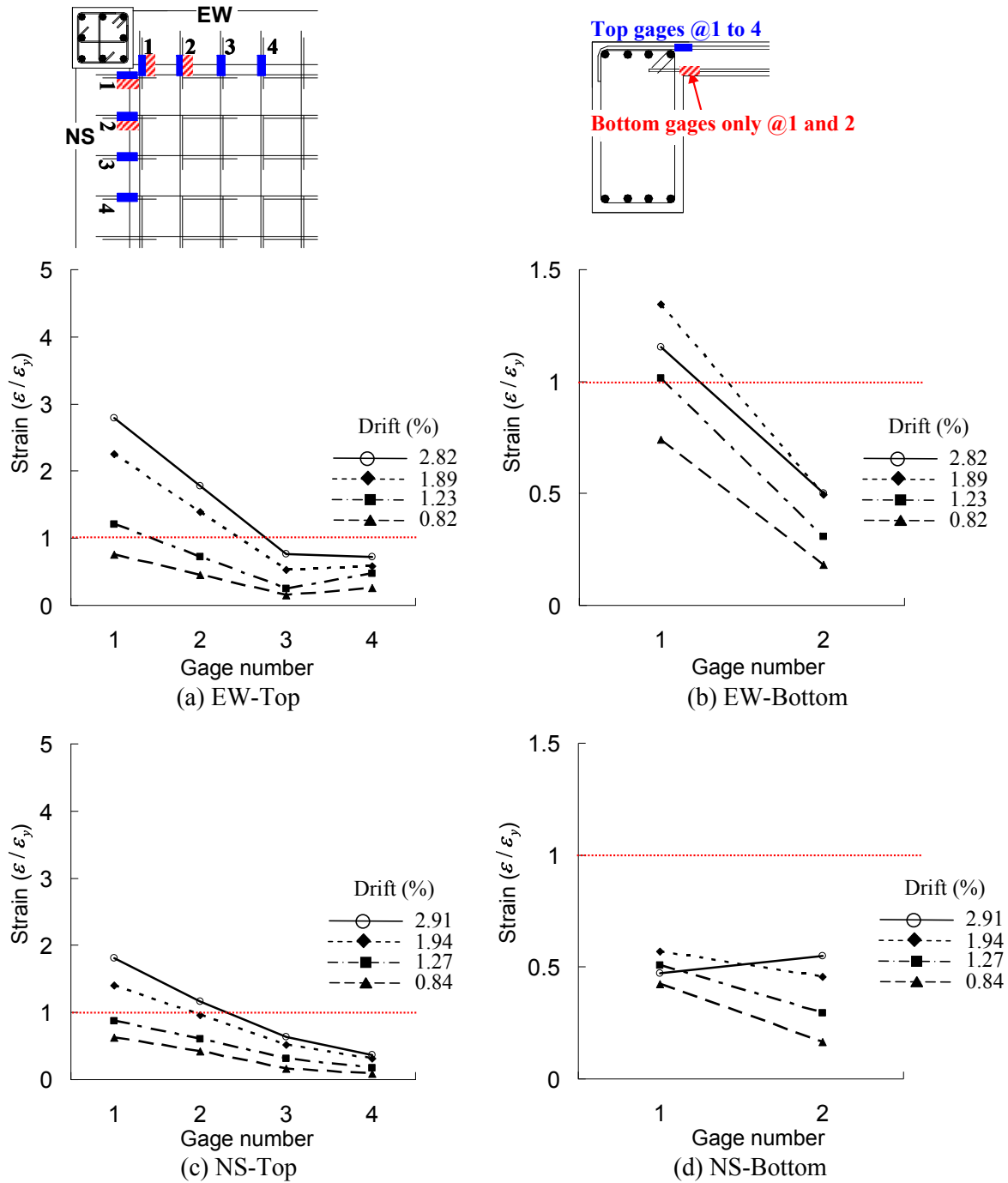
Figure 4.43   Strains of the slab reinforcing bars of SP3.
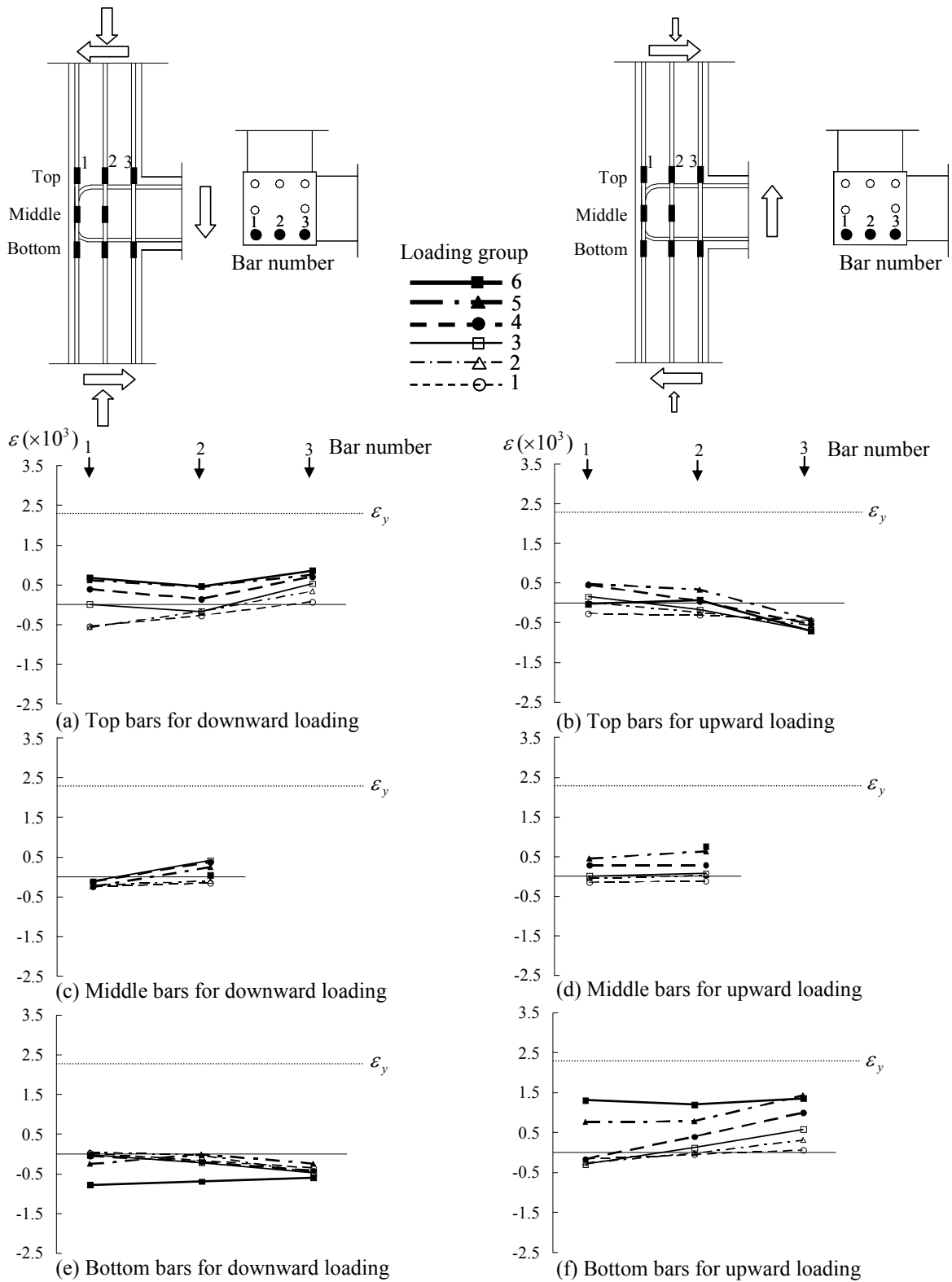
Figure 4.44   Strains of the column reinforcing bars for the EW beam loading, SP3.

116
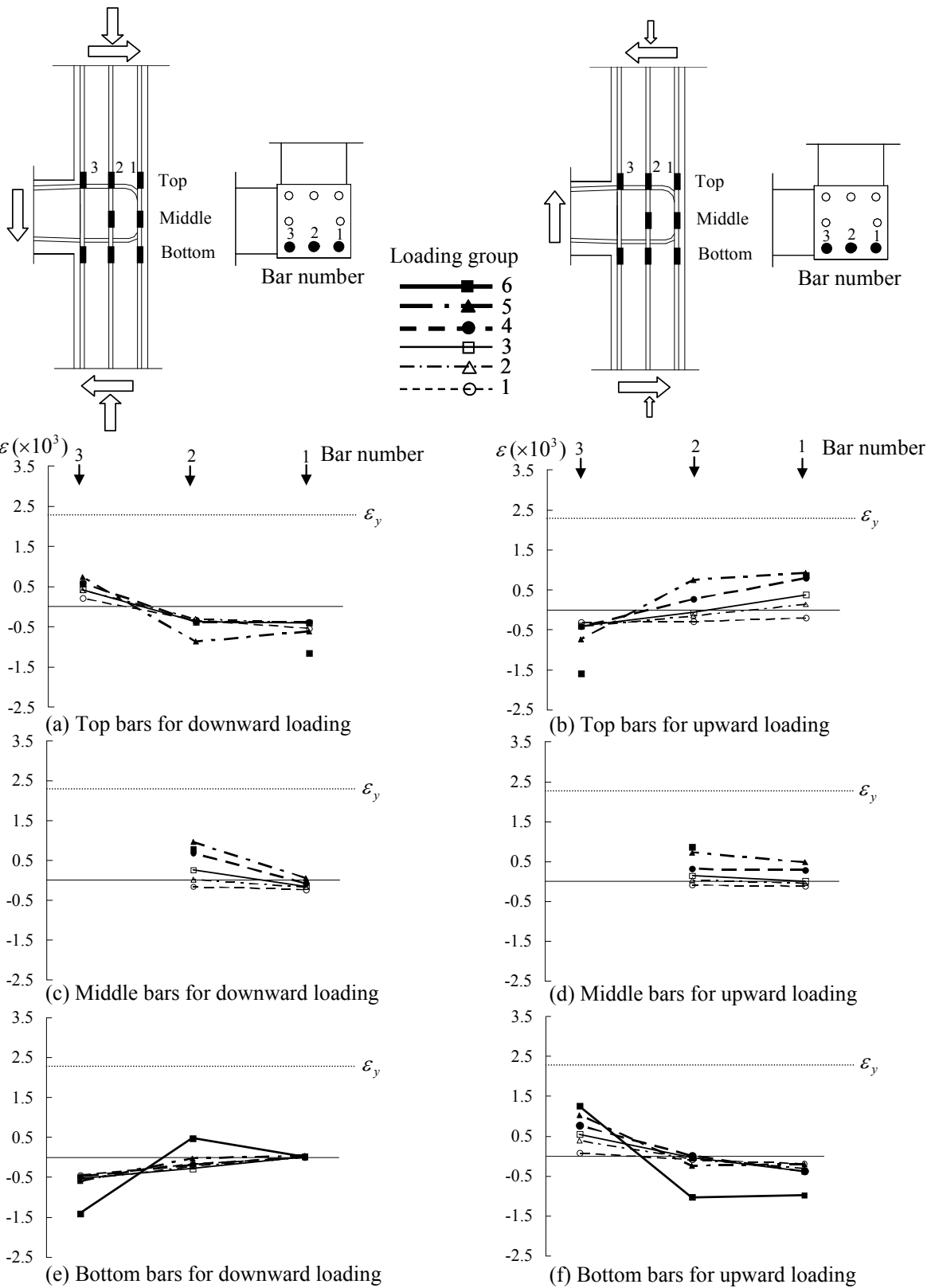
Figure 4.45 Strains of the column reinforcing bars for the NS beam loading, SP3.

117

4.4 SPECIMEN SP4

4.4.1 Load versus Drift Response

The hysteretic applied load versus drift responses of SP4 in the EW and NS directions are shown in Figure 4.46, and their values at the peak of each cyclic loading group are given in Table 4.10. Theoretical beam shear force V_y corresponding to the beam yield strength (ignoring the slab contribution) is shown as horizontal dashed lines in Figure 4.46. The hysteretic load-drift responses showed that both EW and NS beams remained elastic up to the peak loading. The elastic responses were confirmed by the strains of the EW and NS beam longitudinal bars presented in Section 4.4.4. Therefore, the failure of SP4 was designated as joint failure without beam reinforcement yielding (J-type failure); the shear strength of this specimen could serve as a representative upper limit for the joint aspect ratio (h_b/h_c) of 1.67.

The peak loads of EW beam loading were achieved at the fifth loading group, $\left(\Delta_{EW} = -1.94\% \text{ and } \Delta_{EW} = 1.52\%\right)$. The applied loads corresponded to -49.4 kips (-219.8 kN) for the downward loading and 45.6 kips (202.8 kN) for the upward loading. For the NS beam, the peak of the downward loading occurred at the fourth group $\left(\Delta_{NS} = -1.29\%\right)$. The applied load was -43.8 kips (-194.8 kN); for the upward loading. The peak occurred at the fifth loading group, $\left(\Delta_{NS} = 1.53\%\right)$, and the applied load was 39.2 kips (174.4 kN). Note that the one bottom reinforcement slightly yielded at the peak of upward loading of both EW and NS beams, and its strain hysteretic responses remained elastic. The applied beam loads in the EW beam reduced sharply after the peak loads, while the peak load in the NS beam for the downward loading was maintained with 0.2 kips (0.9 kN) reduction during the subsequent loading group, i.e., the fifth loading group.

Based on the hysteretic responses, it was postulated that the specimen began to lose its load-carrying capacity in both directions during the fifth group. A comparison of hysteretic responses between SP3 and SP4 showed that the peak loads were achieved at similar drift levels even though the peak loads were larger in SP4. The applied beam loads reduced significantly after the peak, and the reduction was more significant than that observed in SP1 and SP2 (see Section 4.3.1). Similar to SP3, the pinching behavior of SP4 began to appear after the peak loading due to the propagation of existing cracks in the joint panel, see Figure 4.46.

Figure 4.47 shows the column response of SP4. The column axial loads were controlled to follow Equation (3.2b). As a result, the column compressive axial load varied from 2 kips (9 kN) to 187 kips (832 kN). These column axial loads corresponded to the column axial load ratio of 0.2% and 14.6%, respectively. Note that the column axial load equations, i.e., Equations (3.2a) and (3.2b), intended that similar column axial loads were applied for SP2 and SP4. However, the maximum column axial load ratio of SP4 was less than that of SP1, i.e., $0.15 f_c' A_g$ for SP3 and $0.23 f_c' A_g$ for SP2, and no tension was applied to the column in SP4. Why there were less column axial loads in SP4 was because the failure of SP4 occurred before beam reinforcement yielding, while SP2 experienced joint failure after beam reinforcement yielding. Nevertheless, the effect of less column axial loads on the results of SP4 was expected to be negligible in comparison with the results SP2 because the column axial load ratios did not vary beyond the value of $0.2 f_c' A_g$, as discussed in Park and Mosalam [2009]. Finally, the peak

vertical displacements were 0.084 in. (2.13 mm) in elongation and 0.118 in. (3.00 mm) in contraction, Figure 4.47(b).

Table 4.10   Load versus drift response of SP4.

Group No.	SP4							
	EW direction				NS direction			
	Downward (-)		Upward (+)		Downward (-)		Upward (+)	
	Δ (%)	V_b (kip)	Δ (%)	V_b (kip)	Δ (%)	V_b (kip)	Δ (%)	V_b (kip)
1	-0.41	-24.5	-0.01	9.5	-0.41	-25.2	-0.02	8.9
2	-0.62	-32.2	0.21	20.3	-0.63	-34.3	0.20	19.3
3	-0.85	-38.9	0.42	27.1	-0.84	-39.8	0.43	26.2
4	-1.28	-45.9	0.86	37.6	-1.29	-43.8[*2]	0.86	34.3
5	-1.94	-49.4[*2]	1.52	45.6[*1*2]	-1.96	-43.6	1.53	39.2[*1*2]
6	-2.96	-43.0	2.51	43.0	-2.98	-35.5	2.52	37.1
7	-4.46	-31.6	4.01	37.9	-4.49	-24.3	4.00	28.9
8	-6.58	-20.4	6.23	23.7	-6.79	-9.5	6.20	17.2

[*1]first yielding of beam reinforcement
[*2]peak loading
Note: 1 kip = 4.45 kN

(a) EW direction

(b) NS direction
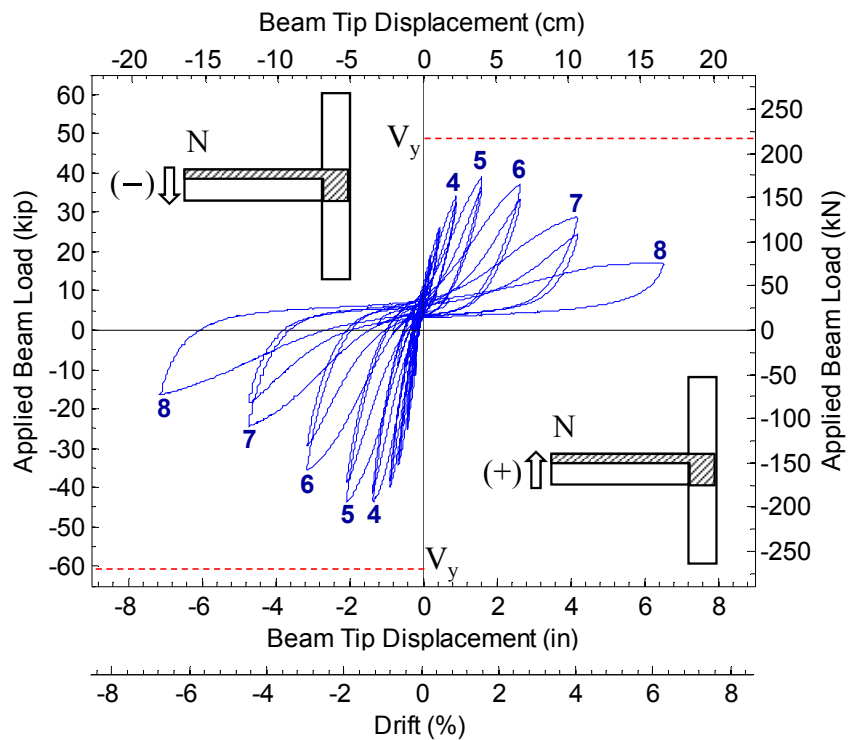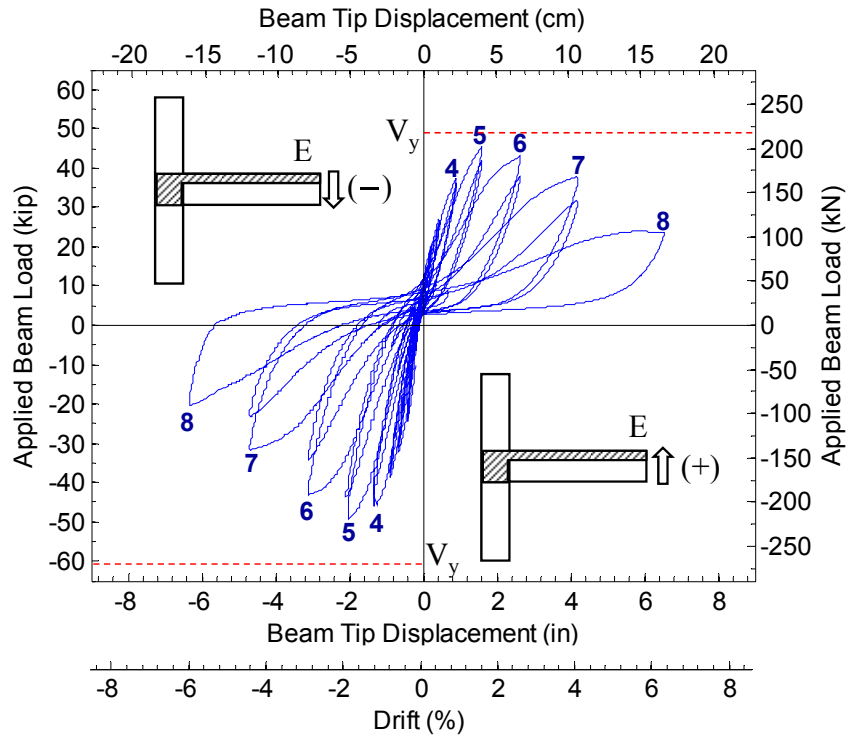
Figure 4.46   Load versus drift response of SP4.

120
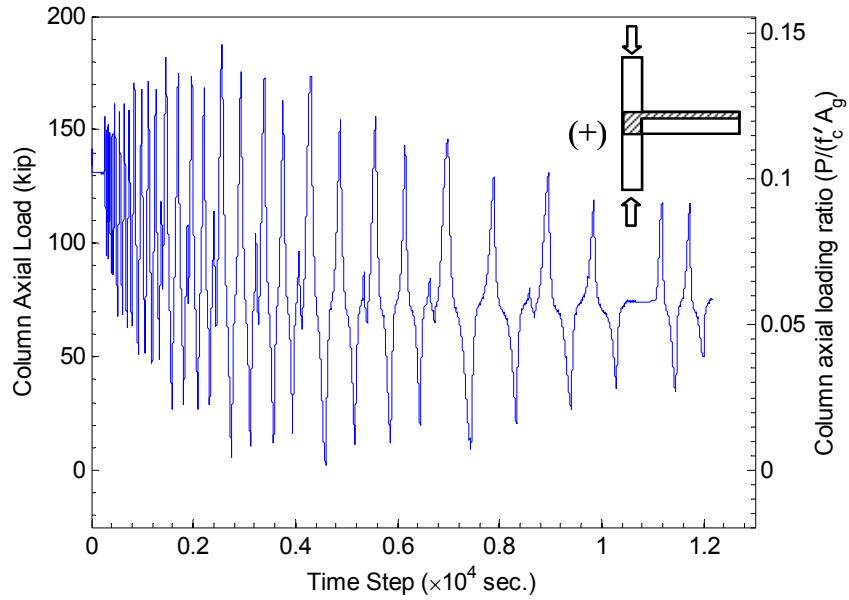
(a) column axial load
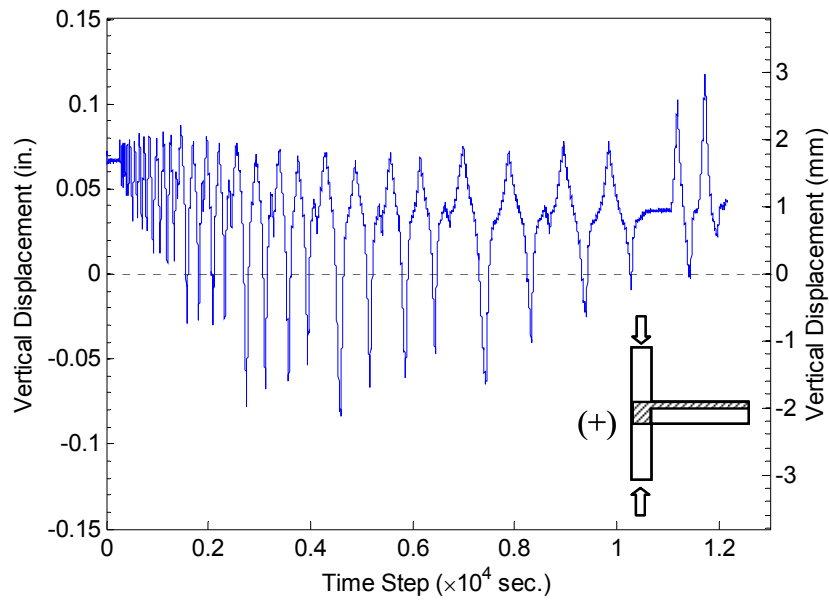
(b) vertical displacement

Figure 4.47   Column response of SP4.

4.4.2 Observed Damage Progression

The qualitative damage progression of SP4 is summarized in Table 4.11, and the photographs of the specimen taken during testing and at the end of the test are presented in Figures 4.48 through 4.52.

4.4.2.1 East-West Direction

JOINT REGION

Multiple diagonal joint cracks developed, leading to joint failure during the test. A first downward joint diagonal crack (↘) was observed at the first loading group $\left(\Delta_{EW} = -0.41\%\right)$, and additional downward cracks appeared in the subsequent loading group. A first upward diagonal crack (↗) initiated during the third loading group $\left(\Delta_{EW} = 0.42\%\right)$; thereafter additional upward cracks developed. Noticeable opening of the first developed downward diagonal crack was observed at the fourth loading group ($\Delta_{EW} = -1.28\%$), and, subsequently, other downward cracks widened showing similar propagation of the main diagonal crack at the peak loading ($\Delta_{EW} = -1.94\%$).

The first upward diagonal crack exclusively widened up to the peak loading ($\Delta_{EW} = 1.52\%$), although additional minor upward cracks formed in the joint panel. Note that the propagation pattern and width of the diagonal cracks were remarkably similar to those observed in SP3, see to Figure 4.33(a) and (b) and Figure 4.48(b) and (c). After the peak loading, the joint experienced severe damage by widening of the diagonal cracks, and the cover concrete spalled in the joint panel. A wedge of corner concrete in the joint detached, and joint core concrete was crushed. Figure 4.48 presents the progression of joint damage as the applied drift increased.

During the NS beam upward loading, a horizontal crack formed at the top of EW joint panel as observed in the other three specimens, see Figure 4.49(a). The top horizontal crack was closely located at the layer of beam top reinforcement.

BEAM AND SLAB

The first flexural crack initiated in the beam and slab during pre-loading, followed by splitting crack at the beam-joint interface during the downward loading at the first group. The beam and slab had more flexural cracks at top and bottom with the increase of drift level, but all these cracks were not quite visible, see Figure 4.48. There was no noticeable crack opening at the beam-joint interface up to the peak, which was confirmed by the rotation instrumented at the beam-joint interface as discussed earlier. In contrast,, a splitting crack along beam-slab interface continued to widen and dominated other flexural cracks in the slab. After the peak loading, the width of flexural cracks reduced because of the large opening of joint cracks, but the splitting crack at the beam-joint interface began to widen. Based on the damage of beams and slab, it was evident that the specimen lost its load-carrying capacity by joint failure without plastic hinge forming in the beam.

For the NS beam loading, a pair of inclined cracks occurred on the side of the EW beam, see Figure 4.49(a). The beam-joint interface was almost intact until peak loading; thereafter, splitting cracks damaged the beam-joint interface. Note that these observations were similar to those observed in SP3. Figure 4.50 shows the residual cracks in the beam and slab after test.

4.4.2.2 North-South Direction

JOINT REGION

The joint panel in the NS direction followed a similar crack pattern to that exhibited in the EW direction. A first downward crack (↙) in the joint appeared in the second group $(\Delta_{NS} = -0.63\%)$, while a first upward diagonal crack (↖) occurred during the fourth group $(\Delta_{NS} = 0.86\%)$. The first joint cracking in the NS direction took place at slightly larger drift level than in the EW direction. At the peak of the NS beam downward loading, i.e., the fourth loading group $(\Delta_{NS} = -1.29\%)$, the first developed downward diagonal crack widened significantly, and a new downward diagonal crack developed next to it. At the fifth loading group $(\Delta_{NS} = -1.96\%)$, a second downward diagonal crack developed, showing a big opening. At the peak of the EW beam upward loading, i.e., the fifth loading group $(\Delta_{NS} = 1.53\%)$, the upward diagonal crack that had developed first widened. After the peak loading, the joint diagonal cracks continued to widen further, particularly around the location of the 90° hooks of the beam top and bottom bars. The joint cover concrete split into several pieces along the cracks, and the core concrete was also heavily damaged such that the loose concrete pieces could be detached by hand. Figure 4.51 presents the progression of joint damage in the NS direction.

During the EW beam loading, horizontal cracks developed at the top and bottom of the joint panel, but the top horizontal crack opening for the upward loading was more considerable than the bottom horizontal crack, Figure 4.49(b).

BEAM AND SLAB

A first flexural crack in the beam and slab was observed at the first loading group, and a beam-slab interface splitting crack initiated at the third loading group. No splitting crack at the beam-joint interface was observed up to the peak load. Flexural cracks propagated slightly in the subsequent loading groups, but the propagation was not quite observed in the series of photographs. After the peak load, there was no further propagation of flexural and splitting cracks because joint cracks were a dominant contributor to the total responses. Inclined cracks occurred in the NS beam during the EW beam downward loading; these cracks remained minor up to the peak loading, Figure 4.49(b).

4.4.2.3 Summary

A first joint crack appeared in the EW and NS joint panel around the drift level of 0.4% and 0.6%, respectively. During the fourth group of loading $(\Delta_{down} = -1.29\%; \Delta_{up} = 0.86\%)$, the first downward diagonal crack that developed showed a significant propagation, but the upward diagonal crack showed little propagation. At the peak loading $(\Delta_{down} = -1.95\%; \Delta_{up} = 1.53\%)$, the second downward crack that developed was as wide as the first downward diagonal crack. The first upward diagonal crack opening was dominant, although minor multiple inclined cracks newly formed. Beyond the peak loading, the joint was severely damaged by spalling and crushing. Consequently, total drift was attributed to the joint rotation. The remarkable observation in the joint cracking was that the propagation pattern and width of the joint cracks were very similar at the same drift level in both SP3 and SP4, compare Figure 4.48 and 4.51 with Figure 4.33 and 4.36.

The damage of the beam and slab can be described as follows: the first flexural and splitting cracks that developed during the pre-loading or the first loading group continued to increase in width up to the peak loading; however, these cracks were relatively minor. In other words, the beam was intact at the end of test, except for a little damaged due to torsion, see Figure 4.52.

The crack pattern of the transverse joint panel and beam during the longitudinal beam loading was similar to that observed in the first three specimens, consisting of horizontal cracks in the joint panel and inclined cracks in the side of transverse beam. The propagation of these cracks was not significant, so that the joint responses in the longitudinal direction were little affected by previously developed these cracks.

Table 4.11   Qualitative damage description of SP4.

Drift (%)	EW direction	NS direction
$\Delta_0 = -0.2$	- First flexural crack in beam	-
$\Delta_{up} = -0,02$ $\Delta_{down} = -0.41$	- First downward diagonal crack in joint - Splitting cracks at beam-joint and beam-slab interfaces	- First flexural crack in beam and slab
$\Delta_{up} = 0.21$ $\Delta_{down} = -0.63$	- Additional flexural cracks in beam and slab	- First downward diagonal crack in joint - Additional flexural cracks in beam and slab - Splitting cracks at beam-joint and beam-slab interfaces
$\Delta_{up} = 0.43$ $\Delta_{down} = -0.85$	- Second downward diagonal crack in joint - First upward diagonal crack in joint	- First upward diagonal crack in joint
$\Delta_{up} = 0.86$ $\Delta_{down} = -1.29$	- Large opening of the first downward diagonal crack in joint - Additional downward and upward diagonal cracks in joint	- Large opening of the first downward diagonal crack in joint - Additional downward and upward diagonal cracks in joint
$\Delta_{up} = 1.53$ $\Delta_{down} = -1.95$	- Large opening of the later developed downward diagonal cracks in joint - Large opening of the first upward diagonal crack in joint	- Large opening of the later developed downward diagonal cracks in joint - Large opening of the first upward diagonal crack in joint
$\Delta_{up} = 2.52$ $\Delta_{down} = -2.97$	- Spalling of joint cover concrete - Reduction of beam flexural cracks width	- Bulging of joint cover concrete with large opening of joint cracks - Reduction of beam flexural cracks width
$\Delta_{up} = 4.01$ $\Delta_{down} = -4.48$	- Crushing of joint core concrete	- Crushing of joint core concrete
$\Delta_{up} = 6.22$ $\Delta_{down} = -6.69$	- Straightening of beam bars anchorage tail	- Straightening of beam bars anchorage tail
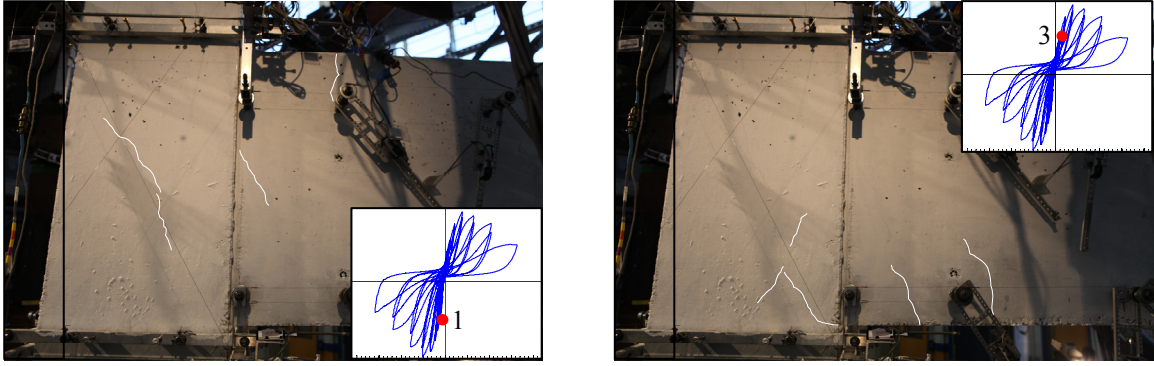
(a) first joint crack
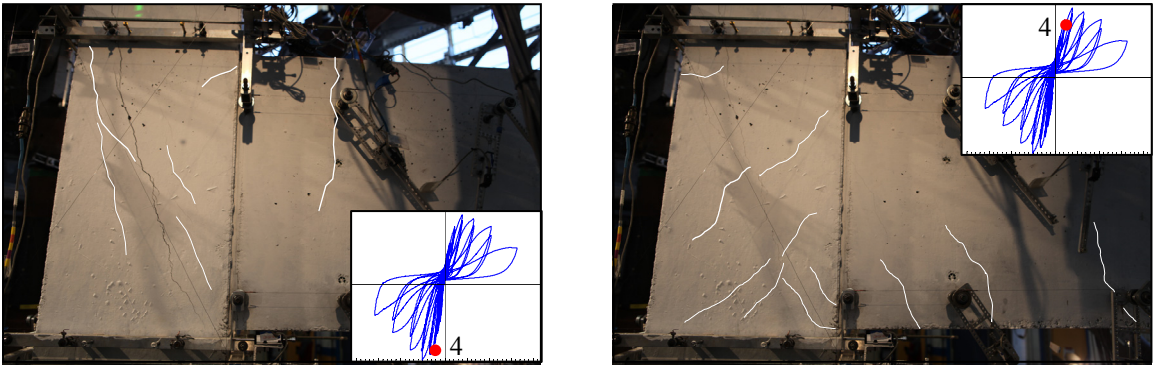
(b) propagation of joint cracking
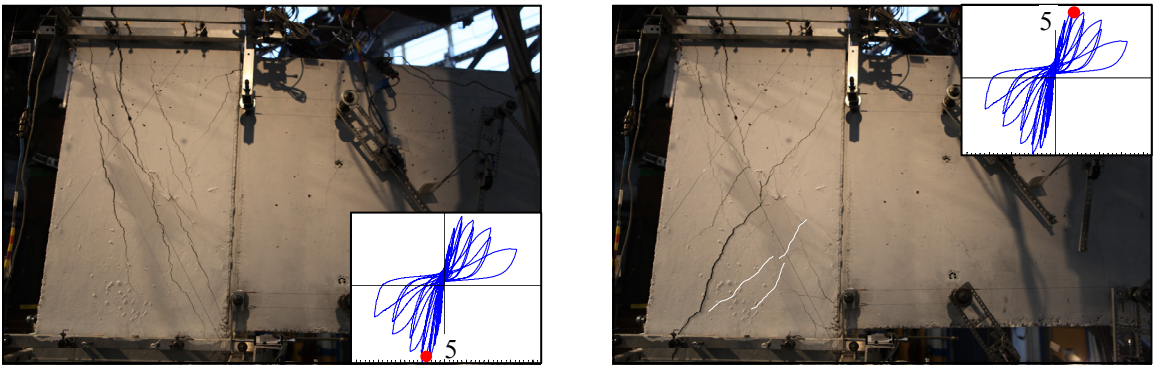
(c) joint cracking before joint failure

(d) joint damage at end of test

Figure 4.48   Damage progression of joint in EW direction, SP4.

Δ_{NS} = -1.29% Δ_{NS} = 0.86%

(a) crack pattern in the EW joint and beam by NS beam loading

Δ_{NS} = -1.94% Δ_{NS} = 1.52%

(b) crack pattern in the NS joint and beam by EW beam loading
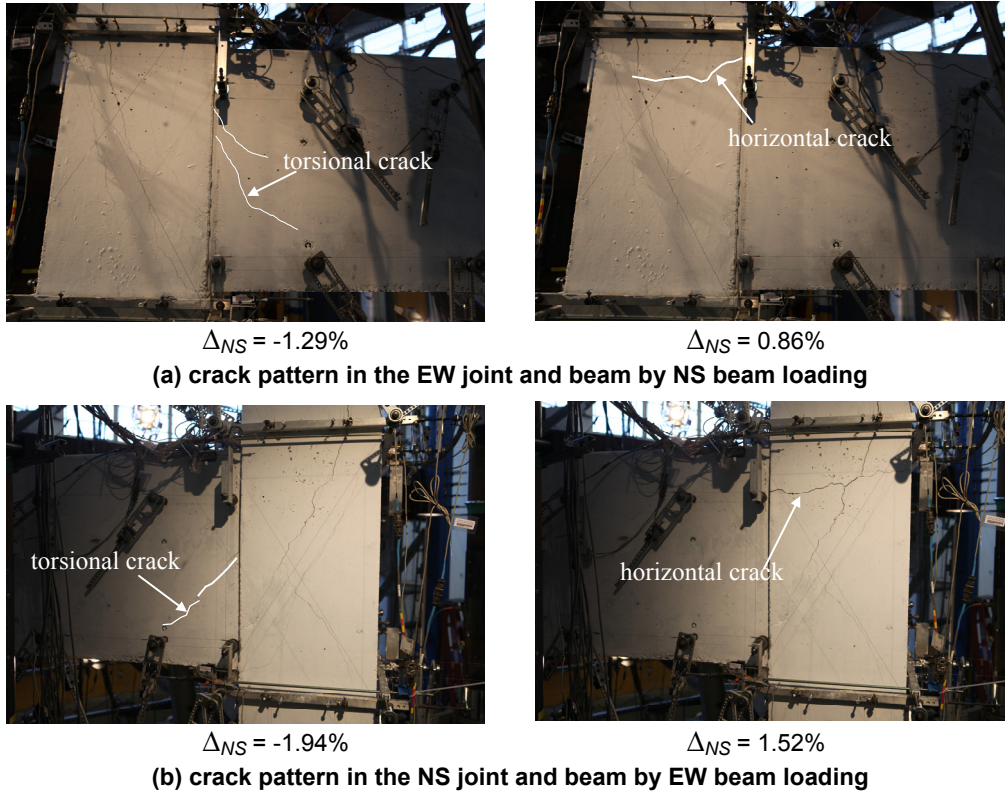
Figure 4.49   Crack pattern for the orthogonal beam loading, SP4.

(a) cracks in EW beam

(b) cracks in NS beam

(c) cracks on slab
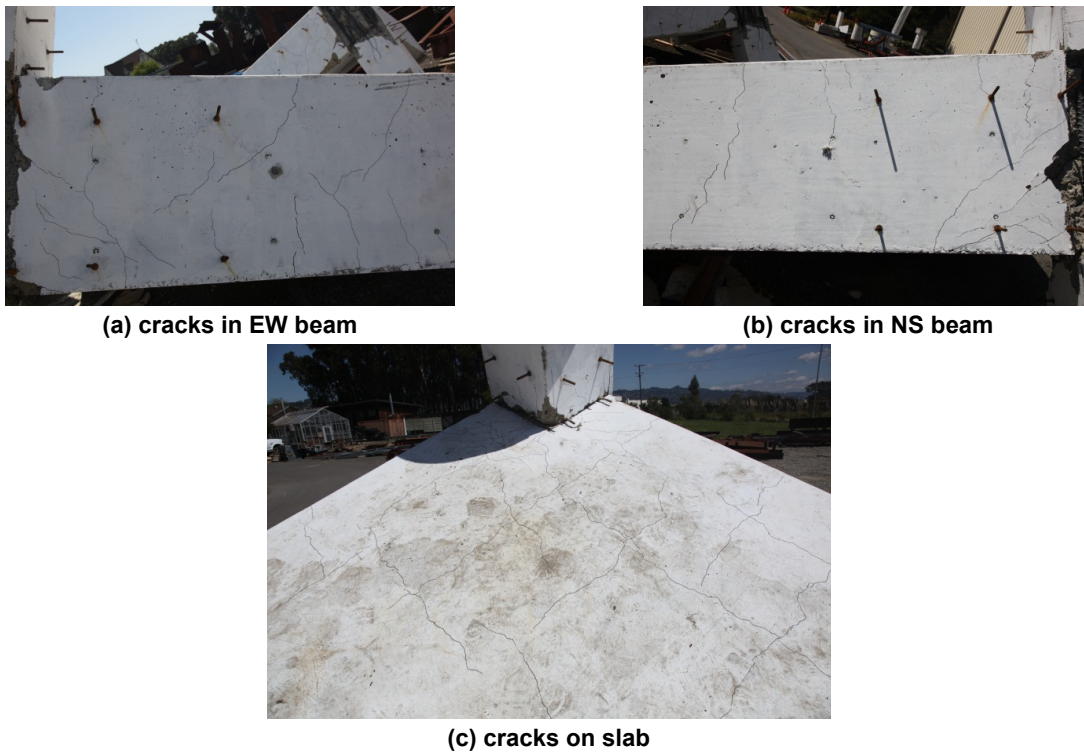
Figure 4.50   Existing cracks after testing, SP4.
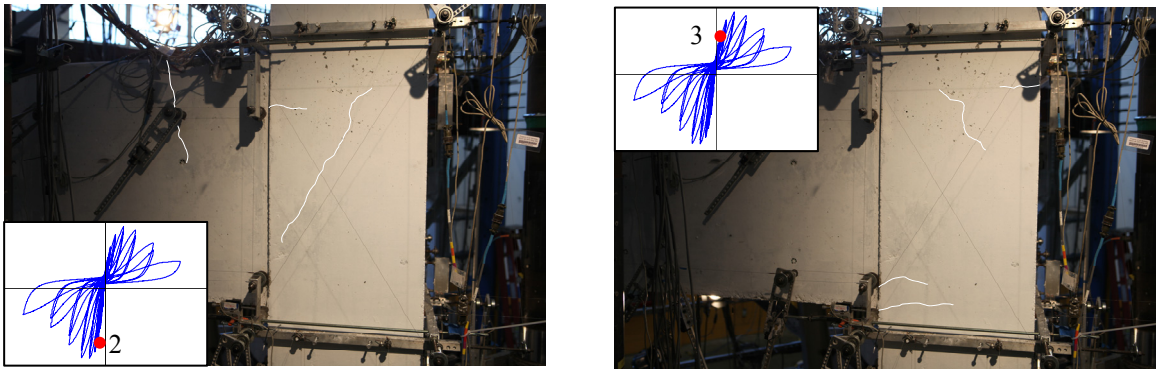
(a) first joint crack
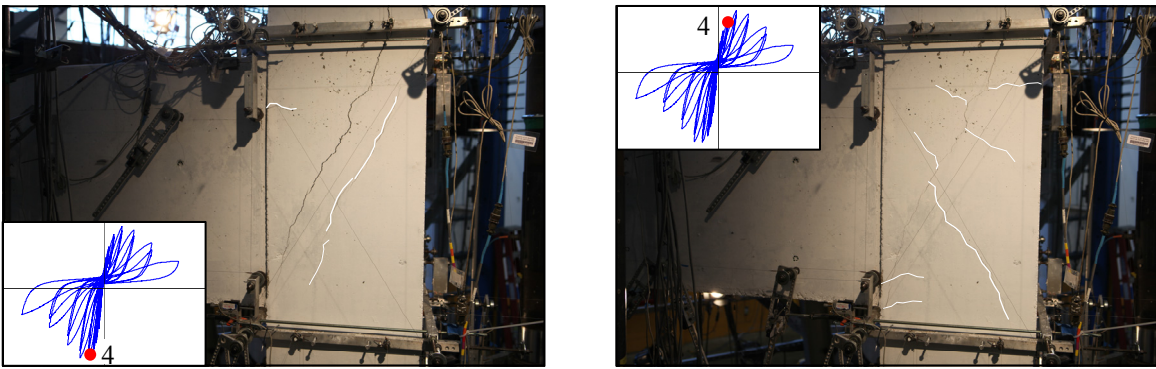
(b) propagation of joint cracking
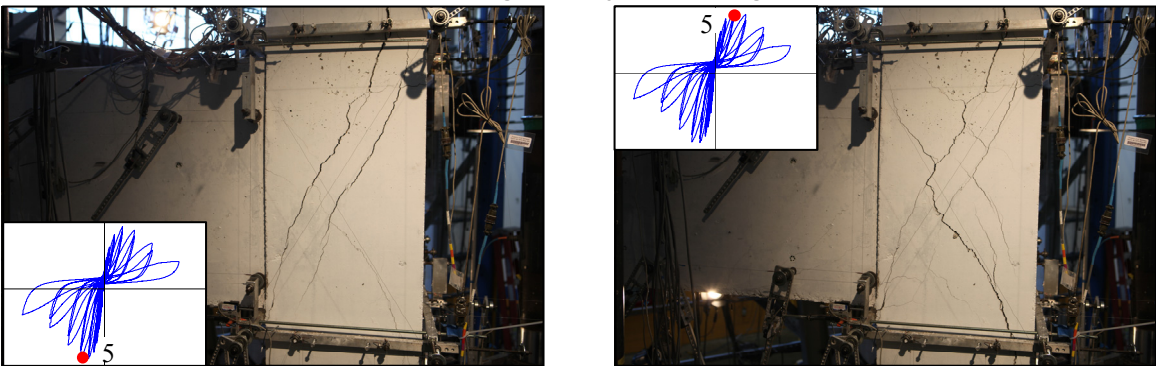
(c) joint cracking before joint failure
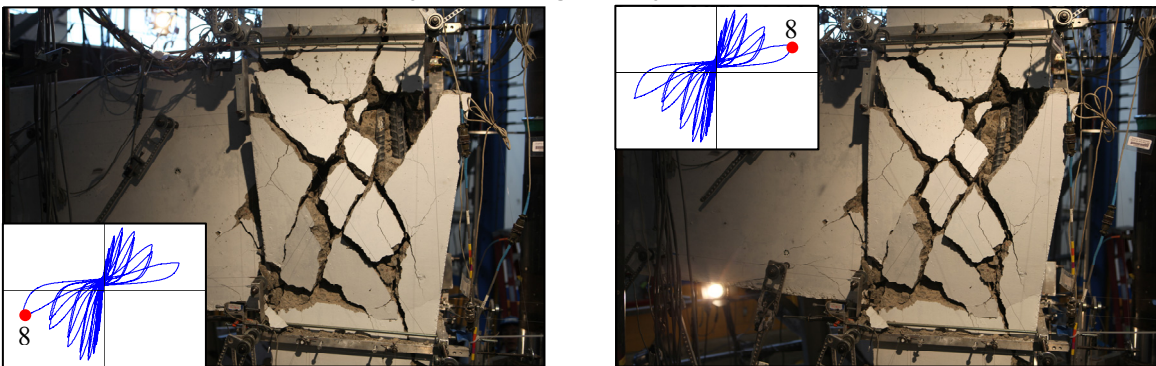
(d) joint damage at end of test

Figure 4.51   Damage progression of joint in NS direction, SP4.

127

(a) global view of specimen

(b) inside corner joint

(c) NS beam

(d) EW beam

Figure 4.52   Failure of SP4 after removing concrete fragments.

4.4.3 Joint Shear Stress versus Rotation Response

The joint shear stress versus strain responses up to the sixth group of loading are shown in Table 4.12 and Figure 4.53. Since the yielding of beam top bars was not clearly evident from the strain data at the beam-joint interface, 0.875 times the beam effective depth was assumed to be a constant moment arm. Slab top four reinforcing bars were considered to calculate the effective depth of L-shape beam cross section. The maximum joint shear stresses in the EW direction were 548 psi (3.78 MPa) for the downward loading and 471 psi (3.25 MPa) for upward loading; the corresponding values of $\gamma = v_{jh}/\sqrt{f_c'}$ were 8.7 psi$^{0.5}$ (0.72 MPa$^{0.5}$) and 7.5 psi$^{0.5}$ (0.62 MPa$^{0.5}$), respectively. In the NS direction, they were 467 psi (3.22 MPa) for downward loading and 423 psi (2.92 MPa) for upward loading; the corresponding values of $\gamma = v_{jh}/\sqrt{f_c'}$ were 7.4 psi$^{0.5}$ (0.61 MPa$^{0.5}$) and 6.7 psi$^{0.5}$ (0.56 MPa$^{0.5}$), respectively. These maximum normalized joint shear stresses were greater than the ASCE 41 recommendation, as indicated by dashed lines in Figure 4.53. To sum up the strength comparison between ASCE 41 and the tested four specimens, the ASCE41 provisions are expected to underestimate the shear strength of unreinforced exterior joints in cases with lower joint aspect ratios and higher beam longitudinal reinforcement ratios.

Table 4.12   Joint response of SP4.

Dir.	EW											
Group No.	**Downward**						**Upward**					
	v_{jh} (psi)	γ (psi$^{0.5}$)	Δ (rad)	γ_{xy} (rad)	θ_j (rad)	θ_j/Δ	v_{jh} (psi)	γ (psi$^{0.5}$)	Δ (rad)	γ_{xy} (rad)	θ_j (rad)	θ_j/Δ
1	272	4.3	0.0041	-	-	-	98	1.6	0.00	-	-	-
2	357	5.7	0.0062	0.0013	0.0027	0.44	210	3.3	0.0021	0.00	0.0003	0.14
3	431	6.9	0.0085	0.0019	0.0040	0.47	280	4.4	0.0042	0.0007	0.0013	0.31
4	509	8.1	0.0128	0.0029	0.0059	0.46	388	6.2	0.0086	0.0034	0.0055	0.64
5	548[*2]	8.7	0.0194	0.0063	0.011	0.57	471[*1*2]	7.5	0.0152	0.0089	0.012	0.79
6	477	7.6	0.0296	0.012	0.019	0.64	444	7.1	0.0251	0.023	0.028	>1.0
7	350	5.6	0.0446	0.024	0.035	0.78	391	6.2	0.0401	0.036	0.043	>1.0
8	226	3.6	0.0658	-	-	-	245	3.9	0.0623	-	-	-

Dir.	NS											
Group No.	**Downward**						**Upward**					
	v_{jh} (psi)	γ (psi$^{0.5}$)	Δ (rad)	γ_{xy} (rad)	θ_j (rad)	θ_j/Δ	v_{jh} (psi)	γ (psi$^{0.5}$)	Δ (rad)	γ_{xy} (rad)	θ_j (rad)	θ_j/Δ
1	269	4.3	0.0041	-	-	-	96	1.5	0.00	-	-	-
2	366	5.8	0.0063	0.0008	0.0025	0.40	208	3.3	0.0020	0.0005	0.0006	0.30
3	424	6.7	0.0084	0.0015	0.0043	0.51	283	4.5	0.0043	0.0013	0.0017	0.40
4	467[*2]	7.4	0.0129	0.0045	0.0081	0.63	370	5.9	0.0086	0.0038	0.0051	0.59
5	465	7.4	0.0196	0.0010	0.015	0.77	423[*1*2]	6.7	0.0153	0.0098	0.012	0.78
6	378	6.0	0.0298	0.022	0.029	0.97	400	6.4	0.0252	0.018	0.022	0.87
7	259	4.1	0.0449	0.043	0.054	>1.0	312	5.0	0.0400	0.028	0.031	0.78
8	101	1.6	0.0679	-	-	-	186	2.9	0.0620	-	-	-

*1 first yielding of beam reinforcement
*2 peak loading

Note: 1 psi = 0.0069 MPa; $1.0\sqrt{f'_c}$ psi$^{0.5}$ = $0.083\sqrt{f'_c}$ MPa$^{0.5}$

The joint shear strains at the peak load were 0.0063 rad. for the downward loading and 0.0089 rads for the upward loading in the EW direction; 0.0045 rads for the downward loading and 0.0098 rad. for the upward loading in the NS direction. The rotations at the beam-joint interface and total joint rotations are presented in Figures 4.54 and 4.55, respectively. The total joint rotations at the peak load were 0.011 rads for the downward loading and 0.012 rads for the upward loading in the EW direction; 0.0081 rads for the downward loading and 0.012 rads for the upward loading in the NS direction.

Comparison of the joint deformation between SP3 and SP4 shows that the two specimens had very similar joint shear strain and beam-joint interface rotation at the same loading groups, although they have different joint shear stresses at the same loading group. Note that joint shear strains had a greater portion of the joint total rotation in SP3 and SP4, while the joint total rotations were mostly due to the rotation at the beam-joint interface in the low aspect ratio

specimens, SP1 and SP2. Table 4.12 indicates that joint total rotation contributed significantly to the total drift in SP4, increasing by more than about 50% from the fourth group of loading.
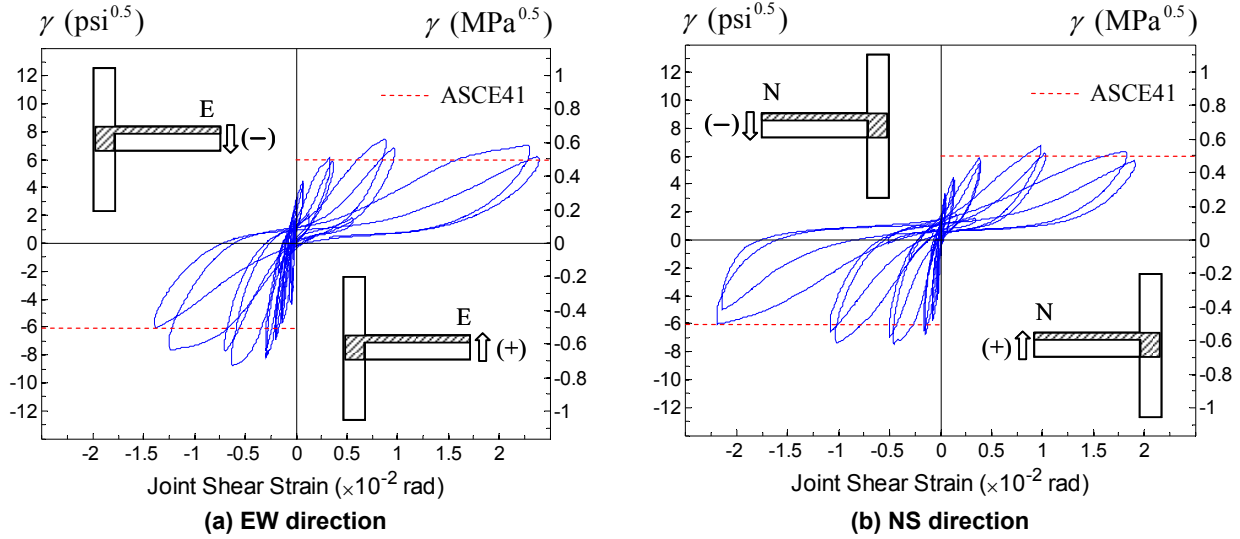
Figure 4.53   Joint shear stress versus strain response of SP4.
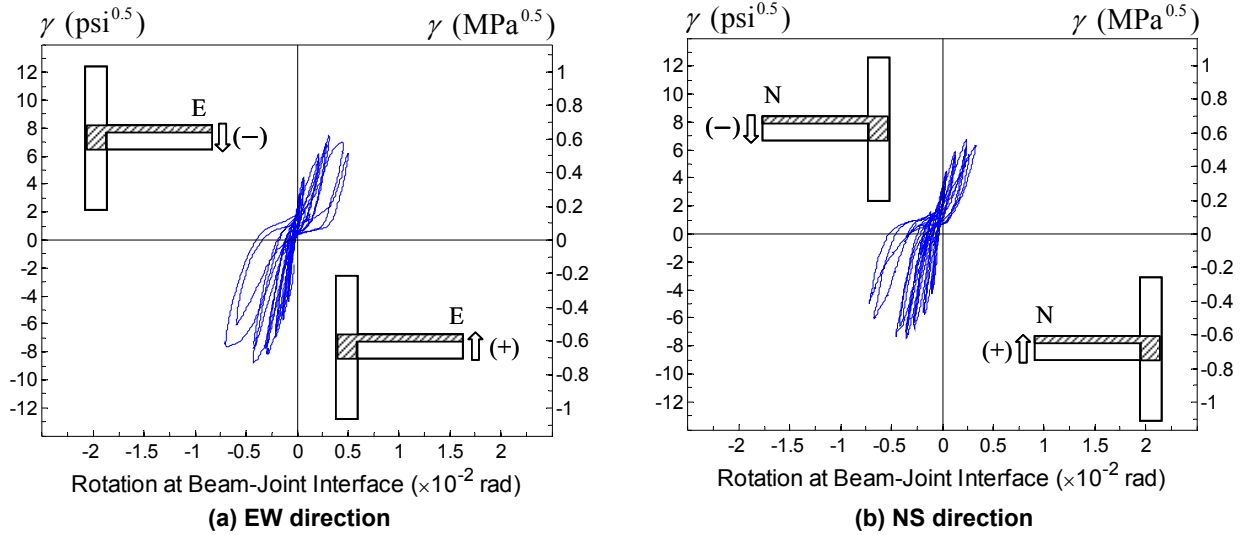
Figure 4.54   Joint shear stress versus rotation at beam-joint interface of SP4.
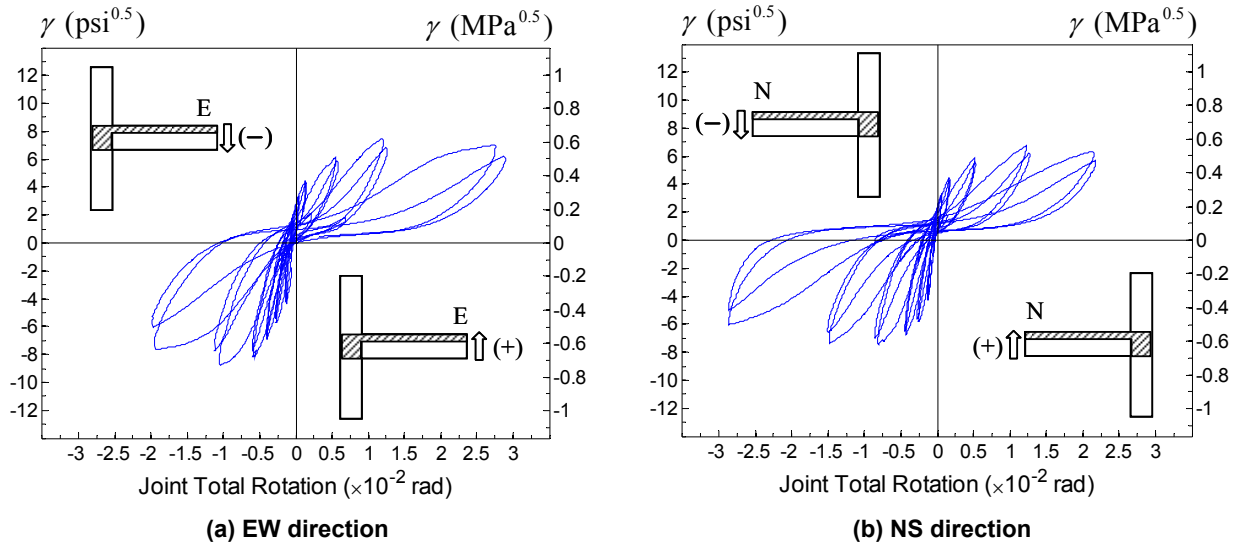
Figure 4.55   Joint shear stress versus total rotation of SP4.

4.4.4 Strain Measurement

4.4.4.1 Beam Reinforcement

The strain gage measurements of the beam longitudinal bars in the EW and NS directions are shown in Figures 4.56 and 4.57. The strains of both EW and NS beam longitudinal bars measured at the beam-joint interface, i.e., gage number 3, were slightly less than the yield strain or barely reached the yield strain until the peak loading, i.e., fifth group of loading. Strain values of the beam longitudinal bars in SP4 were less than those measured in SP3. Considering the load-drift response and strain gage measurements, the SP4 beams were expected to remain elastic. In some cases, the beam longitudinal bars yielded at the inner side of the joint, i.e., at gage number 2. However, this yielding did not represent the beams flexural yielding because it occurred at the sixth loading group, which was after peak loading. Instead, the damage of joint panel and the consequent bond deterioration might have caused this yielding.

4.4.4.2 Slab Reinforcement

The strain gage measurements of the slab reinforcing bars in the EW and NS directions are presented in Figure 4.58. The measured strains of slab reinforcement showed that these bars did not yield during testing of SP4. The first gage on the EW slab top reinforcement did not function properly, and the second gage was also damaged at the fifth loading group which was the peak of the EW beam loading; thus no strain data of these two bars were available around the peak load. However, their strains were expected to be less or conservatively close to the yield strain considering the strain value of the internal layer of the beam top longitudinal bar, Figure 4.56(b), which was very next to the gage number 1 of slab top reinforcement.

4.4.4.3 Column Reinforcement

The strain gage measurements of the column longitudinal bars are presented from Figures 4.59 and 4.60. As the column was designed to remain elastic, the strains of all the column reinforcing bars were less than the yield strain until the peak loading. The strain distribution of longitudinal

column intermediate bars was measured over the height in the joint region. The tensile strain at the mid-height was greater than the strains at the top and bottom gages in the joint panel, but this strain remained at small value, i.e., less than half the yield strain. Therefore, it was expected that the column intermediate reinforcing bars did not act as a tension tie in the joint.

Note: 1" = 25.4 mm

(a) EW-Top-Ext.

(b) EW-Top-Int.

(c) EW-Bottom-Ext.

(d) EW-Bottom-Int.
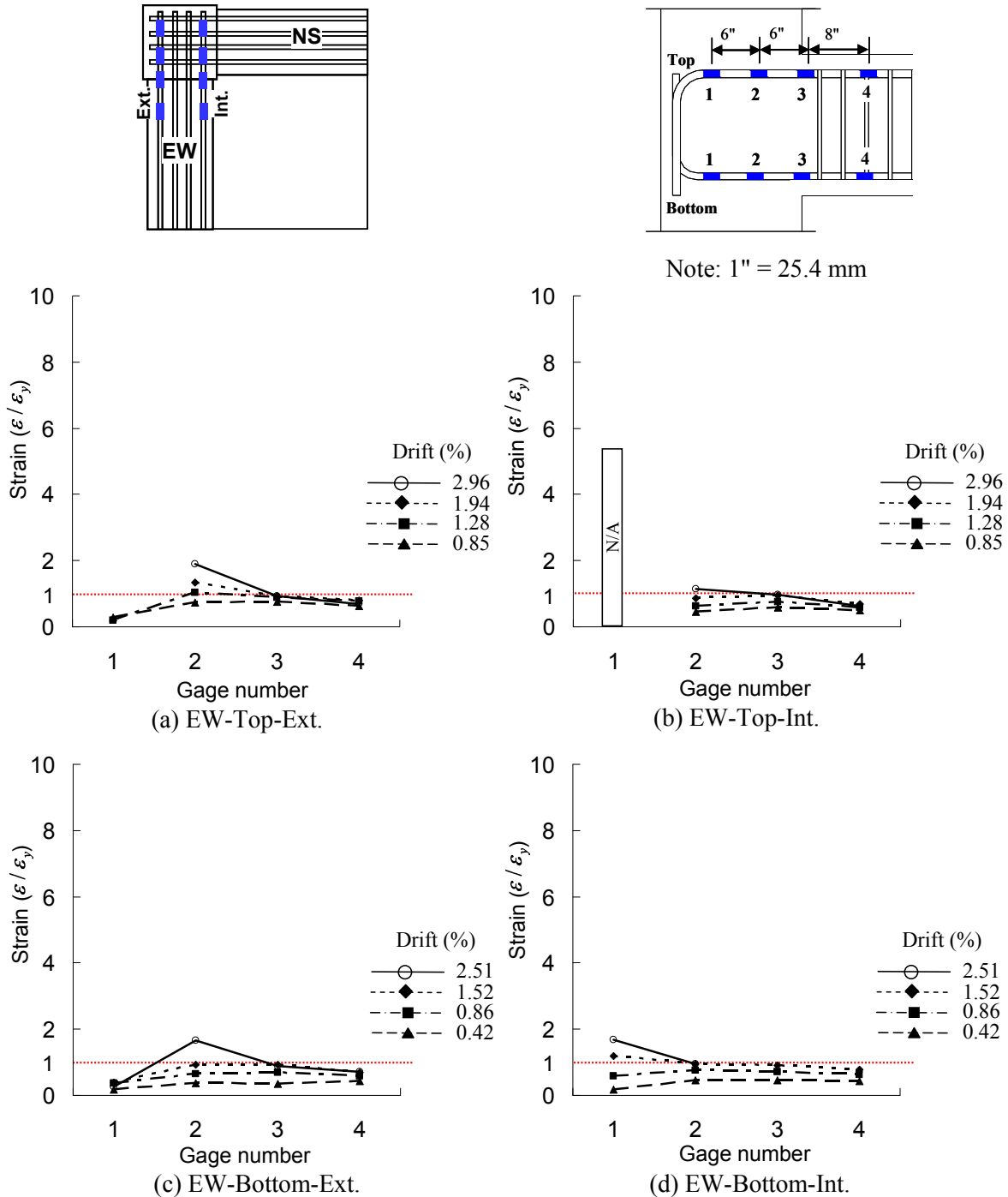
Figure 4.56   Strains of the EW beam reinforcing bars of SP4.
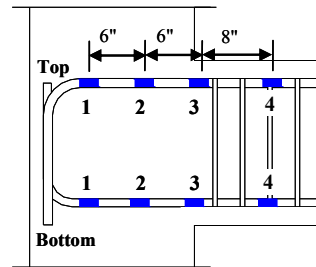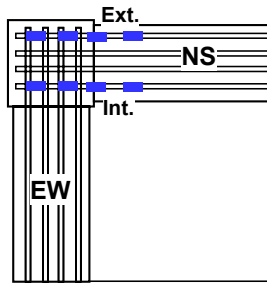
Note: 1" = 25.4 mm
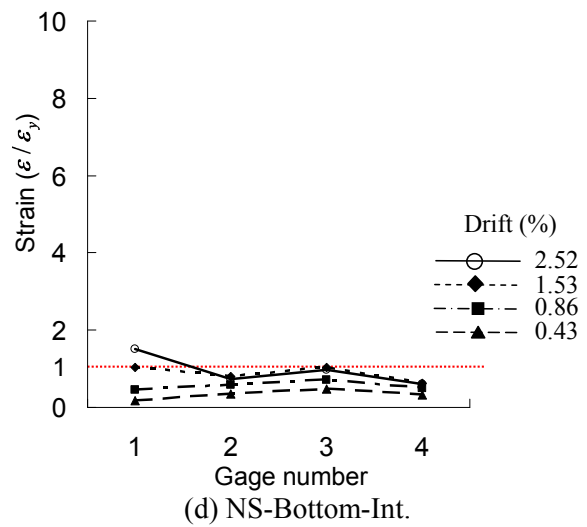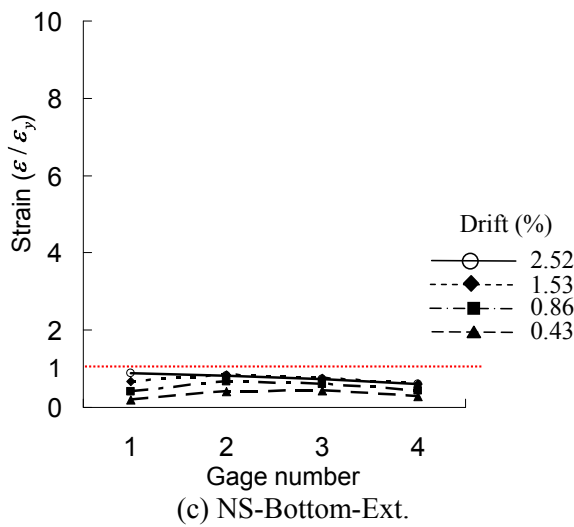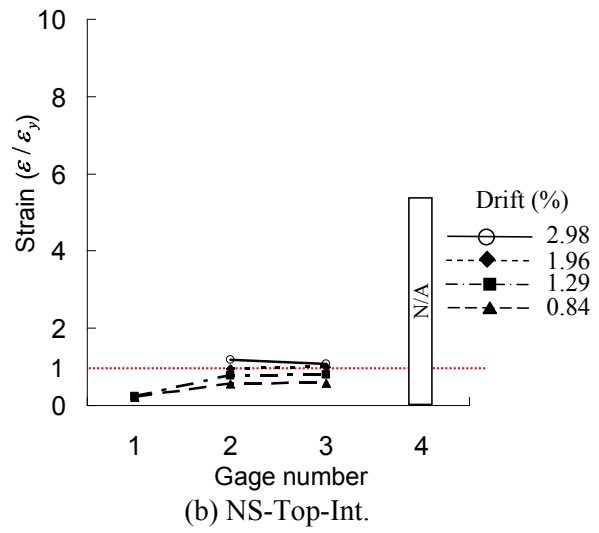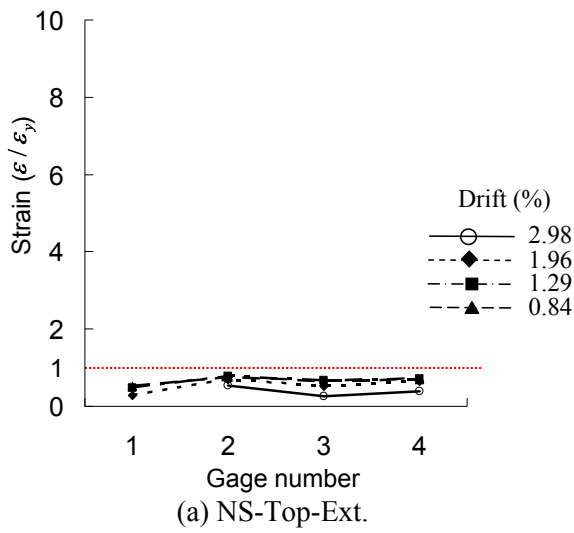
Figure 4.57   Strains of the NS beam reinforcing bars of SP4.
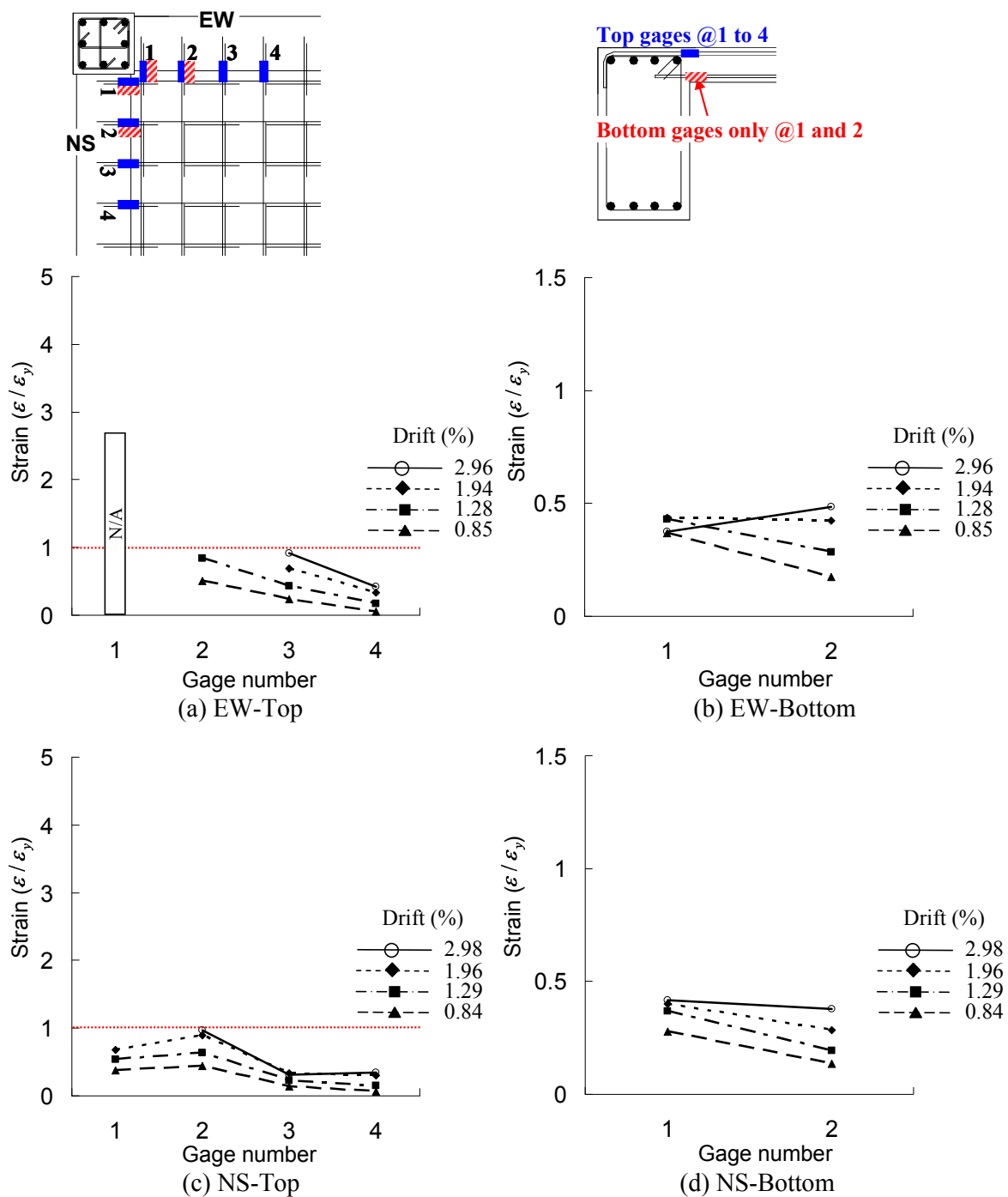
Figure 4.58   Strains of the slab reinforcing bars of SP4.
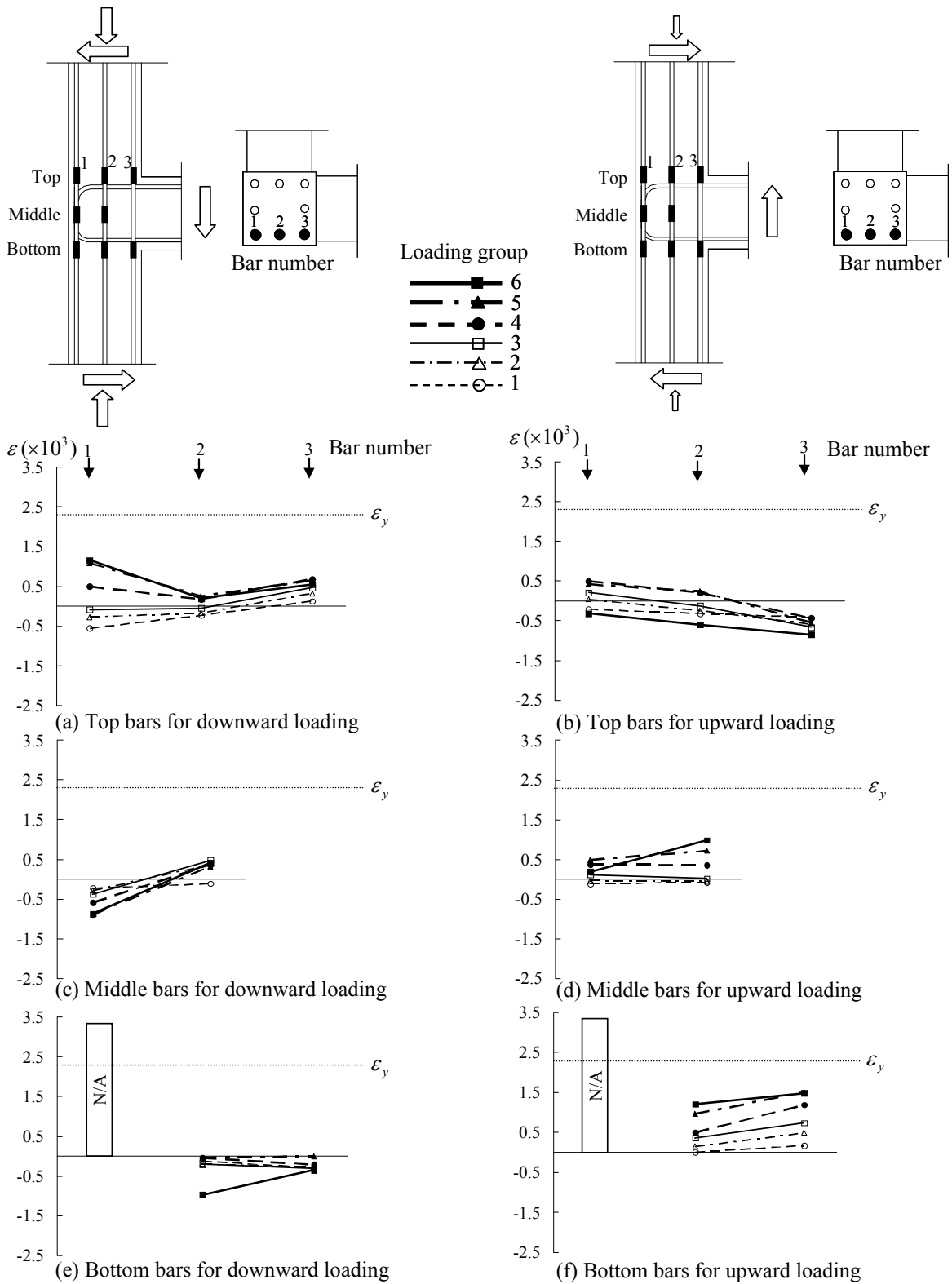
Figure 4.59   Strains of the column reinforcing bars for the EW beam loading, SP4.

135
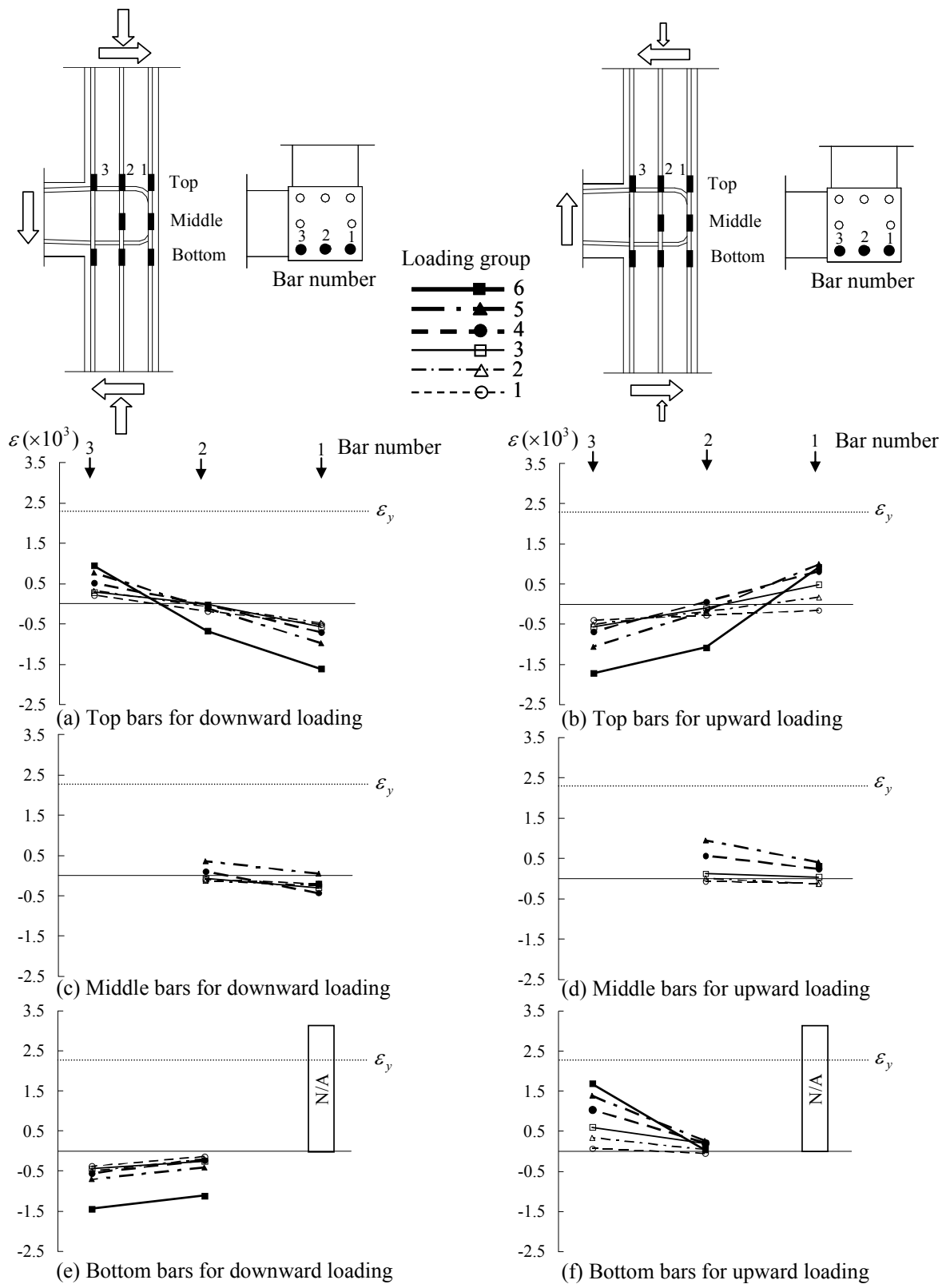
Figure 4.60　Strains of the column reinforcing bars for the NS beam loading, SP4.

5 Discussion of Experimental Results

5.1 EVALUATION OF JOINT SHEAR STRENGTH

For comparison of the test results among the four specimens, joint shear stresses were evaluated at three following critical events among their overall responses. The joint shear stress at the peak load represented the joint shear strength of each specimen. It was also used to assess the joint shear stress at the onset of first cracking in the joint and at yielding of the beam longitudinal bars, if these bars yielded, for developing backbone relationships of joint macro-model. The normalized joint shear stresses for those three events are presented in Table 5.1. In each specimen, the normalized joint shear stresses were evaluated for the EW and NS beams downward and upward loading separately. Note that the normalized joint shear stresses at first cracking and at the peak were evaluated using the peak load of the first cycle in the loading group when these events were observed, while the normalized joint shear stresses at first beam reinforcement yielding were determined from the beam loads when the strain of beam longitudinal bars reached their yield strain by tracking the strain gage measurements.

Table 5.1 Evaluation of normalized joint shear stress, γ (psi$^{0.5}$).

Observation	SP1 EW Down[1]	SP1 EW Up[2]	SP1 NS Down[1]	SP1 NS Up[2]	SP2 EW Down[1]	SP2 EW Up[2]	SP2 NS Down[1]	SP2 NS Up[2]
First crack	5.6	6.6	7.2	6.9	8.0	7.9	10.4	7.8
First yield	6.7	7.5		7.5	12.2	9.1	12.4	9.4
Peak	**8.5**	**8.5**	**7.9**	**8.1**	**12.6**	**10.0**		**9.7**

Observation	SP3 EW Down[1]	SP3 EW Up[2]	SP3 NS Down[1]	SP3 NS Up[2]	SP4 EW Down[1]	SP4 EW Up[2]	SP4 NS Down[1]	SP4 NS Up[2]
First crack	-[3]	-[3]	4.3	3.5	4.3	4.4	5.8	4.5
First yield	6.7	6.2	6.0	5.9	No yield	7.5	No yield	6.7
Peak	**7.2**	**6.3**	**6.3**		**8.7**		**7.4**	

[1] beam loaded downward
[2] beam loaded upward
[3] onset of cracking was not accurately detected for specimen SP3

5.2   COMPARISON OF TEST RESULTS WITH MODEL PREDICTIONS

The shear strengths of the four specimens were compared with predictions using the three models introduced in Chapter 2: namely, the semi-empirical model, the analytical model and the simplified model. As summarized in Table 5.2, the proposed semi-empirical model, analytical model, and simplified model accurately predicted the shear strengths with 4%, 6%, and 1% errors, respectively. If only the EW joint shear strengths are considered for this comparison—because lower strengths are generally obtained in the NS direction due to the loading sequence, —the accuracy of the semi-empirical model improved. The analytical model, however, underestimated the joint shear strength by 10%. This underestimation comes from the predictions for SP2 and SP4, where relatively a larger diameter of beam longitudinal bars were used because the fraction factor is dependent on a diameter of beam longitudinal bar such that a large diameter of bar increases the values of fraction factor α_1 and α_2 (Figure 2.8) without limitation. The fraction factor is bounded in the simplified model, which shows better accuracy of strength predictions compared to the analytical model.

Table 5.2   Comparison of test results with predictions by the proposed models.

Specimen	Joint Face	Loading direction	Test results γ_{test} [psi$^{0.5}$]	Semi-empirical γ_{model} [psi$^{0.5}$]	Analytical γ_{model} [psi$^{0.5}$]	Simplified model γ_{model} [psi$^{0.5}$]
SP1	EW	Down	8.5	9.2(0.92)	8.5(1.00)	8.7(0.98)
		Up	8.5	7.8(1.08)	7.3(1.17)	7.3(1.17)
	NS	Down	7.9	9.2(0.86)	8.5(0.93)	8.7(0.91)
		Up	8.1	7.8(1.03)	7.3(1.11)	7.3(1.11)
SP2	EW	Down	12.6	11.7(1.08)	10.5(1.20)	12.0(1.05)
		Up	10.0	9.5(1.06)	8.4(1.20)	8.9(1.12)
	NS	Down	12.4	11.7(1.06)	10.5(1.18)	12.0(1.03)
		Up	9.7	9.5(1.02)	8.4(1.16)	8.9(1.09)
SP3	EW	Down	7.2	7.8(0.91)	7.1(1.01)	7.7(0.93)
		Up	6.3	6.8(0.93)	6.0(1.05)	6.4(0.98)
	NS	Down	6.3	7.8(0.80)	7.1(0.88)	7.7(0.81)
		Up	5.9	6.8(0.86)	6.0(0.97)	6.4(0.91)
SP4	EW	Down	8.7	8.2(1.07)	8.2(1.06)	8.7(1.00)
		Up	7.5	7.7(0.97)	6.8(1.10)	7.6(0.99)
	NS	Down	7.4	8.2(0.91)	8.2(0.90)	8.7(0.85)
		Up	6.7	7.7(0.87)	6.8(0.99)	7.6(0.98)
Both EW and NS directions, $\gamma_{test}/\gamma_{model}$			Mean	0.96	1.06	0.99
			COV	0.09	0.12	0.10
Only for EW direction, $\gamma_{test}/\gamma_{model}$			Mean	1.00	1.10	1.03
			COV	0.08	0.13	0.09

5.3   EFFECT OF JOINT ASPECT RATIO

The joint shear strengths of the tested specimens were plotted against the corresponding joint aspect ratio together with the literature test data points to further investigate the consistency of the joint aspect ratio effect, as shown in Figure 5.1. Note that amongst the shear stress calculations for each specimen during the downward and upward loadings in the two directions, only the largest and smallest shear strengths calculated are presented. The joint aspect ratio, h_b/h_c , is equal to 1.0 for specimens SP1 and SP2, and 1.7 for specimens SP3 and SP4. Using the simplified model in Equation (2.30), the upper and lower bounds of shear strength are defined as

$$\gamma_{max} = 12\frac{\cos\theta}{\cos(\pi/4)}, \ \gamma_{min} = 4.8\frac{\cos\theta}{\cos(\pi/4)} \tag{5.1}$$

In the joint aspect ratio of $h_b/h_c = 1.0$, the joint shear strengths of SP1 are distributed between $\gamma_n = 7.9$ psi$^{0.5}$ (0.66 MPa$^{0.5}$) and 8.5 psi$^{0.5}$ (0.71 MPa$^{0.5}$), as indicated with solid circle, while the minimum and maximum joint shear strengths of SP2 are $\gamma_n = 9.7$ psi$^{0.5}$ (0.87 MPa$^{0.5}$) and 12.6 psi$^{0.5}$ (1.05 MPa$^{0.5}$), respectively, as indicated with open circle. In the joint aspect ratio of $h_b/h_c = 1.7$, the joint shear strengths of SP3 ranged from $\gamma_n = 5.9$ psi$^{0.5}$ (0.49 MPa$^{0.5}$) to 7.2 psi$^{0.5}$ (0.60 MPa$^{0.5}$), as indicated with solid triangle, and those of SP4 ranged from $\gamma_n = 8.7$ psi$^{0.5}$ (0.72 MPa$^{0.5}$) to 6.7 psi$^{0.5}$ (0.56 MPa$^{0.5}$), as indicated with open triangle.

Recalling the beam reinforcement details illustrated in Chapter 3, the same beam longitudinal bars were used for SP1 and SP3, and for SP2 and SP4, and slab reinforcement was identical in all the tested four specimens. Considering the beam and slab reinforcement details for the two pairs of specimens, i.e., SP1 and SP3 and SP2 and SP4, it is obvious that the reduction of the joint shear strength from SP1 to SP3 and from SP2 to SP4 is attributed to the increase of the joint aspect ratio. The effect of joint aspect ratio observed in the tested four specimens is consistent with the trend observed in the literature test data. In addition, the maximum values of test results exceeded slightly the proposed upper limit which is also drawn by a solid line in Figure 5.1. The upper limits are adopted from the simplified model presented in Chapter 2, i.e., 12.0 psi$^{0.5}$ (1.0 MPa$^{0.5}$) for $h_b/h_c = 1.0$ and 8.7 psi$^{0.5}$ (0.73 MPa$^{0.5}$) for $h_b/h_c = 1.7$. The ASCE 41 provisions, however, suggest a constant shear strength of 6.0 psi$^{0.5}$ (0.5 MPa$^{0.5}$), regardless of joint aspect ratio, resulting in conservative estimates of strengths particularly for the case of lower joint aspect ratio and higher beam longitudinal reinforcement ratio.

The effect of the joint aspect ratio can be explained by the SAT idealization where a steeper diagonal strut develops in the unreinforced joint with a high aspect ratio. Consequently, this steeper diagonal strut results in less effective shear resistance to equilibrate the horizontal joint shear force. Hence, the shear strength of unreinforced exterior and corner joints decreases with an increase of the joint aspect ratio, as discussed in Chapter 2. Note that the variation of the joint shear strength between the two curves for a specific joint aspect ratio is explained by the effect of the beam reinforcement ratio, discussed next. Note that unlike the unreinforced exterior and corner joints, the effect of joint aspect ratio is not observed in the same types of reinforced joints [Kim and LaFave 2007] and is therefore not addressed in current code provisions. This is

explained by the fact that a diagonal strut crossing the opposite corners of the unreinforced joint panel is dominant, while additional inclined struts can develop in the reinforced joint due to the transverse reinforcement; thus the strength of the reinforced joint does not solely depend on the diagonal strut geometry.
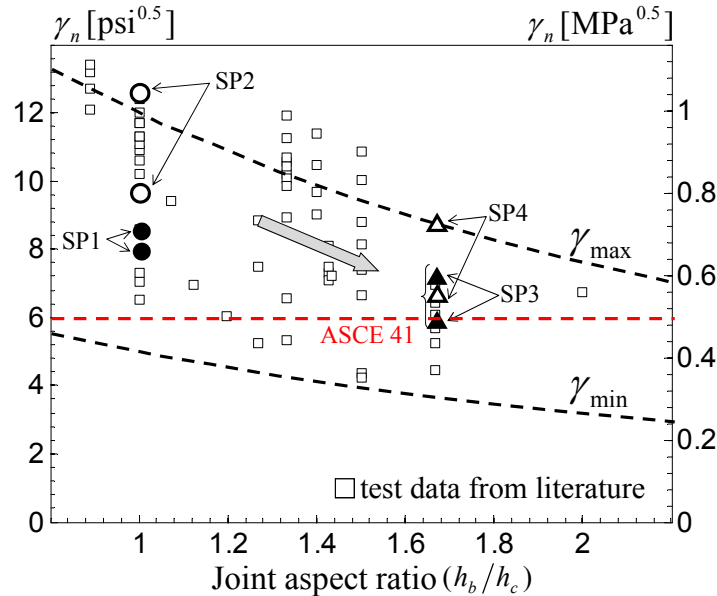
Figure 5.1 **Test results of normalized joint shear strength versus the joint aspect ratio.**

5.4 EFFECT OF BEAM LONGITUDINAL REINFORCEMENT RATIO

The investigation of the effect of the beam longitudinal reinforcement ratio focused on the variation of joint shear strength and the yield propagation of beam longitudinal bars into the joint. The joint shear strengths of the four test specimens are plotted in Figure 5.2 against the corresponding joint shear index [Equation (2.13)] in addition to the test data from the database in [Park and Mosalam 2009]. The plots are separated for low joint aspect ratio ($0.9 \leq h_b/h_c \leq 1.3$) and for high joint aspect ratio ($1.4 \leq h_b/h_c \leq 2.0$). For the joint aspect ratio $h_b/h_c = 1.0$ corresponding to SP1 and SP2, and 1.7 corresponding to SP3 and SP4, the upper (γ_{max}) and lower (γ_{min}) bounds of shear strength [Equation (5.1)] are connected by dashed lines. Based on the material properties and design details, the joint shear indices of SP1 and SP3 are indeed between γ_{max} and γ_{min} while those of SP2 and SP4 are close to γ_{max}, as shown in Figure 5.1.

The test results indicate that the joint shear strength clearly increases with the increase of the beam reinforcement ratio, i.e., from SP1 to SP2 and from SP3 to SP4. In Figure 5.2, the joint shear strengths labelled with "a" and "b" are calculated for the downward and upward loadings, respectively. Moreover, these strengths are given for the EW and NS beams where the EW beam has mostly higher strength than that of the NS beam because the EW beam was loaded first. This is discussed in the Section 5.7.

140

The test results support the trend that the joint shear strength is proportional to the joint shear index between the upper and lower bounds for a given joint aspect ratio. This proportionality is explained by an analysis of the test database [Park and Mosalam 2009]. If the joint shear index is between the upper and lower bounds, the joint experiences BJ-type failure, where the beam longitudinal reinforcement yielding is followed by joint failure and thus the joint shear strength is limited by the joint shear index. If the joint shear index is greater than the upper bound owing to large beam longitudinal reinforcement ratio, the joint experiences J-type failure, where the joint fails prior to beam yielding. Thus the joint shear strength is limited by the upper bound, which can be considered as joint shear capacity. The upper bound will be further clarified by ongoing tests having larger beam longitudinal reinforcement ratio than that provided in SP2 and SP4.

In mechanistic respects, the analytical model presented in Chapter 2 explains the increase of shear strength as the joint shear index increases, using bond resistance of the concrete surrounding the anchored beam longitudinal bars within the joint region. The basic idea is that since beam yielding is followed by joint shear failure, i.e., BJ-type failure, in the case of lower joint shear index, the yielding of beam bars penetrates into the joint with loss of bond resistance, thus joint failure eventually occurs at lower level of shear stress. The strains of the beam longitudinal bars of the specimens having relatively less beam reinforcement ratio, i.e., SP1 and SP3, are greater than those measured in the counterpart specimens, i.e., SP2 and SP4. Thus, the yielding of the beam longitudinal bars penetrated further into the joint in specimens SP1 and SP3. The strain values of SP1 and SP2 are compared in Figure 5.3.

The BJ-type of joint failure may not occur in a reinforced joint because such joints maintain their deformability until the adjacent beam sustains flexural ductile behavior. However, the absence of transverse reinforcement in the joint region results in significant yield penetration of the beam longitudinal reinforcement into the joint and eventually loss of bond resistance leading to joint failure at a lower joint shear demand than that for an equivalent J-type joint failure. Some strength models use either ductility factor [Park 1997; Hakuto et al. 2000] or bond resistance of the concrete surrounding the anchored beam longitudinal bars within the joint region (the analytical model presented in Chapter 2) to predict the BJ type of joint failure.

Table 5.3 compares the calculated joint shear indices with the joint shear stresses measured at the onset of the beam longitudinal bars yielding. The joint shear indices for negative bending, i.e., slab in tension, are calculated separately with and without consideration of slab reinforcement contribution. The slab reinforcement was taken within the effective flange width according to ASCE 41. Consequently, slab top four reinforcing bars were included to calculate the joint shear indices of the four specimens. Note that the joint shear index equation is independent of the shape of beam cross section such as T-shape and L-shape because the cross-sectional height, h_b, is the same for either rectangular or other two shapes of beam cross-section. Therefore, total sectional area of the considered slab reinforcement was added to the cross-sectional area of beam longitudinal bars in tension, A_s for negative bending, while the sectional area of the bottom longitudinal bars only is included in A_s in the joint shear index for positive bending, i.e., slab in compression. As shown in Table 5.3, the joint shear indices were close to the joint shear stresses at the onset of beam longitudinal bars yielding ($\gamma_{test @ yield}$), particularly if the contribution of slab reinforcement is taken into consideration with the exception of SP1. Note that the presented normalized joint shear stresses correspond to the values for the EW direction in each of the tested four specimens.

Table 5.3   Joint shear index (SI_j).

Specimen	SP1			SP2			SP3			SP4		
	Top		Bottom	Top		Bottom	Top		Bottom	Top		Bottom
Tension region	without slab bars	with slab bars		without slab bars	with slab bars		without slab bars	with slab bars		without slab bars	with slab bars	
SI_j	6.8	7.5	6.8	11.2	12.0	8.7	6.2	6.9	6.2	9.8	10.5	7.5
$\gamma_{\text{test@yield}}$	6.7		7.5	12.2		9.1	6.7		6.2	-		7.5
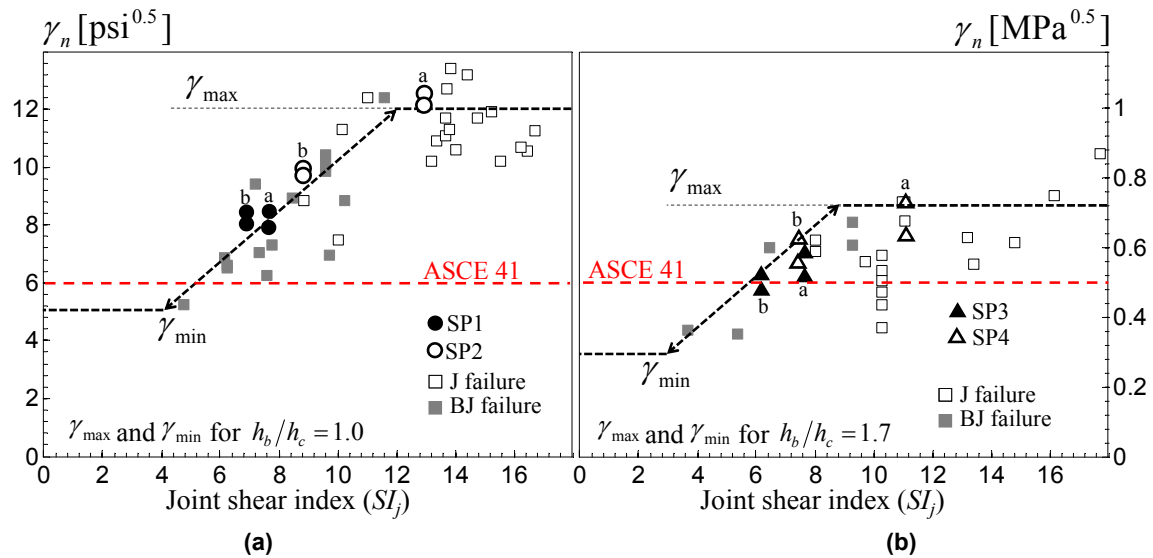
Figure 5.2   Effect of beam longitudinal reinforcement ratio: (a) for low joint aspect ratio $\left(0.9 \le h_b/h_c \le 1.3\right)$; and (b) for high joint aspect ratio $\left(1.4 \le h_b/h_c \le 2.0\right)$.
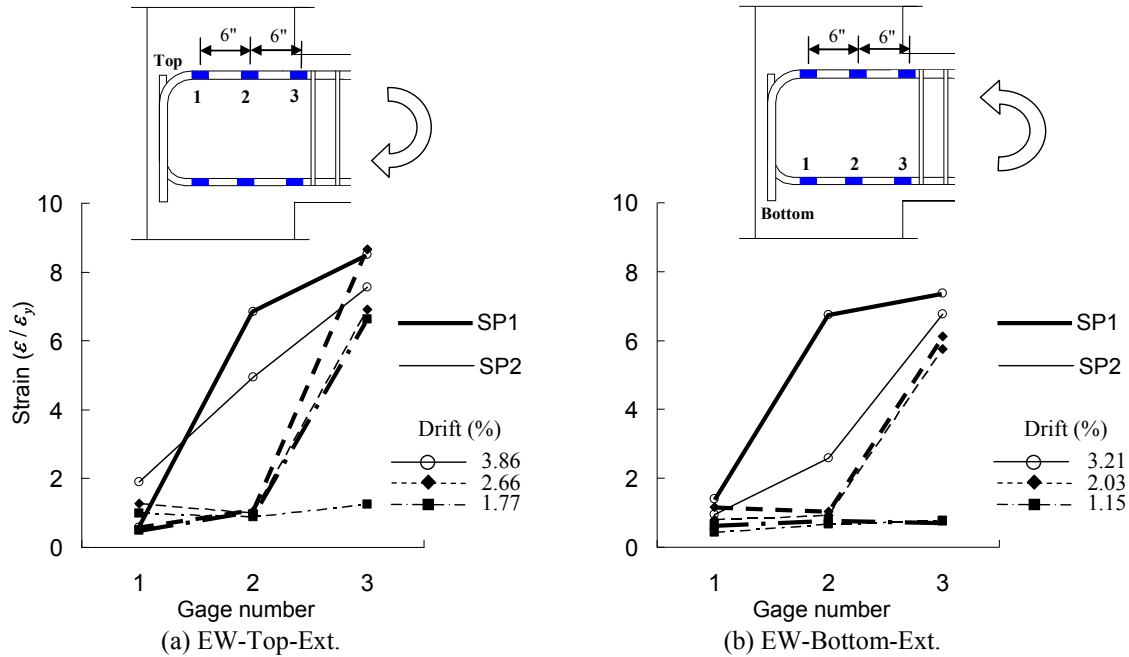
Figure 5.3   Comparison of beam longitudinal bar strains for specimens SP1 and SP2.

5.5   EFFECT OF COLUMN AXIAL LOAD

The joint shear strengths of the four specimens tested are plotted in Figure 5.4 against the column axial load ratio with the same database. To focus on the effect of column axial load, the other two effects, namely joint aspect ratio and beam reinforcement ratio, are addressed in Figure 5.4 as follows: (1) joint shear strengths on the vertical axis were normalized by the upper limit γ_{max} in Equation (5.1) to eliminate the effect of joint aspect ratio; and (2) two joint shear failure types, i.e., J-type failure and BJ-type failure, depending on the beam reinforcement ratio are indicated with different markers.

Minimal and/or unclear influence on joint shear strength for column axial load less than $0.25 f_c' A_g$ where A_g is the gross area of the column cross section was found. For example, the normalized shear strength of SP1 was 8.5 psi$^{0.5}$ (0.71 MPa$^{0.5}$) for downward and upward loadings, although the column was subjected to tension ($0.07 f_c' A_g$) for upward loading and compression ($0.11 f_c' A_g$) for downward loading. Note that the larger shear strengths of SP2 and SP4 for the high column axial load shown in Figure 5.4 are attributed to the larger cross-sectional area of the top beam longitudinal bars rather than due to benefit from column axial load. Including this study, most of previous joint tests were conducted under column axial load less than $0.25 f_c' A_g$. Thus more test data for the cases of higher column axial load are needed to clarify the effect of high column axial load on the joint shear strength.
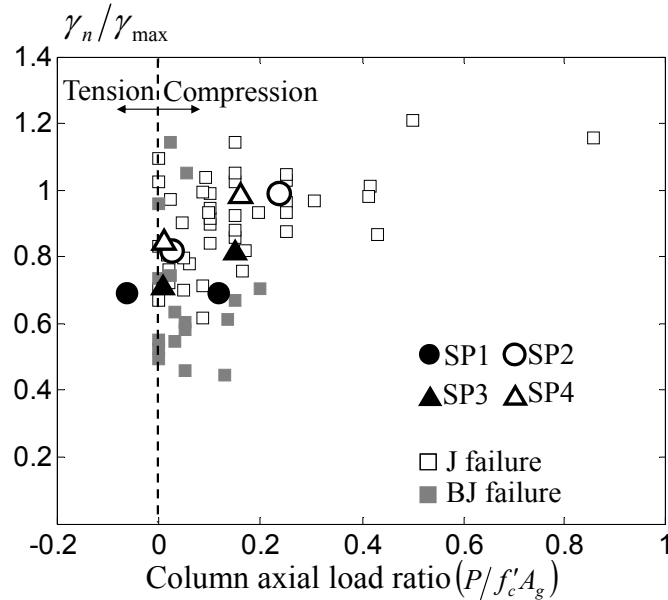
Figure 5.4 **Test results of normalized joint shear strength versus the joint shear index.**

5.6 EFFECT OF SLAB

The strain distributions of the slab top reinforcement presented in Chapter 4 show a decrease in the strain value away from the column face. A similar observation can be made from the crack pattern at the top of the slab, as shown in Figure 5.5. Therefore, it can be stated that the slab reinforcement contributed to the negative flexural moment capacity of the longitudinal beams. To estimate the contribution of the slab in tension, the measured negative flexural moments from the known geometry and applied shear forces were compared to the computed values (M_{eq}) using section analyses of equivalent L-shaped beam cross sections. The results are presented in Figure 5.6 where the effective slab widths recommended in two code provisions, namely ASCE 41 and that of the New Zealand Society for Earthquake Engineering [NZSEE, 2006], are also indicated.

According to ASCE 41, the combined stiffness and strength for flexural and axial loading shall be calculated considering a width of effective flange on each side of the web equal to the smaller of: (1) the provided flange width, (2) eight times the flange thickness, (3) half the distance to the next web, or (4) one-fifth of the span for beams. When the flange is in compression, both the concrete and reinforcement within the effective width shall be considered effective in resisting flexure and axial loads. When the flange is in tension, longitudinal reinforcement within the effective width and that which is developed beyond the critical section shall be considered fully effective for resisting flexure and axial loads. In the NZSEE [2006], at each side of the beam centerline a value corresponding to the lesser of (1) one-fourth of the beam span, (2) half the span of the slab transverse to the beam under consideration, and (3) one-fourth of the span of the transverse edge beam, must be considered. In most cases including the tested four specimens, the last criterion for both ASCE 41 and NZSEE controlled the effective width.

Based on a comparison of the four test specimens, it was found that the contribution of the slab varied according to the strain level of the beam longitudinal reinforcement where this contribution was negligible when joint failure occurred prior to the yielding of the beam

144

longitudinal bars as in SP4 and increased from SP3 to SP2 to SP1 as the joint failure occurred at larger post-yield strain of the beam longitudinal bars. Note that the effective slab widths in the code provisions are estimated assuming that joints can fully sustain the flexural ductility (e.g., drift level of 2%) of L- or T-shaped beams. Hence, this effective slab width may not be appropriate in the case when joint failure precedes beam flexural failure, e.g., J-type failure in unreinforced joints. Further investigation is needed to clarify the effective slab width. In this study, slab top four reinforcing bars are considered for the contribution of slab to flexural strength of L-shape beams without taking into consideration the bottom bars because slab bottom bars are not fully developed, according to ASCE 41 as described above.

Figure 5.5   **Flexural cracks in the slab of SP3.**
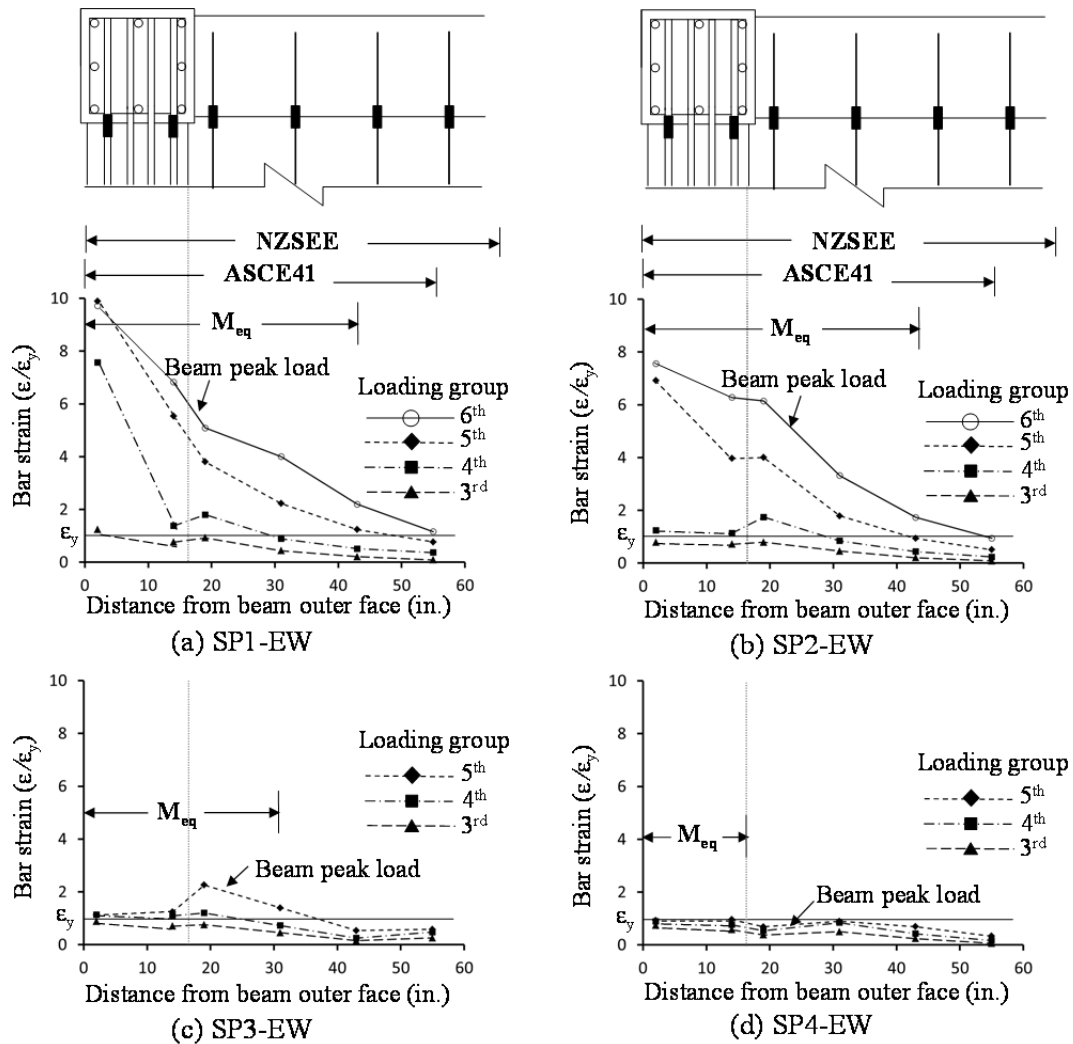
Figure 5.6   Strain and stress distributions of slab reinforcement.

5.7   EFFECT OF LOADING SEQUENCE

The lateral loading was applied in the EW beam prior to the NS beam in each group of cyclic loading. This alternation of the loading between the two directions made the peak load of each loading group generally greater in the EW direction than in the NS direction. As shown in Figure 5.7, the joint shear stresses of SP1 and SP2 were similar in both EW and NS direction until the beams yielded, while in SP3 and SP4, similar joint shear stresses were maintained up to 0.85% drift before yielding of the beams. Thereafter, larger joint shear stresses were induced in the EW direction than in the NS direction because of significant damage in the joint during the EW beam loading prior to the NS beam loading. Based on the strength reduction due to the loading sequence, the joint shear strengths for the EW beam loading are taken as representative of joint responses for developing backbone relationships presented in Chapter 6.

During the longitudinal beam loading, the transverse beam was subjected to torsion due to the slab connecting the two orthogonal beams. Note that the definitions of longitudinal and transverse beams were given in Chapter 1, where the former is the beam in the direction of

146

loading and the latter is the one in the direction perpendicular to the loaded beam. Two different types of cracks were observed in the transverse beam and joint panel during the longitudinal beam downward and upward loading. Inclined cracks took place in the transverse beam when the longitudinal beam was loaded down, as shown in Figure 5.8(a). Horizontal cracks developed at the top of the joint panel in the transverse direction when the longitudinal beam was loaded up, as shown in Figure 5.8(b). The mechanisms of these cracks are depicted using free body diagrams in Figure 5.8. These two types of cracks closed when the beam loading was switched to the same directional beam. For example, horizontal and inclined cracks formed in the joint and beam in the EW direction during the NS beam loading, as shown in Figure 5.8, but these cracks closed during the subsequent EW beam loading.

During each beam loading, the transverse beam was twisted by torsion because of the slab effect. The twisting angle was measured at three locations A, B, and C of the transverse beam, as shown in Figure 5.9. The increase of twisting angle in the transverse direction was concentrated between locations A and B for the longitudinal beam downward loading, while the twisting angle was uniformly distributed from A to C for the upward loading. Based on the crack pattern and the different variation of twisting angles in the transverse direction for the downward and upward loadings of the longitudinal beam, it can be concluded that twisting was localized around the inclined crack of the transverse beam when the longitudinal beam was loaded down. But during the longitudinal beam upward loading, the entire transverse beam twisted causing a horizontal crack at the top of the joint panel in the transverse direction.
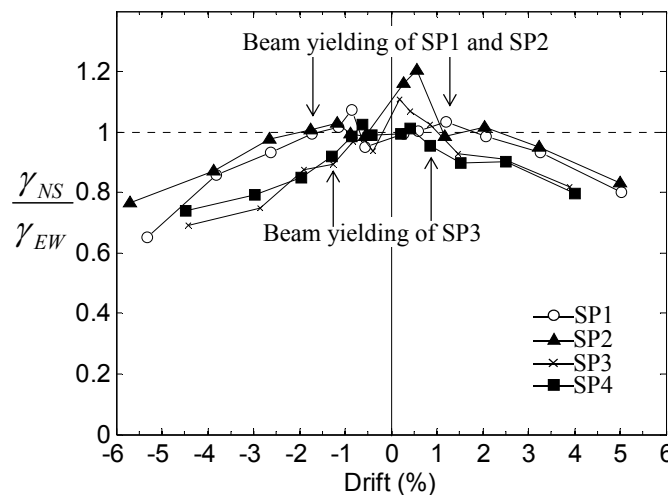
Figure 5.7   Comparison of applied load ratios between the EW and NS beams.
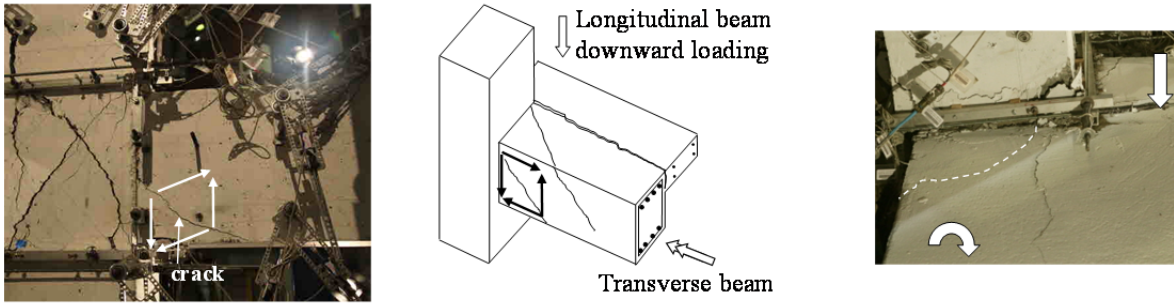
(a) inclined cracks in the EW beam during the NS beam downward loading
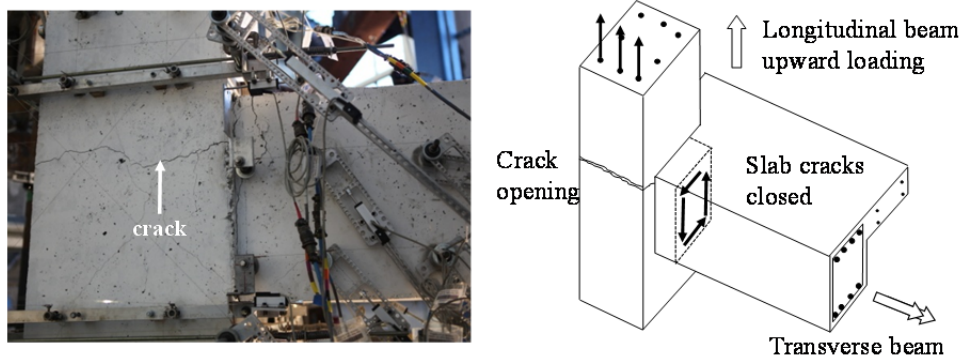
(b) horizontal crack in the EW joint during the NS beam upward loading

Figure 5.8   Crack pattern in the transverse beam during the longitudinal beam loading.
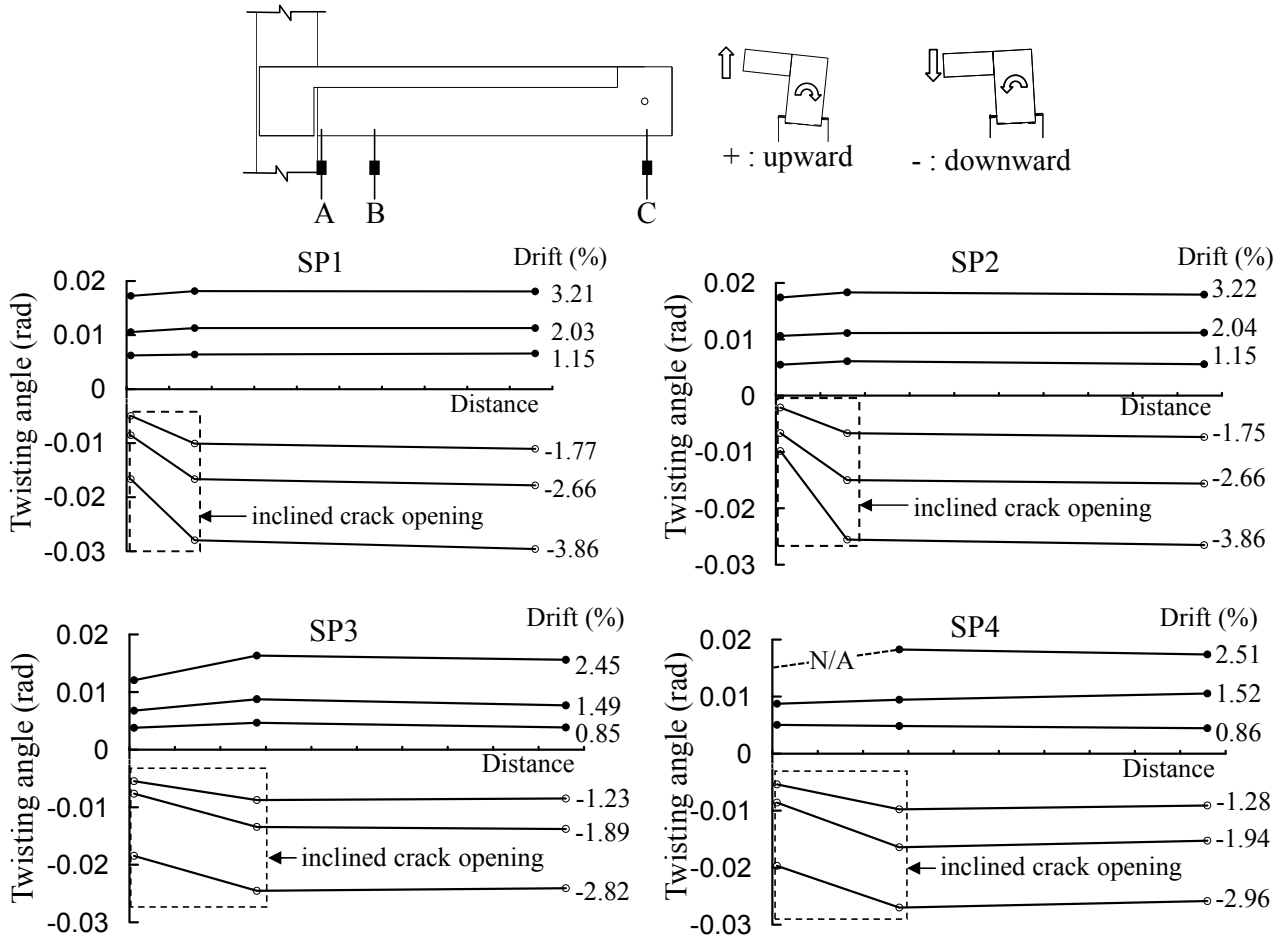
Figure 5.9   Twisting angles in the transverse (EW) beam during the longitudinal (NS) beam loading.

5.8   ROLE OF COLUMN INTERMEDIATE BARS

Hwang et al. [2005] claim that column intermediate bar(s) can carry vertical tension force F_v, as shown in Figure 5.10, if the bond capacity between the column longitudinal bars and surrounding concrete is maintained. To investigate the role of the column intermediate bars, the strain variation of these bars along the joint cross-section height was measured and the results are presented in Figure 5.11 and 5.12. In specimens SP1 and SP2 (having 8-#8 column longitudinal bars), the tensile strain at the joint mid-height location was less than either the strain at the joint top or the strain at the joint bottom. In specimens SP3 and SP4 (having 8-#10 column longitudinal bars), the tensile strain at the joint mid-height location was greater than the strains at the joint top or the strain at the joint bottom for some beam loadings; However, this is not clear evidence that a column intermediate bar acted as a tension tie in joint shear resisting mechanism. Unlike reinforced joints, it appears that two inclined struts between the two column bars did not develop simultaneously (see Figure 5.10) because of the steep angle and the bond deterioration around the column longitudinal bars.
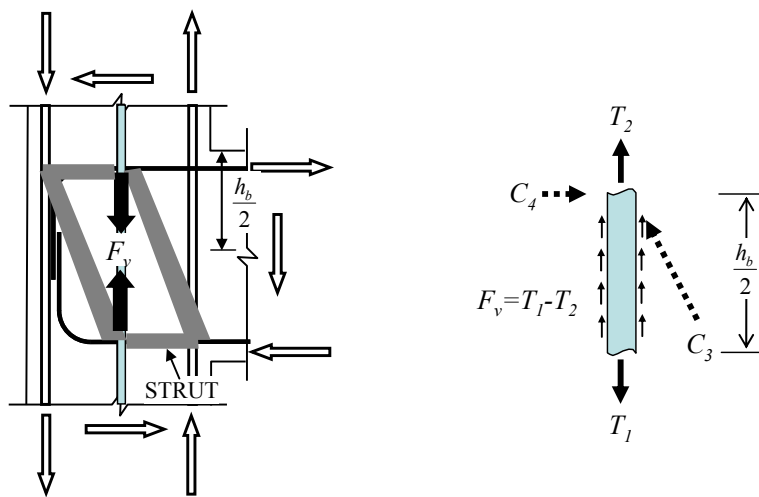
Figure 5.10   Role of column intermediate bars as a tension tie [Hwang et al. 2005].
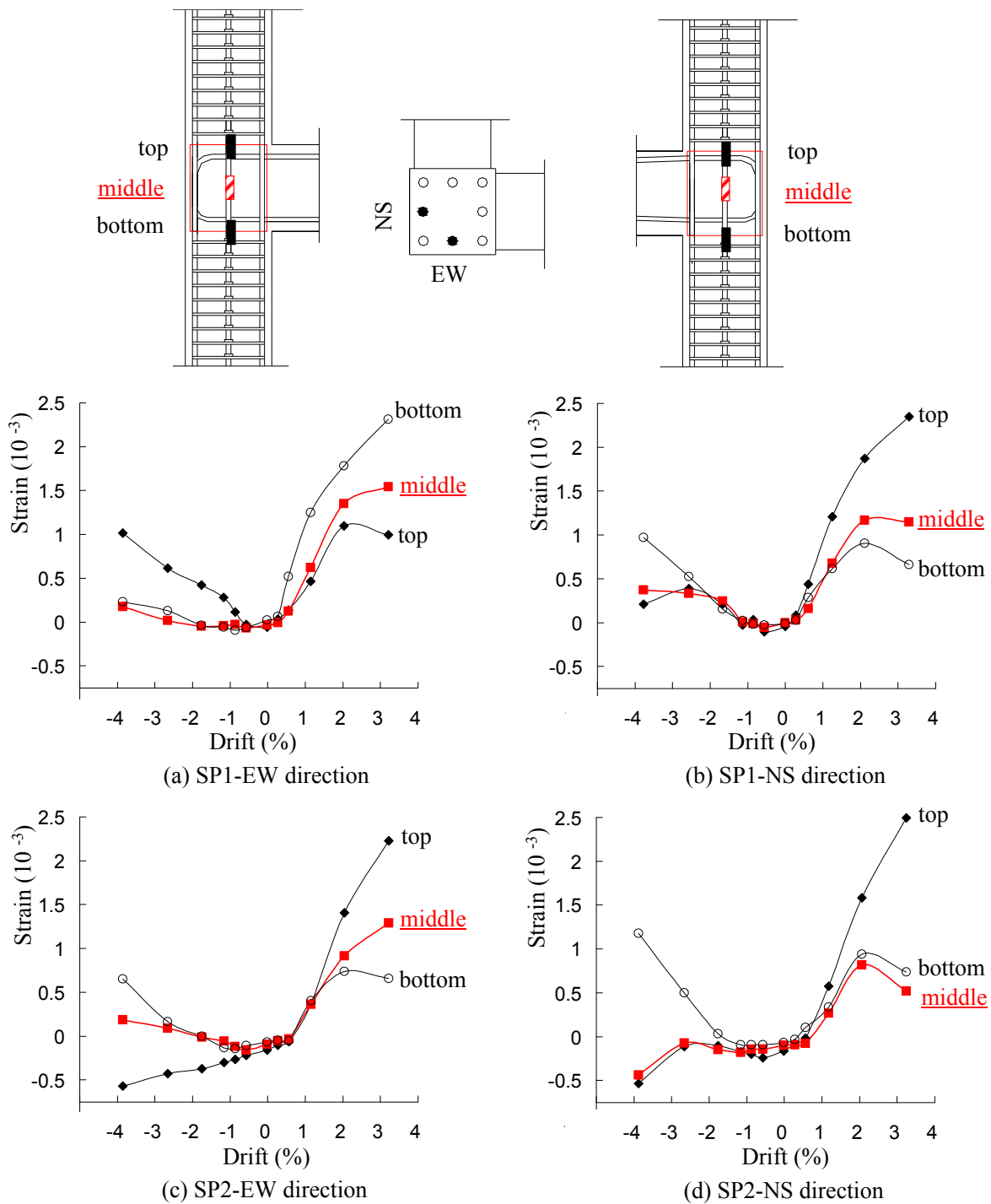
Figure 5.11   Strain distributions of column intermediate bars in SP1 and SP2.
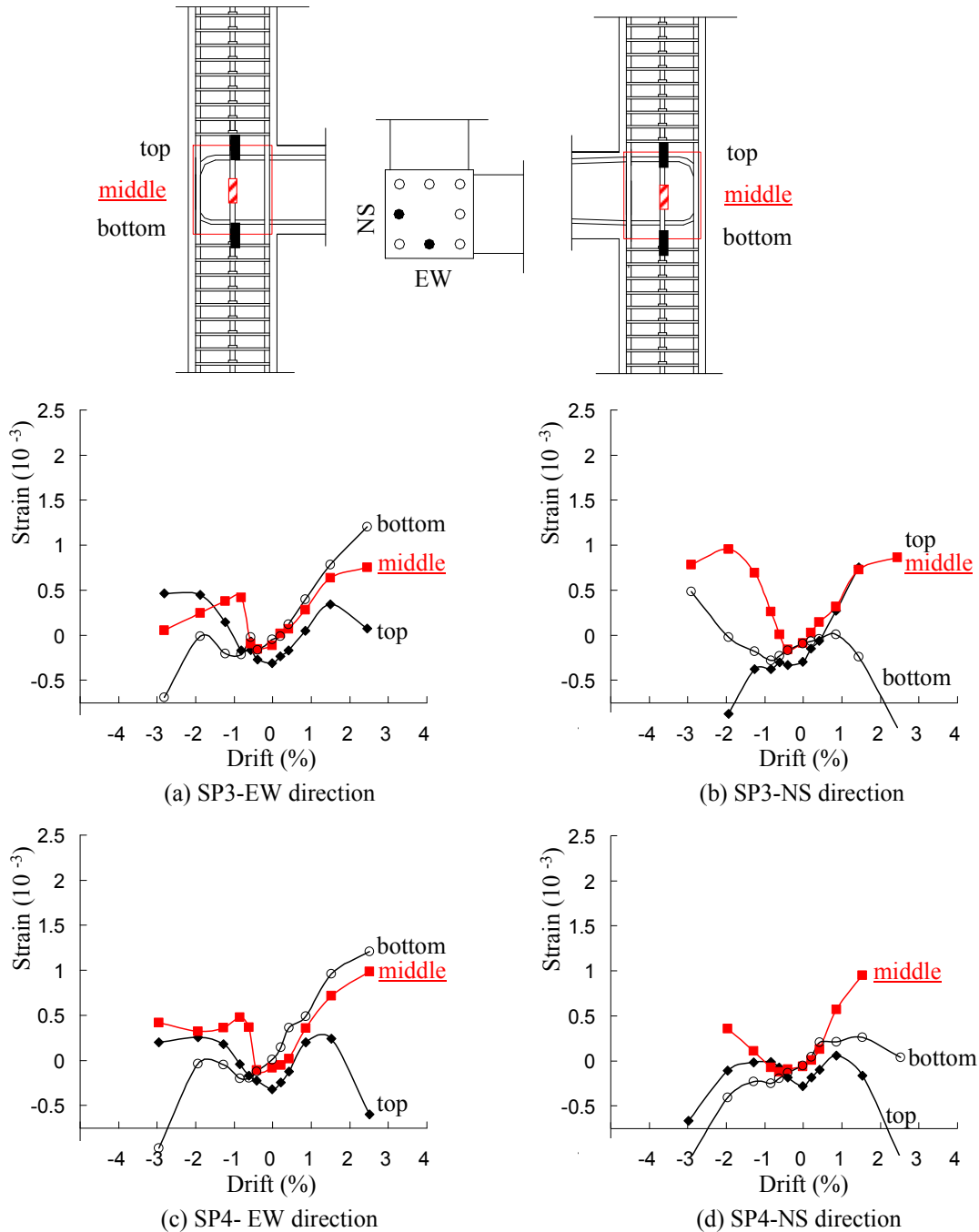
Figure 5.12   Strain distributions of column intermediate bars in SP3 and SP4.

5.9   DEFORMABILITY OF UNREINFORCED CORNER JOINT

In terms of the effects of joint aspect ratio and beam reinforcement ratio on joint shear strength, the trends and range of strength of the tested four corner joint specimens were similar to those of many previous exterior joint specimens constructed without transverse beams and floor slabs. Hence, the same joint shear strength can be applied for predicting the response of both planar

exterior joints and corner joints, which is consistent with the recommendation of ACI-ASCE 352-02.

Applying the SAT idealization to represent the joint shear resisting mechanism, the joint shear force was transferred to the beam and the column by compression through a diagonal strut as considered in the code provisions of USA and Japan [ACI 318-11 2011; ACI-ASCE 352-02 2002]; AIJ 1994], respectively. The unreinforced joint resembles an unconfined concrete rectangular cuboid idealized using a diagonal strut whose compressive strength is controlled by its compressive strain ε_0. This supports the hypothesis that the failure of unreinforced joints initiates at a certain joint shear strain, namely 0.005 rads in the ASCE joint shear stress-strain relationship and 0.007 rads according to Priestley [1997]. The failure of the four test specimens initiated when the joint shear strain reached a value between 0.006 rads and 0.008 rads.

To compare the joint shear strain responses of the four test specimens, the envelopes of the joint shear stress-shear strain responses in the EW direction were redrawn in Figure 5.13(a) with the ordinates expressed as the ratio of the joint shear stress of each loading cycle to the maximum joint shear stress, i.e., joint shear strength. These normalized envelopes are comparatively similar, meaning that the joint failure of the four specimens took place at different joint shear stress values due to the effects of the joint aspect ratio and the beam reinforcement ratio, but the joint shear strain values were not significantly affected by these two parameters. However, the negative slope of the envelopes was slightly steeper for high compressive column load (negative side) than for small compressive or tensile column load (positive side).

The contribution of the joint shear strain to the total drift is shown in Figure 5.13(b). A significant portion of the total drift was attributed to the joint shear strains in SP3 and SP4, whereas the joint shear strain of SP1 and SP2 contributed less. This is because, as mentioned above, the joint shear strain responses of the four test specimens were similar but SP1 and SP2 had (1) larger rotations at the beam-joint interface and (2) relatively less flexural strength of the beams, resulting in larger elastic and inelastic drifts. The different contribution of the joint shear strain to the total drift affected the global load-drift responses of SP3 and SP4, which had a high joint aspect ratio, and their response was relatively brittle compared to those of SP1 and SP2 with a low joint aspect ratio.

The specimens tested in this study did not show complete loss of axial load carrying capacity by the end of testing. This behavior is similar to that observed from tests of unreinforced interior joint specimens [Walker 2001; Alire 2002]. This gradual strength degradation was attributed to the presence of transverse beam and floor slab rather than to the well-confined beams and column. In other words, the damage of core concrete in the corner joints was retarded by the monolithically cast orthogonal transverse beam and floor slab.
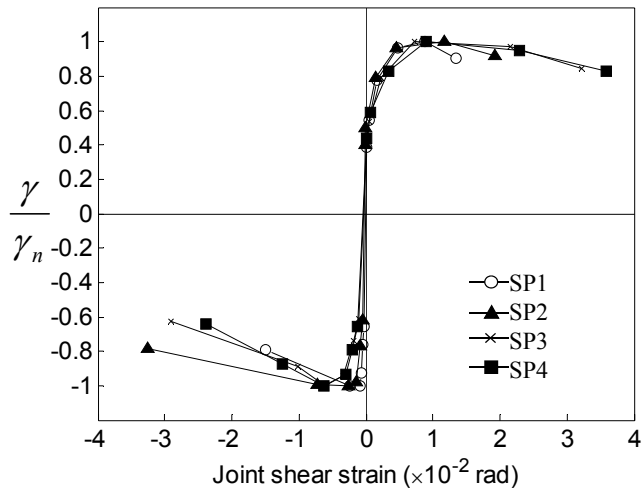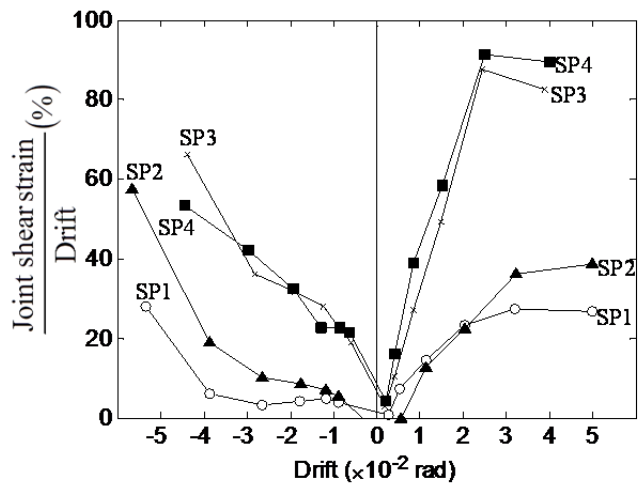
Figure 5.13   (a) Normalized joint shear stress-shear strain responses in the EW direction; and (b) contribution of the joint shear strain to the total drift in the EW direction.

154

6 Simulation of Reinforced Concrete Frames with Joint Flexibility

6.1 DEVELOPMENT OF BACKBONE RELATIONSHIPS

In conventional simulations of RC buildings, joints are modeled as a node where one-dimensional (1D) beam and column elements intersect, i.e., the orthogonality between beams and supporting columns is maintained during the analysis. However, this orthogonality is not sustained in unreinforced joints because of shear failure and shear deformation. To account for joint shear failure and flexibility in building simulations, a nonlinear joint macro-model using a single rotational spring was developed. Joint macro-models by Bidda and Ghobara [1999] and Lowes and Altoontash [2003] have used concrete softening models from Hsu [1988] and Vecchio and Collins [1986], respectively, to define the constitutive relationship of the joint panel. However, these softening models are inappropriate for lightly reinforced joints and especially for unreinforced joints [LaFave and Shin 2005]. Using test data obtained from the joint responses and visual observations, this study developed an empirically based backbone curve

For modeling of joint flexibility, two types of joint macro-models, namely explicit and implicit modeling, were considered. For explicit modeling, ASCE 41 proposes a joint shear stress-strain relationship for unreinforced exterior beam-column joints as shown in Figure 6.1(a) where the nominal joint shear strength is defined as $\gamma_n = 6$ psi$^{0.5}$ [0.5 MPa$^{0.5}$] for unreinforced exterior joints as presented in Table 2.1. Priestley [1997] also proposed a shear strength model for unreinforced exterior joints as shown in Figure 6.1(b). The joint shear strength V_n is determined by a limit of the principal tensile stress, $\sigma_1 = 5\sqrt{f_c'}$ psi $[0.42\sqrt{f_c'}$ MPa$]$ and the principal compressive stress, $\sigma_2 = 72.6 f_c'$ psi $[0.5 f_c'$ MPa$]$

$$V_n = A_g \sqrt{\sigma_1^2 + \sigma_1 \left(\frac{P}{A_g}\right)} \leq A_g \sqrt{\sigma_2^2 - \sigma_2 \left(\frac{P}{A_g}\right)} \tag{6.1}$$

This study adopted implicit modeling because it is a practical option for simulating a building with large number of degrees of freedom. To this end, joint shear strain (γ_{xy}) and rotation at the beam-joint interface (θ_s) due to bar slip and/or crack opening were measured separately, as shown in Figure 6.2. The rotation of the joint spring, θ_j, is defined as the sum of the joint shear strain and the rotation at the beam-joint interface, i.e., $\theta_j = \gamma_{xy} + \theta_s$. Note that

155

rotation at the column-joint interface is assumed to be negligible because of the considered strong column-weak beam configuration, as mentioned before.
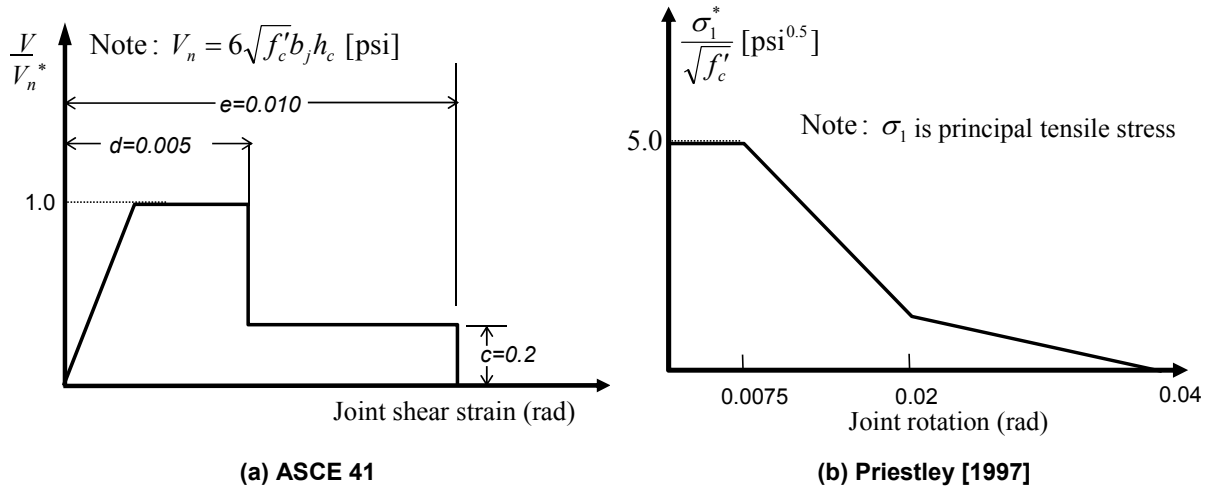
Figure 6.1 Backbone curve of unreinforced exterior joints.

$$\gamma_{xy} = \frac{1}{4}\left\{\sum_{i=1,2,5,6}\left(\omega'_i - \omega^0_i\right) - \sum_{j=3,4,7,8}\left(\omega'_j - \omega^0_j\right)\right\}$$

(a) joint shear strain

$$\theta_s = \frac{\Delta_b - \Delta_t}{d_b}$$

(b) rotation at the beam-joint interface
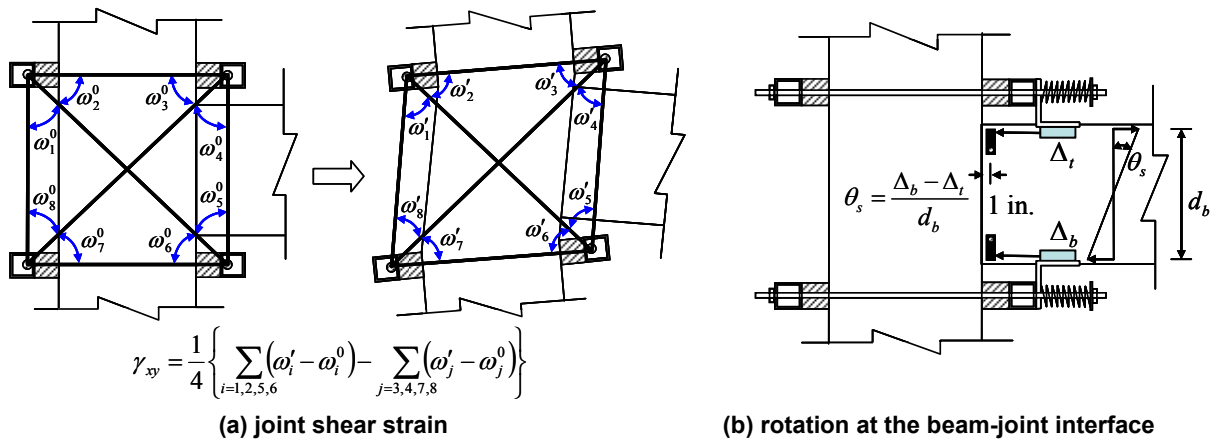
Figure 6.2 Instrumentation for measuring the joint deformations.

The joint shear stress-shear strain relationships in the EW direction of the four specimens are plotted in Figure 6.3. Note that the joint shear stresses on the vertical axes of these plots were normalized by $\sqrt{f'_c}$, i.e., $\gamma = v_{jh}/\sqrt{f'_c}$. The average joint shear strains of the values measured at the downward and upward peak loads were 0.006 rads for SP1, 0.007 rads for SP2 and SP3, and 0.008 rads for SP4. The evaluated joint shear stress-shear strain responses were compared to two backbone curves proposed by ASCE 41 and Priestley [1997] in Figure 6.3. In addition to the large discrepancy in the strength prediction, these latter two models are conservative for predicting post-peak drift capacity of unreinforced corner joints.

156

The envelopes relating bar stress to deformation measured at the beam-joint interface of the four specimens are plotted in Figure 6.4(a) as illustrated by the insert in the figure where the shown deformation is the relative deformation between the column and the beam. The bar stress did not reduce after the peak loads [marked by arrows for the four specimens in Figure 6.4(a)], implying that the capacity of the anchorage was maintained in the loading subsequent to the peak loads. Note that the deformation at the beam-joint interface was not significantly dependent on the bar stress, which is related to the beam longitudinal reinforcement ratio. This observation is based on measuring similar deformations at the peak load for each pair of specimens having different beam reinforcement ratio (and accordingly different stress in the beam longitudinal bars) but having same joint aspect ratio, i.e., (SP1 and SP2) and (SP3 and SP4). Note that the average deformation at the peak loads was smaller in the high joint aspect ratio specimens, i.e., 0.13 in. for SP3 and SP4, than in the low joint aspect ratio specimens, i.e., 0.21 in. for SP1 and SP2. This smaller deformation leads to the smaller rotation at the beam-joint interface of SP3 and SP4 as shown in Figure 6.4(b). Accordingly, it is postulated that the rotation at the beam-joint interface is more influenced by the joint aspect ratio than by the beam reinforcement ratio.
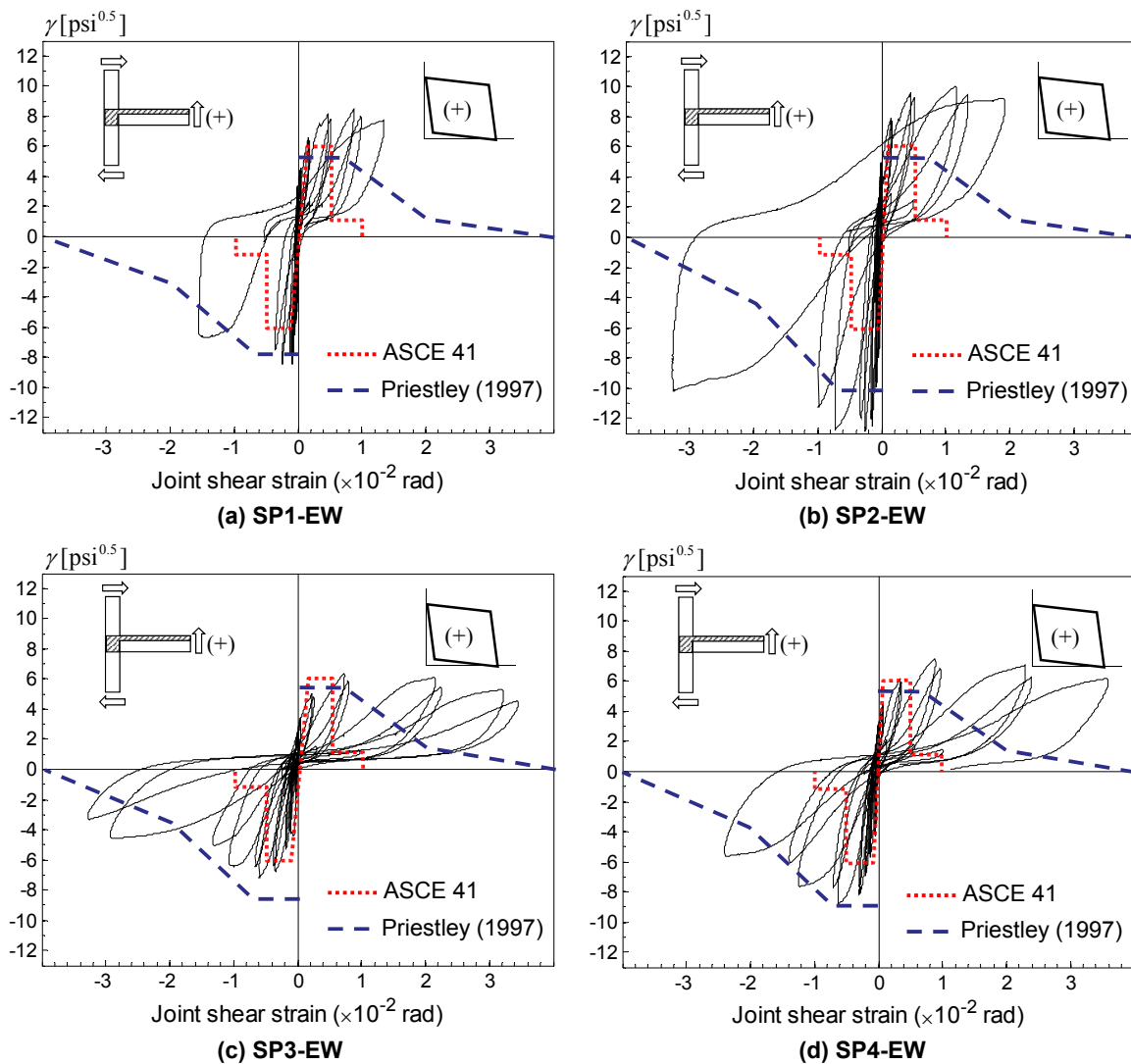
Figure 6.3   Comparison of joint shear stress versus rotation responses.

157

The above joint shear stress versus shear strain and joint shear stress versus rotation at the beam-joint interface responses are redrawn in Figure 6.5 where the joint shear stresses in the ordinate are normalized by the overall maximum, i.e., joint shear strength.

Based on the joint shear stress-rotation measurement and visual observations of the tested four specimens, a multi-linear backbone relationship (Figure 6.6) was developed based on the peak values of the first cycle to a specific level of displacement in the joint responses (see Figure 6.5) and the joint damage progression observed from the tested four specimens. Modeling parameters were defined at the following responses: (1) λ_1 and θ_a represent initial joint cracking, (2) λ_2 and θ_b represent either beam reinforcement yielding or significant opening of existing joint crack, (3) θ_c represents either existing joint crack further propagation or additional joint crack opening at the peak loading, and (4) λ_3 and θ_d represent the residual joint shear stress ratio and rotation when the damage of joint is severe. Note that the joint shear strength corresponding to V_n can be accurately predicted by the proposed joint shear strength models. Each modeling parameter is evaluated in Table 6.1.

(a) bar stress versus deformation (b) joint shear stress versus rotation
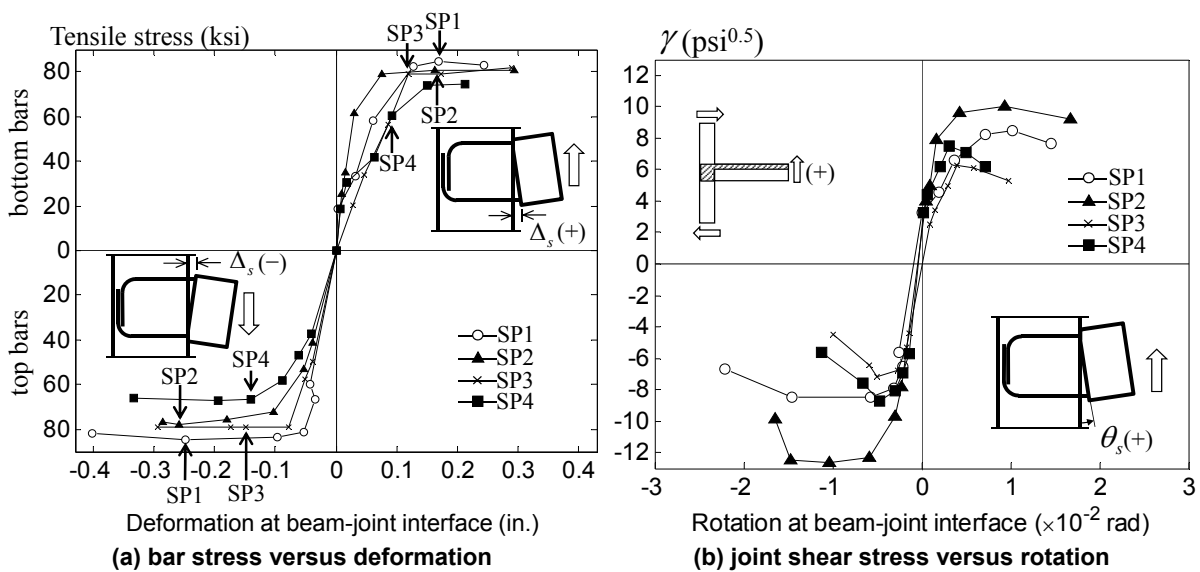
Figure 6.4   Measured responses at the beam-joint interface.

158
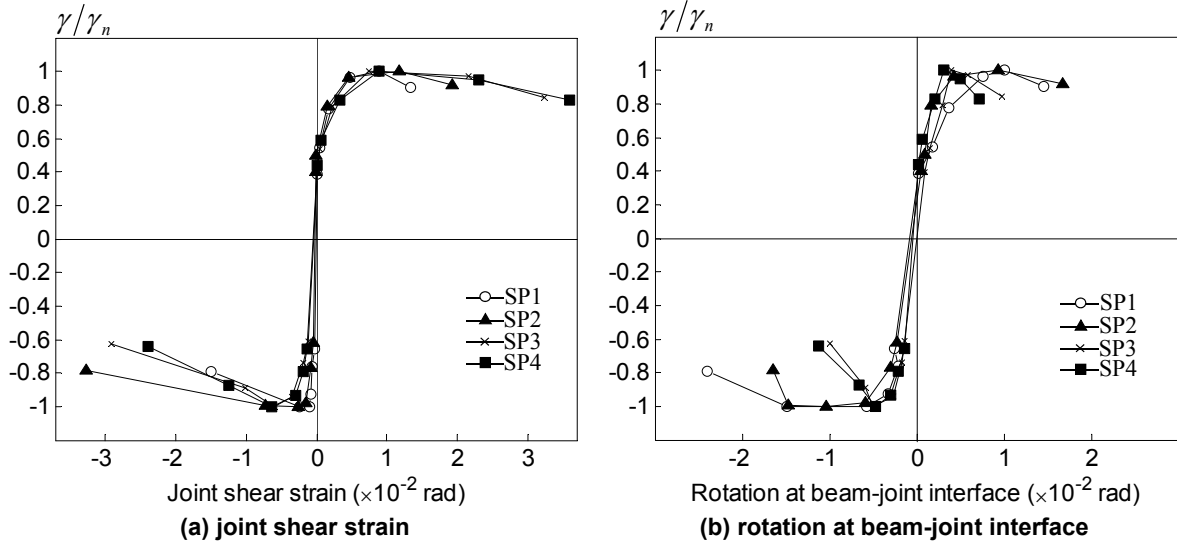
Figure 6.5   Normalized joint shear stress versus joint deformation.

From the four test specimens, the parameters λ_1, λ_2, θ_a and θ_b are found to be insensitive to the joint aspect ratio and the beam longitudinal reinforcement ratio so that they are selected as listed in Table 6.1. The values of these parameters are defined based on the mean of the values measured from the four test specimens. Note that the parameter θ_b was selected as 0.0050 instead of 0.0057 in this study for better comparison with the ASCE 41 backbone. The parameter θ_c representing joint rotation at the peak load was affected by the joint aspect ratio such that the value of θ_c became smaller as the joint aspect ratio increased. Changing the beam longitudinal reinforcement ratio for the specimens with the same aspect ratio made little difference in the value of θ_c. Therefore, θ_c is intended to reflect the effect of the joint aspect ratio and its equation is proposed as follows,

$$\theta_c = 0.0325 - 0.0125\left(h_b/h_c\right) \tag{6.2}$$

Equation (6.2) gives 0.0200 and 0.0116 for the joint aspect ratios (h_b/h_c) of 1.00 and 1.67, respectively, and these values are close to 0.0196 (mean value of θ_c from SP1 and SP2) and 0.0113 (mean value of θ_c from SP3 and SP4), respectively. Note that Equation (6.2) shows good agreement with the results of previous tests reported by Clyde et al. [2000] and Pantelides et al. [2002]. The parameters λ_3 and θ_d were selected by fitting the negative slope of the global load-displacement responses of the four test specimens because the instruments were not reliable after severe joint damage. These selections are

$$\lambda_3 = 0.5, \quad \theta_d = \theta_c + 0.03 \tag{6.3}$$

Knowing the dimensions of the RC frame and its joints, the moment at the center of the joint, M_j, is obtained from the joint shear stress as follows,

$$M_j = \frac{V_{jh}}{\eta}, \quad \eta = \frac{L}{\left(L + h_c/2\right)jd_b} - \frac{1}{H} \tag{6.4}$$

159

To express the backbone relationship in terms of joint moment and rotation, the vertical axis values are transformed into the joint moment using Equation (6.4) where $V_{jh} = v_{jh} b_j h_c$ and $v_{jh} = \gamma \sqrt{f_c'}$.
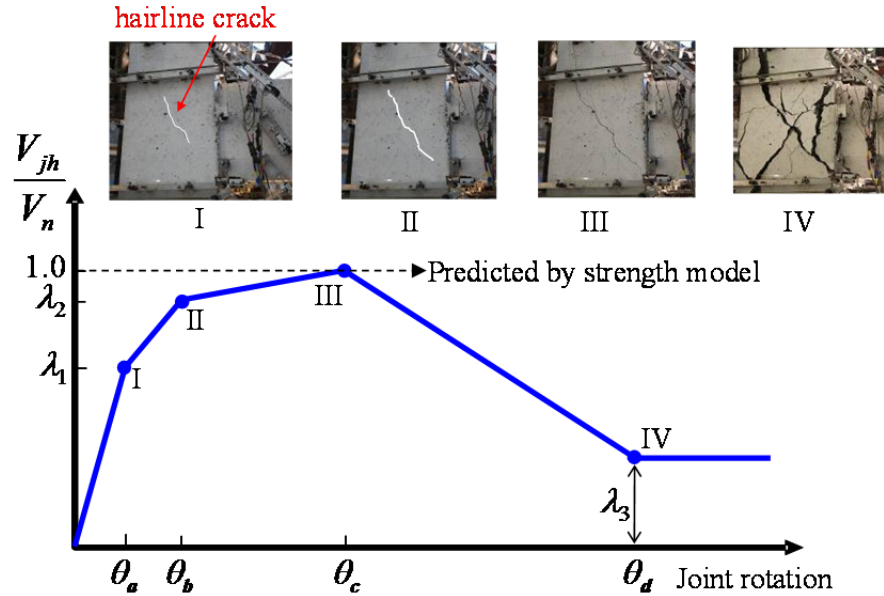
Figure 6.6   **Proposed backbone relationship from the test specimens.**

Table 6.1   **Evaluation of backbone curve parameters.**

	SP1		SP2		SP3		SP4		Mean	Proposed Model
	Down[*1]	Up[*2]	Down[*1]	Up[*2]	Down[*1]	Up[*2]	Down[*1]	Up[*2]		
λ_1	0.66	0.54	0.63	0.78	0.61	0.54	0.65	0.59	0.63	0.65
λ_2	0.94	0.87	0.92	0.90	0.95	0.80	0.93	0.82	0.88	0.90
θ_a	0.0025	0.0024	0.0027	0.0032	0.0019	0.0020	0.0027	0.0013	0.0023	0.0025
θ_b	0.0050	0.0068	0.0054	0.0057	0.0061	0.0052	0.0059	0.0055	0.0057	0.0050
θ_c	0.0170	0.0189	0.0218	0.0207	0.0111	0.0114	0.0105	0.0121	-	Eq. (6.2)
	Mean of SP1 and SP2 = 0.0196				Mean of SP3 and SP4 = 0.0113					

[*1]beam loaded downward
[*2]beam loaded upward

6.2   VERIFICATION OF PROPOSED BACKBONE RELATIONSHIP

6.2.1   Corner Joint Specimens

Simulations were performed on the tested four corner joint specimens using the proposed backbone curve for verification. Since the lateral loads were applied in an alternating pattern

between the two orthogonal beams, two-dimensional (2D) analysis was assumed to be reasonable to simulate separately the responses of the EW and NS directions. To address the effect of the slab, the beam cross section was modeled as an L-shape with effective slab width according to ASCE 41. The strength and ultimate strain of core concrete confined by hoops for column and closed stirrups for beam were calculated using the models by Mander et al. [1988], Qi and Moehle [1991], and Saatçioğlu and Razvi [1992].

The beam-column subassemblies were modeled with two types of idealizations using OpenSees [2010]. The first considers the 1D beam and column elements intersecting at the joint (rigid joint), Figure 6.7(a), while the second is similar to the first but the joint region is modeled with a rotational spring and joint offsets, see Figure 6.7(b). The beam and column elements were modeled using *nonlinearBeamColumn* elements based on the force method formulation where there was no need to define a plastic hinge length. Five integration points are assigned to each element. The constitutive model for the joint rotational spring was defined as the relationship between moment and rotation at the center of the joint panel which is calculated from the proposed backbone curve shown in Figure 6.6. The $M_j - \theta_j$ relationship shown in Figure 6.8 was implemented using a multi-linear hysteresis material (*Pinching4*) available in OpenSees [2010]. The envelope of each positive and negative direction consists of a quad-linear curve that connects four key points that are defined by the parameters of the proposed backbone curve. Note that in Figure 6.8, nM_n and pM_n represent the respective negative and positive moments obtained from the joint shear strength, γ_n. θ_{min} and $M(\theta_{min})$ [θ_{max} and $M(\theta_{max})$] are the minimum (maximum) rotation and the corresponding moment in the hysteretic response until the current excursion.

The adopted hysteresis rules follow a tri-linear unloading-reloading path as follows: (1) linear unloading with the initial stiffness until the moment reaches a fraction (defined by the parameter uForce) of nM_n or pM_n; (2) linear pinching until reaching the reloading points specified as fractions (defined by the parameters rDisp and rForce) of θ_{min}, $M(\theta_{min})$ or θ_{max}, $M(\theta_{max})$, see Figure 6.8; and (3) upon reaching the reloading points, linear loading to θ_{min}, $M(\theta_{min})$ or θ_{max}, $M(\theta_{max})$. The parameters for unloading and reloading in *pinching4* material are selected as follows: uForce=0.05, rForce=0.25, and rDisp=0.5 to match the experimental load-drift responses, which show that the beam loads at zero displacement were positive (i.e., upward) because the slab pulled down the beam as the transverse beam orthogonal to the loaded beam remained at a negative position. Note that the strength and stiffness degradation parameters in *pinching4* material [OpenSees, 2010] were ignored for simplicity and because these material damage parameters are insignificant in modeling structural collapse [Haselton et al. 2008]. The joint panel finite size represented by rigid links in Figure 6.7(b) were modeled by the joint offset command in OpenSees [2010].
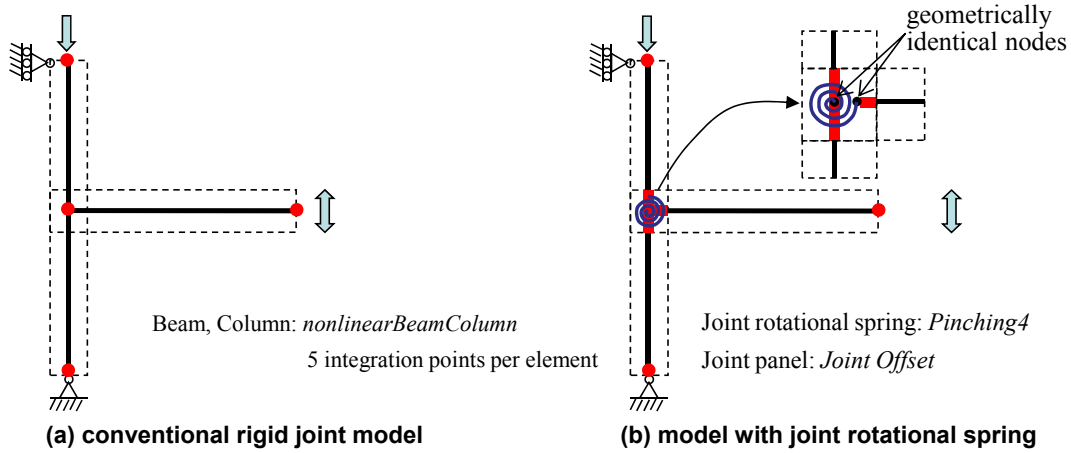
Figure 6.7 Modeling of beam-column subassemblies of the tested corner specimens.
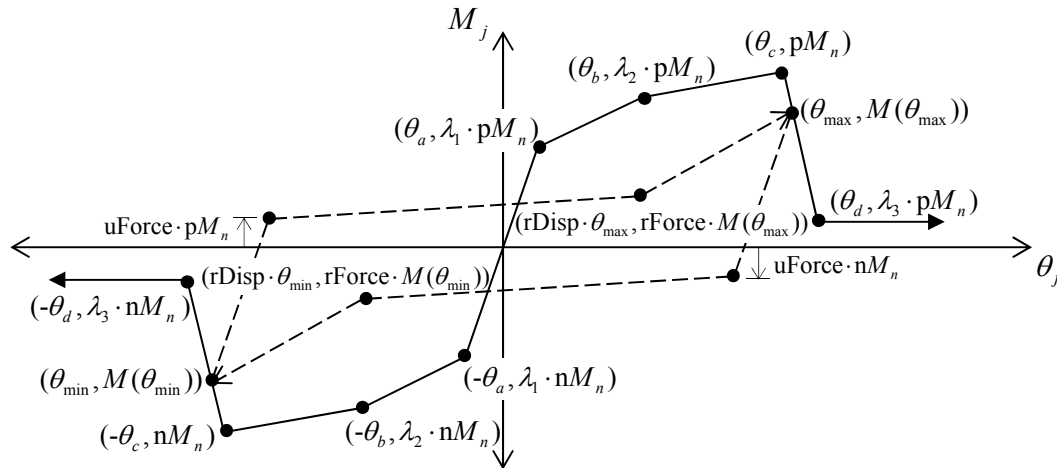
Figure 6.8 Modeling of beam-column subassemblies of the tested corner specimens.

The simulated load-displacement responses are compared to the test results in Figure 6.9 where the post-peak strength degradation of the tested corner joint specimens was gradual with most of damage concentrated in the joint region. This moderate strength degradation is attributed to the presence of transverse beam and floor slab rather than to the well confined beams and column. In other words, it is believed that the damage of the core concrete in the corner joints was reduced by the monolithically cast orthogonal transverse beam and floor slab. Further investigation is needed to support this conclusion. In the simulations with the proposed backbone curve, the strengths of the four specimens are calculated using the simplified model, Equation (2.32). Furthermore, additional simulations were performed using the ASCE 41 backbone curve with explicit addition of a bilinear bond-slip model [Lehman and Moehle 2000] at the beam-joint interface and the envelopes of the simulated responses are included as thick solid lines in Figure 6.9. Based on a comparison of the simulated versus the test results, the implicit joint macro-modeling with the proposed backbone curve accurately predicted the load-displacement responses of the four specimens, with slight discrepancies at the peak loads due to the shear strength prediction imperfection using the simplified model. The rigid joint model, however,

clearly did not predict the responses adequately. Moreover, the ASCE 41 backbone curve with the added bond-slip model [Lehman and Moehle 2000] did not successfully reproduce the load-displacement responses because it underestimated the shear strength and post-peak drift capacity, as shown in the joint responses in Figure 6.3. In addition, the contribution of the bar slip model was negligible, except for specimen SP3, because the beam longitudinal bar stresses remained elastic at the maximum joint shear stresses predicted by the ASCE 41 strength recommendation.
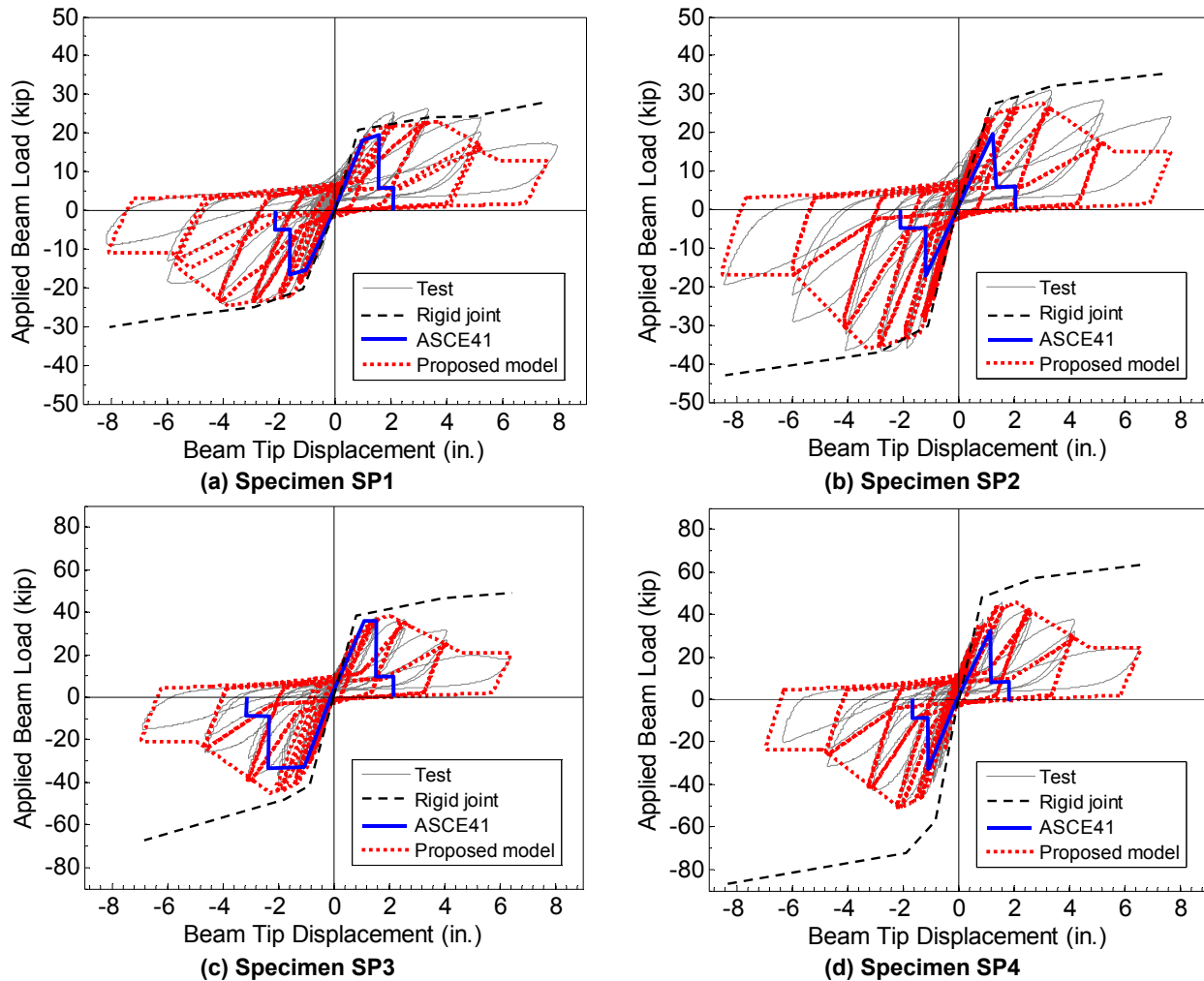
Figure 6.9   **Comparison of simulated and experimental results of tested corner joints.**

6.2.2 Four Planar Exterior Joint Specimens

Four unreinforced exterior joint specimens without lateral beams and floor slab, referred to as planar (2D) exterior joints, tested by Wong [2005] are selected for verifying the proposed backbone curve for joint aspect ratios ranging from 1.0 to 2.0. Material properties, test set up and details of the selected four specimens are presented in Table 6.2 and Figure 6.10. The joint aspect ratios of specimens BS-L-300, JA-NN03, BS-L-450, and BS-L-600 are 1.00, 1.33, 1.50, and 2.00, respectively. Specimens JA-NN03 and BS-L-450 were tested using load control until the beam yielded; thereafter, testing continued by displacement control, while specimens BS-L-

300 and BS-L-600 were tested under displacement control only. The column axial loads were kept constant at $0.03 f_c' A_g$ for JA-NN03 and $0.15 f_c' A_g$ for the other three specimens.

Table 6.2   Material properties of specimens by Wong [2005].

	Concrete [ksi (MPa)]		Yield strength of reinforcing bars [ksi (MPa)]
	Cube strength	**Cylinder strength**	
BS-L-300	6.17 (42.6)	4.94 (34.1)	
JA-NN-03	8.12 (56.0)	6.49 (44.8)	75.4 (520)
BS-L-450	5.59 (38.6)	4.48 (30.9)	
BS-L-600	6.59 (45.5)	5.28 (36.4)	
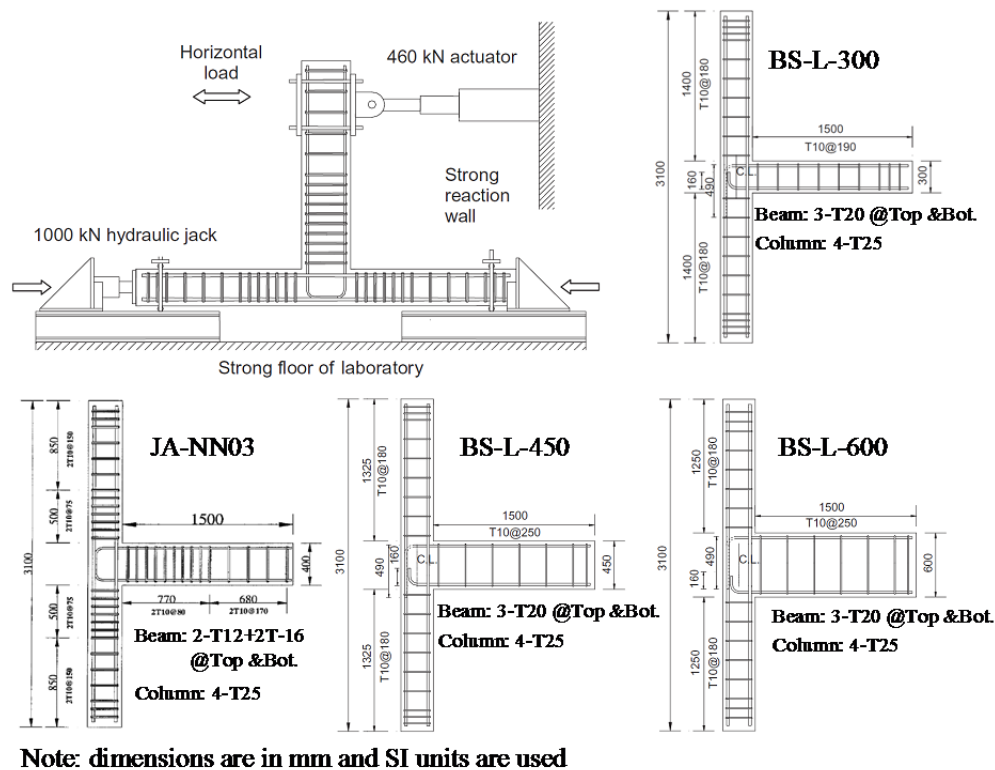
Figure 6.10   Details of planar unreinforced exterior joint specimens [Wong 2005].

The force-displacement responses of the four specimens were simulated by modeling the joints with rotational springs based on the proposed backbone curve depicted in Figure 6.11. For these simulations, the displacement histories were reproduced from the load-displacement plots illustrated in Wong [2005]. The shear strengths of the selected specimens were predicted using the simplified model. Figure 6.11 compares the simulated responses in dashed lines with the test result as solid lines. Note that the dashed horizontal lines in Figure 6.11 for the specimens with low joint aspect ratios, namely BS-L-30 and JA-NN03, indicate the experimentally determined yield levels of the beam longitudinal reinforcement.

164

For each specimen, the simulated responses are symmetric for both loading directions because beam longitudinal bars are identically placed at the top and bottom without an overhanging slab (unlike the corner joint simulations discussed in the previous subsection). In contrast, the experimental responses were not symmetric because the joint strength was not maintained for both loading directions if the joint was severely damaged by the previous rightward or leftward loading. The simulations using the proposed model were in good agreement with the experimental responses in terms of the displacement at the peak force and post-peak behavior, although the predicted peak forces are a little mismatched, arising from imperfection of the model predictions. Consequently, the simulations of the four specimens tested by Wong [2005] reasonably confirm the adequacy of the proposed backbone curve for simulating the seismic response of unreinforced planar exterior joints.

(a) BS-L-300 (h_b/h_c=1.00)

(b) JA-NN03 (h_b/h_c=1.33)

(c) BS-L-450 (h_b/h_c=1.50)

(d) BS-L-600 (h_b/h_c=2.00)
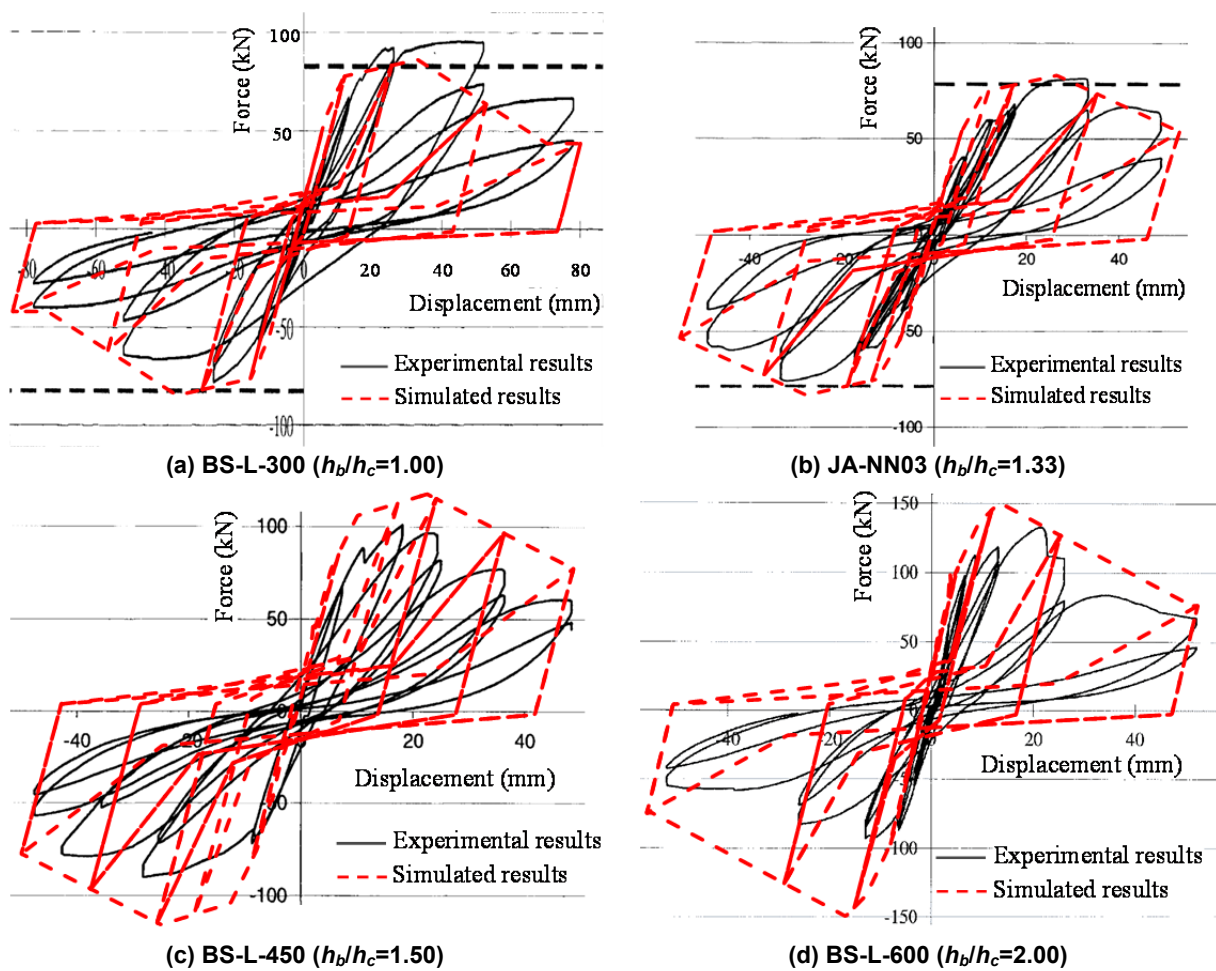
Figure 6.11   Simulations of four specimens tested by Wong [2005] using the proposed model.

6.3   MODELING OF INTERIOR AND ROOF JOINTS

For analysis of a whole building frame, strength predictions and backbone curves for interior and roof joints are also needed in addition to those for previously determined exterior (including

corner) joints. A principle of joint shear strength recommendations in ACI 352-02 and ASCE 41 provisions was adopted for prediction of shear strength for unreinforced interior and roof joints, as illustrated in Figure 6.12. This principle is that joint shear strength is affected by joint confinement conditions provided by the surrounding beams and columns, and there exists certain shear strength ratios among the different types of joints. Table 6.3 presents the ratio of shear strengths for three joint types with respect to the exterior joint shear strength. Note that the strength ratio factor for interior joints is selected as the ratio obtained from the recommendations of ASCE 41 because the ratio per ACI 352-02 significantly underestimates the maximum shear strength of interior joints ($\gamma_n = 15$ psi$^{0.5}$) compared to the results of interior joint specimens tested by Alire [2002] where the measured maximum shear strength was $\gamma_n = 25$ psi$^{0.5}$. Using the strength ratio factor, Γ, the simplified model was modified for predicting the joint shear strengths for interior and roof joints as follows,

$$V_n = k \left[\Gamma \times 12 \sqrt{f_c'} \, b_j h_c \frac{\cos \theta}{\cos(\pi/4)} \right]; \quad \text{psi units} \tag{6.5a}$$

$$k = 0.4 + 0.6 \left(\frac{SI_j - X_1}{X_2 - X_1} \right) \leq 1.0, \quad X_1 = \Gamma \times 4 \frac{\cos \theta}{\cos(\pi/4)},$$

$$X_2 = \Gamma \times 12 \frac{\cos \theta}{\cos(\pi/4)}; \quad \text{psi units} \tag{6.5b}$$

where Γ is listed in the last column of Table 6.3. Note that the joint shear index equation presented in Equation (2.13) is also applicable to other joint types because it is based on global equilibrium. For interior joints, the total cross-sectional area of beam longitudinal reinforcement in tension becomes the sum of the cross-sectional area of top bars in one side of the joint and bottom bars in the other side of the joint. For roof joints, the height (H) between upper and lower column inflection points used in Equation (2.13) was taken as half of the top-story height.
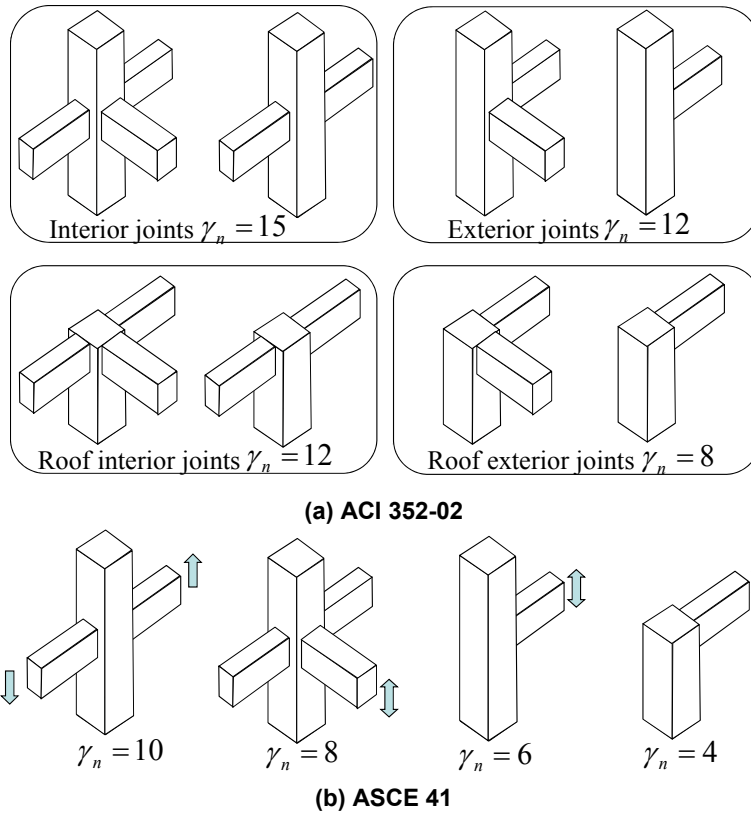
(a) ACI 352-02

(b) ASCE 41

Figure 6.12   Joint shear strengths code recommendations.

Table 6.3   Ratios of shear strengths of different joint types.

Joint type	ACI 352-02		ASCE 41		Selected
	γ_n	Γ^{*1}	γ_n	Γ^{*1}	Γ^{*1}
Exterior	12	1.00	6	1.00	1.00
Roof exterior	8	0.66	4	0.66	0.66
Interior	15	1.25	10	1.67	1.67
Roof interior	12	1.00	6^{*2}	1.00	1.00

[*1] $\Gamma = \gamma / \gamma_{exterior}$

[*2] This value is not explicitly specified but it can be postulated that this joint type has similar strength to that of the exterior joint because these two joints are geometrically identical with a 90° turn.

The modeling parameters of the backbone curve for an interior joint may be different from those for an exterior joint because two longitudinal beams are framing into the interior joints instead of one beam in the exterior joints. To determine the modeling parameters of the backbone curve and to evaluate the above modification of the shear strength prediction for interior joints, four unreinforced interior joint specimens tested by Alire [2002] were simulated with varying parameters of the backbone curve to best fit the test results. The simulations with

the selected modeling parameters as dashed lines were compared to the test results shown in Figure 6.13. The strength predictions were comparatively acceptable even though the predictions were somewhat conservative, especially for positive column shear in Figure 6.13(d).

The selected joint rotation parameters of the backbone curve, θ's in Figure 6.6, for all unreinforced beam-column joint types are presented in Table 6.4. Because of the lack of test data on unreinforced roof joints, it is assumed that the proposed strength prediction and backbone curves for exterior and interior joints (located in lower and middle stories) can be used for exterior and interior joints in the top story, respectively. Note that other parameters for the backbone curve in terms of normalized joint shear force (λ's in Figure 6.6) were kept the same for all joint types as those defined in Figure 6.6.

Table 6.4 Selected joint rotation parameters of the backbone curves for different types of joints.

Joint type	θ_a	θ_b	θ_c	θ_d
Exterior	0.0025	0.005	$0.0325 - 0.0125 \left(h_b / h_c \right)$	$\theta_c + 0.03$
Roof exterior				
Interior	0.0050	0.010		
Roof interior				

(a) PEER-0850 (b) PEER-0995

(c) PEER-1595 (d) PEER-4150
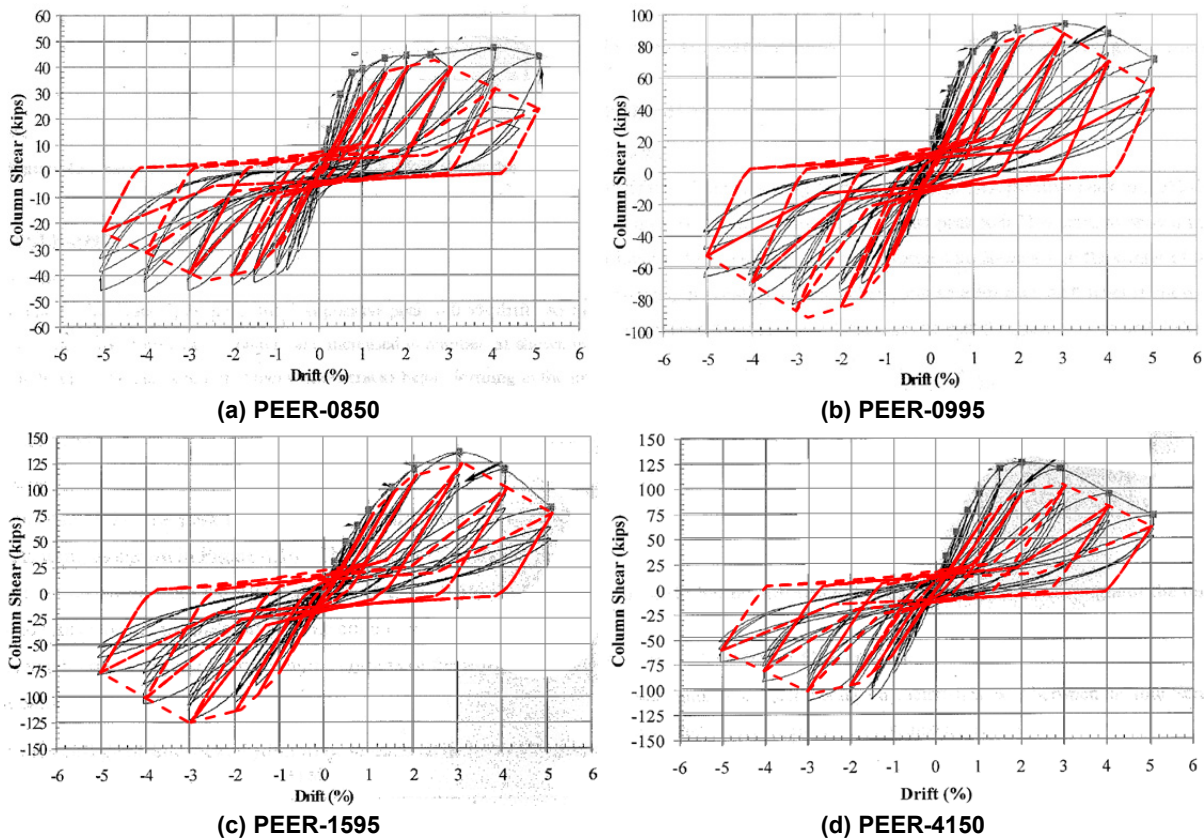
Figure 6.13   Simulations of tested four interior joint specimens [Alire 2002].

168

6.4 BUILDING FRAME SIMULATIONS WITH JOINT FLEXIBILITY

6.4.1 Descriptions

Three hypothetical building frames were designed with guidelines from the design details of the Van Nuys Holiday Inn building model [Krawinkler 2005] and used as the prototype of the test matrix. The transverse frame of the structure, which has three bays, is considered for the presented simulations. The lateral load resisting system of the considered frames is RC moment frame. Designed per Los Angeles City Building Code 64 and built in 1966, the design details of this structure can be considered to represent non-ductile older-type RC buildings. The frame dimensions, beam and column cross-sections, and design details are presented in Figure 6.14.

A reference building frame is designed to be identical to the original details of the Van Nuys Holiday Inn, except for the shear reinforcement in the columns and beams as discussed below. This building frame is referred to hereafter as "Type-I"; the design details are presented in Table 6.5. From the shear strength prediction of the beam-column joints in Type-I frame using the simplified model, the shear strengths of the beam-column joints were close to the lower bound at which the failure of the beam-column joint occurs at the ultimate flexural strength of the beams. To investigate the change of the lateral response for different levels of joint shear strength, two additional building frames were considered by simply increasing the yield strength of the beams, $f_{y,\text{beam}}$, and columns, $f_{y,\text{column}}$, from those used in Type-I building frame. With the increase of $f_{y,\text{beam}}$ and $f_{y,\text{column}}$ by 25%, the shear strengths of the beam-column joints in the second building frame (referred to as "Type-II") were located between the upper and lower bounds so that the failure of the beam-column joints is accompanied by yielding of the beams longitudinal reinforcement but less than their ultimate strengths. The beam-column joints in the third building frame (referred to as "Type-III") were specified with the increase of $f_{y,\text{beam}}$ and $f_{y,\text{column}}$ by 62.5% so that most of the beam-column joints were subjected to shear failure prior to yielding of the beams longitudinal reinforcement.

Modeling all the seismic deficiencies found in older RC framed structures, especially shear-critical columns, will change the output of these simulations because of premature column shear failures, anchorage loss, or P-Δ effects. Prior to conducting complete collapse analysis [Talaat and Mosalam 2009] of non-ductile RC buildings including all non-seismic details, the dynamic analyses in the next subsection are only focused on the investigation of the influence of shear failure and flexibility of the unreinforced beam-column joints on the lateral responses. For this purpose, beams and columns in the three building Types I, II, and III were assumed to have enough shear reinforcement to prevent their shear failures.

Table 6.5   Details of the reference (Type-I) building.

	Dimension $b_c \times h_c$ [in.]	$f_{y,\text{column}}$ [ksi]	Concrete f_c' [psi]	Floor	C-9	C-18	C-27	C-36
Column	14 × 20	60	5000	1st	8-#9	12-#9	12-#9	8-#9
			4000	2nd	6-#7	8-#9	8-#9	6-#7
		60	3000	3rd	6-#7	8-#9	8-#9	6-#7
				4th	6-#7	6-#9	6-#9	6-#7
				5th -7th	6-#7	6-#7	6-#7	6-#7
	$b_b \times h_b$ [in.]	$f_{y,\text{beam}}$ [ksi]	f_c' [psi]	Floor	Location	B4	B5	B6
Beam	14 × 30	40	4000	2nd (2FS-)	Top	3-#9	3-#9	2-#9
					Bottom	2-#9	2-#8	2-#9
	14 × 22.5	40	3000	3rd -4th (FS-)	Top	3-#10	3-#10	3-#10
					Bottom	2-#8	2-#8	2-#8
				5th -6th (FS-)	Top	3-#9	3-#9	3-#9
					Bottom	2-#8	2-#8	2-#8
				7th (FS-)	Top	2-#9	3-#8	2-#9
					Bottom	2-#8	2-#8	2-#8
	14 × 22	40	3000	Roof (RS-)	Top	2-#8	3-#7	2-#8
					Bottom	2-#7	2-#7	2-#7

(a) elevation   (b) cross-sections of beams and columns
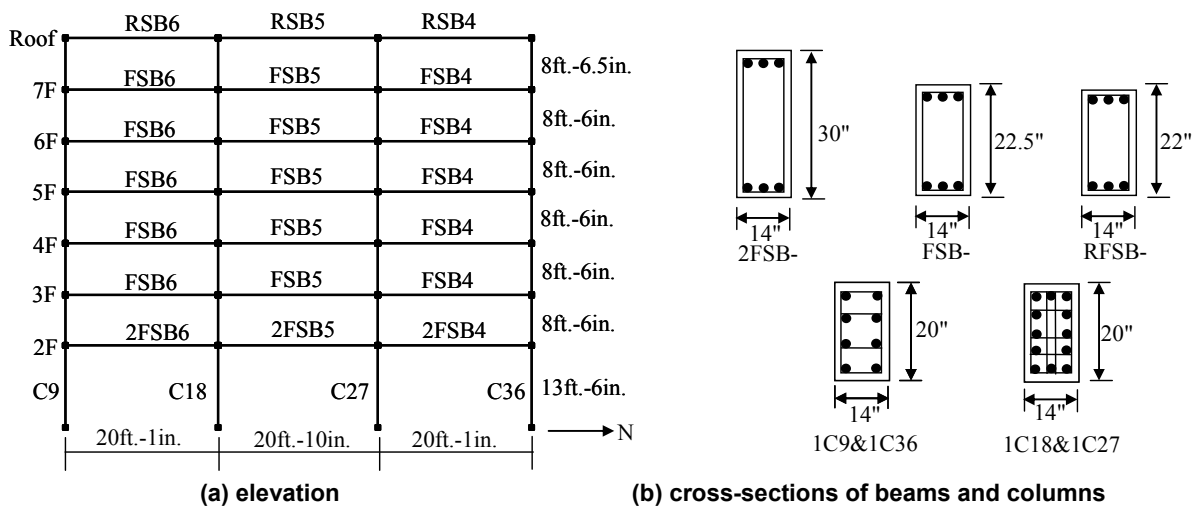
Figure 6.14   Layout of Van Nuys Holiday Inn building [Krawinkler 2005].

6.4.2 Nonlinear Dynamic Analysis

The beam-column joints in the hypothetical building frames were modeled in two different ways: namely, rigid joint modeling and joint rotational spring modeling, as shown in Figure 6.7(a) and (b), respectively. The fundamental periods of the three building frames are presented in Table 6.6. It is obvious that the fundamental periods of the three building frames were greater in the model with the proposed joint springs than in the model with rigid joints because the rotational springs make the frames more flexible. Note that the fundamental periods of the three building frames with rigid joints are close because the initial stiffness values of these frames are similar. The change of the fundamental period according to whether joint flexibility is considered or ignored in the computational model produces different dynamic responses. Hence, nonlinear time history analyses were performed for the three building frames under multiple ground motions scaled to produce increasing spectral accelerations.

The ground motion acceleration recorded during the 1994 Northridge earthquake (Tarzana station), shown in Figure 6.15, was used for these dynamic analyses. This ground acceleration history was scaled such that the scaled ground motions would produce a spectral acceleration at the natural period of the frame (T_1) of 0.1g to 1.0g with increments of 0.1g, based on the ASCE-7 [2006] design response spectrum. Note that the average of the fundamental periods listed in Table 5 (referred to as T_1 in Figure 6.15 and is taken as 1.48 sec) is considered for the scaling of the ground motion.

Figure 6.16(a)-(c) illustrates the simulation results of maximum interstory drift, θ_{max}, versus spectral acceleration at the fundamental period of the three building frames, $S_a(T_1)$. As expected, the proposed joint rotational spring model introduces additional interstory drifts to those of the rigid joint models. The increase of the maximum interstory drift due to joint rotation was more significant as the spectral acceleration increased, but this increase reduces for larger spectral accelerations when the beams and columns are subjected to large strain hardening in the rigid joint model. This behavior is reflected in Figure 6.16(d), where the increase of the interstory drift due to the joint rotation fell sharply at higher spectral acceleration (> 0.70g) for the more flexible building frames like Type-I, where at $S_a(T_1) > 0.9$g, maximum interstory drift was greater in the model with rigid joints because of yielding of first story columns.

Table 6.6   Fundamental periods of the analyzed three building frames.

Building	Type-I		Type-II		Type-III	
Joint model	Rigid joints	Proposed joint springs	Rigid joints	Proposed joint springs	Rigid joints	Proposed joint springs
Period, T1 [sec]	1.29	1.75	1.29	1.67	1.29	1.60
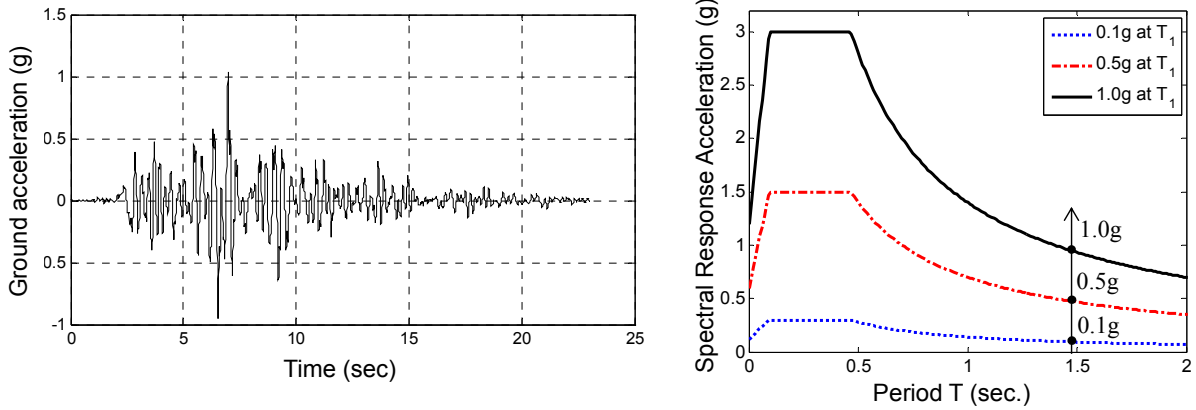
Figure 6.15   Northridge earthquake recorded at Tarzana station.

(a) Type-I building frame

(b) Type-II building frame

(c) Type-III building frame

(d) increase of interstory drift due to joint rotation
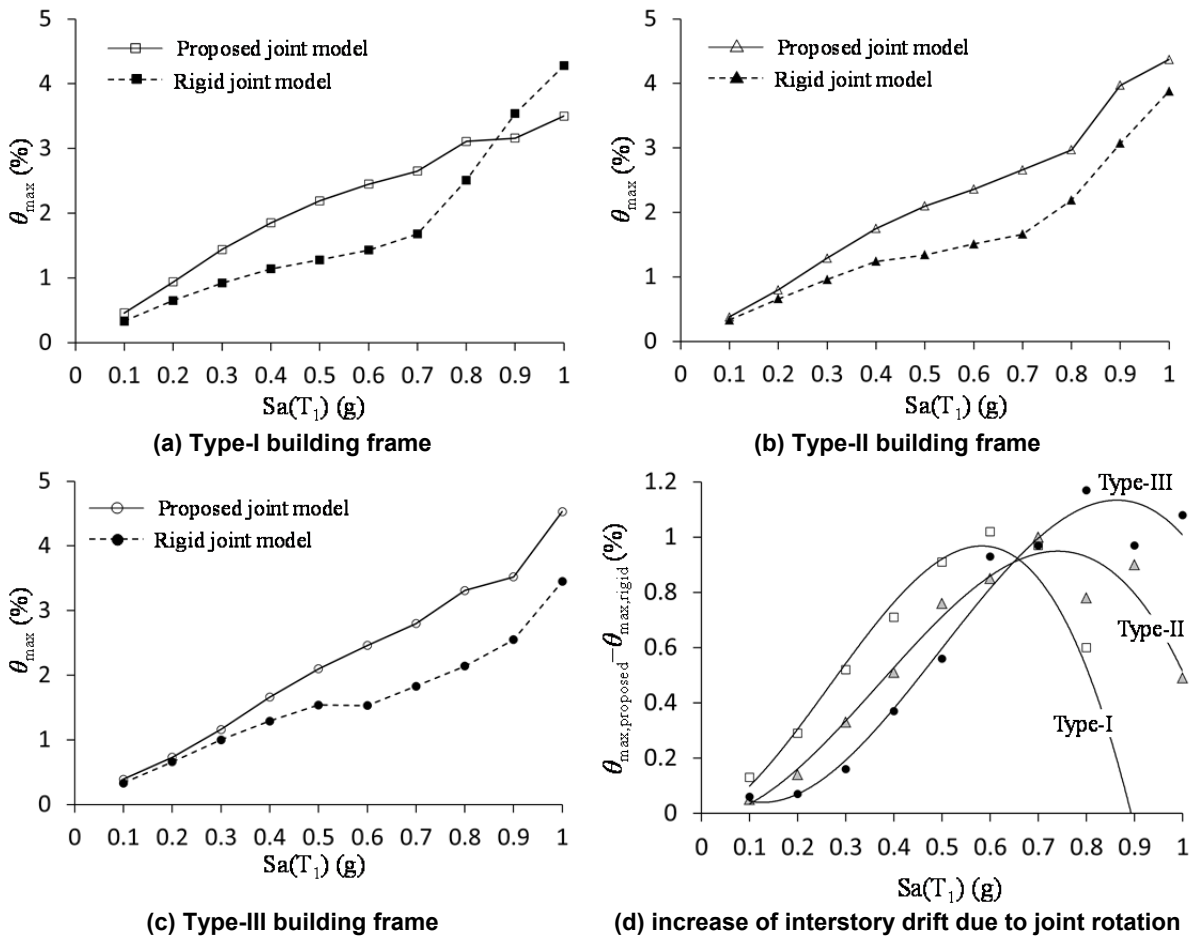
Figure 6.16   Maximum interstory drift results of the analyzed three building frames.

The results of the three building frames are compared in Figure 6.17(a). Between the two different types of joint idealizations a significant difference of the spectral accelerations was observed around 2% interstory drift, at which a performance level is defined as incurring

172

significant structural damage [Celik and Ellingwood 2010]. Consequently, this difference produces a significant shift of the seismic vulnerability functions for non-ductile RC buildings designed with unreinforced joints such as the fragility curve for a certain structural damage limit state, as shown schematically in Figure 6.17(b). Therefore, the importance of joint flexibility should be carefully recognized in the earthquake simulation and seismic assessment of non-ductile RC buildings having unreinforced beam-column joints.
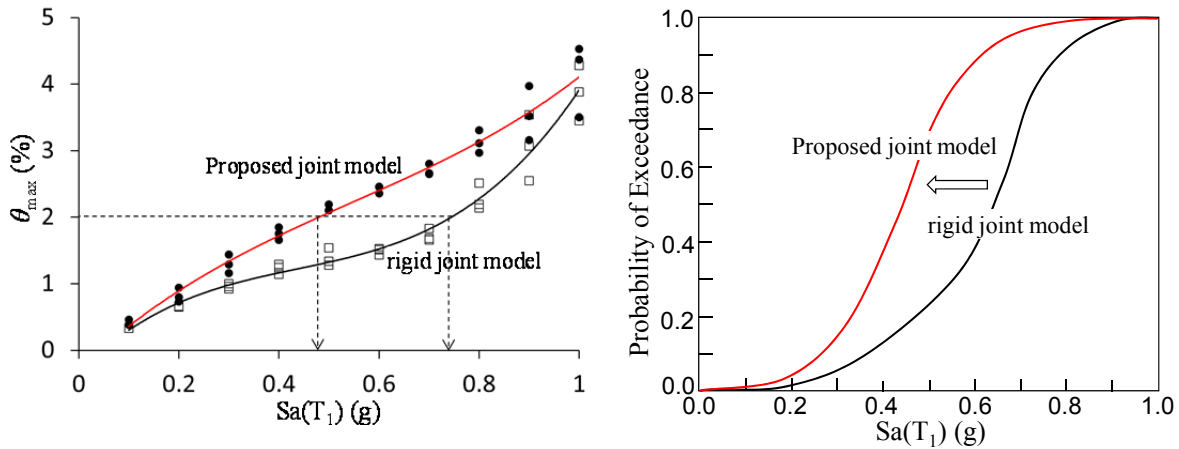
(a) comparison of interstory drift for the model with rigid joints and proposed joint springs

(b) Shift of the fragility curve for significant structural damage (schematic)

Figure 6.17   Effect of joint flexibility on seismic assessment of non-ductile RC buildings.

7 Summary, Conclusions, and Future Extensions

7.1 SUMMARY AND CONCLUSIONS

Increasing the understanding and modeling the behavior of unreinforced beam-column joints under earthquake loading was of interest in this study. Therefore,, an analytical and experimental research program is performed.

Analytical study on shear strength models for unreinforced exterior and corner joints was reported in Park and Mosalam [2009] in which a large amount of unreinforced exterior and corner joint test data from the published literature were collected into a test database. A parametric study was conducted using this database that revealed that shear strength of unreinforced exterior joints is strongly affected by two parameters: (1) joint aspect ratio and (2) joint shear index, which is dependent on the beam longitudinal tension reinforcement ratio and its strength. Subsequently, a parametric equation to represent the effect of joint aspect ratio was derived based on a SAT concept using equilibrium in the joint region and a softening concrete model, and the joint shear index equation was derived from global equilibrium in a beam-column subassembly and approximations of some variables. With the parametric equations of the aforementioned two parameters, two shear-strength models have been developed using semi-empirical and analytical approaches, and an integrating of these two models into a unified framework with simplifications resulted in a practical model, which has been proposed herein. The three models successfully predict the shear strength of the test specimens reported in the literature. The derivation and validation of these three models are presented in Chapter 2.

For experimental investigation, four full-scale corner beam-column joint specimens were constructed with RC slabs. The test matrix addressed two parameters: (1) the joint aspect ratio, and (2) the beam longitudinal reinforcement ratio. The test matrix consisted of four specimens with two different joint aspect ratios and two different beam longitudinal reinforcement ratios. The lateral load was quasi-statically applied through the vertical displacement control at the end of the beam, which is assumed to be an inflection point of the beam. This lateral loading alternated between the two (EW and NS) beams, i.e., one beam remained at a stationary point during the loading of the other orthogonal beam. Column axial load varied in real time according to a linear equation, which was derived from the pushover analysis of a hypothetical prototype structure obtained by modifying the Van Nuys Holiday Inn building model [Krawinkler 2005]. The joint shear strengths of the test specimens were evaluated and compared with predictions using the proposed joint shear strength models. Test results were discussed, focusing on the effects of the joint aspect ratio, the beam longitudinal reinforcement ratio, the column axial load, the slab contribution, the loading sequence, and the column intermediate bars. The joint shear

strain and rotation at the beam-joint interface were measured in order to provide benchmark data for the next stage of this research. Based on the experimental study, the following conclusions are drawn:

1. The semi-empirical model, analytical model, and simplified model accurately predict the shear strengths of four specimens with 4% overestimation, 6% underestimation, and 1% overestimation errors, respectively. It is found that the analytical model underestimated the specimens with larger diameter of longitudinal bars in the beam where the fraction factor increased without limitation. The fraction factor was, however, bounded in the simplified model; its predictions were more accurate than those produced of the analytical model.

2. The shear strengths of the tested four corner joint specimens were mainly affected by the joint aspect ratio and the beam longitudinal reinforcement ratio, which is parameterized as a joint shear index. The joint shear strengths decreased with an increasing joint aspect ratio and were proportional to the joint shear index in the range of variables investigated in this study. However, the shear strengths were minimally influenced by the column axial loads varying from tension of $0.07 f_c' A_g$ to compression of $0.25 f_c' A_g$. Including this study, most of previous joint tests were conducted under column axial load less than $0.25 f_c' A_g$ and thus more test data for the cases of higher column axial load are needed to clarify the effect of high column axial load on the joint shear strength. The trends and range of strength of the four corner joint test specimens were similar to those observed in many previous tests on exterior joints without transverse beams and floor slabs.

3. The joint shear strengths of the four test specimens were compared to the strength recommendation of the ASCE 41. The comparison indicates that the ASCE 41 provisions for shear strength are conservative and for accurate predictions, the effects of joint aspect ratio and beam reinforcement ratio need to be taken into account.

4. The effective slab width was not accurately estimated by an analytical approach because the contribution of the slab varies according to the strain level of the beam longitudinal reinforcement. This slab contribution was negligible when joint failure occurred prior to the yielding of the beam longitudinal bars (as in SP4) and it increased from SP3 to SP2 to SP1 as the joint failure occurred at larger post-yield strain of the beam longitudinal bars. Accordingly, further investigation is needed to evaluate the effective slab width in tension of L-shaped beams for the case when joint failure precedes beam flexural failure, e.g.,. a J-type failure in unreinforced joints.

5. The lateral loading was applied in the EW beam prior to the NS beam in each group of cyclic loading. The joint shear stresses of SP1 and SP2 were similar in both EW and NS direction until the beams yielded, while in SP3 and SP4, similar joint shear stresses were maintained up to 0.85% drift before yielding of the beams. Thereafter, larger joint shear stresses were induced in the EW direction than in the NS direction because of significant damage in the joint during the preceding EW beam loading. Therefore, the joint responses obtained in the EW direction were taken as representative response for developing backbone relationships.

6. During the longitudinal beam loading, two different types of cracks were observed in the transverse beam and joint panel: (1) inclined cracks took place in the transverse beam when the longitudinal beam was loaded down; and (2) horizontal cracks developed at the top of the joint panel in the transverse direction when the longitudinal beam was loaded up. This crack pattern and the measured angle of twist along the transverse beam revealed that twisting was localized around the inclined crack of the transverse beam during the longitudinal beam downward loading, whereas the entire transverse beam was twisted during the longitudinal beam upward loading.

7. There is no strong evidence that the column intermediate longitudinal bars acted as tension ties in joint shear resisting mechanism. This is attributed to the fact that inclined struts between the column intermediate and outer bars were minimal because of the steep angle of these struts and the bond deterioration of these bars.

For computational simulation on a structural system level, a backbone relationship for unreinforced corner joints was developed. The proposed backbone relationship was validated by analytical simulations of the beam-column subassemblies of the tested four corner joint specimens and other four planar exterior joint specimens taken from the literature. Furthermore, the proposed backbone relationship and adopted shear strength model were modified for modeling of interior and roof joints. Lastly, nonlinear dynamic analyses were performed for three hypothetical RC building frames using the developed backbone curves to preliminarily investigate the contribution of joint flexibility to the lateral response of non-ductile RC buildings. From the simulations using the proposed backbone relationships, the following conclusions were drawn:

1. Based on the measured joint shear stress-rotation and visual observation of the tested four exterior joint specimens, multi-linear backbone relationships were proposed to reflect the following aspects: (1) initial joint cracking, (2) either beam reinforcement yielding or significant opening of existing joint cracks, (3) either further propagation of existing joint crack or additional joint crack opening, and (4) residual joint shear stress and rotation when the joint damage is severe.

2. The accuracy of the proposed backbone curves was demonstrated by accurate reproduction of the load-displacement responses for the tested four corner joint specimens and eight other exterior and interior joint specimens taken from the literature. Therefore, the proposed backbone relationships were proven to be adequate for simulations of older-type RC buildings having unreinforced joints. However, the recommendations of ASCE 41 provisions were shown to be conservative for predicting the shear strength and deformability of unreinforced joints.

3. The proposed joint rotational spring model introduced additional interstory drifts to those of the rigid joint models. The increase of the maximum interstory drift due to joint rotation was more significant as the spectral acceleration increased, thus this increase changed the assessment of the seismic performance, such as the fragility curve for non-ductile RC buildings designed with unreinforced joints. Therefore, the importance of joint flexibility should be carefully recognized and the proposed backbone models are recommended in the earthquake simulation and seismic assessment of non-ductile RC buildings having unreinforced beam-column joints.

7.2 FUTURE RESEARCH

This study should ultimately culminate in developing progressive collapse analysis of older-type RC buildings that accurately predicts the partial and complete collapse fragility functions for this class of buildings under earthquake loads. To reach this ultimate goal, the following tasks should be considered in the future:

1. More test data including shaking table tests on unreinforced exterior joints are required to evaluate the proposed backbone relationships. In particular, the influence of high column axial load on the backbone relationship is to be investigated, focusing on the axial failure of the joint.

2. Further investigation of simultaneous bi-directional loading effects on shear strength and deformability of unreinforced joints is necessary for three-dimensional analyses of older-type RC buildings.

3. The proposed shear strength models and backbone relationship need to be augmented in order to take into account strength degradation due to cyclic loading, different types of reinforcement (e.g., smooth bar) and anchorage details.

4. Further verification is required to justify the extension of the proposed shear strength models and backbone relationship to interior joints, knee joints, and others.

5. For the case of weak column/strong beam, the behavior of unreinforced exterior joints is to be investigated.

6. The progressive collapse analysis necessitates the development of element removal criteria [Talaat and Mosalam 2009] for unreinforced joints. Furthermore, this requires procedures to be developed to re-define the connectivity and type or internal degrees-of-freedom of beams and columns associated with the removed beam-column joints.

7. Several prototypes of older-type RC buildings need to be identified and idealized for fragility analysis.

8. The joint modeling with a rotational spring and rigid links to beams and columns can be implemented as a standalone element in OpenSees, BuildingTcl [Mazzoni 2010] for easy adoption in modeling RC structural systems.

REFERENCES

American Concrete Institute (2011). *Building Code Requirements for Structural Concrete (ACI 318-11) and Commentary (318R-11)*, Farmington Hills, MI.

American Concrete Institute (2002). *Recommendations for design of beam-column connections in monolithic reinforced concrete structures (ACI 352R-02),* Farmington Hills, Michigan.

American Society of Civil Engineers (2007). *Seismic Rehabilitation of Existing Buildings (ASCE/SEI 41-06)*, Reston, VA.

American Society for Testing Materials (2004a). *Standard Test Method for Splitting Tensile Strength of Cylindrical Concrete Specimens: Designation C496/C496M-04*, West Conshohocken, Pa.

American Society for Testing Materials (2004b). *Standard Specification for Low-Alloy Steel Deformed and Plain Bars for Concrete Reinforcement: Designation A706-04*, West Conshohocken, Pa.

American Society for Testing Materials (2005). *Standard Test Method for Compressive Strength of Cylindrical Concrete Specimens: Designation C39/C39M-05*, West Conshohocken, Pa.

Architectural Institute of Japan (1994). *Structural Design Guidelines for Reinforced Concrete Buildings*, Tokyo, Japan.

Alire, D.A. (2002). *Seismic Evaluation of Existing Unconfined Reinforced Concrete Beam–Column Joints*. MSCE thesis, University of Washington, Seattle, WA.

Beres, A., White, R.N., Gergely, P. (1992). Seismic performance of interior and exterior beam-to-column joints related to lightly RC frame buildings: Detailed experimental results, *Structural Engineering Report 92-7*, School of Civil and Environmental Engineering, Cornell University. Ithaca, NY.

Biddah, A., Ghobarah, A. (1999). Modelling of shear deformation and bond slip in reinforced concrete joints, *Struct. Engrg. Mech.*, **7**(4):413–432.

Booth, E. (Editor) (1994) *Concrete Structures in Earthquake Regions: Design and Analysis*. New York: Longman Scientific and Technical.

Celik, O.Z., Ellingwood, B.R. (2010). Seismic fragilities for non-ductile reinforced concrete frames–Role of aleatoric and epistemic uncertainties, *Structural Safety*, 32:1–12.

Clyde, C., Pantelides, C.P., Reaveley, L.D. (2000). Performance-based evaluation of exterior RC building joints for seismic excitation, *PEER 2000/05*, Pacific Earthquake Engineering Research Center, University of California, Berkeley, CA.

Comité Euro-International du Béton (1993). Bulletin d'Information No. 213/214 CEB-FIP Model Code 1990. Thomas Telford, London, UK.

El-Attar, A.G., White, R.N., Gergely, P. (1991). Shake table test of a 1/6 scale 2-story lightly reinforced concrete building, *NCEER-91-0017*, National Center for Earthquake Engineering Research, State University of New York, Buffalo, NY.

Elwood, K.J., Moehle, J.P. (2003). Shake table tests and analytical studies on the gravity load collapse of reinforced concrete frames, *PEER 2003/01*, Pacific Earthquake Engineering Research Center, University of California, Berkeley, CA.

French, C.W., Moehle, J.P. (1991). Effect of floor slab on behavior of slab-beam-column connections, *ACI Struct. J. SP123*, pp. 225–258.

Ghannoum, W.M. (2007). *Experimental and Analytical Dynamic Collapse Study of a Reinforced Concrete Frame with Light Transverse Reinforcement*, PhD Dissertation, Department of Civil and Environmental Engineering, University of California, Berkeley, CA.

Ghobarah, A., Said, A. (2001). Seismic rehabilitation of beam-column joints using FRP laminates, *J. Earthq. Engrg.*, 5(1)113–129.

Günay, S.M., Mosalam, K.M. (2010). Structural engineering reconnaissance of the April 6, 2009, Abruzzo, Italy, earthquake and lessons learned, *PEER 2010/105*, Pacific Earthquake Engineering Research Center, University of California, Berkeley, CA.

Hakuto, S., Park, R., Tanaka, H. (1999). Effect of deterioration of bond of beam bars passing through interior beam-column joints on flexural strength and ductility, *ACI Struct. J.*, 96(5):858–864.

Hakuto, S., Park, R., Tanaka, H. (2000). Seismic load tests on interior and exterior beam-column joints with substandard reinforcing details, *ACI Struct. J.*, 97(1):11–25.

Haselton, C.B., Liel, A.B., Lange, S.T., and Deierlein G.G. (2008). Beam-Column Element Model Calibrated for Predicting Flexural Response Leading to Global Collapse of RC Frame Buildings, *PEER 2007/03*, Pacific Earthquake Engineering Research Center, University of California, Berkeley, CA.

Hassan, W.M., Park, S., Lopez, R.R., Mosalam, K.M., Moehle J.P. (2010). Seismic response of older-type reinforced concrete corner joints, *Proc., 9th U.S. National and 10th Canadian Conference on Earthquake Engineering*, Toronto, Canada.

Hsu, T.T.C. (1988). Softened truss model theory for shear and torsion, *ACI Struct. J.*, 85(6):624–634.

Hwang, S.J., Lee, H.J. (1999). Analytical model for predicting shear strength of exterior reinforced concrete beam-column joints for seismic resistance, *ACI Struct. J.*, 96(5):846–858.

Hwang, S.J., Lee, H.J. (2002). Strength prediction for discontinuity regions by softened strut-and-tie model, ASCE, *J. Struct. Engrg.*, 128(12):1519–1526.

Hwang, S.J., Lee, H.J., Liao, T.F., Wang, K.C., Tsai, H.H. (2005). Role of hoops on shear strength of reinforced concrete beam-column joints, *ACI Struct. J.*, 102(3): 445–453.

Karayannis, C.G., Chalioris, C.E., Sirkelis, G.M. (2008). Local retrofit of exterior RC beam-column joints using thin RC jackets- An experimental study, *Earthq. Engrg. Struct. Dyn.*, 37:727–746.

Kim, J., LaFave, J.M. (2007). Key influence parameters for the joint shear behavior of reinforced concrete (RC) beam-column connections, *Engrg. Struct.*, 29(10):2523–2539.

Krawinkler, H. (Editor) (2005). Van Nuys Hotel building testbed report: Exercising seismic performance assessment, *PEER 2005/11*, Pacific Earthquake Engineering Research Center, University of California, Berkeley, CA.

LaFave, J.M., Shin, M. (2005). Discussion of "Modeling reinforced concrete beam-column joints subjected to cyclic loading" by Laura N. Lowes and Arash Altoontash, ASCE, *J. Struct. Engrg.*, 131(6):992–993.

Lehman, D.E., Moehle, J.P. (2000). Seismic performance of well-confined concrete bridge columns, *PEER 1998/01*, Pacific Earthquake Engineering Research Center, University of California, Berkeley, CA.

Li, B., Wang, Z., Mosalam, K.M., Xie, H. (2008). Wenchuan earthquake field reconnaissance on reinforced concrete framed buildings with and without masonry infill walls, *Proc., 14th World Conference on Earthquake Engineering*, Beijing, China.

Lowes L.N., Altoontash, A. (2003). Modeling reinforced-concrete beam-column joints subjected to cyclic loading, ASCE, *J. Struct. Engrg.*, 129(12):1686–1697.

Lynn, A.C. (2001). *Seismic Behavior of Existing Reinforced Concrete Building Columns*. PhD Dissertation, Department of Civil and Environmental Engineering, University of California, Berkeley. CA.

Mander, J.B., Priestley, M.J.N., Park, R. (1988). Theoretical stress-strain model for confined concrete, ASCE, *J. Struct. Engrg.*, 114(8):1804–1826.

Mazzoni, S. (2010). OpenSees Building Tcl., Pacific Earthquake Engineering Research Center, University of California, Berkeley. http://opensees.berkeley.edu/wiki/index.php/BuildingTcl.

Meinheit, D.F., Jirsa, J.O. (1977). The shear strength of reinforced concrete beam-column joints, *CESRL Report No. 77-1*, University of Texas, Austin, TX.

Moehle, J.P., Lehman, D., Lowes, L. (2006). Beam-column connections. Presentation to New information on the seismic performance of existing buildings, EERI Technical Seminar.

Moiser, W.G. (2000). *Seismic Assessment of Reinforced Concrete Beam–Column Joints*, MSCE thesis, University of Washington. Seattle, WA.

New Zealand Society for Earthquake Engineering (2006). *Assessment and Improvement of the Structural Performance of Buildings in Earthquakes*, Wellington, New Zealand.

OpenSees (2010). Open System for Earthquake Simulation, Pacific Earthquake Engineering Research Center, University of California, Berkeley. http://opensees.berkeley.edu.

Ortiz, I.R. (1993). *Strut-and-Tie Modeling of Reinforce Concrete Short Beams and Beam-Column Joints*, PhD Dissertation, University of Westminster. London, UK.

Pampanin, S., Calvi, G.M., Moratti, M. (2002). Seismic behavior of RC beam-column joints designed for gravity loads, *Proc*., *12th European Conference on Earthquake Engineering*, London, UK.

Pantelides, C.P., Hansen, J., Nadauld, J., Reaveley, L.D. (2002). Assessment of reinforced concrete building exterior joints with substandard details, *PEER 2002/18*, Pacific Earthquake Engineering Research Center, University of California, Berkeley, CA.

Park, R. (1997). A static force-based procedure for the seismic assessment of existing reinforced concrete moment resisting frames, *Bull. New Zealand Soc. Earthq. Engrg.*, 30(3):213–226.

Park, S., Mosalam, K.M. (2009). Shear strength models of exterior beam-column joints without transverse reinforcement, *PEER 2009/106*, Pacific Earthquake Engineering Research Center, University of California, Berkeley, CA.

Park, S. (2010). *Experimental and Analytical Studies on Old Reinforced Concrete Buildings with Seismically Vulnerable Beam-Column Joints*, PhD Dissertation, Department of Civil and Environmental Engineering, University of California, Berkeley, CA.

Paspuleti, C. (2002). *Seismic Analysis of Older Reinforced Concrete Frame Structure*, MSCE thesis, University of Washington, Seattle, WA.

Pessiki, S.P., Conley, C., Gergely, P., White, R.N. (1990). Seismic behavior of lightly-reinforced concrete column and beam column joint details, *NCEER-90-0014*, National Center for Earthquake Engineering Research, State University of New York, Buffalo, NY.

Priestley, M.J.N. (1997). Displacement-based seismic assessment of reinforced concrete buildings, *J. Earthq. Engrg.*, 1(1):157–192.

Qi, X., Moehle, J.P. (1991). Displacement design approach for reinforced concrete structures subjected to earthquakes, *UCB/EERC-91/02*, Earthquake Engineering Research Center, University of California, Berkeley, CA.

Saatçioğlu, M., Razvi, S.R. (1992). Strength and ductility of confined concrete, ASCE, *J. Struct. Engrg.*, 118(6):1590–1607.

Sezen, H. (2002). *Seismic Behavior and Modeling of Reinforced Concrete Building Columns*. PhD Dissertation, Department of Civil and Environmental Engineering, University of California, Berkeley. CA.

Sezen, H., Elwood, K.J., Whittaker, A.S., Mosalam, K.M., Wallace, J.W., Stanton, J.F. (2000). Structural engineering reconnaissance of the August 17, 1999 earthquake: Kocaeli (Izmit), Turkey, *PEER 2000/09*, University of California, Berkeley, CA.

Sezen, H., Moehle, J.P. (2004). Shear Strength Model for Lightly Reinforced Concrete Column. ACSE, *J. Struct. Engrg.*, 130(11):1692–1703.

Shin, Y.B. (2007). *Shaking Table Tests on Reinforced Concrete Columns*, PhD Dissertation, Department of Civil and Environmental Engineering, University of California, Berkeley. CA.

Talaat, M., Mosalam, K.M. (2009). Modeling progressive collapse in reinforced concrete buildings using direct element removal, *Earthq. Engrg. Struct. Dyn.*, 38(5):609–634.

Uang, C.M., Elgamal, A., Li, W.S., Chou, C.C. (1999). *Ji-Ji Taiwan Earthquake of September 21, 1999: A Brief Reconnaissance Report*, University of California, San Diego, CA, http://www.structures.ucsd.edu/Taiwaneq.

Vecchio, F.J., Collins, M.P. (1986). The modified compression field theory for reinforced concrete elements subjected to shear, *ACI Struct. J.*, 83(2)219–231.

Vollum, R.L. (1998). *Design and Analysis of Exterior Beam Column Connections*, PhD Dissertation, Imperial College of Science Technology and Medicine-University of London, London, UK.

Walker, S.G. (2001). *Seismic Performance of Existing RC Beam–Column Joints*. MSCE thesis, University of Washington, Seattle, WA.

Wong, H.F. (2005). *Shear Strength and Seismic Performance of Non-Seismically Designed Reinforced Concrete Beam-Column Joints*, PhD Dissertation, Hong Kong University of Science and Technology, Hong Kong.

Zhang, L.X., Hsu, T.C. (1998). Behavior and analysis of 100MPa concrete membrane elements, ACSE, *J. Struct. Engrg.*, 124(1):24–34.

Appendix A: Drawings of Specimens and Test Set Up

A.1 SPECIMEN DRAWINGS

Plan

Elevation
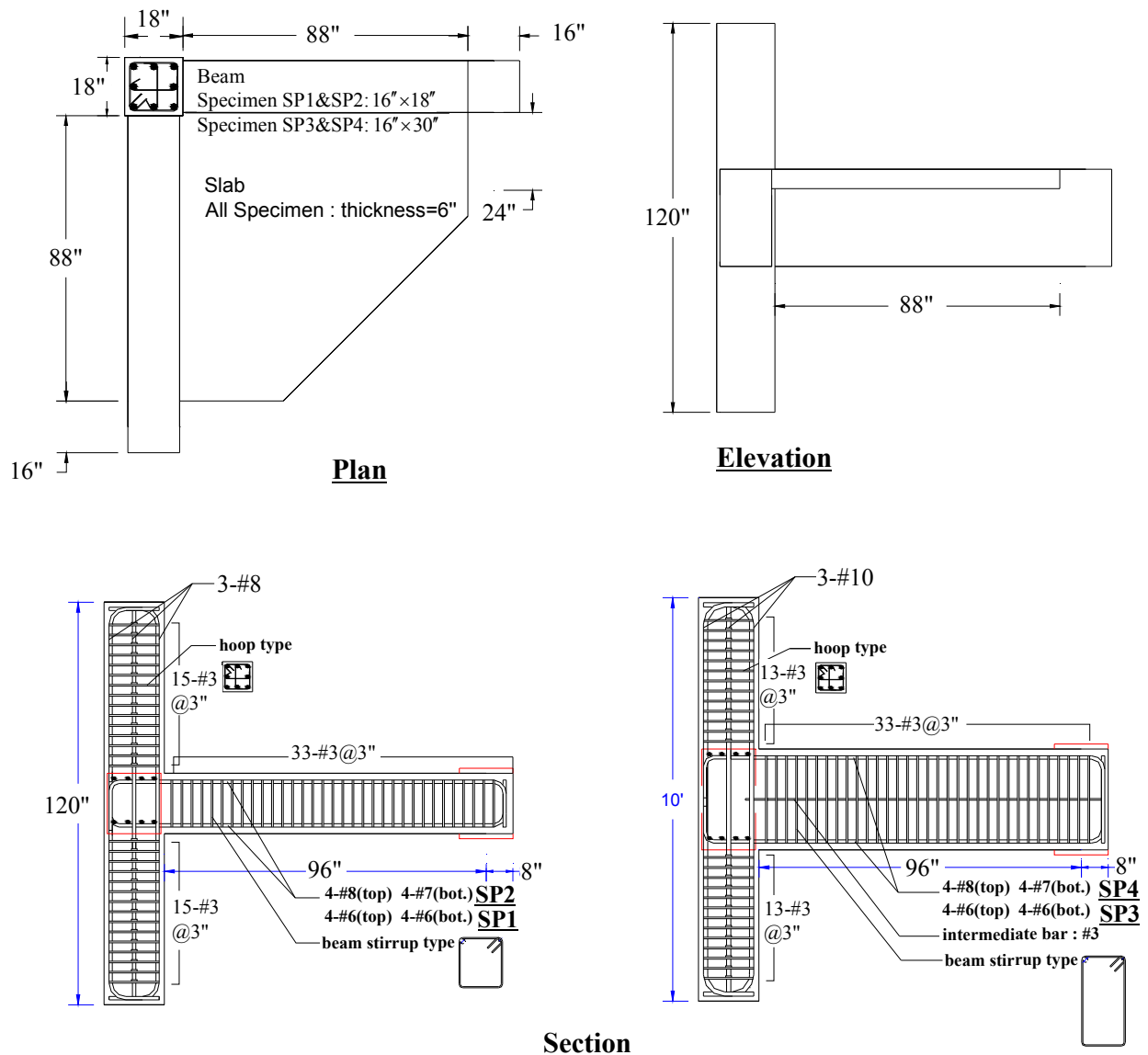
Section

Figure A.1   Specimen drawings.

Column Details

SP1&SP2 **SP3&SP4**

Note: column bar numbering

Beam Details

SP1

SP2

SP3

SP4

Slab Details

top & bottom slab reinforcement : #3@12''
cover 3/4''

①: 4bars X=13.5''+97''=110.5''
②: 2bars X=13.5''+94''=107.5''
③: 2bars X=13.5''+82''=95.5''
④: 2bars X=13.5''+70''=83.5''
⑤: 2bars X=13.5''+58''=71.5''
⑥: 2bars X=13.5''+46''=59.5''
⑦: 2bars X=13.5''+34''=47.5''

variable X

variable Y

①: 4bars Y=6''+97''=103''
②: 2bars Y=6''+94''=100''
③: 2bars Y=6''+82''=88''
④: 2bars Y=6''+70''=76''
⑤: 2bars Y=6''+58''=64''
⑥: 2bars Y=6''+46''=52''
⑦: 2bars Y=6''+34''=40''

Figure A.2   Specimens reinforcement details.

184

A.2 TEST SET UP DRAWINGS
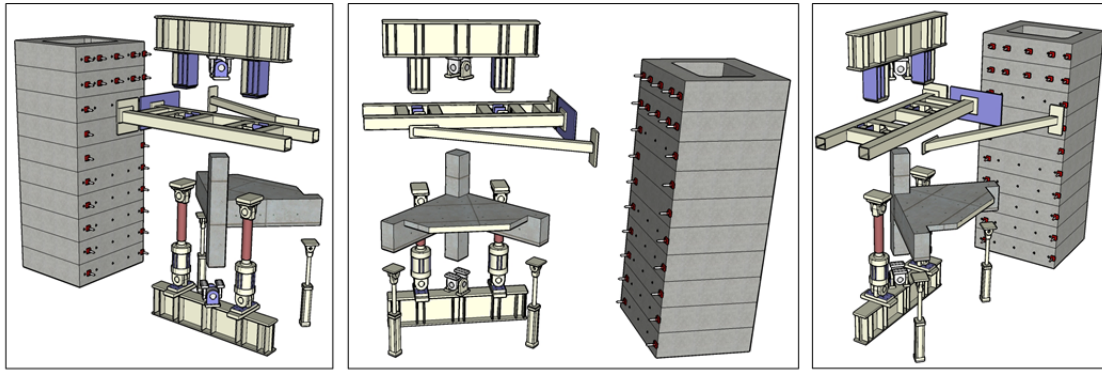
Global view
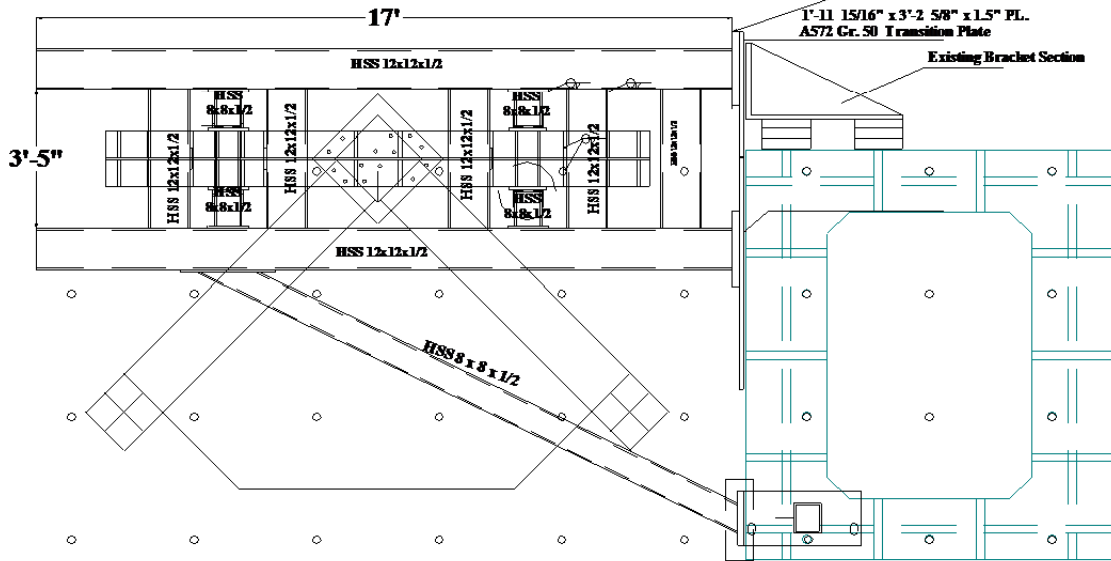
Plan
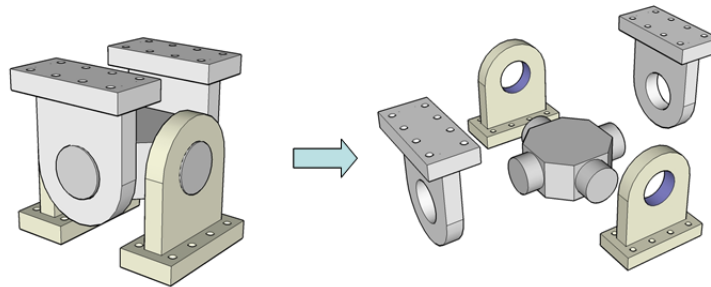
Bidirectional Clevis

Figure A.3   Test set up drawings.

Side View   Elevation

Vertical Frame

PLATE D
PLATE B

HSS 12x12x1/2

HSS 8x8x1/2
HSS 12x12x1/2
HSS 8x8x1/2
HSS 12x12x1/2
HSS 12x12x1/2

HSS 12x12x1/2
HSS 8x8x1/2
HSS 12x12x1/2
HSS 8x8x1/2
HSS 12x12x1/2

PLATE A
PLATE C

HSS 12x12x1/2

Lateral Restraining Frame

1-3/8" diameter.

HSS 8 x 8 x 1/2
14'-8"
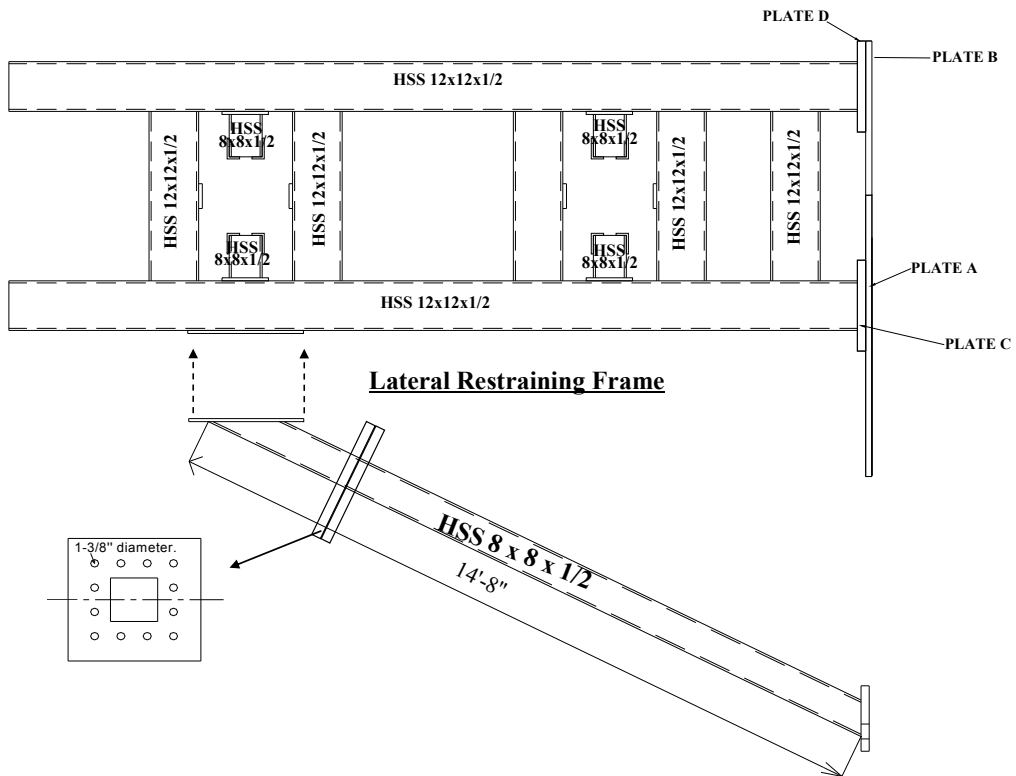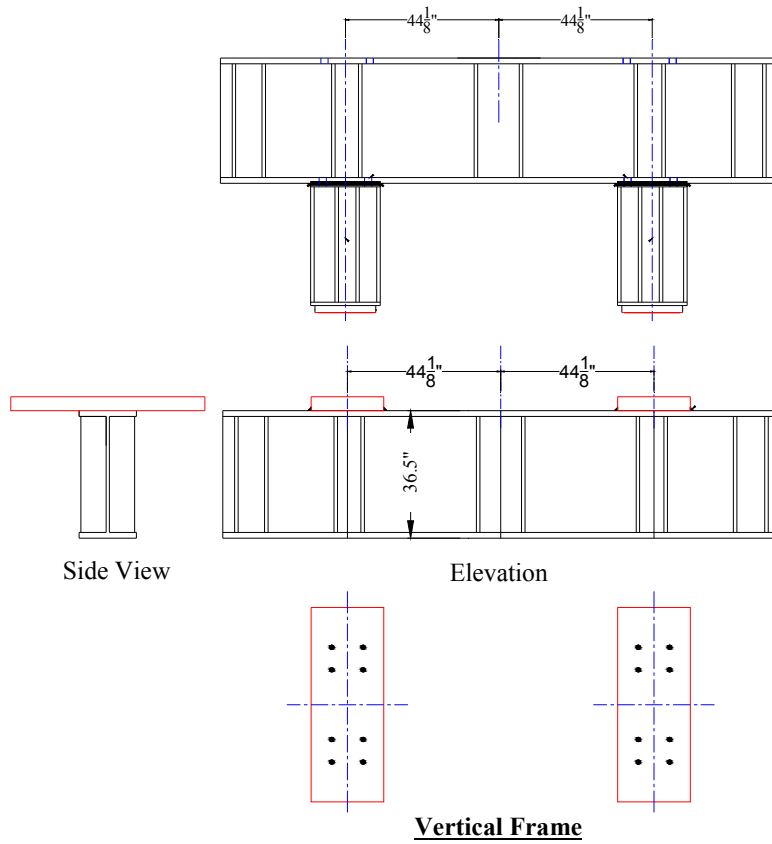
Brace of Lateral Restraining Frame

Figure A.4   Test set up details.

186

Appendix B: Material Properties

B.1   CONCRETE PROPERTIES

B.1.1 MIX DESIGN

The relevant concrete mixes were selected to test the four full-scale test specimens designed according to typical older type reinforced concrete buildings. Specimens SP1 and SP2 concrete were cast using one mix truck from a single batch (referred to as "Mix1"), and the other two specimens SP3 and SP4 were cast using two mix trucks having the same concrete mix (referred to as "Mix2") due to the capacity of a mix truck. Maximum aggregate size was equal to 1 in. (25.4 mm) for both two mixes.

For the Mix1, the concrete compressive strength was quite lower than its targeted strength at 28th day. Accordingly, the water/cement ratio was increased for the Mix2. The two mix designs are summarized in Tables B.1 and B.2.

Table B.1   SP1 and SP2 concrete mix design (Mix1).

Material	Saturated Surface Dry Weight (lb)	Absolute Volume (ft^3)
Cement ASTM C-150 Type II-V	323.0	1.64
Fly Ash ASTM C-618 Class F	57.0	0.39
Fine Aggregate ASTM C-33	1714.7	9.88
Aggregate ASTM C-33 1 in.×#4	1750.0	9.73
Water reducer ASTM C-494 Type A	13.0 fl. oz.	
Water ASTM C-94	283.7	4.55
Air	-	0.81
Total	4128	27.00

Water/Cement Ratio = 0.75
Slump = 4 $\pm$ 1 (in.)
Anticipated Strength @28th day = 3500 $\pm$ 500 psi

Table B.2   SP3 and SP4 concrete mix design (Mix2).

Material	Saturated Surface Dry Weight (lb)	Absolute Volume (ft^3)
Cement ASTM C-150 Type II-V	470.0	2.39
Aggregate 1 in. × #4	1500.0	8.94
Regular top sand	1235.0	7.41
SR blend sand	514.0	3.17
Water reducer ASTM C-494 Type A	23.5 fl. oz.	0.41
Water	292.0	4.68
Total	4001	27.00

Water/Cement Ratio = 0.621

Slump = 4 $\pm$ 1 (in.)

Anticipated Strength @28 day s= 3500 $\pm$ 500 psi

B.1.2 CONCRETE TEST RESULTS

To test the compressive and tensile strength of the cast concrete, standard 6 in. × 12 in. (152 × 305 mm) cylinders were made and cured in the same condition of the specimens except for 7 and 14 days testing cylinders of Mix1, refer to Figure B.1. The plastic forms of the cylinders were stripped on the same day when the specimen forms were removed. The six cylinders of Mix1 for 7 and 14 days testing were stripped at 4days to be capped with high-strength sulfur.

The low compressive strength of Mix1 21 days after casting required maintaining the form of SP1 and SP2 until 60 days after casting. To improve the compressive strength, the exposed surface was watered three times a day. After watering, this surface was covered by a blanket and plastic. After 60 days, the forms were stripped. The compressive strength of Mix2 showed acceptable values at 14 days testing and the forms of SP3 and SP4 were stripped at that point.

According to ASTM C39-05(ASTM 2005), the cylinders were capped with a sulfur compound and were tested in a Universal Testing Machine at a rate of 35 psi/min (0.241 MPa/min). At the day of testing, another three cylinders were used for split tests to measure the tensile strength according to ASTM C496 (ASTM 2004a). The concrete cylinder test results are summarized in Tables B.3 and B.4. Concrete stress-strain curves are given in Figure B.2 for the results of compressive tests conducted at the testing day.

Table B.3   Concrete cylinder test results of SP1 and SP2 (Mix1).

Specimen	SP1 and SP2							Tensile Strength
Test	Compressive Strength (ksi)							Tensile Strength
after casting	7	15	21	26	50	295 (SP1[*1])	358 (SP2[*2])	359
Cylinder 1	1.44	1.91	2.07	2.16	2.84	3.66	3.56	0.37
Cylinder 2	1.38	1.87	1.90	-	2.74	3.76	3.48	0.32
Cylinder 3	1.37	1.80	1.83	-	-	3.31[*]	3.54	0.33
Avg.	1.39	1.86	1.93	2.16	2.8	3.58	3.53	0.34

[*1]day of testing SP1.
[*2]day of testing SP2.

Table B.4   Concrete cylinder test results of SP3 and SP4 (Mix2).

Specimen	SP3							Tensile Strength
Test	Compressive Strength (ksi)							Tensile Strength
after casting	7	14	21	28	63	324	378	378
Cylinder 1	2.08	3.25	3.15	3.70	3.86	3.82	3.59	0.32
Cylinder 2	2.14	3.09	3.30	3.06	3.68	3.82	3.57	0.34
Cylinder 3	2.25	3.29	3.24	3.23	3.77	3.95	3.66	0.31
Avg.	2.16	3.21	3.23	3.33	3.77	3.86	3.60	0.32
Specimen	SP4							Tensile Strength
Test	Compressive Strength (ksi)							Tensile Strength
after casting	7	14	21	28	63	324	421	421
Cylinder 1	2.11	3.07	3.32	3.82	3.97	4.07	4.06	0.48
Cylinder 2	2.13	3.00	3.36	3.61	4.23	3.80	3.73	0.42
Cylinder 3	2.14	3.02	3.26	3.60	4.32	4.01	4.09	0.43
Avg.	2.13	3.03	3.32	3.68	4.17	3.96	3.96	0.44

Figure B.1   Slump test and curing.

(a) SP1

(b) SP2

(c) SP3

(d) SP4
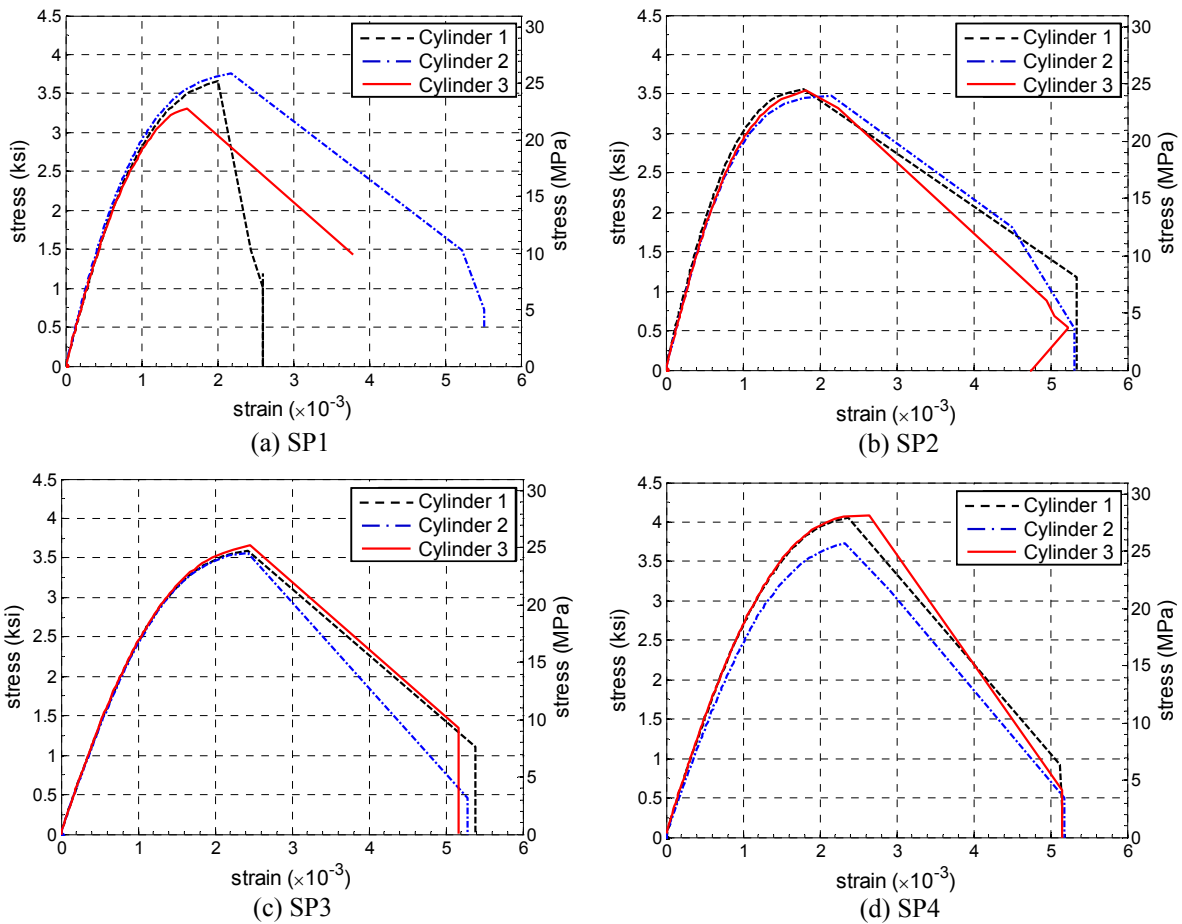
Figure B.2   Concrete stress versus strain curves.

B.2   REINFORCING STEEL PROPERTIES

Five different bar sizes (#3, #6, #7, #8, and #10) were used in the four test specimens. The local contractor provided the metric bar sizes, D10, D19, D22, D25, and D32, which correspond to the above U.S. standard bars, respectively. The column longitudinal bars were designed with #8 bars in SP1 and SP2, and #10 bars in SP3 and SP4. The beam longitudinal bars of SP1 and SP3 were designed with #6 bars at the top and bottom of the beams, and those of SP2 and SP4 were designed with #8 and #7 bars at the top and bottom of the beams, respectively. Number 3 bars were used for the slab reinforcement, column hoops, and beam stirrups of the four test specimens.

All reinforcing bars used in the four test specimens were tested to confirm that the material properties corresponded to the ASTM A706-04 (ASTM 2004b). For each bar size, three coupons were tested in tension. The selected reinforcing bars were cut into 24 in. (609.6 mm) lengths, and the cross-section within the middle of 6 in. (152.4 mm) length was machined to reduce sectional area. The measured data are summarized in Table B.5. For the #3 bars, the yield stress and strain were defined using the 0.1% offset method. For other bars, the yield stress was defined as the stress at the plateau, and the yield strain was taken as the strain corresponding to the yield stress. The stress-strain curve of the coupon tests are shown in Figure B.3.

Table B.5   Reinforcing bars material properties.

Bar size	#3 (D10)	#6 (D19)	#7 (D22)	#8 (D25)	#10 (D32)
Yield stress(ksi)	73.5*	78.6	73.3	72.2	68.3
Ultimate stress	115	104.5	103.1	102.6	100.5
Yield strain	0.0035*	0.0028	0.0027	0.0025	0.0023
Plateau strain	-	0.0195	0.0127	0.0133	0.0124
Ultimate strain	0.105	0.12	0.12	0.12	0.12
Fracture strain	0.157	0.223	0.225	0.226	0.222
Elastic Modulus	28200	27900	26700	28900	29600

*determined by 0.1% offset method

(a) #3 (D10) Bar

(b) #6 (D19) Bar

(c) #7 (D22) Bar

(d) #8 (D25) Bar

(e) #10 (D32) Bar
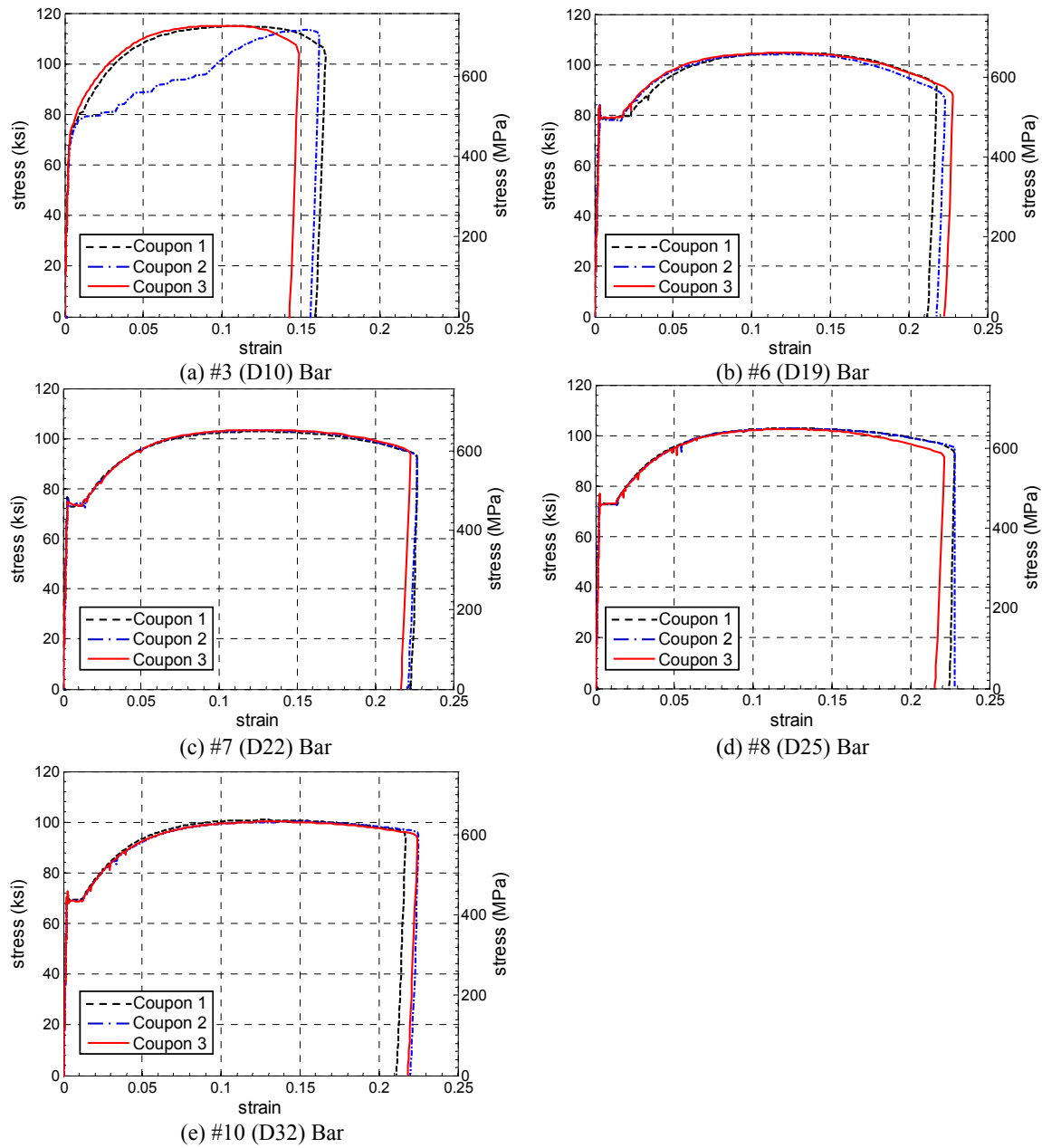
Figure B.3   Reinforcing bars stress versus strain curves.

PEER REPORTS

PEER reports are available individually or by yearly subscription. PEER reports can be ordered at http://peer.berkeley.edu/publications/peer_reports.html or by contacting the Pacific Earthquake Engineering Research Center, 325 Davis Hall mail code 1792, Berkeley, CA 94720. Tel.: (510) 642-3437; Fax: (510) 665-1655; Email: peer_editor@berkeley.edu

PEER 2012/03 *Experimental and Analytical Studies on Reinforced Concrete Buildings with Seismically Vulnerable Beam-Column Joints.* Sangjoon Park and Khalid M. Mosalam. October 2012.

PEER 2012/02 *Seismic Performance of Reinforced Concrete Bridges Allowed to Uplift during Multi-Directional Excitation.* Andres Oscar Espinoza and Stephen A. Mahin. July 2012.

PEER 2012/01 *Spectral Damping Scaling Factors for Shallow Crustal Earthquakes in Active Tectonic Regions.* Sanaz Rezaeian, Yousef Bozorgnia, I. M. Idriss, Kenneth Campbell, Norman Abrahamson, and Walter Silva. July 2012.

PEER 2011/10 *Earthquake Engineering for Resilient Communities: 2011 PEER Internship Program Research Report Collection.* Eds. Heidi Faison and Stephen A. Mahin. December 2011.

PEER 2011/09 *Calibration of Semi-Stochastic Procedure for Simulating High-Frequency Ground Motions.* Jonathan P. Stewart, Emel Seyhan, and Robert W. Graves. December 2011.

PEER 2011/08 *Water Supply in regard to Fire Following Earthquake.* Charles Scawthorn. November 2011.

PEER 2011/07 *Seismic Risk Management in Urban Areas. Proceedings of a U.S.-Iran-Turkey Seismic Workshop.* September 2011.

PEER 2011/06 *The Use of Base Isolation Systems to Achieve Complex Seismic Performance Objectives.* Troy A. Morgan and Stephen A. Mahin. July 2011.

PEER 2011/05 *Case Studies of the Seismic Performance of Tall Buildings Designed by Alternative Means.* Task 12 Report for the Tall Buildings Initiative. Jack Moehle, Yousef Bozorgnia, Nirmal Jayaram, Pierson Jones, Mohsen Rahnama, Nilesh Shome, Zeynep Tuna, John Wallace, Tony Yang, and Farzin Zareian. July 2011.

PEER 2011/04 *Recommended Design Practice for Pile Foundations in Laterally Spreading Ground.* Scott A. Ashford, Ross W. Boulanger, and Scott J. Brandenberg. June 2011.

PEER 2011/03 *New Ground Motion Selection Procedures and Selected Motions for the PEER Transportation Research Program.* Jack W. Baker, Ting Lin, Shrey K. Shahi, and Nirmal Jayaram. March 2011.

PEER 2011/02 *A Bayesian Network Methodology for Infrastructure Seismic Risk Assessment and Decision Support.* Michelle T. Bensi, Armen Der Kiureghian, and Daniel Straub. March 2011.

PEER 2011/01 *Demand Fragility Surfaces for Bridges in Liquefied and Laterally Spreading Ground.* Scott J. Brandenberg, Jian Zhang, Pirooz Kashighandi, Yili Huo, and Minxing Zhao. March 2011.

PEER 2010/05 *Guidelines for Performance-Based Seismic Design of Tall Buildings.* Developed by the Tall Buildings Initiative. November 2010.

PEER 2010/04 *Application Guide for the Design of Flexible and Rigid Bus Connections between Substation Equipment Subjected to Earthquakes.* Jean-Bernard Dastous and Armen Der Kiureghian. September 2010.

PEER 2010/03 *Shear Wave Velocity as a Statistical Function of Standard Penetration Test Resistance and Vertical Effective Stress at Caltrans Bridge Sites.* Scott J. Brandenberg, Naresh Bellana, and Thomas Shantz. June 2010.

PEER 2010/02 *Stochastic Modeling and Simulation of Ground Motions for Performance-Based Earthquake Engineering.* Sanaz Rezaeian and Armen Der Kiureghian. June 2010.

PEER 2010/01 *Structural Response and Cost Characterization of Bridge Construction Using Seismic Performance Enhancement Strategies.* Ady Aviram, Božidar Stojadinović, Gustavo J. Parra-Montesinos, and Kevin R. Mackie. March 2010.

PEER 2009/03 *The Integration of Experimental and Simulation Data in the Study of Reinforced Concrete Bridge Systems Including Soil-Foundation-Structure Interaction.* Matthew Dryden and Gregory L. Fenves. November 2009.

PEER 2009/02 *Improving Earthquake Mitigation through Innovations and Applications in Seismic Science, Engineering, Communication, and Response. Proceedings of a U.S.-Iran Seismic Workshop.* October 2009.

PEER 2009/01 *Evaluation of Ground Motion Selection and Modification Methods: Predicting Median Interstory Drift Response of Buildings.* Curt B. Haselton, Ed. June 2009.

PEER 2008/10 *Technical Manual for Strata.* Albert R. Kottke and Ellen M. Rathje. February 2009.

PEER 2008/09 *NGA Model for Average Horizontal Component of Peak Ground Motion and Response Spectra.* Brian S.-J. Chiou and Robert R. Youngs. November 2008.

PEER 2008/08   *Toward Earthquake-Resistant Design of Concentrically Braced Steel Structures.* Patxi Uriz and Stephen A. Mahin. November 2008.

PEER 2008/07   *Using OpenSees for Performance-Based Evaluation of Bridges on Liquefiable Soils.* Stephen L. Kramer, Pedro Arduino, and HyungSuk Shin. November 2008.

PEER 2008/06   *Shaking Table Tests and Numerical Investigation of Self-Centering Reinforced Concrete Bridge Columns.* Hyung IL Jeong, Junichi Sakai, and Stephen A. Mahin. September 2008.

PEER 2008/05   *Performance-Based Earthquake Engineering Design Evaluation Procedure for Bridge Foundations Undergoing Liquefaction-Induced Lateral Ground Displacement.* Christian A. Ledezma and Jonathan D. Bray. August 2008.

PEER 2008/04   *Benchmarking of Nonlinear Geotechnical Ground Response Analysis Procedures.* Jonathan P. Stewart, Annie On-Lei Kwok, Yousseff M. A. Hashash, Neven Matasovic, Robert Pyke, Zhiliang Wang, and Zhaohui Yang. August 2008.

PEER 2008/03   *Guidelines for Nonlinear Analysis of Bridge Structures in California.* Ady Aviram, Kevin R. Mackie, and Božidar Stojadinović. August 2008.

PEER 2008/02   *Treatment of Uncertainties in Seismic-Risk Analysis of Transportation Systems.* Evangelos Stergiou and Anne S. Kiremidjian. July 2008.

PEER 2008/01   *Seismic Performance Objectives for Tall Buildings.* William T. Holmes, Charles Kircher, William Petak, and Nabih Youssef. August 2008.

PEER 2007/12   *An Assessment to Benchmark the Seismic Performance of a Code-Conforming Reinforced Concrete Moment-Frame Building.* Curt Haselton, Christine A. Goulet, Judith Mitrani-Reiser, James L. Beck, Gregory G. Deierlein, Keith A. Porter, Jonathan P. Stewart, and Ertugrul Taciroglu. August 2008.

PEER 2007/11   *Bar Buckling in Reinforced Concrete Bridge Columns.* Wayne A. Brown, Dawn E. Lehman, and John F. Stanton. February 2008.

PEER 2007/10   *Computational Modeling of Progressive Collapse in Reinforced Concrete Frame Structures.* Mohamed M. Talaat and Khalid M. Mosalam. May 2008.

PEER 2007/09   *Integrated Probabilistic Performance-Based Evaluation of Benchmark Reinforced Concrete Bridges.* Kevin R. Mackie, John-Michael Wong, and Božidar Stojadinović. January 2008.

PEER 2007/08   *Assessing Seismic Collapse Safety of Modern Reinforced Concrete Moment-Frame Buildings.* Curt B. Haselton and Gregory G. Deierlein. February 2008.

PEER 2007/07   *Performance Modeling Strategies for Modern Reinforced Concrete Bridge Columns.* Michael P. Berry and Marc O. Eberhard. April 2008.

PEER 2007/06   *Development of Improved Procedures for Seismic Design of Buried and Partially Buried Structures.* Linda Al Atik and Nicholas Sitar. June 2007.

PEER 2007/05   *Uncertainty and Correlation in Seismic Risk Assessment of Transportation Systems.* Renee G. Lee and Anne S. Kiremidjian. July 2007.

PEER 2007/04   *Numerical Models for Analysis and Performance-Based Design of Shallow Foundations Subjected to Seismic Loading.* Sivapalan Gajan, Tara C. Hutchinson, Bruce L. Kutter, Prishati Raychowdhury, José A. Ugalde, and Jonathan P. Stewart. May 2008.

PEER 2007/03   *Beam-Column Element Model Calibrated for Predicting Flexural Response Leading to Global Collapse of RC Frame Buildings.* Curt B. Haselton, Abbie B. Liel, Sarah Taylor Lange, and Gregory G. Deierlein. May 2008.

PEER 2007/02   *Campbell-Bozorgnia NGA Ground Motion Relations for the Geometric Mean Horizontal Component of Peak and Spectral Ground Motion Parameters.* Kenneth W. Campbell and Yousef Bozorgnia. May 2007.

PEER 2007/01   *Boore-Atkinson NGA Ground Motion Relations for the Geometric Mean Horizontal Component of Peak and Spectral Ground Motion Parameters.* David M. Boore and Gail M. Atkinson. May. May 2007.

PEER 2006/12   *Societal Implications of Performance-Based Earthquake Engineering.* Peter J. May. May 2007.

PEER 2006/11   *Probabilistic Seismic Demand Analysis Using Advanced Ground Motion Intensity Measures, Attenuation Relationships, and Near-Fault Effects.* Polsak Tothong and C. Allin Cornell. March 2007.

PEER 2006/10   *Application of the PEER PBEE Methodology to the I-880 Viaduct.* Sashi Kunnath. February 2007.

PEER 2006/09   *Quantifying Economic Losses from Travel Forgone Following a Large Metropolitan Earthquake.* James Moore, Sungbin Cho, Yue Yue Fan, and Stuart Werner. November 2006.

PEER 2006/08   *Vector-Valued Ground Motion Intensity Measures for Probabilistic Seismic Demand Analysis.* Jack W. Baker and C. Allin Cornell. October 2006.

PEER 2006/07   *Analytical Modeling of Reinforced Concrete Walls for Predicting Flexural and Coupled–Shear-Flexural Responses.* Kutay Orakcal, Leonardo M. Massone, and John W. Wallace. October 2006.

PEER 2006/06   *Nonlinear Analysis of a Soil-Drilled Pier System under Static and Dynamic Axial Loading.* Gang Wang and Nicholas Sitar. November 2006.

PEER 2006/05   *Advanced Seismic Assessment Guidelines.* Paolo Bazzurro, C. Allin Cornell, Charles Menun, Maziar Motahari, and Nicolas Luco. September 2006.

PEER 2006/04   *Probabilistic Seismic Evaluation of Reinforced Concrete Structural Components and Systems.* Tae Hyung Lee and Khalid M. Mosalam. August 2006.

PEER 2006/03   *Performance of Lifelines Subjected to Lateral Spreading.* Scott A. Ashford and Teerawut Juirnarongrit. July 2006.

PEER 2006/02   *Pacific Earthquake Engineering Research Center Highway Demonstration Project.* Anne Kiremidjian, James Moore, Yue Yue Fan, Nesrin Basoz, Ozgur Yazali, and Meredith Williams. April 2006.

PEER 2006/01   *Bracing Berkeley. A Guide to Seismic Safety on the UC Berkeley Campus.* Mary C. Comerio, Stephen Tobriner, and Ariane Fehrenkamp. January 2006.

PEER 2005/16   *Seismic Response and Reliability of Electrical Substation Equipment and Systems.* Junho Song, Armen Der Kiureghian, and Jerome L. Sackman. April 2006.

PEER 2005/15   *CPT-Based Probabilistic Assessment of Seismic Soil Liquefaction Initiation.* R. E. S. Moss, R. B. Seed, R. E. Kayen, J. P. Stewart, and A. Der Kiureghian. April 2006.

PEER 2005/14   *Workshop on Modeling of Nonlinear Cyclic Load-Deformation Behavior of Shallow Foundations.* Bruce L. Kutter, Geoffrey Martin, Tara Hutchinson, Chad Harden, Sivapalan Gajan, and Justin Phalen. March 2006.

PEER 2005/13   *Stochastic Characterization and Decision Bases under Time-Dependent Aftershock Risk in Performance-Based Earthquake Engineering.* Gee Liek Yeo and C. Allin Cornell. July 2005.

PEER 2005/12   *PEER Testbed Study on a Laboratory Building: Exercising Seismic Performance Assessment.* Mary C. Comerio, editor. November 2005.

PEER 2005/11   *Van Nuys Hotel Building Testbed Report: Exercising Seismic Performance Assessment.* Helmut Krawinkler, editor. October 2005.

PEER 2005/10   *First NEES/E-Defense Workshop on Collapse Simulation of Reinforced Concrete Building Structures.* September 2005.

PEER 2005/09   *Test Applications of Advanced Seismic Assessment Guidelines.* Joe Maffei, Karl Telleen, Danya Mohr, William Holmes, and Yuki Nakayama. August 2006.

PEER 2005/08   *Damage Accumulation in Lightly Confined Reinforced Concrete Bridge Columns.* R. Tyler Ranf, Jared M. Nelson, Zach Price, Marc O. Eberhard, and John F. Stanton. April 2006.

PEER 2005/07   *Experimental and Analytical Studies on the Seismic Response of Freestanding and Anchored Laboratory Equipment.* Dimitrios Konstantinidis and Nicos Makris. January 2005.

PEER 2005/06   *Global Collapse of Frame Structures under Seismic Excitations.* Luis F. Ibarra and Helmut Krawinkler. September 2005.

PEER 2005//05   *Performance Characterization of Bench- and Shelf-Mounted Equipment.* Samit Ray Chaudhuri and Tara C. Hutchinson. May 2006.

PEER 2005/04   *Numerical Modeling of the Nonlinear Cyclic Response of Shallow Foundations.* Chad Harden, Tara Hutchinson, Geoffrey R. Martin, and Bruce L. Kutter. August 2005.

PEER 2005/03   *A Taxonomy of Building Components for Performance-Based Earthquake Engineering.* Keith A. Porter. September 2005.

PEER 2005/02   *Fragility Basis for California Highway Overpass Bridge Seismic Decision Making.* Kevin R. Mackie and Božidar Stojadinović. June 2005.

PEER 2005/01   *Empirical Characterization of Site Conditions on Strong Ground Motion.* Jonathan P. Stewart, Yoojoong Choi, and Robert W. Graves. June 2005.

PEER 2004/09   *Electrical Substation Equipment Interaction: Experimental Rigid Conductor Studies.* Christopher Stearns and André Filiatrault. February 2005.

PEER 2004/08   *Seismic Qualification and Fragility Testing of Line Break 550-kV Disconnect Switches.* Shakhzod M. Takhirov, Gregory L. Fenves, and Eric Fujisaki. January 2005.

PEER 2004/07   *Ground Motions for Earthquake Simulator Qualification of Electrical Substation Equipment.* Shakhzod M. Takhirov, Gregory L. Fenves, Eric Fujisaki, and Don Clyde. January 2005.

PEER 2004/06   *Performance-Based Regulation and Regulatory Regimes.* Peter J. May and Chris Koski. September 2004.

PEER 2004/05   *Performance-Based Seismic Design Concepts and Implementation: Proceedings of an International Workshop.* Peter Fajfar and Helmut Krawinkler, editors. September 2004.

PEER 2004/04   *Seismic Performance of an Instrumented Tilt-up Wall Building.* James C. Anderson and Vitelmo V. Bertero. July 2004.

PEER 2004/03   *Evaluation and Application of Concrete Tilt-up Assessment Methodologies.* Timothy Graf and James O. Malley. October 2004.

PEER 2004/02   *Analytical Investigations of New Methods for Reducing Residual Displacements of Reinforced Concrete Bridge Columns.* Junichi Sakai and Stephen A. Mahin. August 2004.

PEER 2004/01   *Seismic Performance of Masonry Buildings and Design Implications.* Kerri Anne Taeko Tokoro, James C. Anderson, and Vitelmo V. Bertero. February 2004.

PEER 2003/18   *Performance Models for Flexural Damage in Reinforced Concrete Columns.* Michael Berry and Marc Eberhard. August 2003.

PEER 2003/17   *Predicting Earthquake Damage in Older Reinforced Concrete Beam-Column Joints.* Catherine Pagni and Laura Lowes. October 2004.

PEER 2003/16   *Seismic Demands for Performance-Based Design of Bridges.* Kevin Mackie and Božidar Stojadinović. August 2003.

PEER 2003/15   *Seismic Demands for Nondeteriorating Frame Structures and Their Dependence on Ground Motions.* Ricardo Antonio Medina and Helmut Krawinkler. May 2004.

PEER 2003/14   *Finite Element Reliability and Sensitivity Methods for Performance-Based Earthquake Engineering.* Terje Haukaas and Armen Der Kiureghian. April 2004.

PEER 2003/13   *Effects of Connection Hysteretic Degradation on the Seismic Behavior of Steel Moment-Resisting Frames.* Janise E. Rodgers and Stephen A. Mahin. March 2004.

PEER 2003/12   *Implementation Manual for the Seismic Protection of Laboratory Contents: Format and Case Studies.* William T. Holmes and Mary C. Comerio. October 2003.

PEER 2003/11   *Fifth U.S.-Japan Workshop on Performance-Based Earthquake Engineering Methodology for Reinforced Concrete Building Structures.* February 2004.

PEER 2003/10   *A Beam-Column Joint Model for Simulating the Earthquake Response of Reinforced Concrete Frames.* Laura N. Lowes, Nilanjan Mitra, and Arash Altoontash. February 2004.

PEER 2003/09   *Sequencing Repairs after an Earthquake: An Economic Approach.* Marco Casari and Simon J. Wilkie. April 2004.

PEER 2003/08   *A Technical Framework for Probability-Based Demand and Capacity Factor Design (DCFD) Seismic Formats.* Fatemeh Jalayer and C. Allin Cornell. November 2003.

PEER 2003/07   *Uncertainty Specification and Propagation for Loss Estimation Using FOSM Methods.* Jack W. Baker and C. Allin Cornell. September 2003.

PEER 2003/06   *Performance of Circular Reinforced Concrete Bridge Columns under Bidirectional Earthquake Loading.* Mahmoud M. Hachem, Stephen A. Mahin, and Jack P. Moehle. February 2003.

PEER 2003/05   *Response Assessment for Building-Specific Loss Estimation.* Eduardo Miranda and Shahram Taghavi. September 2003.

PEER 2003/04   *Experimental Assessment of Columns with Short Lap Splices Subjected to Cyclic Loads.* Murat Melek, John W. Wallace, and Joel Conte. April 2003.

PEER 2003/03   *Probabilistic Response Assessment for Building-Specific Loss Estimation.* Eduardo Miranda and Hesameddin Aslani. September 2003.

PEER 2003/02   *Software Framework for Collaborative Development of Nonlinear Dynamic Analysis Program.* Jun Peng and Kincho H. Law. September 2003.

PEER 2003/01   *Shake Table Tests and Analytical Studies on the Gravity Load Collapse of Reinforced Concrete Frames.* Kenneth John Elwood and Jack P. Moehle. November 2003.

PEER 2002/24   *Performance of Beam to Column Bridge Joints Subjected to a Large Velocity Pulse.* Natalie Gibson, André Filiatrault, and Scott A. Ashford. April 2002.

PEER 2002/23   *Effects of Large Velocity Pulses on Reinforced Concrete Bridge Columns.* Greg L. Orozco and Scott A. Ashford. April 2002.

PEER 2002/22 *Characterization of Large Velocity Pulses for Laboratory Testing.* Kenneth E. Cox and Scott A. Ashford. April 2002.

PEER 2002/21 *Fourth U.S.-Japan Workshop on Performance-Based Earthquake Engineering Methodology for Reinforced Concrete Building Structures.* December 2002.

PEER 2002/20 *Barriers to Adoption and Implementation of PBEE Innovations.* Peter J. May. August 2002.

PEER 2002/19 *Economic-Engineered Integrated Models for Earthquakes: Socioeconomic Impacts.* Peter Gordon, James E. Moore II, and Harry W. Richardson. July 2002.

PEER 2002/18 *Assessment of Reinforced Concrete Building Exterior Joints with Substandard Details.* Chris P. Pantelides, Jon Hansen, Justin Nadauld, and Lawrence D. Reaveley. May 2002.

PEER 2002/17 *Structural Characterization and Seismic Response Analysis of a Highway Overcrossing Equipped with Elastomeric Bearings and Fluid Dampers: A Case Study.* Nicos Makris and Jian Zhang. November 2002.

PEER 2002/16 *Estimation of Uncertainty in Geotechnical Properties for Performance-Based Earthquake Engineering.* Allen L. Jones, Steven L. Kramer, and Pedro Arduino. December 2002.

PEER 2002/15 *Seismic Behavior of Bridge Columns Subjected to Various Loading Patterns.* Asadollah Esmaeily-Gh. and Yan Xiao. December 2002.

PEER 2002/14 *Inelastic Seismic Response of Extended Pile Shaft Supported Bridge Structures.* T.C. Hutchinson, R.W. Boulanger, Y.H. Chai, and I.M. Idriss. December 2002.

PEER 2002/13 *Probabilistic Models and Fragility Estimates for Bridge Components and Systems.* Paolo Gardoni, Armen Der Kiureghian, and Khalid M. Mosalam. June 2002.

PEER 2002/12 *Effects of Fault Dip and Slip Rake on Near-Source Ground Motions: Why Chi-Chi Was a Relatively Mild M7.6 Earthquake.* Brad T. Aagaard, John F. Hall, and Thomas H. Heaton. December 2002.

PEER 2002/11 *Analytical and Experimental Study of Fiber-Reinforced Strip Isolators.* James M. Kelly and Shakhzod M. Takhirov. September 2002.

PEER 2002/10 *Centrifuge Modeling of Settlement and Lateral Spreading with Comparisons to Numerical Analyses.* Sivapalan Gajan and Bruce L. Kutter. January 2003.

PEER 2002/09 *Documentation and Analysis of Field Case Histories of Seismic Compression during the 1994 Northridge, California, Earthquake.* Jonathan P. Stewart, Patrick M. Smith, Daniel H. Whang, and Jonathan D. Bray. October 2002.

PEER 2002/08 *Component Testing, Stability Analysis and Characterization of Buckling-Restrained Unbonded Braces^{TM}.* Cameron Black, Nicos Makris, and Ian Aiken. September 2002.

PEER 2002/07 *Seismic Performance of Pile-Wharf Connections.* Charles W. Roeder, Robert Graff, Jennifer Soderstrom, and Jun Han Yoo. December 2001.

PEER 2002/06 *The Use of Benefit-Cost Analysis for Evaluation of Performance-Based Earthquake Engineering Decisions.* Richard O. Zerbe and Anthony Falit-Baiamonte. September 2001.

PEER 2002/05 *Guidelines, Specifications, and Seismic Performance Characterization of Nonstructural Building Components and Equipment.* André Filiatrault, Constantin Christopoulos, and Christopher Stearns. September 2001.

PEER 2002/04 *Consortium of Organizations for Strong-Motion Observation Systems and the Pacific Earthquake Engineering Research Center Lifelines Program: Invited Workshop on Archiving and Web Dissemination of Geotechnical Data, 4–5 October 2001.* September 2002.

PEER 2002/03 *Investigation of Sensitivity of Building Loss Estimates to Major Uncertain Variables for the Van Nuys Testbed.* Keith A. Porter, James L. Beck, and Rustem V. Shaikhutdinov. August 2002.

PEER 2002/02 *The Third U.S.-Japan Workshop on Performance-Based Earthquake Engineering Methodology for Reinforced Concrete Building Structures.* July 2002.

PEER 2002/01 *Nonstructural Loss Estimation: The UC Berkeley Case Study.* Mary C. Comerio and John C. Stallmeyer. December 2001.

PEER 2001/16 *Statistics of SDF-System Estimate of Roof Displacement for Pushover Analysis of Buildings.* Anil K. Chopra, Rakesh K. Goel, and Chatpan Chintanapakdee. December 2001.

PEER 2001/15 *Damage to Bridges during the 2001 Nisqually Earthquake.* R. Tyler Ranf, Marc O. Eberhard, and Michael P. Berry. November 2001.

PEER 2001/14 *Rocking Response of Equipment Anchored to a Base Foundation.* Nicos Makris and Cameron J. Black. September 2001.

PEER 2001/13   *Modeling Soil Liquefaction Hazards for Performance-Based Earthquake Engineering.* Steven L. Kramer and Ahmed-W. Elgamal. February 2001.

PEER 2001/12   *Development of Geotechnical Capabilities in OpenSees.* Boris Jeremić. September 2001.

PEER 2001/11   *Analytical and Experimental Study of Fiber-Reinforced Elastomeric Isolators.* James M. Kelly and Shakhzod M. Takhirov. September 2001.

PEER 2001/10   *Amplification Factors for Spectral Acceleration in Active Regions.* Jonathan P. Stewart, Andrew H. Liu, Yoojoong Choi, and Mehmet B. Baturay. December 2001.

PEER 2001/09   *Ground Motion Evaluation Procedures for Performance-Based Design.* Jonathan P. Stewart, Shyh-Jeng Chiou, Jonathan D. Bray, Robert W. Graves, Paul G. Somerville, and Norman A. Abrahamson. September 2001.

PEER 2001/08   *Experimental and Computational Evaluation of Reinforced Concrete Bridge Beam-Column Connections for Seismic Performance.* Clay J. Naito, Jack P. Moehle, and Khalid M. Mosalam. November 2001.

PEER 2001/07   *The Rocking Spectrum and the Shortcomings of Design Guidelines.* Nicos Makris and Dimitrios Konstantinidis. August 2001.

PEER 2001/06   *Development of an Electrical Substation Equipment Performance Database for Evaluation of Equipment Fragilities.* Thalia Agnanos. April 1999.

PEER 2001/05   *Stiffness Analysis of Fiber-Reinforced Elastomeric Isolators.* Hsiang-Chuan Tsai and James M. Kelly. May 2001.

PEER 2001/04   *Organizational and Societal Considerations for Performance-Based Earthquake Engineering.* Peter J. May. April 2001.

PEER 2001/03   *A Modal Pushover Analysis Procedure to Estimate Seismic Demands for Buildings: Theory and Preliminary Evaluation.* Anil K. Chopra and Rakesh K. Goel. January 2001.

PEER 2001/02   *Seismic Response Analysis of Highway Overcrossings Including Soil-Structure Interaction.* Jian Zhang and Nicos Makris. March 2001.

PEER 2001/01   *Experimental Study of Large Seismic Steel Beam-to-Column Connections.* Egor P. Popov and Shakhzod M. Takhirov. November 2000.

PEER 2000/10   *The Second U.S.-Japan Workshop on Performance-Based Earthquake Engineering Methodology for Reinforced Concrete Building Structures.* March 2000.

PEER 2000/09   *Structural Engineering Reconnaissance of the August 17, 1999 Earthquake: Kocaeli (Izmit), Turkey.* Halil Sezen, Kenneth J. Elwood, Andrew S. Whittaker, Khalid Mosalam, John J. Wallace, and John F. Stanton. December 2000.

PEER 2000/08   *Behavior of Reinforced Concrete Bridge Columns Having Varying Aspect Ratios and Varying Lengths of Confinement.* Anthony J. Calderone, Dawn E. Lehman, and Jack P. Moehle. January 2001.

PEER 2000/07   *Cover-Plate and Flange-Plate Reinforced Steel Moment-Resisting Connections.* Taejin Kim, Andrew S. Whittaker, Amir S. Gilani, Vitelmo V. Bertero, and Shakhzod M. Takhirov. September 2000.

PEER 2000/06   *Seismic Evaluation and Analysis of 230-kV Disconnect Switches.* Amir S. J. Gilani, Andrew S. Whittaker, Gregory L. Fenves, Chun-Hao Chen, Henry Ho, and Eric Fujisaki. July 2000.

PEER 2000/05   *Performance-Based Evaluation of Exterior Reinforced Concrete Building Joints for Seismic Excitation.* Chandra Clyde, Chris P. Pantelides, and Lawrence D. Reaveley. July 2000.

PEER 2000/04   *An Evaluation of Seismic Energy Demand: An Attenuation Approach.* Chung-Che Chou and Chia-Ming Uang. July 1999.

PEER 2000/03   *Framing Earthquake Retrofitting Decisions: The Case of Hillside Homes in Los Angeles.* Detlof von Winterfeldt, Nels Roselund, and Alicia Kitsuse. March 2000.

PEER 2000/02   *U.S.-Japan Workshop on the Effects of Near-Field Earthquake Shaking.* Andrew Whittaker, ed. July 2000.

PEER 2000/01   *Further Studies on Seismic Interaction in Interconnected Electrical Substation Equipment.* Armen Der Kiureghian, Kee-Jeung Hong, and Jerome L. Sackman. November 1999.

PEER 1999/14   *Seismic Evaluation and Retrofit of 230-kV Porcelain Transformer Bushings.* Amir S. Gilani, Andrew S. Whittaker, Gregory L. Fenves, and Eric Fujisaki. December 1999.

PEER 1999/13   *Building Vulnerability Studies: Modeling and Evaluation of Tilt-up and Steel Reinforced Concrete Buildings.* John W. Wallace, Jonathan P. Stewart, and Andrew S. Whittaker, editors. December 1999.

PEER 1999/12   *Rehabilitation of Nonductile RC Frame Building Using Encasement Plates and Energy-Dissipating Devices.* Mehrdad Sasani, Vitelmo V. Bertero, James C. Anderson. December 1999.

PEER 1999/11   *Performance Evaluation Database for Concrete Bridge Components and Systems under Simulated Seismic Loads.* Yael D. Hose and Frieder Seible. November 1999.

PEER 1999/10   *U.S.-Japan Workshop on Performance-Based Earthquake Engineering Methodology for Reinforced Concrete Building Structures.* December 1999.

PEER 1999/09   *Performance Improvement of Long Period Building Structures Subjected to Severe Pulse-Type Ground Motions.* James C. Anderson, Vitelmo V. Bertero, and Raul Bertero. October 1999.

PEER 1999/08   *Envelopes for Seismic Response Vectors.* Charles Menun and Armen Der Kiureghian. July 1999.

PEER 1999/07   *Documentation of Strengths and Weaknesses of Current Computer Analysis Methods for Seismic Performance of Reinforced Concrete Members.* William F. Cofer. November 1999.

PEER 1999/06   *Rocking Response and Overturning of Anchored Equipment under Seismic Excitations.* Nicos Makris and Jian Zhang. November 1999.

PEER 1999/05   *Seismic Evaluation of 550 kV Porcelain Transformer Bushings.* Amir S. Gilani, Andrew S. Whittaker, Gregory L. Fenves, and Eric Fujisaki. October 1999.

PEER 1999/04   *Adoption and Enforcement of Earthquake Risk-Reduction Measures.* Peter J. May, Raymond J. Burby, T. Jens Feeley, and Robert Wood.

PEER 1999/03   *Task 3 Characterization of Site Response General Site Categories.* Adrian Rodriguez-Marek, Jonathan D. Bray, and Norman Abrahamson. February 1999.

PEER 1999/02   *Capacity-Demand-Diagram Methods for Estimating Seismic Deformation of Inelastic Structures: SDF Systems.* Anil K. Chopra and Rakesh Goel. April 1999.

PEER 1999/01   *Interaction in Interconnected Electrical Substation Equipment Subjected to Earthquake Ground Motions.* Armen Der Kiureghian, Jerome L. Sackman, and Kee-Jeung Hong. February 1999.

PEER 1998/08   *Behavior and Failure Analysis of a Multiple-Frame Highway Bridge in the 1994 Northridge Earthquake.* Gregory L. Fenves and Michael Ellery. December 1998.

PEER 1998/07   *Empirical Evaluation of Inertial Soil-Structure Interaction Effects.* Jonathan P. Stewart, Raymond B. Seed, and Gregory L. Fenves. November 1998.

PEER 1998/06   *Effect of Damping Mechanisms on the Response of Seismic Isolated Structures.* Nicos Makris and Shih-Po Chang. November 1998.

PEER 1998/05   *Rocking Response and Overturning of Equipment under Horizontal Pulse-Type Motions.* Nicos Makris and Yiannis Roussos. October 1998.

PEER 1998/04   *Pacific Earthquake Engineering Research Invitational Workshop Proceedings, May 14–15, 1998: Defining the Links between Planning, Policy Analysis, Economics and Earthquake Engineering.* Mary Comerio and Peter Gordon. September 1998.

PEER 1998/03   *Repair/Upgrade Procedures for Welded Beam to Column Connections.* James C. Anderson and Xiaojing Duan. May 1998.

PEER 1998/02   *Seismic Evaluation of 196 kV Porcelain Transformer Bushings.* Amir S. Gilani, Juan W. Chavez, Gregory L. Fenves, and Andrew S. Whittaker. May 1998.

PEER 1998/01   *Seismic Performance of Well-Confined Concrete Bridge Columns.* Dawn E. Lehman and Jack P. Moehle. December 2000.

ONLINE REPORTS

The following PEER reports are available by Internet only at http://peer.berkeley.edu/publications/peer_reports.html

PEER 2012/101 *Mechanics of Fiber Reinforced Bearings.* James M. Kelly and Andrea Calabrese. February 2012.

PEER 2011/107 *Nonlinear Site Response and Seismic Compression at Vertical Array Strongly Shaken by 2007 Niigata-ken Chuetsu-oki Earthquake.* Eric Yee, Jonathan P. Stewart, and Kohji Tokimatsu. December 2011.

PEER 2011/106 *Self Compacting Hybrid Fiber Reinforced Concrete Composites for Bridge Columns.* Pardeep Kumar, Gabriel Jen, William Trono, Marios Panagiotou, and Claudia Ostertag. September 2011.

PEER 2011/105 *Stochastic Dynamic Analysis of Bridges Subjected to Spacially Varying Ground Motions.* Katerina Konakli and Armen Der Kiureghian. August 2011.

PEER 2011/104 *Design and Instrumentation of the 2010 E-Defense Four-Story Reinforced Concrete and Post-Tensioned Concrete Buildings.* Takuya Nagae, Kenichi Tahara, Taizo Matsumori, Hitoshi Shiohara, Toshimi Kabeyasawa, Susumu Kono, Minehiro Nishiyama (Japanese Research Team) and John Wallace, Wassim Ghannoum, Jack Moehle, Richard Sause, Wesley Keller, Zeynep Tuna (U.S. Research Team). June 2011.

PEER 2011/103 *In-Situ Monitoring of the Force Output of Fluid Dampers: Experimental Investigation.* Dimitrios Konstantinidis, James M. Kelly, and Nicos Makris. April 2011.

PEER 2011/102 *Ground-motion prediction equations 1964 - 2010.* John Douglas. April 2011.

PEER 2011/101 *Report of the Eighth Planning Meeting of NEES/E-Defense Collaborative Research on Earthquake Engineering.* Convened by the Hyogo Earthquake Engineering Research Center (NIED), NEES Consortium, Inc. February 2011.

PEER 2010/111 *Modeling and Acceptance Criteria for Seismic Design and Analysis of Tall Buildings.* Task 7 Report for the Tall Buildings Initiative - Published jointly by the Applied Technology Council. October 2010.

PEER 2010/110 *Seismic Performance Assessment and Probabilistic Repair Cost Analysis of Precast Concrete Cladding Systems for Multistory Buildings.* Jeffrey P. Hunt and Božidar Stojadinovic. November 2010.

PEER 2010/109 *Report of the Seventh Joint Planning Meeting of NEES/E-Defense Collaboration on Earthquake Engineering. Held at the E-Defense, Miki, and Shin-Kobe, Japan, September 18–19, 2009.* August 2010.

PEER 2010/108 *Probabilistic Tsunami Hazard in California.* Hong Kie Thio, Paul Somerville, and Jascha Polet, preparers. October 2010.

PEER 2010/107 *Performance and Reliability of Exposed Column Base Plate Connections for Steel Moment-Resisting Frames.* Ady Aviram, Božidar Stojadinovic, and Armen Der Kiureghian. August 2010.

PEER 2010/106 *Verification of Probabilistic Seismic Hazard Analysis Computer Programs.* Patricia Thomas, Ivan Wong, and Norman Abrahamson. May 2010.

PEER 2010/105 *Structural Engineering Reconnaissance of the April 6, 2009, Abruzzo, Italy, Earthquake, and Lessons Learned.* M. Selim Günay and Khalid M. Mosalam. April 2010.

PEER 2010/104 *Simulating the Inelastic Seismic Behavior of Steel Braced Frames, Including the Effects of Low-Cycle Fatigue.* Yuli Huang and Stephen A. Mahin. April 2010.

PEER 2010/103 *Post-Earthquake Traffic Capacity of Modern Bridges in California.* Vesna Terzic and Božidar Stojadinović. March 2010.

PEER 2010/102 *Analysis of Cumulative Absolute Velocity (CAV) and JMA Instrumental Seismic Intensity (I_{JMA}) Using the PEER–NGA Strong Motion Database.* Kenneth W. Campbell and Yousef Bozorgnia. February 2010.

PEER 2010/101 *Rocking Response of Bridges on Shallow Foundations.* Jose A. Ugalde, Bruce L. Kutter, and Boris Jeremic. April 2010.

PEER 2009/109 *Simulation and Performance-Based Earthquake Engineering Assessment of Self-Centering Post-Tensioned Concrete Bridge Systems.* Won K. Lee and Sarah L. Billington. December 2009.

PEER 2009/108 *PEER Lifelines Geotechnical Virtual Data Center.* J. Carl Stepp, Daniel J. Ponti, Loren L. Turner, Jennifer N. Swift, Sean Devlin, Yang Zhu, Jean Benoit, and John Bobbitt. September 2009.

PEER 2009/107 *Experimental and Computational Evaluation of Current and Innovative In-Span Hinge Details in Reinforced Concrete Box-Girder Bridges: Part 2: Post-Test Analysis and Design Recommendations.* Matias A. Hube and Khalid M. Mosalam. December 2009.

PEER 2009/106 *Shear Strength Models of Exterior Beam-Column Joints without Transverse Reinforcement.* Sangjoon Park and Khalid M. Mosalam. November 2009.

PEER 2009/105 *Reduced Uncertainty of Ground Motion Prediction Equations through Bayesian Variance Analysis.* Robb Eric S. Moss. November 2009.

PEER 2009/104 *Advanced Implementation of Hybrid Simulation.* Andreas H. Schellenberg, Stephen A. Mahin, Gregory L. Fenves. November 2009.

PEER 2009/103 *Performance Evaluation of Innovative Steel Braced Frames.* T. Y. Yang, Jack P. Moehle, and Božidar Stojadinovic. August 2009.

PEER 2009/102 *Reinvestigation of Liquefaction and Nonliquefaction Case Histories from the 1976 Tangshan Earthquake.* Robb Eric Moss, Robert E. Kayen, Liyuan Tong, Songyu Liu, Guojun Cai, and Jiaer Wu. August 2009.

PEER 2009/101 *Report of the First Joint Planning Meeting for the Second Phase of NEES/E-Defense Collaborative Research on Earthquake Engineering.* Stephen A. Mahin et al. July 2009.

PEER 2008/104 *Experimental and Analytical Study of the Seismic Performance of Retaining Structures.* Linda Al Atik and Nicholas Sitar. January 2009.

PEER 2008/103 *Experimental and Computational Evaluation of Current and Innovative In-Span Hinge Details in Reinforced Concrete Box-Girder Bridges. Part 1: Experimental Findings and Pre-Test Analysis.* Matias A. Hube and Khalid M. Mosalam. January 2009.

PEER 2008/102 *Modeling of Unreinforced Masonry Infill Walls Considering In-Plane and Out-of-Plane Interaction.* Stephen Kadysiewski and Khalid M. Mosalam. January 2009.

PEER 2008/101 *Seismic Performance Objectives for Tall Buildings.* William T. Holmes, Charles Kircher, William Petak, and Nabih Youssef. August 2008.

PEER 2007/101 *Generalized Hybrid Simulation Framework for Structural Systems Subjected to Seismic Loading.* Tarek Elkhoraibi and Khalid M. Mosalam. July 2007.

PEER 2007/100 *Seismic Evaluation of Reinforced Concrete Buildings Including Effects of Masonry Infill Walls.* Alidad Hashemi and Khalid M. Mosalam. July 2007.